Investigation of new semiconductor materials for wide band-gap devices

by

Daniel Alasdair Hunter

University of Strathclyde

A thesis submitted to
the Department of Physics
University of Strathclyde
for the degree of
Doctor of Philosophy

October 23, 2023

Declaration of author's right

This thesis is the result of the author's original research. It has been composed by the author and has not been previously submitted for examination which has led to the award of a degree.

The copyright of this thesis belongs to the author under the terms of the United Kingdom Copyright Acts as qualified by University of Strathclyde Regulation 3.50. Due acknowledgement must always be made of the use of any material contained in, or derived from, this thesis.

Signed:

Date:

Abstract

This thesis investigates the compositional and optical properties of wide bandgap III-nitride and gallium oxide semiconductor materials using scanning electron microscopy techniques. The primarily used techniques used here were wavelength dispersive X-ray spectroscopy (WDX) and cathodoluminescence (CL) with other electron microscopy and spectroscopic techniques used to assist in the characterisation of the semiconductor materials. Compositional measurements were performed to determine bulk alloying levels within the semiconductor and trace element analyses e.g doping concentrations. Investigations benefited from the correlative nature of the WDX and CL measurements, allowing simultaneous compositional and optical mapping of the semiconductor, attributing the sample luminescence to compositional spatial regions or features of the material.

Semi- and non-polar $Al_xGa_{1-x}N$ alloys showed similar Al incorporation as polar material, consistent across the entire AlN range. Si incorporation within semi-polar $Al_xGa_{1-x}N$ was found to be independent of bulk composition however the dopant concentration resulting in onset of Si self-compensation increased with AlN composition unlike polar $Al_xGa_{1-x}N$. CL measurements show good agreement with the near-band edge (NBE) emission energy and the material bandgap expected from the alloy concentration for all $Al_xGa_{1-x}N$ crystal orientations. Compared to polar $Al_xGa_{1-x}N$ NBE emission showed a high degree of broadening with increasing AlN content due to compositional variation in the samples. NBE broadening was also accompanied with intense defect luminescence attributed to oxygenated V_{III} complexes.

Indium-gallium oxide (IGO) alloys were grown with low to high In contents with

notable crystallographic phase changes from monoclinic to mixed to cubic as the In content was increased. CL measurements show UV, blue and green luminescence with the spectral intensities shifting from dominant UV in near pure Ga_2O_3 to enhanced blue and green in high In containing materials. Spectral band energies also decreased as the In composition increased due to the reduction of the material bandgap.

The incorporation of Sn into Ga_2O_3 alloys was investigated for thin films grown on various material substrates. Sn alloying levels was found to be dependent on multiple growth factors: Sn availability, substrate choice and growth temperature. Optical properties exhibited similar to the IGO samples for both intensity and energy shifts of the three spectral bands. Electronic investigations into the photodetector properties of the TGO films showed superior responsivity and high gain compared to Ga_2O_3 devices while operating in lower energy UV due to the bandgap reduction.

An investigation into the impact of X-ray secondary fluorescence on WDX measurements on semiconductor thin films was completed as a separate computation study. Results show there was a negligible effect of secondary fluorescence on WDX measurements on multiple semiconductor families with various material substrates, unlike for geological samples. The reduced beam energy required for semiconductor thin film analyses minimises the impact of secondary fluorescence on bulk quantitative measurements. However trace element analyses may be impacted by secondary fluorescence when using the typical beam conditions for thin film specimens, particularly when the substrate also contains the trace element, the impact of secondary fluorescence may be reduced however by operating with the lowest suitable beam energy possible, minimising the size of the secondary excitation volume.

Acknowledgements

I would first like to thank my supervisor, Professor Robert W. Martin, for his guidance and assistance throughout my PhD career. I am extremely grateful for his constant support, direction and academic advice and for the regular laughs in our meetings. Thank you for giving me this opportunity.

Secondly, I would also like to thank my second supervisor Dr Paul R. Edwards. His training on the equipment and troubleshooting when something inevitably went wrong, alongside his help with data analysis and proof reading were fundamental to the completion of the work within this thesis.

I give a special thanks to Dr Naresh Kumar-Gunasekar for his assistance with the experimental investigations within this thesis, for collecting and analysing any EBSD data, sourcing the TGO and IGO materials for these studies and for being available for discussions whenever they were needed.

Thank you to the members of the SSD group, past and present, that made my years as a PhD student enjoyable and full of laughs during the Level 2 lunches or conference meetings. A particular thanks to my office mates, Douglas and James, and those who assisted me with experimental work: David, Fabien and Lucia.

I also give thanks to all my collaborators for providing me with the semiconductor materials investigated here and the additional data they acquired which has been included within this thesis: Dr's Isa Hatipoglu, Partha Mukhopadhyay, Humberto M. Foronda, Holger von Wenckstern and Duc V. Dinh.

The individual list of friends I would like to thank would be too excessive to write down but a special mention to the Livi boys, the CSC and all the friends I met in Glasgow in the last 9 years.

Lastly, to my family, I am forever grateful for the support, both financially and emotionally, and the endless encouragement you have given me throughout my many years in education. A special thanks to my mum and dad, I cannot say thanks enough for everything you have done for me and your constant belief in me.

List of publications

First Authored

1. **D. A. Hunter** , S. P. Lavery, P. R. Edwards and R. W. Martin, *Assessing the Impact of Secondary Fluorescence on X-Ray Microanalysis Results from Semiconductor Thin Films*, Microscopy and Microanalysis, Vol. 28 (2022) pp. 1–12.
2. **D. A. Hunter**, G. Naresh-Kumar, P. R. Edwards, F. C. P. Massabuau, I. Hatipoglu, P. Mukhopadhyay, W. V. Schoenfeld, R. W. Martin, *Optical and compositional analysis of tin-gallium oxide epilayers on a range of material substrates*, In review
3. **D. A. Hunter**, G. Naresh-Kumar, P. R. Edwards, I. Hatipoglu, P. Mukhopadhyay, W. V. Schoenfeld, H. Von Wenckstern, R. W. Martin, *Electron microscopy investigation into the optical properties of indium-gallium oxide alloys*, In preparation

Co-Authored

4. H. M. Foronda, **D. A. Hunter**, M. Pietsch, L. Sulmoni, A. Muhin, S. Graupeter, N. Susilo, M. Schilling, J. Enslin, K. Irmscher, R. W. Martin, T. Wernicke, and M. Kneissl, *Electrical properties of (11-22) Si:AlGaN layers at high Al contents grown by metal-organic vapor phase epitaxy*, Applied Physics Letters, Vol. 117 (2020) pp. 221101.

5. L. Spasevski, B. Buse, P. R. Edwards, **D. A. Hunter**, J. Enslin, H. M. Foronda, T. Wernicke, F. Mehnke, P. J. Parbrook, M. Kneissl and R. W. Martin, *Quantification of Trace-Level Silicon Doping in* $Al_xGa_{1-x}N$ *Films Using Wavelength-Dispersive X-Ray Microanalysis*, Microscopy and Microanalysis, Vol. 27 (2021) pp. 696–704.

6. P. Mukhopadhyay, I. Hatipoglu, T. Selvan Sakthivel, **D. A. Hunter**, P. R. Edwards, R. W. Martin, G. Naresh-Kumar, S. Seal, and W. V. Schoenfeld, *High Figure-of-Merit Gallium Oxide UV Photodetector on Silicon by Molecular Beam Epitaxy: A Path toward Monolithic Integration*, Advanced Photonics Research, Vol. 2 (2021) pp. 2000067.

7. I. Hatipoglu, **D. A. Hunter**, P. Mukhopadhyay, M. S. Williams, P. R. Edwards, R. W. Martin, W. V. Schoenfeld and G. Naresh-Kumar, *Correlation between deep-level defects and functional properties of* β-$(Sn_xGa_{1-x})_2O_3$ *on Si photodetectors*, Journal of Applied Physics, Vol. 130 (2021) pp. 204501.

8. P. Mukhopadhyay, I. Hatipoglu, Y. K. Frodason, J. B. Varley, M. S. Williams, **D. A. Hunter**, G. Naresh-Kumar, P. R. Edwards, R. W. Martin, F. Wu, A. Mauze, J. S. Speck and W. V. Schoenfeld, *Role of defects in ultra-high gain in fast planar tin gallium oxide UV-C photodetector by MBE*, Applied Physics Letters, Vol. 121 (2022) pp. 111105.

Contents

Chapter 1

Introduction

Throughout the 1900s and early 2000s the intense research into semiconductor materials, particularly the wide bandgap III-nitrides, unlocked the ability to manufacture optical emitters and detectors operating in the UV regime. Notable milestones within this time period being the first generation of visible light from an LED, being red emission from a GaP_xAs_{1-x} LED [1]; the growth of the GaN single crystal in 1969 [2]; the fabrication of the first GaN LED emitting within the blue-UV spectral region by Amano and Akasaki in 1989 [3] for which they were honoured with the 2014 Nobel Prize in Physics along with Nakamura [4]. A more recent milestone was the 2006 development of the first AlN LED [5]. These LEDs started an optical revolution, with solid-state lighting being the replacement of traditional, highly inefficient incandescent light bulbs or lamps containing harmful mercury. General lighting aside, there are more advanced applications for UV light across the entire spectral range that are possible since the development of these LEDs.

UV emission is traditionally split into three separate brackets; UV-A (400-315 nm), UV-B (315-280 nm) and UV-C (280-100 nm). Across this energy range their are a number of medical uses for UV radiation from skin therapy in the UV-A and low energy UV-B ranges to the sterilisation of medical equipment using the high energy UV-C [6]. Similarly, specific wavelengths of UV light have been found to be highly effective in degrading toxic impurities within water [7, 8]. As the effectiveness of these water cleansing processes relies on UV light of a specific wavelength traditional devices featuring mercury lamps are non-ideal due to the fixed emission wavelength of the mercury. Alternatively, medical devices can be fabricated using UV LEDs tuned to the required wavelength, through the use of ternary alloys (e.g $Al_xGa_{1-x}N$) in the LED active region. Outside of the health sector there are other prospective applications for UV LEDs such as underwater, space and non-line of sight communication systems [9–11] and UV curing during lithography [12].

Currently the issue of LED efficiency is what is preventing the implementation of these UV devices. III-nitride LED efficiency drops drastically as you move into the UV, with the wall plug efficiency of blue-near UV LED efficiency being ∼80% plummeting to sub 10% for modern UV-C LEDs [12,13]. This is due to a combination of crystallographic, doping, light extraction and intrinsic electrical issues present in III-nitride semiconductors which must be addressed.

The wide bandgap of III-nitride materials making them deep UV emitters also makes them suitable as UV photodetectors. A particular type of UV photodetector of interest is a solar-blind photodetector. This type of photodetector is one that is unaffected by the natural UV light coming from the sun ($\lambda > 280$ nm [14]) . These photodetectors can be applied within a number of fields, particularly for the monitoring of the depletion of the ozone layer [15] and for flame detection used within military defence and industrial safety systems [16, 17].

Another material of particular interest for use within solar-blind photodetectors is gallium oxide, Ga_2O_3. Research into the properties of Ga_2O_3 and its alloys are relatively in their infancy, kicking off from the 60s-90s and properly booming in the recent years of the early 2000s [18]. The high Baliga figure of merit of Ga_2O_3 makes it desirable for high power electronics and current research shows great promise that the material will be well suited within these photodetectors. However, these investigations are still in the preliminary stage [19] and further research is required before the material is fully implemented into devices.

Exhaustive research into the aforementioned semiconductors particularly into growing high quality, low defect materials with suitable n-type and p-type doping and the ideal architecture for the UV devices is currently of paramount importance. This will allow the material to transition from being prospective wide bandgap semiconductors for UV devices to commercially viable optoelectronics.

This thesis features the characterisation of the semiconductor materials $Al_xGa_{1-x}N$, tin-gallium oxide and indium-gallium oxide with these materials being grown and provided from the following collaborators: Dr Duc V. Dinh from Dr M. Pristovsek's research group at the Nagoya University, Dr Humberto M. Foronda in Prof. M. Kneissl's group at the Technische Universität Berlin (TU Berlin); Prof. W. Schoenfeld's group at The University of Central Florida, specifically: Drs Isa Hatipoglu & Partha Mukhopadhyay and Dr Holger von Wenckstern from Universität Leipzig.

The samples have been primarily been characterised through the electron microscopy techniques of WDX and CL, with some SE imaging and spectroscopic measurements also taken. All the above measurements were taken at the University of Strathclyde. Measurements were also provided by the respective collaborators to assist those taken as part of this thesis namely: XRD and AFM from Dr Dinh; transmission spectroscopy & electrical measurements from Dr Foronda; XRD, EBSD and electrical measurements from Dr Hatipoglu. Chapter 4 features the optical, compositional and electronic characterisation of MOCVD grown $Al_xGa_{1-x}N$ with polar, semi-polar and non-polar crystal orientations from Nagoya and of semi-polar Si doped $Al_xGa_{1-x}N$ from Berlin. Chapter 5 investigates the In incorporation and specimen luminescence from PLD grown combinatorial IGO from Leipzig and of a series of MBE grown IGO samples from Florida. Chapter 6 is similar to that of Chapter 5 however for Sn incorporation within Ga_2O_3, and goes on to assess the feasibility of these materials within UV solar-blind photodetectors. Chapter 7 computationally assesses the influence of X-ray secondary fluorescence on compositional WDX measurements and provides a quality check on the physical measurements taken in Chapters 4-7.

Chapter 2

Background

This chapter will detail the key information regarding the semiconductor materials investigated within this thesis; their material properties and applications; doping, alloying, crystal defects and finally the basics of the semiconductor growth mechanisms that have been used to produce the samples studied in this thesis.

2.1 Gallium oxide, Ga_2O_3

Gallium oxide (Ga_2O_3) is an emerging ultra-wide bandgap semiconductor with a bandgap between 4.7-5.3 eV depending on material polymorph [20–22]. This large bandgap makes it an ideal material for uses within modern state of the art, solar-blind UV photodetectors with applications with communication, environmental monitoring and defence systems [10, 11, 15, 16]. Along with this ultra-wide bandgap there is an extremely large breakdown electric field (E_{BD}) associated with the material ($E_{BD} \approx 8$ MV/cm [23]) making it highly desirable for future use within high power electronic devices [24, 25].

2.1.1 Physical properties of Ga_2O_3

Ga_2O_3 exists as five polymorphs: the thermodynamically stable β-Ga_2O_3 and four metastable polymorphs [α, γ, δ, ϵ/κ]-Ga_2O_3. As it is the most stable the monoclinic

β-Ga_2O_3 has been the most extensively researched. From the metastable polymorphs rhombohedral α-Ga_2O_3 is currently the most investigated. High temperature growth ($T_g \leq 500°C$ for α-, $T_g \leq 700°C$ for ϵ/κ-) [26] and annealing of the metastable polymorphs results in crystal breakdown and a phase change to stable β-Ga_2O_3 [27]. A diagram detailing the phase change pathways and the thermodynamic relationship between these polymorphs and their hydrates is shown in Figure 2.1.

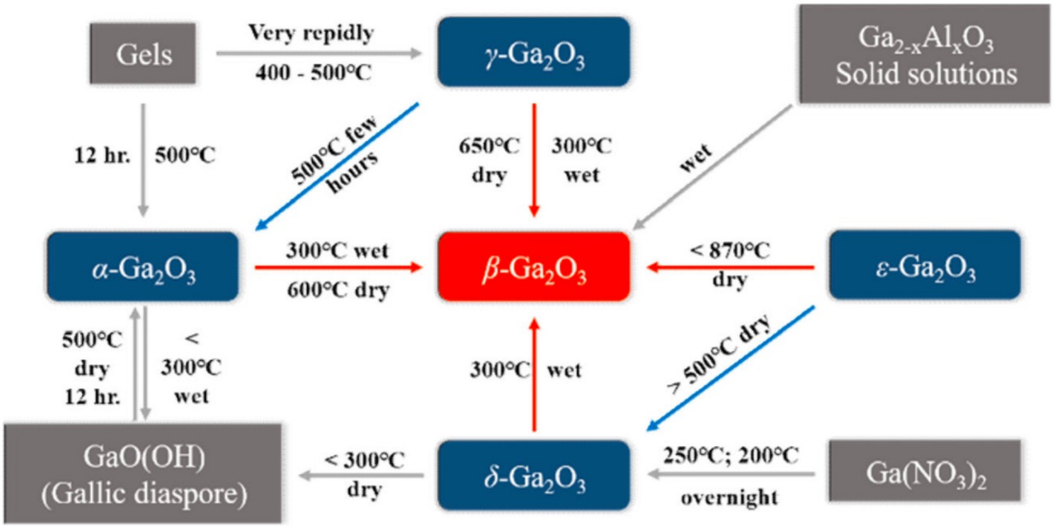

Figure 2.1: Phase change pathways of the Ga_2O_3 polymorphs with temperature, extracted from [20], adapted from [27].

Disregarding the instability of the polymorphs there are benefits which these phases have over β-Ga_2O_3 e.g. crystal structure matching of α-Ga_2O_3 with corundum sapphire (Al_2O_3) substrates allowing high quality film growth [20]. Investigations in this thesis will primarily focus on β-Ga_2O_3 and ternary alloys based on it and this polymorph shall therefore be explained in greater detail.

2.1.2 Crystallographic structure

As mentioned previously β-Ga_2O_3 exists in a monoclinic crystal structure with a C2/m space group. The β-Ga_2O_3 unit cell is shown in Figure 2.2 with the following

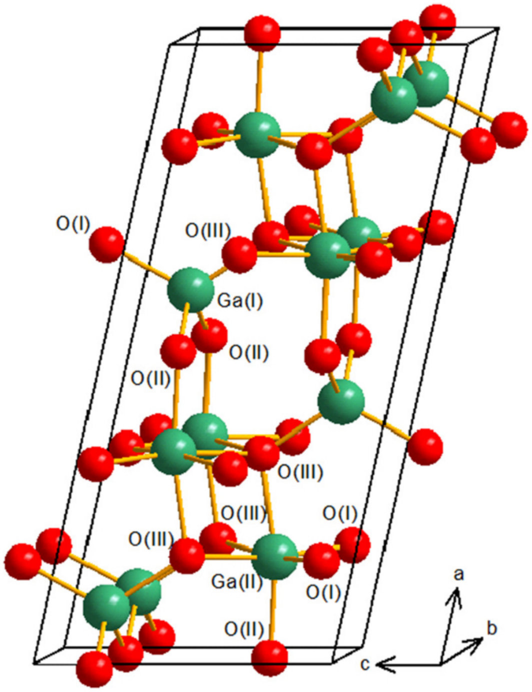

Figure 2.2: β-Ga_2O_3 crystal structure with lattice constants: a =1.22 nm, b =0.30nm, c =0.58nm β =103.8 ° [20]. Extracted from [28]

lattice constants: a =1.22 nm, b =0.30nm, c =0.58nm β =103.8 ° [20]. Within the β-Ga_2O_3 unit cell there are two distinct gallium sites and three distinct oxygen sites. Half of the Ga atoms are situated at a tetrahedral site, surrounded by four O atoms, Ga_I, with the other half of the Ga atoms occupying octahedral sites surrounded by six oxygen atoms, Ga_{II}. O_I and O_{II} are each bonded to three gallium atoms (Ga_I + $2Ga_{II}$ & $2Ga_I$ + Ga_{II} respectively) while O_{III} sites are bonded to four gallium atoms (Ga_I + $3Ga_{II}$).

2.1.3 Band Structure

The semiconductor bandgap of β-Ga_2O_3 is quoted as ≈4.8 eV [20]. The material does feature an indirect bandgap slightly smaller than the direct by approximately a few hundredths of an eV. As direct transitions are more likely than indirect and the similar energies of the direct and indirect bandgaps, β-Ga_2O_3 is "generally" described as a direct semiconductor.

The band structure of Ga_2O_3 has been extensively studied through computational methods e.g. density function theory (DFT) and hybrid functional calculations [29–31]. These calculations reveal the conduction band minimum (CMB) and a valence band maxima occur at the Γ-point of the Brillouin-zone with a direct band gap of approximately 4.87 eV however the true valence band maximum (VBM) occurs at the M-point resulting in an indirect band gap (Γ-M) of 4.83 eV [30].

The same band structure has also been confirmed experimentally [18, 32] with slightly different values for the band gap energies (Γ-Γ E_g =4.9 eV, Γ-M =4.85 eV). As the energy differences between these two transitions is small (≈0.05 eV) and direct transitions are preferred due to the conversation of momentum, Ga_2O_3 is effectively a direct bandgap semiconductor.

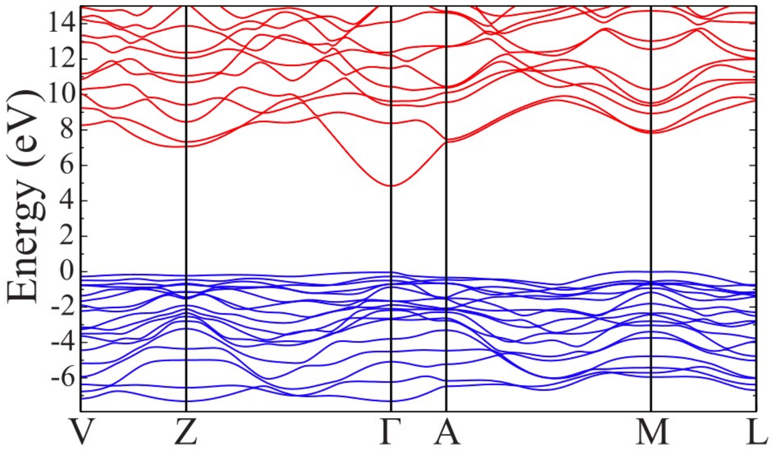

Figure 2.3: Band structure of β-Ga_2O_3. VBM is located at M point with the direct bandgap (E_g ≈4.8 eV) between the Γ-Γ points. Extracted from [30]

2.1.4 Doping

Unintentionally doped (UID) Ga_2O_3 has been found to naturally exhibit *n*-type conductivity, usually attributed to Si impurities [33] but oxygen vacancies (V_O) have also been said to be responsible for this natural conductivity [34]. In order for Ga_2O_3 to be feasible for device applications the conductivity must be controlled through doping.

Doping can be categorised into two different forms, n-type and p-type. N-type doping refers to the substitution of a lattice atom with an atom with a greater number of outer shell electrons. This dopant has added an additional electron into the lattice and is described as a donor. When the dopant contains fewer electrons than the element being substituted a hole is induced in the crystal (holes being a quasi-particle representing the absence of an electron) and the dopant acts as an acceptor, this described as p-type conductivity.

Controlled n-type conductivity is typically achieved in Ga_2O_3 through the substitution of Ga^{3+} ion with a group IV ion such as Si^{4+} or Sn^{4+} [35–37] which act as shallow donors with activation energies of ≤ 50 meV [18,36,38] and ≤ 60 meV [36,39] respectively.

P-type conductivity has proved to be quite difficult to achieve in Ga_2O_3. P-type Ga_2O_3 nanowires were found to be successfully achieved through nitrogen doping [40] while theoretical calculations identify that transition metals such as Cu, Fe or Zn may be possible candidates for p-type conductivity in bulk Ga_2O_3 [41]. The issue with these dopants is the large activation energy, determined by these theoretical calculations to be in the 1 eV range [18, 42].

2.1.5 Alloys of Ga_2O_3

Rather than investigate the properties of binary Ga_2O_3 materials, which are well established in many areas, the main focus of this thesis shall be on the more unknown ternary alloys. Much of the theory mentioned here is general to all ternary semiconductor alloys and applies to other semiconductor families such as the III-Nitrides which shall be described in more detail later within this chapter.

With binary semiconductors (e.g Ga_2O_3, GaN, AlN) the electronic properties of the material are relatively uncontrollable as the material has a fixed bandgap. This restricts the applications of the material as optical devices may only operate at

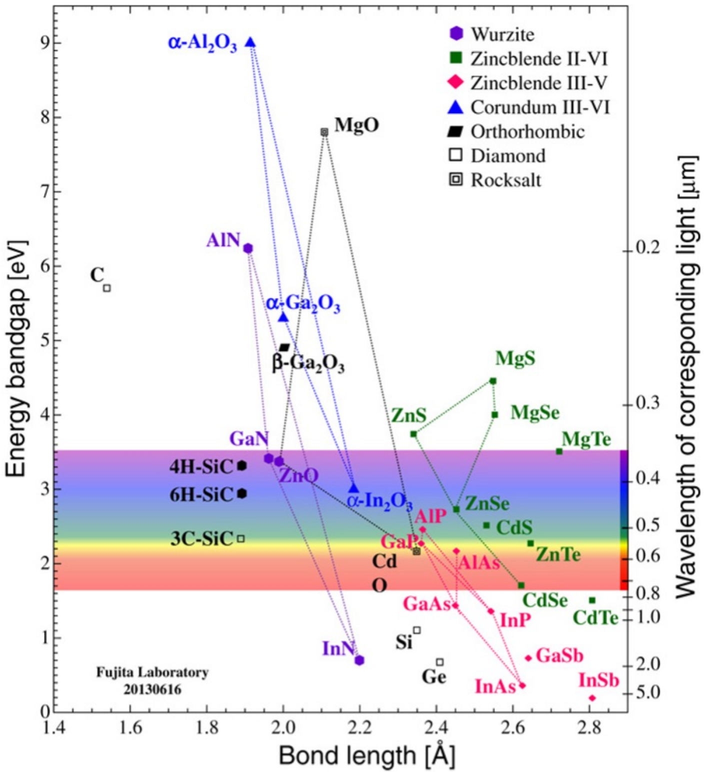

Figure 2.4: Bandgaps of semiconductor materials and families. Dashed lines connect materials indicate the possible bandgap range of ternary alloys of those materials. Extracted from [43]

this one energy. Through combining two binary semiconductors, forming a ternary semiconductor alloy, it is possible to control the bandgap of the material. When two semiconductor materials are alloyed, the resulting material will have an intermediate bandgap between the bandgaps of the two precursor binary materials, as shown in Figure 2.4.

In the case of Ga_2O_3 the bandgap is most commonly modulated through alloying with other sesquioxides. The exact bandgap of indium oxide (In_2O_3) is not as well established as Ga_2O_3 with bandgap values quoted between 2.7-3.8 eV depending on the calculation method [44–47]. This places the In_2O_3 bandgap in the UV-A to visible blue spectral range therefore indium-gallium oxide (IGO) films can be manufactured to produce a material with a desired bandgap within this lower energy range. Alternatively, the higher bandgap of aluminium oxide ($E_g \approx 8.8$ eV [48, 49]) makes it a suitable alloy for optoelectronics operating in the higher energies [50].

$$E_g = xE_{g,A} + (1-x)E_{g,B} - bx(1-x) \tag{2.1}$$

The bandgap of ternary alloys can theoretically be calculated using the expression given in Equation 2.1. Where E_g is the ternary alloy bandgap, $E_{g,A}$ & $E_{g,B}$ are the bandgaps of the two binary semiconductors composing the alloy, x is molar fraction of semiconductor A or B ($0 \leq x \leq 1$) and b is the bowing parameter. In some cases, the change in bandgap does not follow a linear trend. In these cases, a constant value will be assigned to the bowing parameter accounting for the nonlinear bandgap relationship between the two binary semiconductors. The bowing parameter may not be well established and a range of values may be quoted for each ternary alloy [51].

A similar expression to Equation 2.1 known as Vegard's Law also applies when calculating the lattice constants of the ternary semiconductor. In order for Vegard's law to be used to calculate these parameters the materials must share the same crystal structure therefore deviations may be observed for the aforementioned alloys of β-Ga_2O_3. The calculation will be more accurate when the binary semiconductors all feature the same structure e.g. Wurtzite III-Nitrides.

2.1.6 Defects in Ga_2O_3

Numerous defects exist within semiconductor crystals, altering the optical and electrical properties of the material, usually detrimentally. They can, however, be intentionally incorporated for electronic control when applied within devices (e.g doping). The defects mentioned here also apply to the III-Nitride materials mentioned later in this chapter but will only be explained here to prevent repetition.

Common point defects within these crystal included vacancies, a lattice site lying empty which is usually filled with an atom (V_{Ga} or V_O in Ga_2O_3). When an extrinsic atom encounters a vacancy site it may bond to form a vacancy complex, these complexes may take on multiple forms depending on the number of dangling bonds that remain at the complex, producing a point defect with various charge states (e.g

$(V_{Ga}\text{Sn})^-$ or $(V_{Ga}\text{Sn})^0$ [52].

Substitutional defects occur when an incorrect atom lies on an atomic site within the lattice, the substitutional atom may be an intentional dopant or a foreign impurity and may lie on both a cation or anion site (e.g Sn_{Ga} or N_O). Interstitial defects are similar to substitutional ones however rather than the extrinsic atom lying within a lattice site it is located outside the regular lattice positions. Interstitials may be extrinsic (e.g H_i) or self-interstitial (Ga_i or O_i) [30].

A special Ga_2O_3 vacancy that occurs is known as the 'split' V_{Ga}. When a Ga_I atom neighbours a $V_{Ga(\text{I})}$ it becomes energetically favourable for the Ga_I atom to migrate from the lattice site and sit within an intermediate interstitial site forming two 'split' vacancies [53], in this case there are multiple interstitial sites which the Ga_I may migrate to [54].

Another intrinsic defect of β-Ga_2O_3 is the existence of self-trapped holes (STHs). STHs may occur on the O_I and O_III atomic sites as a result of the non-fully bonding of the O resulting in a non-bonding P_z orbital. Holes localize on these O sites producing a trap state, lying within the β-Ga_2O_3 bandgap. As the trap state is a result of a crystal defect rather than from an extrinsic impurity it is referred to as "self-trapped" [53]. Self-trapped holes occur in many oxides however in β-Ga_2O_3 they are believed to be responsible for the UV emission seen within photo and cathodoluminescence studies [55, 56].

While defects impact individual atomic sites within the lattice, dislocations effect planes of atoms in multiple dimensions. The two main classifications of dislocations are edge- and screw-dislocations, shown in Figure 2.5. An edge dislocation occurs when a new row of atoms begins to form within the lattice. A screw-dislocation occurs when a plane of atoms is shifted into the lattice, forming two half planes of atoms: one beginning at the location of the shift and the other ceasing at this point. These two dislocations are described using the Burgers vector, $\overrightarrow{b}$, with the vector being perpendicular to the dislocation direction for edge-dislocations and parallel for screw dislocations, seen in Figure 2.5. Dislocations may occur which contain both a perpendicular and parallel component Burgers vector, in this case the hybrid dislocation is simply called a mixed-dislocation.

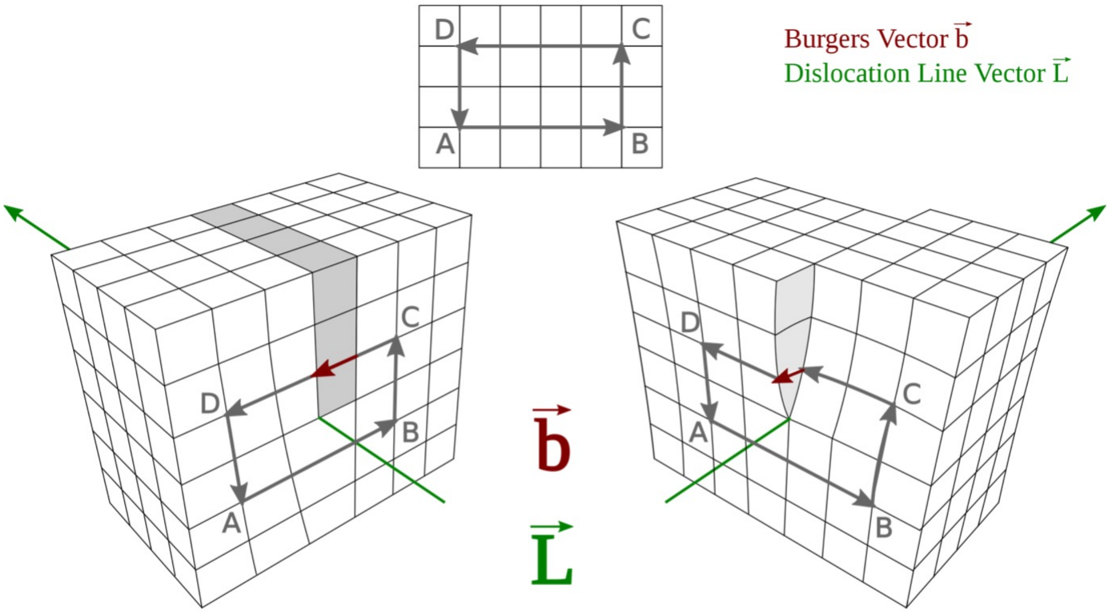

Figure 2.5: Schematic showing edge and screw dislocations within a crystal. Red arrow indicates the Burgers vector which is parallel to the dislocation direction for edge and perpendicular for screw

2.2 III-Nitrides

The III-Nitride semiconductor family consists of materials composed of an element from the traditional group III of the periodic table and nitrogen. These are primarily the binary semiconductor materials aluminium nitride (AlN), gallium nitride (GaN) and indium nitride (InN) and their ternary/quaternary alloys. The binary materials all feature a direct bandgap with the lowest being InN (0.7 eV) to GaN (3.4 eV) up to the highest AlN (6.0 eV) [51], seen in Figure 2.4. This exceptional bandgap range, covering from the infrared (IR) to the deep UV, makes ternary alloys highly tuneable. Through bandgap engineering alloys can be produced with bandgaps within this 0.7 – 6 eV range. The entire visible range can be covered by growing indium-gallium nitride ($In_xGa_{1-x}N$) or indium-aluminium nitride ($In_xAl_{1-x}N$) alloys while aluminium-gallium nitride ($Al_xGa_{1-x}N$) is used to cover the deeper UV ranges. These materials can then be used within the active regions of multi quantum well (MQW) LEDs or in solid state lasers with emission across the mentioned ranges.

2.2.1 Crystallographic structure

The III-Nitride materials typically crystallise with the hexagonal wurtzite crystal structure though it is possible to grow zincblende or rock salt (NaCl) structures under high pressure conditions. Zincblende and NaCl III-nitrides are thermodynamically unstable, as all the III-Nitride semiconductors investigated in this thesis are hexagonal materials this will be the only structure described in detail. An example wurtzite unit cell for GaN can be seen in Figure 2.6

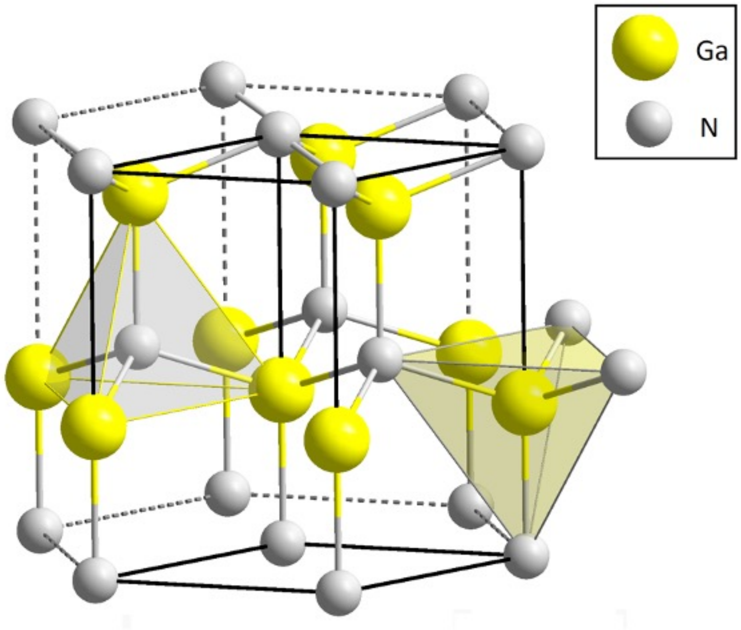

Figure 2.6: Wurtzite crystal structure for GaN. Each gallium atom (yellow) is bonded to 4 nitrogen atoms (grey) and vice versa

Within the wurtzite crystal structure each anion is surrounded by 4 cation atoms arranged in tetrahedral orientation and vice versa. The two interatomic distances described within the wurtzite unit cell are the lattice constants *a* and *c*. Lattice constant *a* defines the distance between two adjacent atoms in the lateral or basal plane whereas *c* defines the height of the hexagonal lattice or interatomic distance in the axial plane.

The wurtzite crystal structure can be considered as two intersecting hexagonal close packed lattices: one consisting of group 3 atoms (Al, Ga, In) and one of nitrogen atoms. This arrangement results in the wurtzite crystal being non symmetric in the c-direction, with the material ending with a plane of N atoms or group III atoms. In growth terms materials grown along the [0001] direction are said to be group III-polar (e.g. Ga-polar) whereas $[000\overline{1}]$(180° inversion of [0001]) are known as N-polar. As N has a greater electronegativity than all group 3 elements the bond length between these elements in non-equivalent. This results in the wurtzite structure being non-symmetric along the c-axis for III-N materials, seen in 2.6.

Due to the differing bond lengths in c and a directions the III-N wurtzite unit cell differs from the ideal structure. In an ideal wurtzite structure the ratio of lattice parameters is $c/a = \sqrt{8/3} = 1.633$ and the interatomic distance ratio of III-N in the c direction, u, is given by $u = 3/8 = 0.375$. Any deviation from these parameters forms a non-zero dipole in the crystal resulting in the occurrence of polarisation fields, in the case of III-Nitrides this polarisation occurs in the c-direction and is known as spontaneous polarisation.

Piezoelectric polarisation occurs when the a and c lattice constants are forced to change to adapt and match the lattice constants of another material. This typically happens during the epitaxial growth of III-Nitride heterostructures, QWs and MQWs. In these cases, the upper film adapts to the lattice constants of the underlying material. When the lattice constants of the crystal change then strain is induced within the crystal. This strain is either compressive or tensile and modifies the electric dipole due to the deviation from the ideal lattice parameters, this induces another internal electric field known as the piezoelectric polarisation field.

2.2.2 The quantum confined Stark effect (QCSE)

Spontaneous polarisation and piezoelectric polarisation are highly detrimental to III-nitride LED performance which induce the quantum confined Stark effect (QCSE), reducing the quantum efficiency and emission energy of these devices.

Figure 2.7 shows an example of the QCSE on the band structure of QW and MQWs. When there are no external or polarisation fields present the wavefunctions

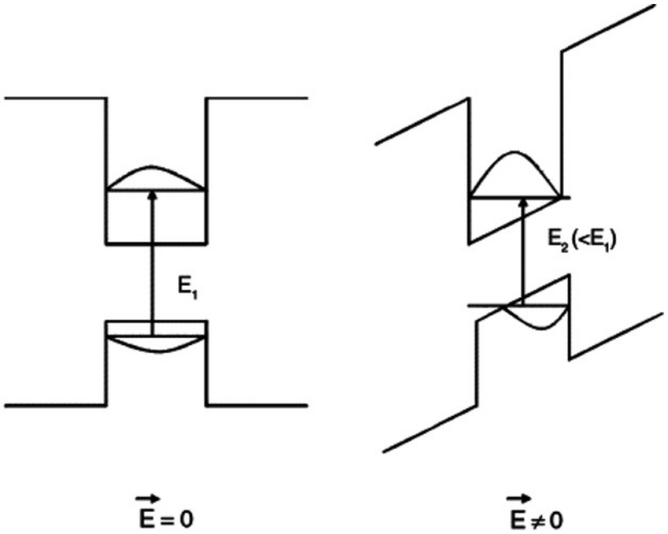

Figure 2.7: Effect of the QCSE on the electronic band structure in a quantum well in the presence of an electric field. From [57].

within the well perfectly overlap allowing a high rate of recombination between the electrons and holes within the well. When influenced by the internal polarisation field the band structure is distorted by the tilting of the conduction and valence bands. This tilting moves the wavefunctions to opposite sides of the QW, reducing the overlap therefore reducing the radiative recombination rate. When applied within optoelectronic devices the QCSE would therefore reduce the quantum efficiency of the device. The tilting of the bands also reduces the emission energy of the QW, red-shifting the emission wavelength of LEDs.

Even though the QCSE is intrinsic to the wurtzite III-Nitrides it is possible to reduce the impact of the effect. Applying external electric fields can counteract the internal polarisation fields and revert the band tilting or growing materials along non-polar or semi-polar orientations can mitigate the occurrence of these polarisation fields and therefore the QCSE.

2.2.3 Wurtzite growth planes

As mentioned previously, spontaneous polarisation occurs along the c-direction with materials grown along the polar c-plane experiencing the greatest impact of the QCSE. Rather than grow the material along the c-plane alternative growth planes can be used, either semi-polar or nonpolar.

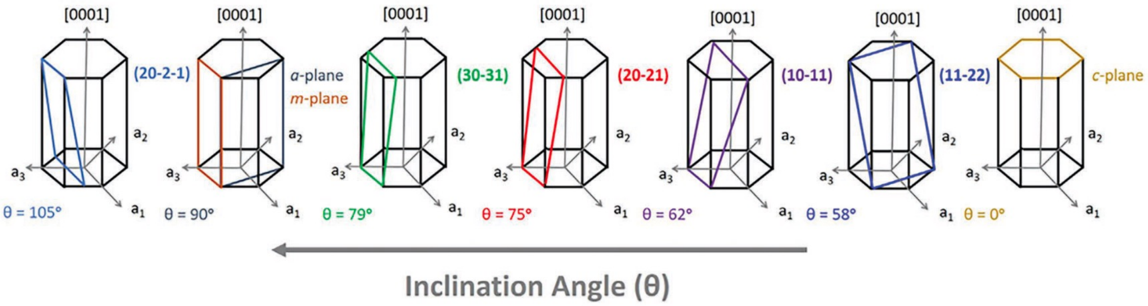

Figure 2.8: Schematic showing possible wurtzite growth planes for nitride materials. Extracted from [58]

Within this thesis the following wurtzite growth planes have been investigated for $Al_xGa_{1-x}N$ films: Polar c-plane (0001), non-polar m-plane $(10\bar{1}0)$ & a-plane $(11\bar{2}0)$ and semi-polar planes $(11\bar{2}2)$ & $(10\bar{1}3)$ (not shown in Figure 2.8). As it is the most commonly grown c-plane $Al_xGa_{1-x}N$ has been the most extensively researched but current focuses lie with semi-polar and non-polar materials. The difficulty lies with growing these materials due to the lack of available substrates capable of producing these crystal orientations [59].

2.2.4 Doping

As mentioned in the previous section, doping is paramount for developing optoelectronic devices such as LEDs. Similarly to Ga_2O_3, the doping of III-Nitride materials is complex and presents with issues. The behaviour of dopants will be considered here for $Al_xGa_{1-x}N$ alloys.

Si is the most commonly used n-type dopant within $Al_xGa_{1-x}N$. Doping with Si is well understood and capable of producing materials with a range of carrier concentrations, from low concentrations 10^{16} cm^{-3} [60] to the higher 10^{20} cm^{-3} range [61] presenting with relatively low activation energies, calculated as 12-17 meV through Hall effect measurements [60]. Typical electron mobilities for these carrier concentrations can lie within the 100 cm^{2}V^{-1}s^{-1} range for heavy doping extending to 1000 cm^{2}V^{-1}s^{-1} for lightly doped samples [62].

The behaviour of Si dopants begins to change as the Al content is increased within these alloys. The n-type conductivity of $Al_xGa_{1-x}N$:Si films has been found to be diminished as the Al content is increased, with sharp declines being reported as x is increased beyond 0.4 [63–65]. This trend continues as the Al concentration is further increased, high Al content films ($0.5 \leq x \leq 0.8$) required for deep UV emitters show a suppressed electron mobility of 20-30 cm^{2}V^{-1}s^{-1} for moderately Si doped $Al_xGa_{1-x}N$ films $n \approx 10^{18}$-10^{19} cm^{-3} [65,66].

This decrease in carrier mobility and n-type conductivity is attributed to the activation energy of the Si dopants increasing as the Al content is increased. A non-linear increase in the Si activation energy has been confirmed by multiple studies. Between $x \leq 0.7$ and AlN the activation energy was found to increase from ∼25 meV to $180 - 250$ meV [67,68]. For lower AlN fractions the increase is less extreme, found to increase by approximately 2-fold [68]. This reduction in carrier mobility means high Al fraction $Al_xGa_{1-x}N$ requires a much greater dopant density to produce the desired n-type conductivity. Germanium (Ge) is another n-type dopant used within $Al_xGa_{1-x}N$ displaying similar behaviour to Si with respect to lower carrier concentrations with increasing AlN fraction [69]. The activation energy of Ge dopants is comparable with Si albeit slightly higher for similar x values, being approximately 40 meV when $x = 0.64$ [69]. As Ge is closer in atomic radii to Ga than Si it means higher doping levels can be achieved by Ge compared to Si before structural breakdown of the AlGaN layer occurs [70].

Magnesium (Mg) has been used as a dopant to achieve p-type conductivity in $Al_xGa_{1-x}N$ materials however with great difficultly. The first issue is the Mg activation energy for GaN, studies determine the energy to be between 150-170 meV [71,72] with that increasing with Al content to a value of ∼630 meV for pure AlN [72]. This extremely high activation energy means there is a low percentage of dopants ionized at room temperature therefore a large dopant density is required to achieve conductivity. Another issue with Mg doping is the tendency for Mg dopants to form V_{Ga}-Mg-H complexes, nullifying the dopant. It is possible to break this complex through irradiation with an electron beam or by thermal annealing, as was done in the development of the first GaN LEDs [3, 73].

An alternative dopant currently researched to achieve *p*-type conductivity in high AlN $Al_xGa_{1-x}N$ is Be. Due to the similarity in atomic radii of Al and Be the activation of the dopant is expected to be lower than that of Mg, calculated by DFT to be ∼340 eV in pure AlN [74]. Though this activation energy is still high, the use of Be doped AlN has been shown to produce *p*-type conductivity with carrier concentrations in the region of $\times 10^{18}$ cm^{-3} [75].

2.3 Optical devices

This section shall describe the operating principle of the two optical devices typically fabricated from Ga_2O_3 and III-Nitride materials: Light emitting diodes (LEDs) and UV photodetectors.

The current limitations of the devices and how they are related to the crystallographic, electric and doping issues mentioned in the previous section shall also be discussed.

2.3.1 Light emitting diodes (LEDs)

The simplest description of a modern LED is a optical device designed to emit light from a active region sandwiched between an *n*-type and *p*-type doped semiconductor layer with the wavelength of the emission dictated by the materials forming the active region.

In the most basic LEDs no additional active region is required and recombination occurs in the *p*-*n* depletion region formed as the electrons (holes) from *n*-type (*p*-type) diffuse over the p-n interface into the *p*-type (*n*-type) material. The accumulation of the opposite charges at either side of the *p*-*n* junction creates an internal electric field that prevents further carrier diffusion across the junction. Under thermal equilibrium there is a net zero charge across the junction. However by applying a forward bias to the *p*-*n* junction this internal electric field is counteracted and a number of carriers are free to diffuse through the depletion region where radiative recombination may occur [76].

In order to enhance the efficiency of devices the active region of LED devices is designed to promote electron confinement typically 2D confinement through a QW or MQW however 1D and 0D confinement is possible in quantum wires or quantum dots. In the case of a QW a potential well is created by inserting a thin semiconductor layer (thickness of a few nanometers) in between two semiconductor layers with a higher bandgap (e.g $Al_{0.2}Ga_{0.8}N/GaN/Al_{0.2}Ga_{0.8}N$) trapping carriers in the well. In a *p*-*n* junction the recombination rate is limited by the diffusion length of the carriers in the material. Restricting the well thickness lower than the carrier diffusion length results in a high trapped carrier density within the well. When a forward bias is applied this greater carrier density then increases the radiative recombination rate of the LED resulting in the enhanced device efficiency for QW LEDs compared to a basic *p*-*n* junction. In the case of a MQW LED the additional QWs results in greater number of trapped carriers, subsequently enhancing the LED efficiency further [76] however for III-nitride materials the MQW active layer is susceptible to the QCSE effect as mentioned in the previous section.

Two fundamental parameters that dictate the quality of any LED is the internal quantum efficiency (IQE) and the external quantum efficiency (EQE). The IQE is the ratio of the number of photons generated in an LED against the number of charge carriers injected into the LED. The IQE accounts for non-radiative and radiative recombination and the generation of Auger electrons as well as considering the charge carriers lost due to injection in non-active zone areas of the LED. The properties of the semiconductor materials within the LED and the quality of growth are generally what dictates the IQE e.g QCSE, defect density, conductivity. Similarly, the EQE is an advancement on the IQE, considering the photon generation rate within the LED while also accounting for light extraction from the device. Advancing on from the IQE, the EQE can be increased through the design of the LED architecture through structuring e.g nanorods increasing the surface area from where light can be emitted.

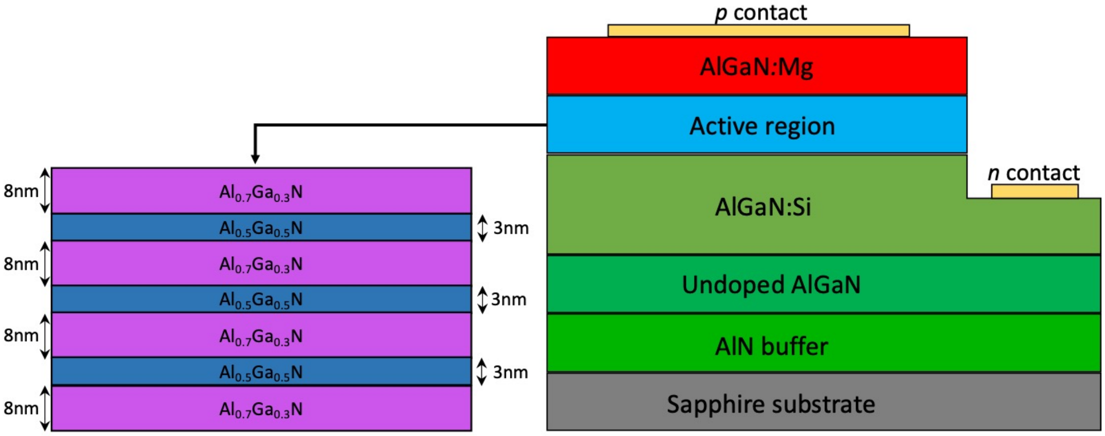

Figure 2.9: Example schematic of an $Al_{0.7}Ga_{0.3}N/Al_{0.5}Ga_{0.5}N$ MQW LED and MQW active layer

An example schematic of the architecture within an $Al_{0.7}Ga_{0.3}N/Al_{0.5}Ga_{0.5}N$ MQW LED is shown if Figure 2.9. The driving force for research into III-Nitride materials and their feasibility in the active region of LEDs was the development of the blue LED. The inability to efficiently p-type dope GaN was a major issue hindering the development of the blue LEDs with GaN films presenting with high resistivity and poor luminescence [77]. This was overcome at Nagoya University by H. Amano when electron beam irradiation was found to increase the conductivity of p-type GaN films, firstly for Zn doping [78] then for Mg [3] leading to the fabrication of a violet-blue GaN LED. Nakamura advanced on this and found that high temperature thermal annealing was also found to increase the conductivity of GaN:Mg films similarly to electron beam irradiation [73].

Through the use of an $Al_xGa_{1-x}N$ active layer within the LED deeper UV emission could be achieved compared to GaN [79] however with additional complications. As mentioned in the previous section of this chapter there is an increase in activation energy of dopants within $Al_xGa_{1-x}N$ films with increasing Al content, particularly for p-type doping. This results in highly resistive contacts within $Al_xGa_{1-x}N$ LEDs hampering the efficiency of the devices [80]. Another issue is the growth of high quality $Al_xGa_{1-x}N$ with minimal crystal defects. $Al_xGa_{1-x}N$ threading dislocations are known to act as non-radiative recombination centres [81] while basal stacking faults (BSFs) are known to produce defect related luminescence bands via excitons bound to the fault [82]. The lack of readily available, low cost lattice matched substrates also adds to the difficulty in growing $Al_xGa_{1-x}N$ films with low crystal defect densities. The necessity for a high AlN fraction *p*-type $Al_xGa_{1-x}N$ layers and current requirement for a foreign material substrates can be seen in Figure 2.9 therefore it is fundamental these issues are mitigated to achieve highly efficient $Al_xGa_{1-x}N$ LEDs.

Another factor in the poor LED efficiency is the switching of the polarisation of the light emitted from the LED with increasing AlN fraction. There is a critical Al content within $Al_xGa_{1-x}N$ films where the emitted polarisation switches from transverse electric (TE) to transverse magnetic (TM) with the latter being poorly extracted from *c*-plane material [83]. Wurtzite III-nitrides have three valence bands at the Brillouin-zone Γ-point: the heavy hole (HH) , light hole (LH) and crystal field split off bands (CH, sometimes also identified as SO). The ordering of these bands differs between GaN (HH uppermost) and AlN (CH uppermost) and therefore switches at a particular Al content, light emitted from HH recombination is TE polarised whereas CH produces TM polarised light [84]. The critical Al concentration at which the switch between TE to TM light in $Al_xGa_{1-x}N$ is quoted as $(x \geq 0.25)$ [85]. The switch from TE to TM polarised light in high AlN $Al_xGa_{1-x}N$ LEDs results in light emission perpendicular to the *c*-axis compared to parallel for low AlN alloys which results in poor light extraction efficiency which is detrimental to the EQE.

As mentioned in Chapter 1 the efficiency of deep UV-C LEDs is currently near 10% [12,13] with the effects mentioned here all contributing to the drop in efficiency compared to that of blue LEDs. In order to improve the efficiency of $Al_xGa_{1-x}N$ LEDs these detrimental effects must be counteracted through improved material growth processes/techniques or through the growth of non *c*-plane materials as has been done within this thesis.

2.3.2 Photodetectors

While the purpose of an LED is to generate light via an electrical current, photodetectors are the opposite, generating electrical current when irradiated by light. The fundamental process behind the operation of a photodetector is as follows: when light is incident on a semiconductor an electron-hole pair may be generated, permitting the absorbed light is of high enough energy to promote an electron to the conduction band via the photoelectric effect. This increases the conductivity of the semiconductor and through applying a bias, the increase in conductivity under illumination can be detected. There are many types of semiconductor photodetectors separated by the structure of the device e.g *p*-*n* photodiodes, Schottky barrier photodiodes and MSM (metal-semiconductor-metal) devices.

p-*n* photodiodes operate on a similar principle to the basic *p*-*n* LEDs mentioned in the previous section however in reverse. The absorption of light may generate electron hole pairs within the depletion region of the *p*-*n* junction, these carriers are then separated by the internal electric field within the junction, resulting in an electrical current as they drift across the depletion layer. When under no external electric field the device is said to be operating in photovoltaic mode however by applying a reverse bias, the width of the depletion region increases. This increases the photocurrent under illumination as more electron-hole pairs can be generated in the expanded depletion region, this is the operational principle of photoconductive mode [86].

In this study Schottky barrier photodetectors have been investigated in Chapter 6 and shall therefore be discussed in greater detail here. The *p*-*n* junctions mentioned in the previous section is formed when two oppositely doped semiconductors are joined together whereas a Schottky barrier is formed at the junction between a metal and an *n*-type semiconductor.

When the work function of the metal is greater than the work function of the semiconductor ($\Phi_m > \Phi_s$) once the metal and semiconductor are brought in contact with each other electrons will diffuse from semiconductor to the metal in order to keep a constant Fermi level across the two materials. This is similar to the formation of the depletion region with *p*-*n* junctions however with very little depletion within the metal [87]. This behaviour cause the upwards bending of the bands at the semiconductor side of the junction interface as shown in Figure 2.10.

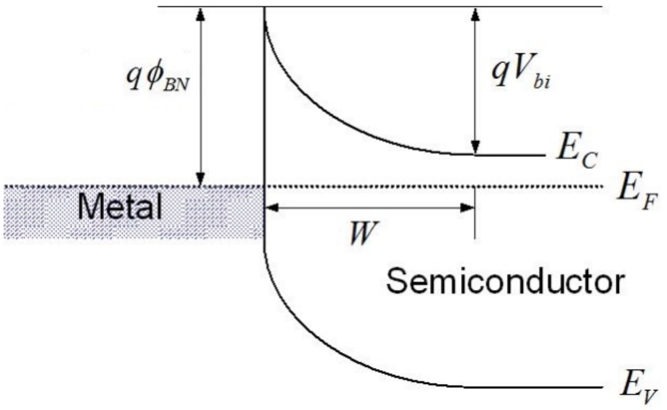

Figure 2.10: Band diagram of a Schottky barrier formed through a metal-semiconductor junction. Φ_{Bn} is defined as the height of the Schottky barrier for electrons, V_{bi} is the built in electric field and W is the depletion width.

In Figure 2.10 Φ_{Bn} is defined as the height of the Schottky barrier for electrons, V_{bi} is the built in electric field and W is the depletion width. Again, similarly to the *p*-*n* junction, by applying a reverse bias a greater electric field at the interface is generated and the width of the depletion region increases. The Schottky barrier is the potential barrier that electrons must overcome to flow from the metal into the semiconductor layer [86]. Under the presence of an electric field at the metal-semiconductor interface the height of the barrier can be modulated via the Schottky effect (also known as image force lowering), allowing for some degree of control over the photodetector conduction. This effect comes from the electron attraction to the electric field, reducing the potential energy required for the electron to overcome the Schottky barrier increasing the device conductivity under illumination. As the semiconductors used for the Schottky photodetectors in this study are of wide bandgap a metal of high work function is required to form the Schottky barrier therefore Pt is used here.

Similarly to an LED, a photodetectors efficiency is defined by the IQE and EQE however the definitions of each are inverted. The EQE of a photodetector is defined as the ratio of the number of photons incident on a photodector against the number of charge carriers generated. Whereas the IQE is the ratio of the number of photons absorbed by the detector over the number of carriers generated.

2.4 Sample growth techniques

The samples within this study have been grown using a variety of growth techniques, the fundamental mechanism behind each technique shall be explained here. The specific growth parameters used for each sample's growth cycle will be detailed in their relevant sections.

2.4.1 Metal organic vapour-phase epitaxy (MOVPE)

MOVPE is an epitaxial growth technique used to produce III-V semiconductors and subsequent alloys. Materials are typically grown in a high temperature, moderate pressure environment (e.g. ~ 1000°C, 1 atm for GaN [4]). The elemental precursors are injected into the growth chamber in a gaseous state, taking the form of metal-organics for the group III elements and hydrides for the group V. Precursors are typically driven into the reaction chamber as a mixture, contained within a carrier gas of H_2 or N_2 [88]. In the case of $Al_xGa_{1-x}N$ growth the elemental precursors are usually trimethylaluminium (TMAl), trimethylgallium (TMGa) and ammonia (NH_3). The growth process is as follows:

The precursors are transported to the reaction chamber, the delivery mechanism is dependent on the growth reactor but there are two main designs. Horizontal growth reactors flow the precursors through the chamber and over the substrate and showerhead reactors where the precursor mixture is introduced directly above the substrate and flows downwards. All the MOVPE grown samples in this thesis are grown in close coupled showerhead MOVPE reactors.

When in the reactor the high temperature of the chamber causes the precursors to dissociate by pyrolysis. The product of this reaction is a mixture of reactive compounds and free atoms which are available for absorption by the heated substrate. During absorption these compounds and atoms nucleate, forming a layer of adatoms and a collection of desorbed gaseous hydrocarbon by-products. These by-products are then exhausted from the chamber, the growth process continues and epitaxial growth is achieved.

Doping is achieved in MOVPE growth by introducing an additional metal-organic gas containing the desired dopant into the precursor mixture. For the previously mentioned dopants n-type materials can be grown by introducing silane (SiH_4), germane (GeH_4) or isobutylgermane (IBGe) [61,89] and biscyclopentadienylmagnesium ($MgCp_2$) acts as a Mg source for p-type materials [90]. To control the composition of ternary alloys the partial pressure of the two group III precursors is varied, increasing the availability of the desired element while keeping the overall pressure within the reactor constant.

2.4.2 Molecular beam epitaxy (MBE)

Another growth technique commonly used to grow semiconductors is MBE, in this study it has been used to grow a variety of tin-gallium oxide and indium-gallium oxide samples. The technique benefits from being capable of growing materials with layer-by-layer atomic control producing semiconductor films with extremely high crystal quality compared to the cost-effective method MOVPE.

In order to produce this superior material quality MBE growth is performed under an ultra-high vacuum (UHV) ($<10^{-8}$ Torr), this is necessary for the growth mechanism as the beam of source atoms require a collision free path to the substrate during growth. The UHV environment also helps reduce the likelihood of contamination from gaseous impurities in the growth chamber.

Figure 2.11 shows an example schematic of an MBE reactor. During MBE the substrate is heated within the UHV chamber, as in MOVPE, however much lower growth temperatures are possible with MBE ($\sim$750-800°C for $Al_xGa_{1-x}N$ [91] & 500-800°C for β-Ga_2O_3 [92]). The effusion cells in Figure 2.11 act as the source of the atoms for epitaxial growth. Each effusion cell consists of a heating element

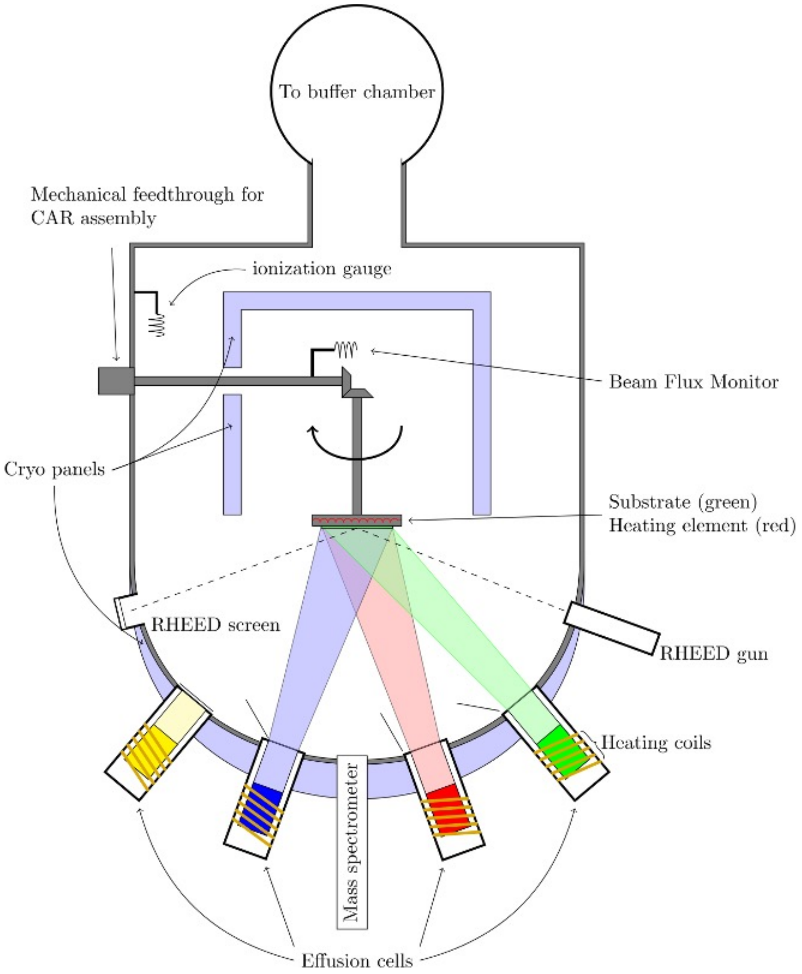

Figure 2.11: Schematic of a molecular beam epitaxy reactor.

attached to a pyrolytic crucible, crucibles must be made from a material with a high melting point (e.g. boron nitride, iridium or tantalum [93]). An ultra-pure source material is placed within each crucible and heated to the point of sublimation in order to generate a vapour. This vapour forms the "molecular beam" of MBE with the atoms dispersing from the effusion cell which condense on the substrate surface and nucleate into the semiconductor film [94].

The flow of each molecular beam can be periodically interrupted by closing the shutters on the effusion cells, allowing the growth to be controlled with monolayer precision. Gaseous elements such as N_2 or O_2 are provided by RF-plasma sources (not shown in Figure 2.11). A reflection high-energy electron diffraction (RHEED) system may be used to analyse the crystal during growth, determining the exact growth rate and monitoring the surface quality of the film.

The composition and growth rate of materials produced by MBE is dependent on the effusion cell temperatures during the growth. As the source material is heated to greater temperatures the rate of sublimation will increase resulting in a greater flux of atoms towards the substrate. Ternary alloy composition is varied by changing the temperature ratio of two (or more) of the cells, increasing T_X/T_Y will produce an alloy with a larger content of metal X where metal X and metal Y are the two cation elements of the semiconductor alloy (e.g Ga and In in indium-gallium oxide). The layer-by-layer control comes at the expense of the growth rate, typical MBE growth rate for Ga_2O_3 being 0.5-2.5 nm/min compared to 10-15 nm/min for MOVPE [92]. Economically MBE is also nonideal due to the reactor costs, UHV requirement and the low growth rate forcing long operational times to grow thick films.

2.4.3 Pulsed laser deposition (PLD)

Laser ablation can be used to deposit a thin film of material on a substrate by the means of pulsed laser deposition (PLD). This technique may occur within an UHV but for these investigations the technique has been performed in a background gas of O_2 to provide the '-oxide' of the indium-gallium oxide.

A schematic of the PLD growth instrumentation is shown in Figure 2.12 The basis of PLD semiconductor growth is that a short high-power laser pulse is directed at a target containing the elements composing the desired semiconductor. The high energy photons within the pulse strip and ionize the surface atoms of the target through laser ablation, generation a plasma plume. The high energy electrons contained within the plume generate free oxygen atoms through electron-impact dissociation (O_2 dissociation energy $E_{Dissoc} = 5.12$ eV) [96]. Free oxygen mixes with the target ions within the plasma plume which can propagate within the growth chamber and deposit upon a heated substrate similarly to the other mentioned growth tech-

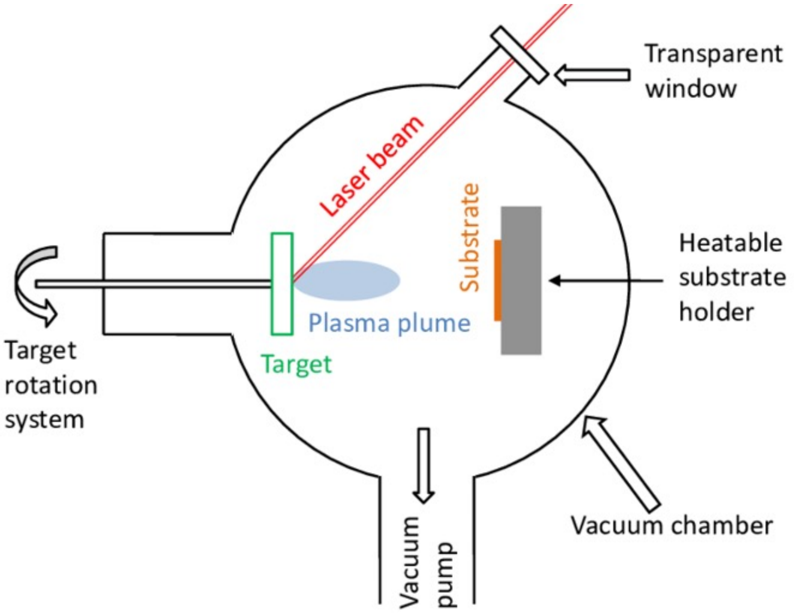

Figure 2.12: Schematic of a pulse laser deposition reactor. Extracted from [95]

niques [97]. This cycle is repeated as the laser is continuously pulsed allowing the nucleation of a semiconductor thin film. During growth the laser target is rotated to ensure successive pulses are ablating material with consistent surface quality and to full utilise the material available for growth [98]. Laser targets are usually thin discs composed of compressed ceramic powders, in the case of ternary (and more complex) alloys a mix of powders is used with the target disc composition matching the desired alloy composition [99]

Segmented targets have also been used to produce ternary alloys with the target consisting of two (or more) areas with distinct compositions through combinatorial growth. In these cases the resulting semiconductor will have a compositional gradient in the lateral direction, this is commonly known as the continuous compositional spread (CCS) technique [99, 100]. The growth rate of semiconductors grown by PLD is dependent on multiple factors. As with the previously mentioned techniques the substrate temperature is variable, in the case of PLD grown β-Ga_2O_3 a growth temperature of 600-700 °C [101,102] is commonly used and found to provide enough thermal energy to adatoms to promote crystallinity [101].

The laser specifications are also critical to the deposition rate in PLD. Firstly the laser wavelength determines the penetration depth into the target, if a laser with a high energy (low wavelength) is used subsurface boiling may occur resulting in an inconsistent deposition rate between pulses [97]. Pulse duration and repetition rate also dictate the growth rate and crystal quality with greater pulse frequencies increasing the growth rate at the expense of forming many small clusters/islands whereas lower frequencies allow the adatoms more time to nucleate into fewer, larger structures [103] . Instrumental issues which can also effect the growth rate during PLD are: Target-substrate distance, temperature gradients within the substrate and target ablation rate [97].

2.4.4 Substrates

As mentioned previously there are multiple substrates which are suitable for semiconductor thin film growth with each possessing various benefits and disadvantages. Here will detail the various substrates that feature in this study, substrate growth processes and the substrate influence on film growth.

Semiconductors are commonly grown upon readily available sapphire substrates due to their thermal stability, conductivity and low cost. The single crystal material used for these substrates can be grown through the Czochralski (CZ) or Kyropoulos (KP) methods. For both methods a high quality seed material is melted within a crucible, a rod is then inserted into the melt with a small piece of crystalline material held on the rod tip. As the rod is extracted from the molten material a filament of single crystal material, taking on the crystal structure of the crystalline tip. From this filament a large piece of bulk single crystal material can be formed with the size and shape of the crystal being dictated by rod rotation & extraction speeds and temperature gradient control during extraction [104, 105]

A similar method used to grow sapphire substrates is the edge-defined film-fed growth (EFG) technique, in this study it has also been used to grow the Ga_2O_3 substrates for the epitaxial growth of tin-gallium oxide thin films [33]. A diagram of the EFG growth process is shown in Figure 2.13

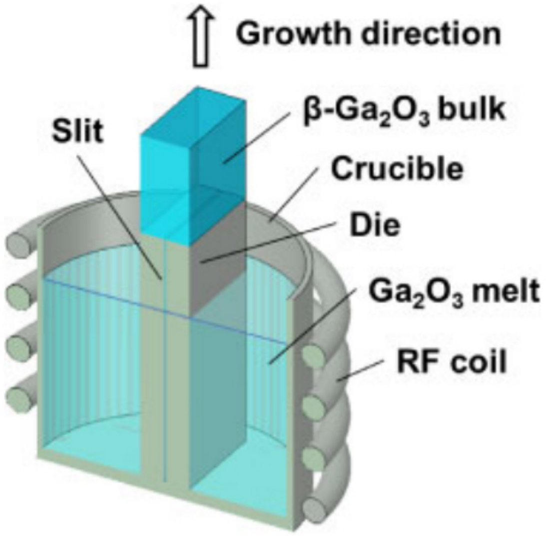

Figure 2.13: EFG growth process for Ga_2O_3 single crystals. Extracted rom [33]

Firstly a powder mixture of Ga_2O_3 and any dopants (Sn for the Ga_2O_3 substrates used within this investigation) is heated within in an iridium crucible. A die containing a narrow slit is then inserted into the molten Ga_2O_3 mixture which then propagates to the top of the die via capillary action [19]. As with the KP and CZ methods a seed crystal is then inserted into the melt at the surface of the dye and a large single crystal ingot may be extracted with the crystal dimensions defined by the shape and size of the die. Thin wafers may then be sliced from the ingot producing the single crystal Ga_2O_3 substrates suitable for epitaxial growth [19, 33].

Due to the high cost of native Ga_2O_3 and III-nitride substrates, sapphire is generally used as an alternative. The major disadvantage to sapphire substrates is the large lattice mismatch to both the III-Nitrides and Ga_2O_3 resulting in the growth of a strained material with a high defect density and featuring a large number of dislocations. There is also a large variation between the thermal expansion coefficient, α_o, of sapphire and these semiconductors hindering the device capabilities of film-sapphire materials.

Substrate	*a (Å)*	*c (Å)*	Lattice mismatch to Al_2O_3 (%)	α_O (10^{-6} K^{-1})	Ref.
Sapphire (Al_2O_3)	4.7759	12.991	-	4.9	[106,107]
Semiconductor					
GaN	3.189	5.185	16.1	4.3	[106,108,109]
AlN	3.112	4.982	13.3	5.27	[106,108,109]
Ga_2O_3	12.2	5.8	$1.62^{(101)}$, $3.12^{(102)}$	7.8	[20,110,111]
In_2O_3	10.11	10.11	-13.2	6.15	[112,113]

Table 2.1: Lattice and thermal expansion parameters for binary semiconductors investigated during this this study.$^{(101)}$ and $^{(102)}$ indicate the mismatch in those particular directions of the (-201) Ga_2O_3 direction

Table 2.1 shows the lattice parameters for the substrates and binary semiconductors key to this investigation. The lattice mismatch to sapphire is also shown.

A viable but less commonly used substrate for growth of both III-Nitrides and Ga_2O_3 is Si. Si is beneficial due to the availability and cost of substrates which are available in large wafer sizes not feasible with other substrates. However similar issues arise as with sapphire and lattice incompatibility leads to high defect densities and cracking with large film thicknesses.

Chapter 3

Experimental Methods

This chapter shall give a brief overview of scanning electron microscopy and further detail the two specific techniques used heavily within this thesis: namely, wavelength-dispersive X-ray spectroscopy (WDX) and cathodoluminescence (CL). The theory of electron-beam interactions, the various signals generated and analytical signals using these techniques shall be explained. For the WDX, the instrumentation used to generate the X-rays and the X-ray detection methods will be explained. Lastly, the calculation process when deriving a material composition from the X-rays shall be detailed. The CL section shall explain electron-hole recombination processes, CL signal acquisition and hyperspectral CL mapping (simultaneously with WDX mapping). The specific software used for data analysis and processing shall be highlighted at their relevant sections.

3.1 Scanning Electron Microscope (SEM)

An SEM is a piece of equipment primarily used for the imaging of samples similarly to an optical microscope. The difference between the two pieces of equipment is that the optical microscope uses light as an illumination source whereas the electron microscope uses a high energy beam of electrons ($E_{Beam} \geq 30$ keV) to excite a specimen, generating various characterising signals during excitation. The basis of SEM imaging is that an electron beam is brought to a focus using a series of electromagnetic lenses and irradiated on a sample in a raster scan. As the electron beam impinges on the sample inelastic interactions between the beam and the specimen electrons result in the generation of low energy secondary electrons (SE) ($E \sim 50$ eV). These low energy SEs can then be detected and produce an image of the specimen as the beam is scanned, with a greater resolution capable than from an optical microscope. In order to prevent electron collisions with the gas molecules in the air the SEM is generally held under vacuum, the pressure of which can be variable depending on the type of specimens being imaged. Low vacuums may be used when specimen charging is an issue, allowing a small volume of gas into the specimen chamber can remove accumulated electrons from the sample and allow clearer imaging. The most extreme case of this is known as environmental-SEM. Along with the SEs there are various other electron-sample interaction signals which will be discussed later in this thesis.

The resolution obtained within an SEM is based on multiple factors: beam energy, beam current, source size and focusing capabilities. The first two factors are largely affected by the source of the electron beam, distinguished by the type of electron gun used. Source size corresponds to the spatial area of the electron gun where electrons are emitted, with smaller tip radii resulting in smaller source size and improved spatial resolution

There are two main forms of electron gun, thermionic and field emission. Only the latter is used for measurements within this thesis however both will be described for clarity. A thermionic emission gun typically consists of a filament of tungsten bent to a point. Alternatively, a lanthanum hexaboride crystal, LaB_6, may be used instead of the tungsten filament with the LaB_6 crystal being preferred due to increased lifetime, brightness and beam stability, however are notability more expensive than tungsten filaments [114].

Electrons are extracted from the tungsten filament by firstly heating the wire to the point of thermionic emission (1800-2800°C). A positive potential is then applied to an anode, allowing the thermionic electrons to accelerate from the filament producing a high energy beam of electrons. The entire electron gun is contained within a Wehnelt cylinder held at a negative potential, this helps control the area of

Parameter	**Tungsten Filament**	**LaB$_6$**	**Schottky FEG**	**Cold FEG**
Operating Temp (°C)	2700	1800	1800	300
Tip radius (µm)	60	10	0.4 - 1	< 0.1
Current Density (Am^{-2})	10^4	10^6	10^7	10^9
Emission current (µA)	200	80	100 - 500	5 - 10
Source size	~50 µm	~15 µm	~20 nm	~5nm
Lifetime (h)	100	1000	> 5000	> 2000
$\triangle$E (eV)	1.5	1.0	0.5	0.3

Table 3.1: A comparison of the important electron gun parameters for SEM, values extracted from [116, 117]

emission from the filament and pinches the electron beam.

The more advanced form of electron gun employed within our measurements is a field emission gun (FEG). The FEG again consists of a piece of tungsten however rather than being bent to a point it has been etched into a sharp tip. By applying a large electric field to the accelerating anode the work function of the tip is reduced, allowing electrons to be emitted from the tip through tunnelling. FEGs can be described as cold FEGs which require no thermionic emission or Schottky FEGs which still retain a thermionic component albeit at much lower temperatures than the tungsten wire filaments. A Schottky FEG tip may also be coated in zirconium dioxide, ZrO_2 to help reduce the work function and increase electron emission [115]. A comparison of the electron gun operating parameters is shown in Table 3.1.

From Table 3.1 it is clear that cold FEG tips produce the highest quality electron beam with a high current density, low energy spread and with a minimum source size allowing high spatial resolution analysis. However, for the X-ray micro-analyses a larger beam current may be required to generate a sufficient number of X-rays therefore a Schottky FEG, or even tungsten filmament, is more suited. Within this thesis two types of SEM have been used: Primarily a JEOL JXA-8530F electron probe microanalyser (EPMA) for WDX & CL measurements and an FEI Quanta FEG 250 SEM for CL measurements in the deep UV spectral range (∼ 200nm) and for high quality sample imaging. Both pieces of equipment are equipped with a Schottky FEG. As it is the primary piece of equipment used within this thesis the EPMA will be discussed in greater detail.

3.1.1 Electron Probe MicroAnalyser (EPMA)

The EPMA is a highly specialised type of SEM dedicated to performing WDX measurements, a schematic of which can be seen in Figure 3.1, with a photo of the EPMA shown in Figure 3.2.

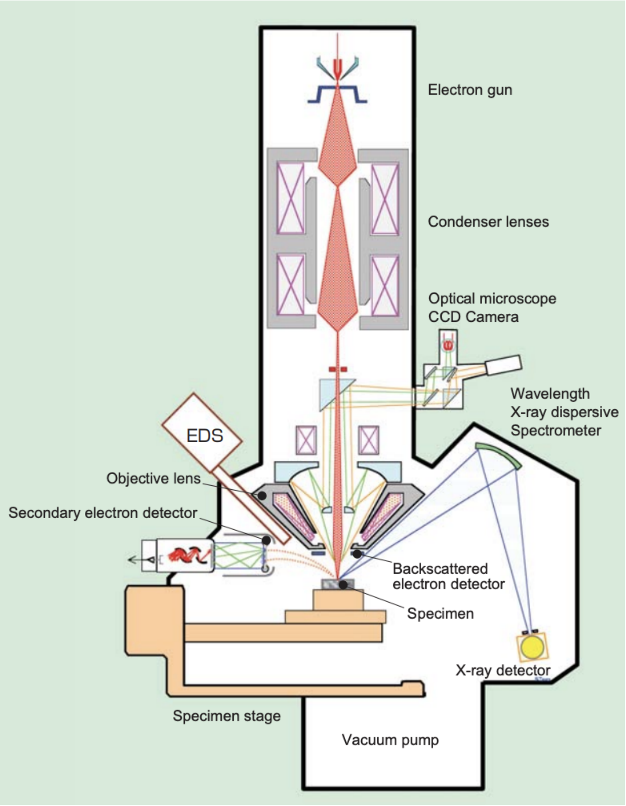

Figure 3.1: A schematic of a JEOL EPMA. Extracted from [118]

The EPMA column structure is very similar to that of a regular SEM featuring a

Figure 3.2: A photo of a JEOL JXA-8530F at the University of Strathclyde

Schottky FEG, a series of electromagnetic lenses to collimate and focus the electron beam (known as condenser and objective lenses) and a series of apertures used to restrict the beam spread. This entire structure is held under a vacuum in order to prevent electrons colliding with gas particles in the air and to prevent contamination.

Once focused the electron beam is allowed to propagate into the specimen chamber, held in a high vacuum, where it impinges on the specimen being investigated and generate the various electron-sample interactions that shall be discussed later. The electron gun remains on at all times within the EPMA but a series of beam blankers, PCDs, are used to control whether the beam enters the specimen chamber. For the JXA-8530F EPMA a probe current detector (PCD) is equipped with a Faraday cup allowing the beam current to be monitored at intervals between measurements. To prevent the venting of the specimen chamber vacuum when inserting samples in to the EPMA, the JXA-8530F is also fitted with an exchange chamber which acts as an airlock between the specimen chamber and the lab environment .

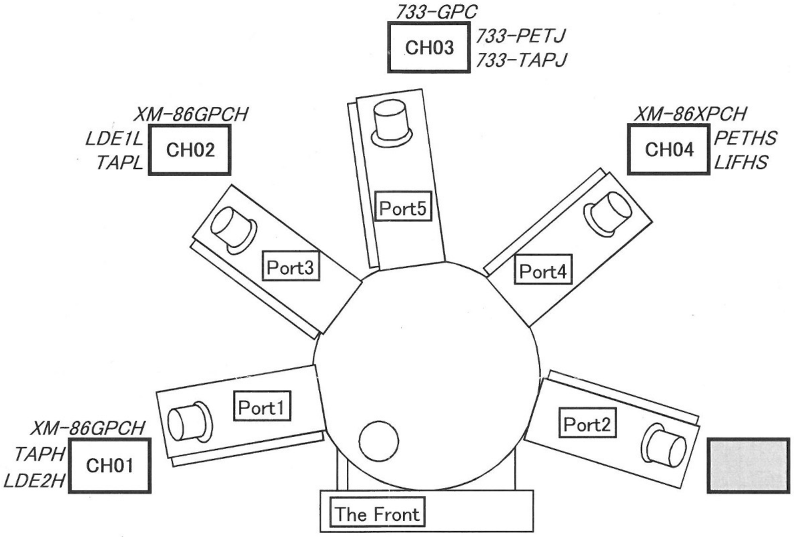

Figure 3.3: A schematic of WDX spectrometer setup on the JXA-8530F EPMA at the University of Strathclyde

A key interaction is the generation of X-rays which are analysed using WDX. The EPMA specialises in WDX measurements as it features multiple WDX spectrometers, typically 4-5. The EPMA used for the measurements within this thesis is equipped with four WDX spectrometers, all containing two X-ray diffracting crystals as shown in Figure 3.3. A WDX spectrometer requires diffracting crystals and detectors to be held within a precise geometry in order to analyse these X-rays, therefore this is controlled entirely by the EPMA with minimal human adjustment. These spectrometers are designed to only accept X-rays propagating from a specific angle with respect to the specimen, known as the take-off angle. In most SEMs there is the ability to tilt the sample for imaging and crystallographic analyses however the EPMA retains the specimen perpendicular to the electron beam to ensure the take-off angle for all WDX spectrometers can be achieved.

Another feature of the EPMA is the optical microscope allowing the observation of the sample surface while in the vacuum chamber, in Figure 3.3 this microscope is located on "The Front" of the EPMA. This optical microscope serves multiple purposes. Firstly, in order to ensure the sample is in focus with the WDX spec-

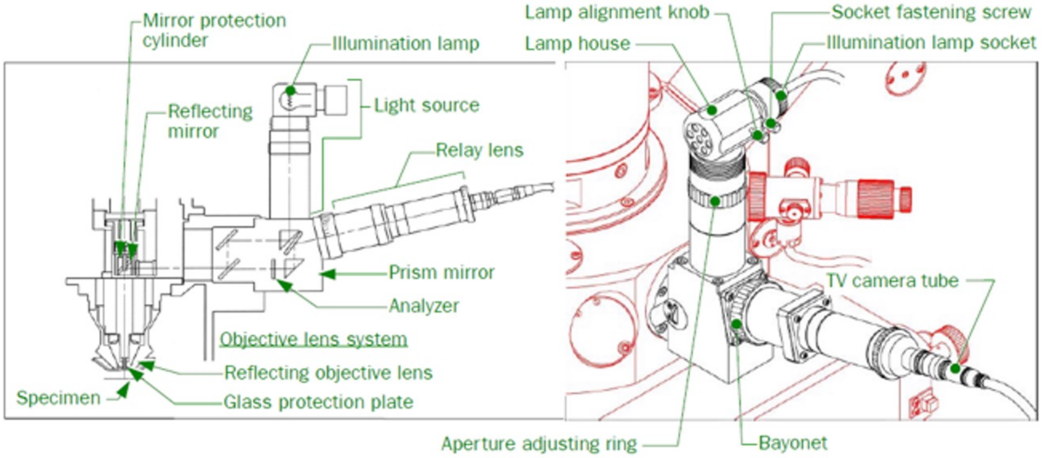

Figure 3.4: A schematic of the optical microscope optics and instrumentation on the JXA-8530F EPMA at the University of Strathclyde

trometers the optical microscope is adjusted to the focal point. The user would set the sample in optical focus by adjusted the stage height, the focal point is achieved when crosshairs on the optical microscope are aligned with the centre of the optical image. The second purpose of the optical microscope is that it acts as the collection mechanism for the CL signal. The custom built optics allow the collection of light from UV-IR wavelengths with minimal chromatic aberration. The optical focus being aligned with the X-ray focus also allows simultaneous acquisition of the CL and WDX signal both in focus, being highly beneficial for mapping of the samples, (explained in greater detail in Chapter 3.4). A diagram of the collection optics of the optical microscope is shown in Figure 3.4. The custom CL system used within this study replaces the relay lens and TV camera tube with either an optical fibre (older system) or a series of mirrors and lenses (newest system) to transmit the CL signal to a spectrometer housed on spectrometer Port 2 of the EPMA, see Figure 3.4.

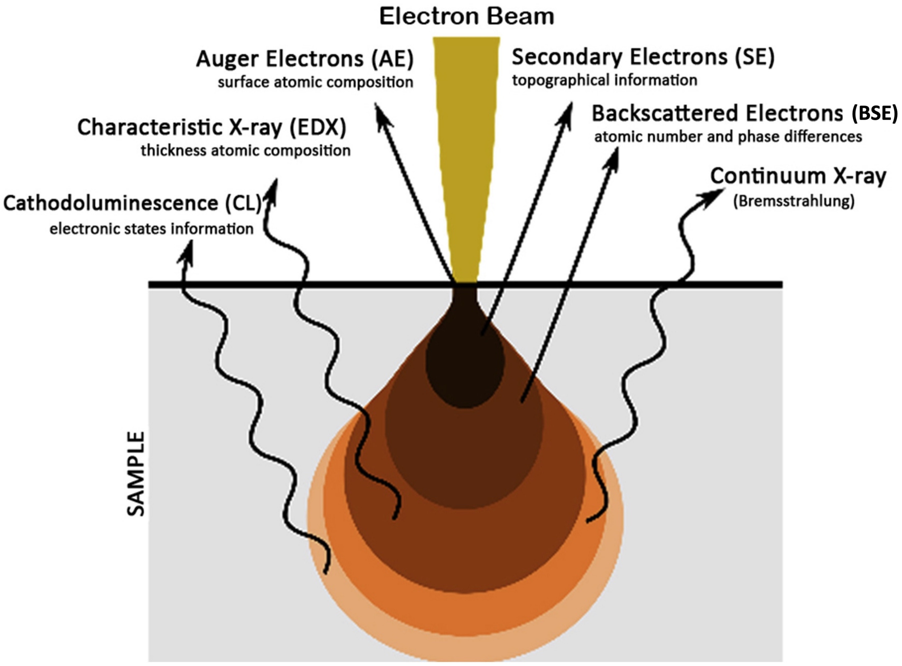

Figure 3.5: Characterising signals and interactions generated during electron beam-specimen irradiation. Extracted from [119]

3.1.2 Electron beam-specimen interactions

As the electron beam irradiates a sample a number of interactions occur each producing a signal which provides characteristic information about the specimen. A diagram showing the various signals produced by the electron beam is found in Figure 3.5

The two signals used for SEM imaging are secondary electrons (SE) and backscattered electrons (BSE). As mentioned previously SEs are produced through the inelastic scattering of beam electrons which ionize specimen atoms resulting in the emission of loosely bound low energy valence electrons (E $\sim$ 50 eV). For SEs the greatest probability of emission is from surface atoms, allowing SE imaging to be used to investigate sample topography and surface morphology.

Alternatively, as the beam electrons propagate throughout the specimen they may be elastically scattered, deflecting from their trajectory as they experiences a

Coulomb force from the nuclei of the specimen atoms. When the scattering angle, ϕ, is $>90^\circ$ these electrons are deflected outwards from the sample and are known as BSEs. The number of BSEs emitted from a material is generally defined by the backscattered electron coefficient shown in equation 3.1.

$$\eta = \frac{I_{\mathrm{BSE}}}{I_{\mathrm{EB}}} \tag{3.1}$$

Where η is the backscattered electron coefficient, I_{BSE} the number of BSEs and I_{EB} is the number of electrons in the incident electron beam. The backscattered electron coefficient is dependent on the atomic number (Z) of the irradiated material, increasing with higher Z [120]. Therefore, compositional information about a specimen can be determined from the contrast in BSE imaging.

X-rays

During irradiation by the high energy electron beam multiple X-rays may be emitted from a specimen. These X-rays are categorised into two brackets: Characteristic X-rays and Bremsstrahlung X-rays.

Characteristic X-rays are a series of X-rays with specific energies generated by the impact ionisation of the specimen atoms. As these inner shell electrons are ejected from an atom they leave behind an inner shell vacancy. An electron held in an outer shell must then fill this vacancy by dropping from a higher energy state. As this happens a photon is emitted with an energy equal to the energy difference between the inner shell vacancy and the electrons original energy state. As each element poses a unique set of quantised energy levels, there is a respective set of characteristic X-ray energies for each element. By analysing the energies of the X-rays emitted from a specimen it is possible to determine which element is responsible for their emission. A diagram showing the electron transitions generating characteristic X-rays is shown in Figure 3.6.

Each electron transition (and subsequent emitted X-ray) is represented a the letters K, L or M depending on which shell the electron vacancy was produced and

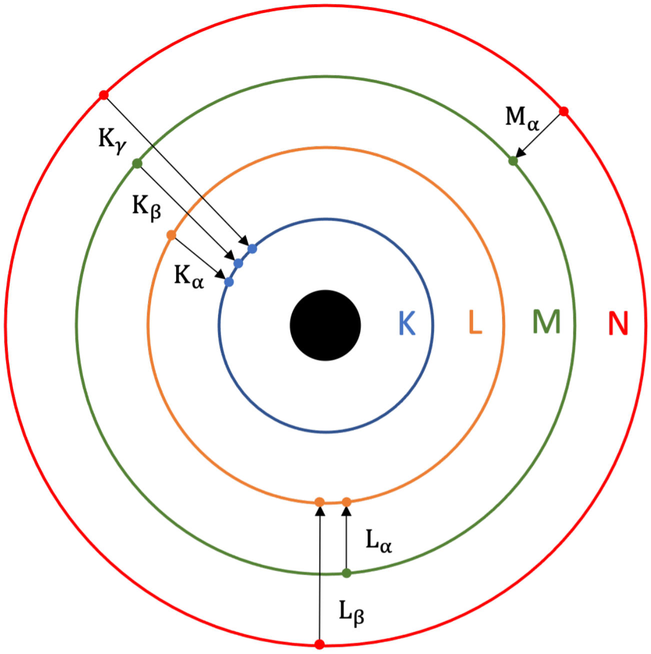

Figure 3.6: Electron shell transitions result in the emission of characteristic X-rays

an α , β or γ to represent the original energy state of the electron (e.g. K_α represents the filling of a K-shell vacancy with an electron from the next highest energy shell, the L-shell. The K_β transition when an M-shell electron fills a K-shell vacancy and K_γ for N-shell electrons).

Within each electron shell exist a number of inner-shell states, increasing with atomic number, resulting in the separation of the X-ray families into multiple distinct X-rays separated by a small energy difference (e.g for $L \rightarrow K$ transitions between $L_2 \rightarrow K$ produces the $K_{\alpha,1}$ X-ray and $L_3 \rightarrow K$ the $K_{\alpha,2}$ X-ray) [121].

These characteristic X-rays are the signal analysed during both WDX and EDX microanalysis, only differing in the detection method of the X-rays. These detection methods shall be explained later in this chapter.

The other type of X-ray generated by the electron beam is Bremsstrahlung X-rays. Bremsstrahlung is German for “breaking radiation” and is a type of X-ray generated as the propagating electron is decelerated by the nuclei of the specimen atoms. The energy of the X-ray emitted is equal to the kinetic energy lost by the electron during deceleration. Bremsstrahlung is referred to as a "continuum", as the kinetic energy lost during deceleration can take any value from zero loss up to the complete loss of kinetic energy. The maximum Bremsstrahlung X-ray energy is equal to the energy of the electrons within the incident beam and the energy of zero Bremsstrahlung intensity is known as the Duane-Hunt limit [122]

Cathodoluminescence

Cathodoluminescence (CL) is defined as the emission of light from a material through the irradiation of an electron beam. As the high energy electrons propagate through a semiconductor they may promote electrons into the CB resulting in radiative emission during electron-hole recombination with the hole induced in the VB. A diagram representing the various electron-hole recombination processes is shown in Figure 3.7

Figure 3.7 shows the following recombination processes: (a) Band-band recombination between an electron in the CB and a hole in the VB; (b) Recombination of an exciton (electron-hole pair) (c) CB electron recombining with a shallow acceptor hole; (d) A donor electron recombining with a hole in the VB; (e) donor-acceptor pair recombination (DAP).

Process (a) represents the recombination between an electron in the CBM and a hole in the VBM across the semiconductor bandgap, E_g. This process may either be direct recombination or indirect, requiring phonon assistance due to the CBM & VBM possessing different momentum-vectors. In the case of process (b) an electron and hole may become electrostatically bound to each other forming a quasi-particle known as an exciton. This generally happens at low temperatures though stable excitons may exist at room temperature in certain materials. In the case of radiative emission, exciton recombination produces reduced energy photons with energy equal to the difference between the bandgap and the exciton binding energy.

During RT cathodoluminescence spectroscopy process (a) result in near band edge (NBE) emission, with an energy indicative of the semiconductor bandgap. When RT stable excitons exist in the material the luminescence peak from process (b) may

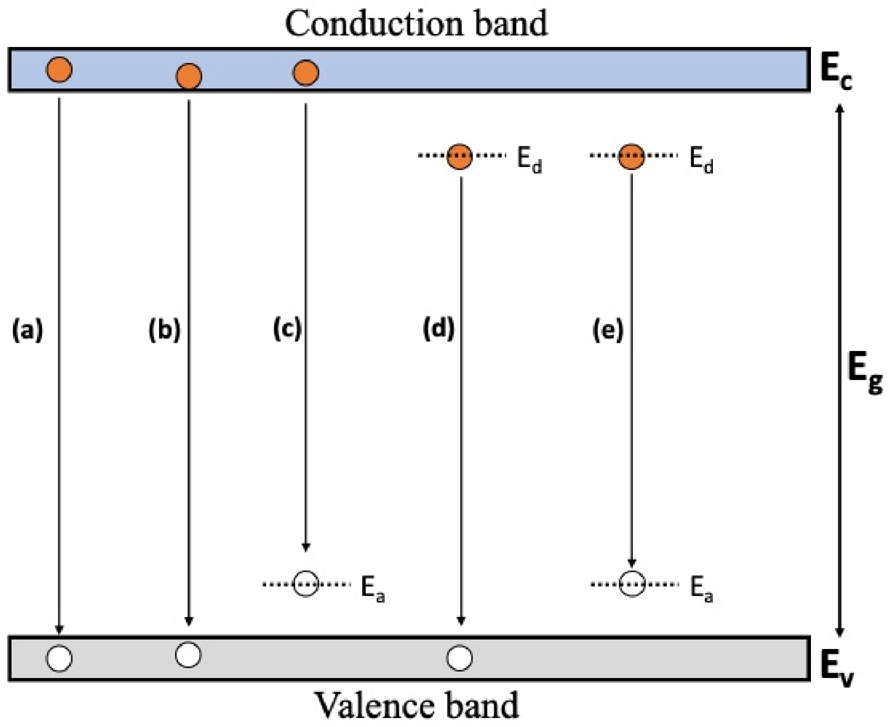

Figure 3.7: General electron-hole recombination processes within a semiconductor

overlap with process (a) resulting in a broadened NBE emission peak.

Process (c) & (d) are recombination mechanism involving defects that produce energy levels within the bandgap. These defect states can be produced by extrinsic atoms within the semiconductor crystal either through doping or impurities. Intrinsic point defects such as vacancy sites may also act as hole trap sites within the crystal and form additional acceptor states allowing radiative emission. Multiple defect states can result in many recombination process with energies lower than the semiconductor bandgap with process (e) producing the lowest energy transitions. This can be reflected in the luminescence spectra as distinct lower energy emission peaks or as a single broad defect band when individual peaks overlap. An example spectra showing NBE emission and various defect luminescence peaks is shown in Figure 3.8

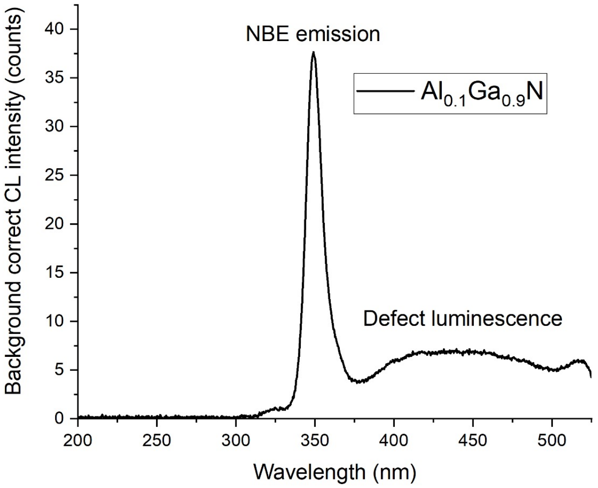

Figure 3.8: Example CL spectrum from $Al_{0.1}Ga_{0.9}N$ sample showing NBE emission and various defect bands

3.2 X-ray microanalysis

Through the analysis of the characteristic X-rays emitted by a sample during electron microscopy it is possible to deduce what elements are present and quantify the composition of the specimen. There are two electron microscopy techniques within the X-ray microanalysis bracket: energy dispersive X-ray (EDX) spectroscopy and wavelength dispersive X-ray (WDX) spectroscopy with both techniques analysing the same characteristic X-rays mentioned in the previous section. The two techniques are very similar with what characterising sample information they can produce however differ in their X-ray detection method and quantitative precision.

3.2.1 Energy-dispersive X-ray spectroscopy (EDX)

EDX is generally described as the more basic approach to X-ray microanalysis, allowing quick identification and quantification of a sample composition albeit with much lower precision capable than for the more complex WDX. Modern EDX systems can produced quantitative measurements with WDX precision however requires a more careful and advanced approach to the standard experimental method [123, 124].

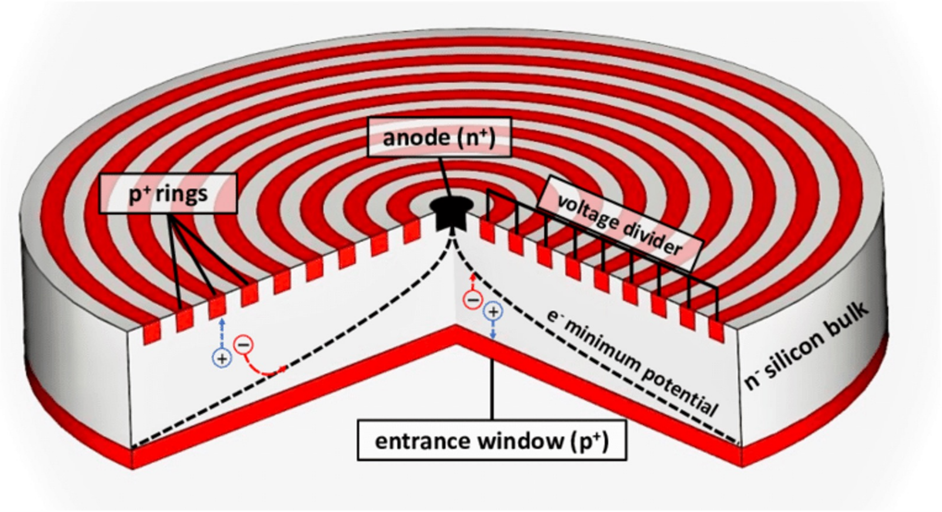

Figure 3.9: Architecture of cylindrical silicon drift detector used during EDX analysis. Extracted from [125]

Within an EDX measurements X-rays are typically detected using a silicon drift detector (SDD). A schematic of a SDD is shown in Figure 3.9. The SDD consists of a plate of high purity n-type doped silicon, on one side of the plate is a thin back contact and the other a set of concentric ring contacts surrounding a collection anode.

X-rays enter the SDD through the thin back contact, acting as an X-ray window and are incident on the silicon plate. The incident X-rays then ionize the Si, promoting a number of electrons to the CB. A negative bias is then applied to the back contact and to each ring contact, with each ring contact having an increasing voltage extending radially outward from the collection anode. This generates an electric field that directed towards the central anode, allowing the electrons to "drift" to a collection electrode, producing a charge equal to the energy of the X-ray [125].

Each charge is then converted to an electrical pulse which is then processed and recognised as an X-ray of a specific energy. This is done by a field effect transistor (FET) preamplifier, where the anode is connected to the gate of the FET and a feedback capacitor. Each X-ray entering the detector will change the output of the FET preamplifier. As the number of electrons accumulating at the anode increases the voltage outputted by the FET increases with individual X-rays recognised as "voltage steps" in the voltage pulse output [126, 127]. The height of each voltage steps is then analysed and translated into an individual X-ray of a specific energy by a multi-channel pulse height analyser (PHA). The PHA then assigns the X-ray to a specific energy channel (with the energy range of each channel determining the resolution of the detector) generating an EDX spectrum of counts vs. X-ray energy (keV). An example EDX spectra is shown in Figure 3.10

As multiple X-rays will enter the detector simultaneously, the differences in voltage step height from the FET preamplifier are recognised as different X-ray energies when processed by the PHA. The feedback capacitor will accumulate charge over time and subsequently discharge, resetting the FET preamplifier and preventing the system from overloading [126].

An EDX detector is limited by a number of factors: Firstly, the detector is prone to electrical noise which must be mitigated through cooling, typically using a Peltier cooler. Secondly, the detector is limited by the number of X-rays it may process at one time. The detector "dead time (DT)" is the time the detector is unable to process the incoming X-rays, in order to ensure all X-rays entering the detector are being adequately processed the detector must be set up suitably. In the case of detector overload the X-ray process time may be decreased, reducing the DT at the expense of energy resolution. Alternatively the amount of X-rays entering the detector may be reduced through the use of apertures or a lowered beam current to reduce the X-ray generation rate.

From an EDX spectra the elements present in the specimen can be deduced from the X-ray energies where peak counts are high (elements are generally auto-identified and assigned to each peak by the EDX software). Whether the specimen under irradiation is charging may also be deduced from the EDX spectra. As Bremsstrahlung background X-rays may be generated with any energy up to the incident beam en-

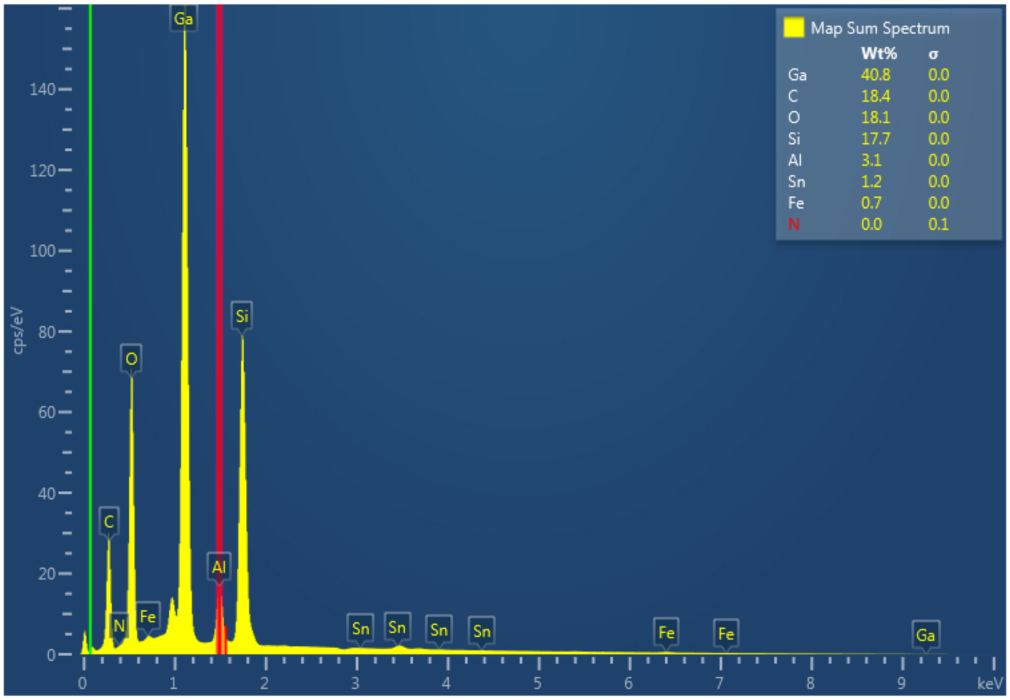

Figure 3.10: Example EDX spectra on a tin-gallium oxide sample with Si substrate showing high numbers of Ga and O X-rays and a low number Sn X-rays. C, Fe, N and Al X-rays come from impurities/rogue X-rays from sample holder.

ergy, the Duane-Hunt limit should match this energy. If the Duane-Hunt limit is less than the beam energy this indicates the sample is charging and the impinging electrons are being decelerated by the accumulating electrons before reaching the sample. In this case sample charging may be mitigated through carbon coating or reducing the beam current.

3.2.2 Wavelength-dispersive X-ray spectroscopy (WDX)

As mentioned previously WDX is a more advanced approach to X-ray microanalysis within the SEM. In EDX X-rays are distinguished by their energy and subsequent charge generated within the SDD whereas WDX is a diffraction based technique requiring the detector instrumentation to be aligned in a specific geometry. A diagram of the key components within a WDX spectrometer is shown in Figure 3.11

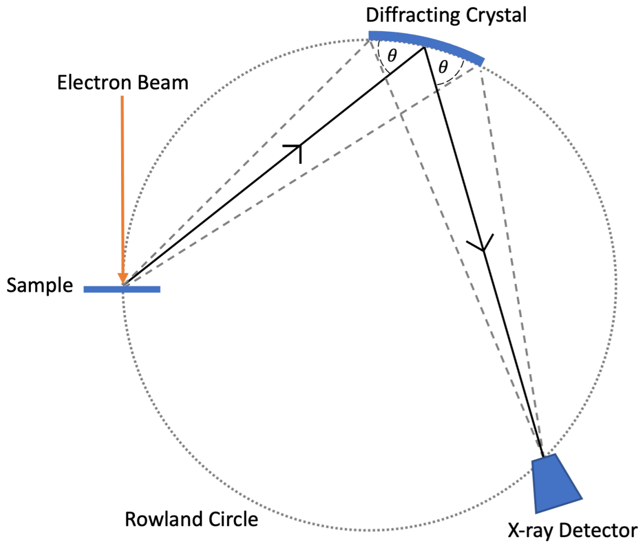

Figure 3.11: Example WDX spectrometer showing X-ray propagation path and components on the Rowland circle

The WDX spectrometer is designed to only allow accept X-rays that enter the spectrometer within a narrow angle. From here the X-rays that enter the spectrometer will encounter an X-ray diffraction crystal. This crystal uses Bragg diffraction to only allow X-rays of a specific wavelength to be diffracted towards the X-ray detector. The wavelength of X-rays that may enter the diffraction crystal is dictated by the Bragg diffraction equation:

$$n\lambda = 2d\sin(\theta) \tag{3.2}$$

By rotating the diffraction crystal the X-ray angle of incidence is changed therefore changing the wavelength of the X-rays allowed to enter the crystal. Therefore for a single crystal a range of X-ray wavelengths can be diffracted, in order to cover the range of X-ray wavelengths produced by the periodic table a number of diffracting crystals will be required with differing lattice spacing (d) values. A table showing the types of diffracting crystal, 2d-spacing and elemental detection range for K and

L X-ray lines is show in Table 3.2

Crystal name	**2*d*-spacing (nm)**	***K*-line range**	***L*-line range**
TAP	2.5757	O - P	Cr - Nb
TAPL	2.5757	O - Si	Cr - Sr
TAPH	2.5757	F - Al	Cr i Br
PET	0.8742	Al - Mn	Kr - Tb
PETL	0.8742	Al - Cr	Kr - Sm
PETH	0.8742	Si - Ti	Rb - Ba
LIFH	0.4027	K - Br	Cd - Fr
LIFL	0.4027	Ca - Ga	Sn - Au
LDE1L	6	C - F	N/A
LDE2L	10	B - O	N/A

Table 3.2: List of WDX diffraction crystals, $2d$-spacing and anayltical range for K and L series X-ray lines from [128]

Within the spectrometer the X-ray diffraction crystal and detector are held in a Rowland circle arrangement, see Figure 3.11. For this arrangement the sample, diffracting crystal and X-ray detector are all held on a circumference of an imaginary circle with a fixed radius. As the diffracting crystal rotates the crystal and detector also move laterally around the circumference while the sample remains in a fixed position. By using the Rowland circle geometry and a curved diffraction crystal (Johannson arrangement) the cone of X-rays entering the crystal will be refocused after diffraction and enter the X-ray detector in focus [129]. The WDX spectrometers used within this investigation come in two forms: H- and L- type. H-type spectrometers have a Rowland circle radius of 100 mm allowing an 2θ range between 36 - 118.5° whereas the L-type feature a larger Rowland circle radius of 140 mm and an greater range of angles of incidence between 25.5 - 136°. The improved angle range of L-type spectrometers allows greater wavelength resolution compared to L-type while also improving the peak-background ratio of the X-ray lines, on the other hand H-type spectrometers produce higher X-ray counts than L-type.

In Table 3.2 the TAP, PET, and LIF crystals are abbreviations for thallium acid phthalate, pentaerythritol and lithium fluoride crystals whereas the LDE1 and

LDE2 are layered psuedo-crystals engineered to have specific $2d$-spacing to allow the detection of light elements with low characteristic X-ray energies. The H and L variants of these diffraction crystals refer to the H and L type spectrometers.

Unlike EDX measurements only a single X-ray wavelength may be detected at one time, therefore when using WDX to acquire the entire X-ray spectrum produced through a specimen the diffraction crystal must be scanned through a range of angles of incidence. This is referred to as a **qualitative** WDX measurement and takes a considerably longer time than the EDX counterpart due to the time required to rotate the crystal and the dwell time used at each angle interval. Usually 3-4 diffraction crystals (and scans) will be required to produce an entire X-ray spectrum therefore further multiplying the qualitative measurement time unless multiple WDX spectrometers can be used simultaneously (as with the EPMA). A qualitative WDX X-ray spectra acquired from a TGO sample on four spectrometers is shown in Figure 3.12

For X-ray detection a gas-proportional detector is used. This detector consists of a chamber of inert gas (for our WDX X-ray detectors a P-10 gas [10% methane & 90% argon] is used) containing a wire anode to which a bias is applied. X-rays propagate through a small, thin polypropylene window within the chamber and can ionise the contained P-10 atoms. The gaseous ions are then attracted to the wire anode, generating an electrical pulse with pulse amplitude relative to the ionizing X-ray energy. The pulse is then processed by a PHA similarly to EDX.

Even though the WDX spectrometer is designed to only allow a singular X-ray wavelength to enter the detector multiple X-ray energies may be present. This can be a result of higher order X-ray reflections passing through the spectrometer (the integer term in Equation 3.2) or from escape peaks due to the ionization of the spectrometer window or fluorescence of the P-10 Ar atoms. Once the pulses have been filtered through the PHA the remaining pulses are then recognised as single X-ray counts.

The gas-proportional counter is the preferred detector for WDX measurements due to the 1:1 counting statistics with no pulse multiplication unlike other detectors e.g. photomultiplier tubes (PMTs). Gas proportional detectors are still susceptible

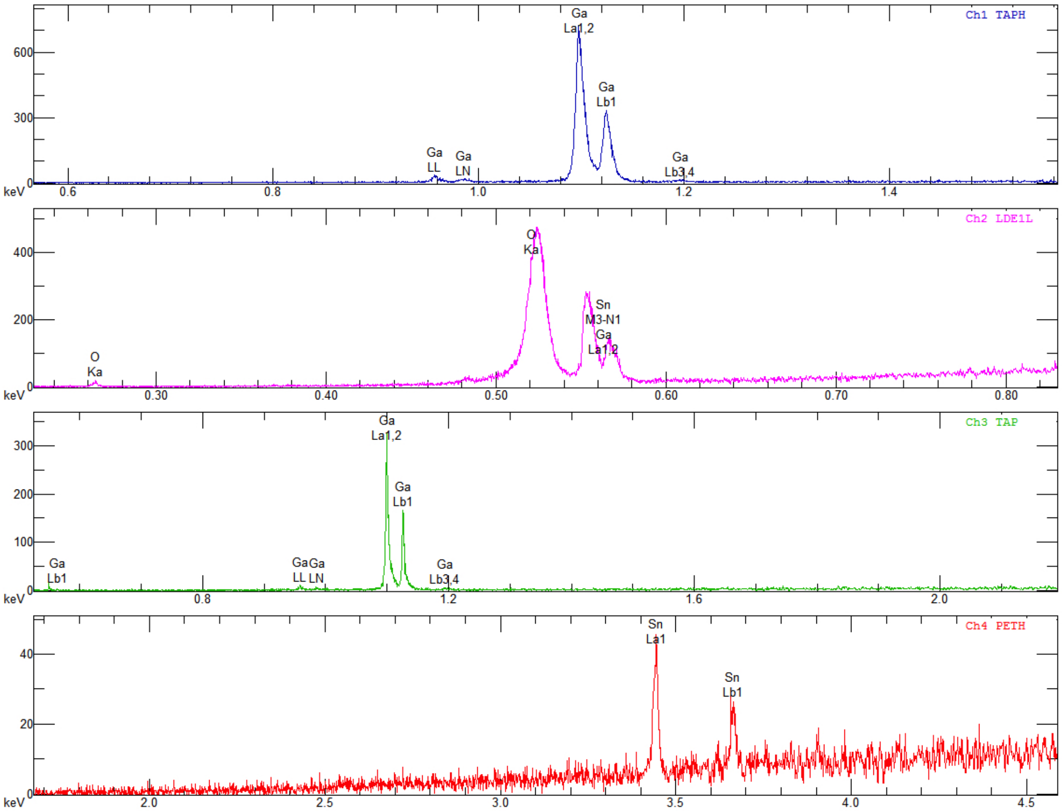

Figure 3.12: Qualitative WDX X-ray spectrum acquired from a TGO sample using a 10 keV, 40nA beam. Spectrometers used in each scan are TAPH, LDE1L, TAP, PETH going from top-bottom.

to detector overload, when the gas ionization rate is too high the ions begin to form a sheath around the wire anode, preventing any further ion detection. Recent studies have used a SDD as an alternative to the gas-proportional detector allowing higher count rates and enhanced energy resolution. However, as with EDX, this requires the integration of heat dissipation components within the spectrometer [130].

The trade-off for the longer operational time for WDX measurements vs EDX is the superior energy resolution capable through WDX, typically stated as 10× the resolution of EDX.

The energy resolution of EDX is limited by the detector and pulse processing times. The energy resolution of EDX detectors also decreases when measuring high energy X-rays, with modern detectors quoting resolutions of 150 meV for the Fe K_α line (6.4 keV) and 40-50 meV at the lowest X-ray energies (100 meV) [131]. These values are also based on operating at the slowest pulse processing times, reducing the processing time to account for high X-ray count rates will deteriorate the resolution further [132]. WDX on the other hand has a much better energy resolution of 6 eV at for Fe K_α X-rays regardless of beam conditions [133]. Generally the WDX resolution is quoted as being on the 2-20 eV scale across the entire measurable X-ray energy range [134].

The improved resolution of WDX allows individual X-ray peaks to be resolved within alloys where the EDX spectra shows a singular broad peak due to the peak overlaps (e.g. N K_α & Ti L_α [135]). As the WDX spectrometer filters out all X-rays apart from ones of the desired wavelength the detector can handle much higher X-ray count rates, processing only the selected X-ray energy rather than all X-ray energies as with the SDD. In turn this improves the X-ray counting statistics generally improving the quantitative performance of WDX over EDX [136].

3.2.3 Quantitative compositional analysis

The basis of a quantitative EDX or WDX measurements is determining the composition of an unknown specimen by comparing the X-ray counts produced from the specimen to that of a material of known composition and extrapolating a composition from the ratio of the counts. These materials are known as standards and are generally ultra-pure cylinders of an element (e.g. pure copper, Cu), basic compounds (e.g. Pyrite, FeS_2) or naturally occurring minerals (e.g. Albite, $NaAlSi_3O_8$). For our measurements the standards consist of both commercial and homegrown materials. The purity of the commercial standards has been confirmed through vigorous X-ray microanalysis and the standards we have sources ourselves consists of pieces of semiconductor materials of high quality confirmed through X-ray microanalysis or through an external measurement technique e.g. secondary ion mass spectrometry (SIMS). The commercial standards used within this thesis were purchased from *PH Developments Ltd.*

The process used to deduce a composition using the specimen and standard X-ray counts is more complex than just a basic comparison, requiring multiple correction factors and recalculations to produce a "true" composition of specimen. Here the specifics behind the calculation process shall be explained.

$$\frac{I_{unk}}{I_{std}} = C_{unk} \cdot ZAF \tag{3.3}$$

Equation 3.3 shows the basic components of the quantitative WDX/EDX calculation where I_{unk} is the X-ray intensity of the unknown specimen, I_{std} is the X-ray intensity from the standard, C_{unk} the calculated mass fraction within the specimen and ZAF corresponds to the three correction factors: the atomic number correction (Z); the absorption correction (A) and the fluorescence correction (F).

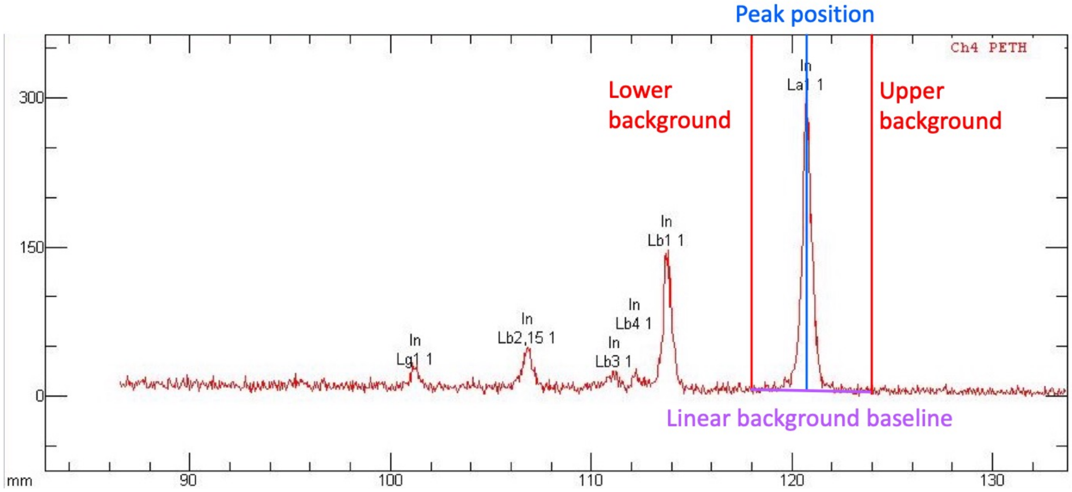

Figure 3.13: Qualitative WDX X-ray spectrum acquired from an indium-gallium oxide showing X-ray spectrum of In L-series from a PETH diffraction crystal. Peak (red), background (blue) and baseline (purple) positions used for quantitative analysis are drawn on the spectrum

In order to ensure that only characteristic X-rays are included within the calculation of I_{unk} and I_{std} a background correction must be made. An X-ray spectra showing the peak and background measurement positions is shown in Figure 3.13. X-rays are initially counted at the peak position providing the uncorrected peak counts. Background measurements are then taken to the left and to the right of the peak at suitable positions away from any other peaks. A linear baseline is then drawn between the two background positions, from this baseline the background counts at the peak position can be extracted allowing the calculation of background corrected I_{unk}. The same process may then be repeated for the standard to calculate the background corrected I_{std}. Different background positions may be used for I_{unk} and I_{std} to account for X-ray peaks not present in both materials but for the greatest experimental accuracy the background positions should be kept consistent. An exponential baseline may be used when the background shows a curved nature.

The only parameter that must stay constant between the two measurements is the beam energy. To account for differences in the beam current (either intentional to generate a suitable number of counts or unintentional current drift) the I_{unk} and I_{std} raw X-ray counts are converted into counts per second per micro-ampere (cps/μA). This also makes the two measurements comparable when different X-ray counting times are used e.g. Trace element measurements requiring an increased counting time [137]. The cps/μA values from the two measurements can then be used to calculate the k-ratio for that particular element, defined in Equation 3.4

$$k = \frac{I_{unk}}{I_{std}} \tag{3.4}$$

$$C_{unk} = k \cdot C_{std} \tag{3.5}$$

The k-ratio can then be used to derive the first approximation of the composition of that element within the specimen using Equation 3.5 where C_{std} is the mass fraction of the element within the standard. The next step in deriving the true composition is to apply the ZAF corrections.

Atomic number correction, Z

The atomic number correction accounts for differences in the atomic number (or average atomic number for compounds) between the specimen and the standard which effects the X-ray generation rate. The Z correction accounts for two effects:

differences in the backscattered electron generation rate and the electron stopping power.

As mentioned previously as Z increases the backscattered electron coefficient increases, *Equation 3.1.* When there is a large difference between the average atomic number of the specimen and standard the number of BSEs can differ substantially, resulting in an nonequivalent number of inelastic scattering events leading to characteristic X-ray generation. This is particularly significant when comparing X-ray counts from a pure element standard (e.g Cu) to those produced from an alloy containing heavy metals (e.g rose gold).

$$S = -\frac{1}{\rho}\frac{\mathrm{dE}}{\mathrm{ds}} \tag{3.6}$$

Stopping power, S, refers to the energy loss rate by an electron propagating through the specimen, the formula for which is shown in Equation 3.6 where S is the stopping power, ρ the density of the material, and dE/ds the rate of energy loss. The Bethe equation for energy loss is used for dE/ds, from which there is a inverse dependence on atomic number with lighter elements increasing the rate of energy loss compared to heavier elements [121].

Absorption correction, A

Not all X-rays that are generated within a sample are emitted. As the X-rays propagate through the sample there is a probability they may be reabsorbed reducing the apparent X-ray counts. In general X-rays generated deeper within a specimen have a greater chance of reabsorption but X-ray absorption is dependent on a number of factors. The mass absorption coefficient (MAC), given by μ/ρ dictates the likelihood that an X-ray will be absorbed by a material, where ρ is the material density and μ the X-ray attenuation length with the material. Every X-ray of different energy will feature a different MAC therefore varying the rate of absorption. The greatest MACs will be found for X-rays with energies within the absorption edges of an element, corresponding to a few eVs greater than the greatest shell transition energies (e.g Al K-absorption edge = 1.60 keV, K_α = 1.49 keV K_β = 1.56 keV). The absorption correction is calculated using Equation 3.7 where h=1.2A/Z^2 (A being atomic mass and Z the atomic number of the element), σ is the Lenard coefficient which takes into account the electron beam energy. χ is defined in Equation 3.8 where μ/ρ is the MAC and ψ is the X-ray take-off angle (assumed to be 40°) [138, 139].

$$A = f(\chi) = \frac{1+h}{(1+\chi/\sigma)[1+h(1+\chi/\sigma)]} \tag{3.7}$$

$$\chi = \frac{\mu}{\rho} \cdot \operatorname{cosec}(\psi) \tag{3.8}$$

Fluorescence correction, F

If a re-absorbed X-ray is of a high enough energy it may be possible to generate the emission of another characteristic X-ray via a process known as X-ray fluorescence. X-ray fluorescence can be split into two forms depending on the type of X-ray generating the fluorescence: Characteristic secondary fluorescence (CSF) and Bremsstrahlung secondary fluorescence (BSF).

During CSF there is a loss of a characteristic X-ray from one element and an X-ray gain for another element. The magnitude of CSF is at its greatest when the energy of the exciting X-ray lies at or above an X-ray absorption edge of the fluorescing element, particularly an issue when involving two transition metals near-adjacent to each other in the periodic table. As CSF involves characteristic X-rays for excitation, the highest energy characteristic X-ray is unable to be generated through this method. BSF has a lesser effect than CSF but is capable of exciting all characteristic X-rays with energies up to the Duane-Hunt limit. As the Bremsstrahlung generation rate decreases for higher energy X-rays, BSF has the greatest magnitude for lower energy X-ray lines.

$$F = \frac{1}{1+I_f/I_A} \tag{3.9}$$

The simplified fluorescence correction formula is shown in Equation 3.9 [140], where F is the fluorescence correction factor, I_f is the fluorescence X-ray intensity and I_A the primary X-ray intensity. This correction assumes that the exciting and generated X-ray are both from K-lines, when other X-ray lines are involved the correction weakens as the fluorescent yields of these lines is not as well established.

Another shortcoming of the F correction is the inability to distinguish the origin of an X-ray. X-ray fluorescence extends the excitation volume beyond that of the primary X-ray generation volume. In the case of layered materials or materials featuring grain boundaries this can result in unwanted X-ray generation from outwith these boundaries. The F correction is unable to correct for this resulting in these X-rays skewing any compositional calculations.

Once the ZAF corrections have been applied and a first approximation has been derived for each elements present in the specimen an iterative cycle begins to calculate the true composition of a material. Combining equations 3.3, 3.4 & 3.5 and applying the calculated ZAF correction allows the derivation of C_{unk}. C_{unk} is still only an approximation of the specimen composition. To generate a more accurate composition the ZAF corrections are then recalculated using C_{unk} as a base composition then reapplied to produce a new composition C_1. This cycle then repeats, deriving C_2 from C_1 and so forth, shown in Equation 3.10

$$C_{unk} \cdot [ZAF]_1 = C_1 \rightarrow C_1 \cdot [ZAF]_2 = C_2 \rightarrow C_2 \cdot [ZAF]_3 = C_3 \rightarrow \ldots \tag{3.10}$$

This process repeats over a number of iterations until the results of each consecutive composition converge to one value (the true composition) or a user set maximum number of iterations have been performed. By using standards with a composition similar to that of the unknown specimen the reliance on the ZAF to produce the true composition from the first approximations is reduced and the calculation should require fewer iterations. Alternative correction factors are available for quantitative analyses such as the PAP or $\phi(\rho Z)$ models. The JEOL software performs quantitative measurements using the following ZAF corrections: Philibert-Tixier method for Z [141], Philibert method for A [142] and Reed method for F [140].

Quantitative EDX is usually known as "standardless" analysis, requiring a measurement of the specimen only to calculate a quantitative composition. This greatly reduces the acquisition time for compositional measurements while increasing the uncertainty present. There are two forms of "standardless" measurements: The first uses a database of pre-existing standard results to derive the K-ratios from the EDX spectra counts.

The second is a "first principle" calculation, theoretically approximating the number of characteristic X-rays generated in a pure material and using that as a "standard" to derive the K-ratio. The first principle calculation formula is given in Equation 3.11 where I_{ch} the characteristic X-ray intensity, N_A is Avogadro's number, ρ is density, A is atomic number, ω the fluorescence yield, R describes the backscattered electron correction, E_c the critical energy require for X-ray generation, E_0 the beam energy, Q_x the ionization cross section and dE/ds is the energy loss rate [143].

$$I_{ch} = (\frac{N_A \rho}{A}) \omega R \int_{E_0}^{E_c} \frac{Q_x}{dE/ds} dE \tag{3.11}$$

.

The sheer number of parameters in Equation 3.11 shows the complexity of first principle calculations, in turn highlighting the uncertainty contained due to the number of approximations that are made when calculating I_{ch}.

3.3 Monte Carlo simulations

Throughout this thesis two simulation packages are used to assist experimental electron microscopy measurements and to allow theoretical studies to be performed to understand the interactions within these measurements.

CASINO

The CASINO Monte Carlo simulation program [144] is a useful tool for understanding electron-solid interactions when performing electron beam analyses on a specimen. The program simulates an electron beam impinging on a sample, simulating a number of electron trajectories to represent a measurement within an SEM. CASINO allows the user to select multiple parameters to tune the simulation to the experimental conditions the user requires (e.g. material composition density, beam energy and angle of incidence). The number of electron trajectories required is also user selected with low numbers producing more disperse results and a greater number providing a well represented average.

From these trajectories the beam excitation volume within the specimen can be calculated and the electron energy distribution in both the lateral and vertical directions (Only 2D simulations have been used within this thesis however 3D simulations can be performed). Knowing the energy distribution within the specimen allows CASINO to calculate the X-ray generation and absorption depths of the characteristic X-ray lines present within the material. A number of CASINO simulations at different beam energies are shown in Figure 3.14

These outputs from CASINO allow the user to determine the required beam parameters to correctly perform their EDX/WDX measurement ensuring X-ray generation remains within the upper film of layered samples and indicate if beam over-voltage may be problematic for thin film quantification (Ideally a beam over-voltage of 2× the highest characteristic X-ray energy is used however this is not always possible when measuring layered materials). In order for CASINO to be utilised properly prior knowledge of the specimen composition is required however it may still be used to determine upper and lower beam energy boundaries for layered samples if only basic compositional information is known. Within this thesis the CASINO simulations assume a perfectly flat, evenly distributed specimen however more complex structures can be simulated at the expense of increased simulation time.

DTSA-II

DTSA-II is an X-ray simulation package that allows the user to simulate EDX experiments and derive compositions using the in built quantitative program [145]. As with CASINO the user has full control of the specimen composition and beam pa-

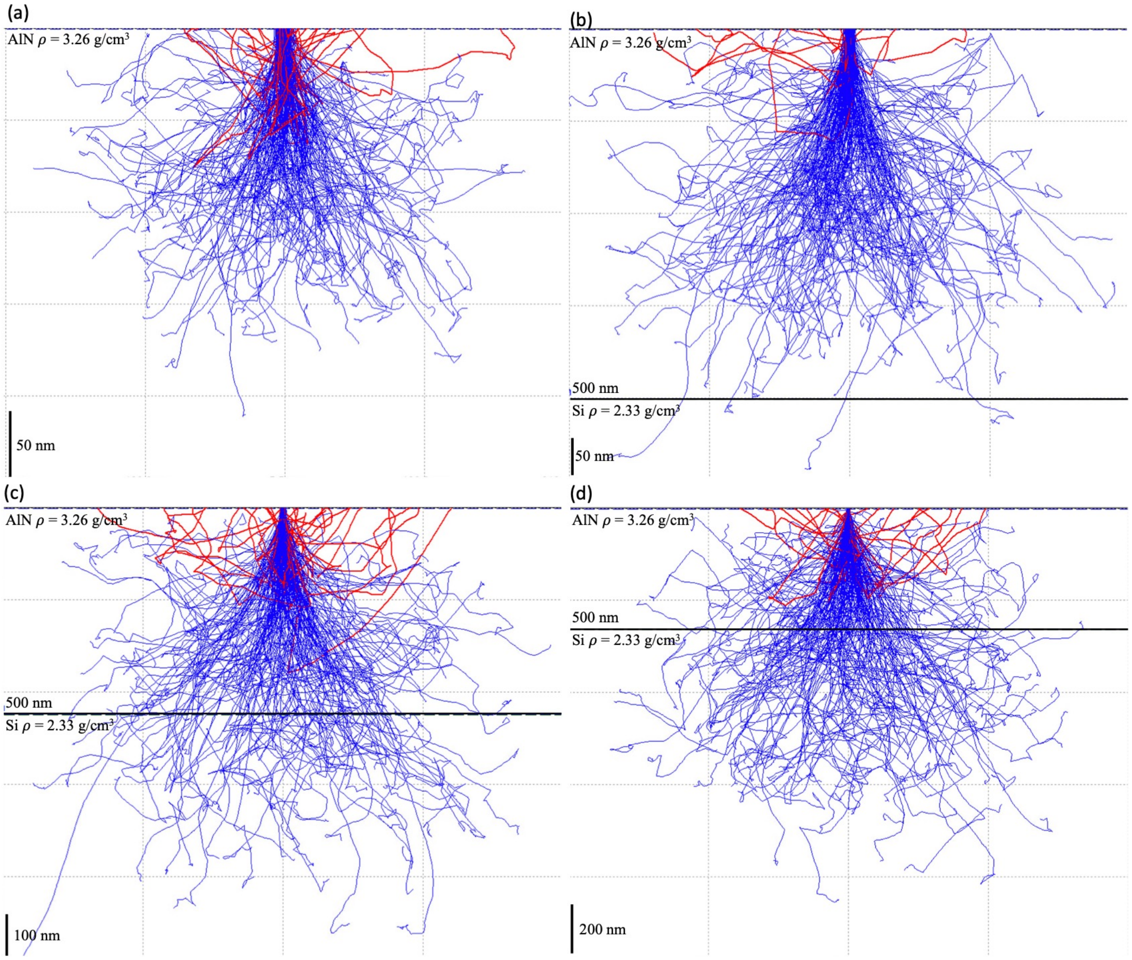

Figure 3.14: CASINO simulation results showing the electron penetration depths within a 500 nm AlN film ($\rho = 3.26$ g/cm^3) on a Si substrate ($\rho = 2.33$ g/cm^3) using 20,000 electron trajectories and a beam voltage of (a) 5 kV, (b) 7.5 kV, (c) 10 kV and (d) 15 kV

rameters and produces similar outputs (e.g. excitation volume and X-ray generation depths). Rather than selecting a set number of electron trajectories DTSA-II uses dose time [beam current (nA) × dwell time (s)] to represent the irradiation from the electron beam, more inline with experimental work.

For X-ray analysis DTSA-II goes a step further than CASINO by simulating the number of X-ray transitions produced by the simulation and generating the respective EDX spectra from this measurement. DTSA-II does this by first calculating the underlying X-ray intensity emitted from each characteristic X-ray lines and then broadening to fit the energy channel range set by the user and reflect the detector parameters used. The ability to calibrate the detector used within the simulation allows the user to upload experimental EDX spectra and compare to simulated data with results being independent of the detector response. When simulating the X-rays generated within the specimen DTSA-II separates the X-ray counts into their type and source of excitation: Characteristic X-rays generated by the electron beam, Bremsstrahlung generated by the electron beam, CSF and BSF. This allows the user to investigate the fluorescence behaviour within the specimen which was previously impossible through experimental methods. This can be advanced further as the user is able to turn off certain types of X-ray generation from the simulation allowing simulations to focus on particular X-ray types (e.g secondary fluorescence) or generate a spectra only containing one X-ray type (e.g Bremsstrahlung spectrum). An example of a DTSA-II simulation showing underlying characteristic X-ray counts and the respective EDX spectra is shown below in Figure 3.15. The DTSA-II simulations within this thesis are all performed assuming a perfectly flat, film-substrate material but more complex geometries and multilayered structures can be measured through supplementary python scripting.

3.4 Specimen mapping

Using the previously mentioned techniques (WDX and CL) it is possible to use scan across the sample surface or cross section to generate correlative WDX and CL maps. With the EPMA used within this study it is possible to map any compositional variation within a sample on length scales down to 20 nm per pixel, though the excitation volume within the sample will exceed this pixel size. Through simultaneous acquisition of the CL signal during WDX mapping it is possible to determine how the optical properties of the material are dependent on the material composition. Compositional variation across the sample may result in the enhancement (or suppression) of particular luminescence bands or produce shifts in peak energies,

Figure 3.15: EDX X-ray spectra produced by a DTSA-II simulation on 1 μm Ga_2O_3/Si thin film using an electron beam energy of 10 keV and probe dose of 4000As

through correlative mapping optical variation may be attributed to spatial regions of the sample which would previously be screened through broad WDX and CL point measurements.

When performing WDX mapping the spectrometer is first set to the wavelength of a characteristic X-ray of the element to be mapped. The next step is to select the region of interest for the map and decide an appropriate map size. The map takes the form of an array of pixels with the pixel size and number dictating the map dimensions. Within each pixel a specific beam dwell time is assigned from which the software will calculate the required raster scan speed to cover the whole map array. As the dwell time will be significantly less than the measurement time within quantitative measurements the number of X-rays generated and reaching the detector will be substantially lower so a greater beam current may be required. Therefore, a balance between dwell time, beam current and pixel size & number must be met to ensure the required map resolution is achieved. Generally the pixel size used would be near the smallest possible to provide the best resolution e.g 40-80 nm × 40-80 nm using a 40 nA beam with dwell time of between 150-250 ms. This would allow the acquisition of 100 × 100 or 200 × 200 maps (2-8μm × 2-8μm or 4-16μm × 4-16μm) in 1-3 hours and should allow the generation of a sufficient number of X-ray for all elements.

Joint CL and WDX mapping is where the strengths of the EPMA come to light. For the WDX the acquisition time of a single scan of the full map can range from a few minutes to multiple hours, when multiple elements are required (10+ common for geological samples) the acquisition time is greatly increased. Having 4 WDX spectrometers allows high resolution multi-elemental maps to be generated while keeping the acquisition time within a manageable range. More commonly used EDX detectors may acquire maps for all energies/elements simultaneously they are unable to distinguish between overlapping X-ray lines and to the same resolution as what is capable using the EPMA WDX spectrometers. As mentioned previously, the EPMA features an optical microscope which is used to make sure the sample is in focus with the WDX spectrometers. This optical microscope acts as the collection source for the CL signal, allowing the CL signal to also be acquired in focus with both the sample and the X-ray signal. Both signals acquired in focus ensures the correlative WDX and CL maps are showing similar spatial resolution.

The JEOL software used to operate the EPMA has may features assisting the acquisition of the WDX-CL maps: any drift in the automated stage during the map acquisition can be corrected for using SE imaging. By acquiring an SE image before and at regular intervals during the map any stage drift can be calculated by the software and the stage moved accordingly to reverse the effect, improving the map quality and retaining the nm scale spatial resolution. The EPMA stage can be controlled in all three spatial dimensions, this allows the mapping of rough samples or films with thickness variations while retaining optical focus. When acquiring a large map heavily effected by the thickness variations multiple smaller map sections may be acquired, with the EPMA gradually adjusting the focus to account for the height differences. The software can then stitch the subsections together, generating the full combined map with no focusing issues.

Another key piece of software used within these investigations during sample mapping is the cathodoluminescence hyperspectral imaging and manipulation program (CHIMP) created by Dr Paul R. Edwards. CHIMP acts as both the acquisition and post-processing program for the CL mapping.

The type of CL mapping performed here is hyperspectral CL imaging, collecting an entire spectrum at each pixel. This generates a data cube of spectral information within a fixed spatial region. Post CL acquisition CHIMP is used to extract various optical parameters from this data cube. Peak fitting can be performed to isolate individual luminescence peaks from complex spectra, determining the properties of the deconvolved peaks (e.g intensity, FWHM). As a entire spectrum is collected at each interval the changes to these peak properties can be mapped unlike conventional monochromatic CL imaging. From the hyperspectral data cube monochromatic CL intensity slices may also be extracted by integrating over a define energy range allowing single maps to be generated for particular optical bands. Other possible properties which may be mapped through CHIMP are peak centroids (the centre of "mass" of the peak) or true colour in the case of visible light spectroscopy. This is particularly useful when correlated with WDX mapping as peak broadening or shifts in peak energy will also accompany the intensity variation reflected in the compositional variation of a sample or surface feature.

Chapter 4

AlGaN

4.1 Introduction

Using WDX and CL spectroscopy the optical and compositional properties of wide-bandgap aluminium-gallium nitride thin films grown with polar, semi-polar and non-polar crystal orientations have been investigated.

As the ultrawide bandgap of $Al_xGa_{1-x}N$ films can be engineered from 3.4 - 6 eV [51] it makes them highly desirable for LEDs operating in the deep UV spectral range. Such LEDs can then be applied within devices for medical sterilisation, water purification and UV communication [67, 146, 147].

As mentioned in Chapter 2 there are a number of complications impacting the efficiency of $Al_xGa_{1-x}N$ LEDs, particularly for high AlN contents. Firstly, doping is a major issue, the increasing activation energy of commonly used Si n-type dopants (180 – 250 meV for pure AlN) and Mg *p*-type ($\sim$ 630 meV) [67, 68] results in poor film conductivity, aggravated by the low hole mobility in high AlN fraction films. Another issue of these devices is the switch in the light polarization extracted from these devices with increasing levels of AlN, flipping from transverse electric to transverse magnetic, reducing the light extraction efficiency of high AlN $Al_xGa_{1-x}N$ LEDs [83]. III-Nitride LED and MQW structures also feature large internal polarization fields impacting the functionality of these devices by reducing the quantum efficiency and redshifting the emission energies [148,149]. This chapter will focus on the characterisation of $\mathrm{Al}_x\mathrm{Ga}_{1-x}\mathrm{N}$ thin films grown along different crystal orientations (semi-polar, non-polar) as a way to minimise the impact these internal polarization fields common to c-plane, polar III-Nitrides.

As these polarization fields are along the c-plane direction in the wurtzite crystal their impact can be mitigated by growing materials along non/semi-polar directions [150, 151]. However growth along these crystal orientations proves difficult with different challenges such as suitable substrate availability, low defect growth and unknown optical behaviour of the films [151, 152]. The difficulty in growing such materials has resulted in the device properties being poorly established, with only two published papers featuring semipolar LEDs (to the best of my knowledge). The first published report of a semipolar $\mathrm{Al}_x\mathrm{Ga}_{1-x}\mathrm{N}$ LED described operation at an emission wavelength of 307 nm [153] and more recently a report of an r-plane $\mathrm{Al}_x\mathrm{Ga}_{1-x}\mathrm{N}$ LED operating in the 270 nm range was published [154].

Non-polar LEDs are just as unknown as their semi-polar counterparts however the enhanced efficiency of semi/non-polar has been investigated and shown through computational modelling [155]. Alternatively, through the fabrication of nanostructures there are reported cases of LEDs being fabricated from the non-polar growth of GaN & $\mathrm{Al}_x\mathrm{Ga}_{1-x}\mathrm{N}$ MQWs on the facets of nanorods [156–159]. Before progress can be made in the fabrication (and operation) of these structures and devices it will be instructive to investigate the fundamental properties of the materials through bulk thin film characterisation. Within this chapter a series of MOCVD grown wurtzite $\mathrm{Al}_x\mathrm{Ga}_{1-x}\mathrm{N}$ films with polar, semi and non-polar orientations were analysed: Polar c-plane (0001), non-polar m-plane $(10\bar{1}0)$ & a-plane $(11\bar{2}0)$ and semi-polar planes $(11\bar{2}2)$ & $(10\bar{1}3)$. A set of undoped $\mathrm{Al}_x\mathrm{Ga}_{1-x}\mathrm{N}$ samples spanning the entire AlN compositional range for each orientation was provided by Dr. Duc V. Dinh and Prof. Markus Pristovsek from the Institute of Materials and Systems for Sustainability, Nagoya University [59, 160, 161]. An additional set of Si doped $(11\bar{2}2)$ $\mathrm{Al}_x\mathrm{Ga}_{1-x}\mathrm{N}$ samples with high Al compositions were provided by Drs. Humberto Foronda Tim Wernicke and Prof. Michael Kneissl from the Technische Universität Berlin (TU Berlin) [66].

4.2 Growth of $Al_xGa_{1-x}N$ films and semi/non-polar substrates

Both sets of samples were grown using a close-coupled showerhead MOVPE reactor with ammonia (NH_3), trimethylgallium (TMGa) and trimethylaluminium (TMAl) being used as the precursors. The Si doping for the TU Berlin samples was provided by introducing silane (SiH_4) into the reactor during growth. For the Nagoya samples and substrates the following procedure was used:

Rather than directly growing the $Al_xGa_{1-x}N$ layer directly upon the sapphire substrate a thin buffer layer of AlN was grown prior to the $Al_xGa_{1-x}N$ film. In order to promote $Al_xGa_{1-x}N$ growth along the desired crystal orientations differently oriented sapphire substrates were used with the AlN buffer layer forming a template for the semi- and non-polar $Al_xGa_{1-x}N$ layer to follow. The following sapphire substrates were used to produce the differently oriented AlN/sapphire templates allowing the growth of the semi/non-polar $Al_xGa_{1-x}N$ layers: (0001) AlN ($d\approx$ 800 nm) on c-plane sapphire, $(11\bar{2}2)$ AlN ($d\approx$ 1000 nm) on m-plane sapphire, $(10\bar{1}0)$ AlN ($d\approx$ 350 nm) on m-plane sapphire, and $(11\bar{2}0)$ AlN ($d\approx$ 350 nm) on r-plane sapphire [160]. To produce the $(10\bar{1}3)$ AlN template, a 10 nm $(10\bar{1}3)$ AlN layer was initially sputtered onto a 2-inch m-plane sapphire wafer using directional sputtering. Afterwards, this wafer was loaded into the reactor chamber to grow a 300 nm $(10\bar{1}3)$ AlN layer [59]. The exact growth parameters for the AlN/sapphire templates are found in Refs. [59,160].

For the $Al_xGa_{1-x}N$ film growth, about 100 nm AlN was initially grown on these templates at 1290°C at a reactor pressure of 27 hPa. Afterwards, $Al_xGa_{1-x}N$ layers with a nominal thickness of 1.5 μm were grown at 1150°C at a reactor pressure of 100 hPa. The $Al_xGa_{1-x}N$ composition was varied by changing the partial pressures of TMGa and TMAl while keeping the overall flow rate and the NH_3 flow constant [59]. For each orientation $Al_xGa_{1-x}N$ films were grown with expected contents of $x = 0$ (GaN), 0.1, 0.2, 0.4, 0.6, 0.8 & 1 (AlN). The growth cycle for $x = 0.6$ was also repeated a further time.

The $Al_xGa_{1-x}N$ samples provided by TU Berlin were grown using a similar approach [66]. Firstly, semi-polar growth was achieved through growth on nitrated m-plane $(10\bar{1}0)$ sapphire at 1135°C. As with the Nagoya samples the $\mathrm{Al}_x\mathrm{Ga}_{1-x}\mathrm{N}$ composition was controlled by the partial pressures of the precursors with expected $\mathrm{Al}_x\mathrm{Ga}_{1-x}\mathrm{N}$ compositions of approximately $x = 0.6$ & 0.8. A growth temperature of 1095-1100°C and reactor pressure of 500 hPa was kept constant for all samples. *In situ* reflectance measurements determine the film thickness to be approximately 1.15μm for $x = 0.6$ and 0.75 μm when $x = 0.8$. The dopant concentration was controlled by varying the SiH_4/III partial pressure ratio, which was between 1.5×10^{-5} to 3×10^{-4} for $x = 0.6$ and 5×10^{-5} to 6×10^{-4} for $x = 0.8$ [66].

4.3 Compositional measurements

The WDX and CL measurements were performed on a JEOL JXA-8530F EPMA. Two WDX measurements were completed to determine the entire composition of the film:

1. The major element components (Al, Ga & N) were determined using a beam energy of 10 keV, 40 nA beam current and a beam spot size of 10μm. X-rays were counted for 60s at the peak position and 30s at each side of the peak for the background.

2. Due to the reduced concentration the Si dopant density was measured separately. This measurement used a increased beam current of 400 nA and extended X-ray counting times of 360s on the peak and 180s for each background. The remaining parameters remained the same as measurement 1.

The results from the two measurements were then combined using the JEOL EPMA software and the entire composition of the film was recalculated. The k-ratios used to determine the material compositions were calculated using the following standards: AlN for Al & N, GaN for Ga and Si for Si. A thallium acid phthalate (TAP) crystal was used for the Al K_α, Ga L_α and Si K_α X-rays and a synthetic layered pseudo-crystal was required for the N K_α X-rays [162]. Samples were carbon coated prior to WDX measurement to prevent sample charging from electron accumulation. For consistency the standards used were also carbon coated.

9 measurement points were taken for each sample in a 3 × 3 grid with 0.25-0.5 mm spacing, the average sample composition and random error were then calculated. The quality of each individual measurement was assessed using the calculated total Wt% and the N at%, which should be 100 and 50 respectively. In general, measurements with a total Wt% lying between 98-102% were considered acceptable and measurements outwith this range were discounted, for high AlN samples a greater tolerance was accepted as the measurement was impacted by sample charging. As the $\mathrm{Al}_x\mathrm{Ga}_{1-x}\mathrm{N}$ alloy has the same stoichiometry as the two binary semiconductors (AlN and GaN) the N content should be 50 at%. Measurements producing dissimilar N at% values were also removed from the analysis (48 at% $\leq$ N $\leq$ 52 at%).

As mentioned, sample charging is the most probable reason for WDX measurements producing results with a Wt% or N at% lying outside the acceptable range. The accumulation of electrons reduces the effective beam energy resulting in a lesser number of X-rays being generated from the sample. This is reflected in a reduced Wt% when the number of X-rays produced by the sample is compared to that produced from the standards used during quantification. Other possible reasons for unsatisfactory Wt% or incorrect cation-anion stochiometries may be: Surface contamination; a rough sample surface resulting in poor alignment between the sample and WDX spectrometers or poor standard choice. As mentioned in Chapter 3, by choosing standards similar in composition to the unknown sample (AlN and GaN for $\mathrm{Al}_x\mathrm{Ga}_{1-x}\mathrm{N}$ in this case) the reliance on the ZAF correction factors to calculate the true sample composition is reduced. Quantitative measurements using exotic standards compared to the unknown will require large correction factors for which there can be a high level of uncertainty. This can affect the calculated composition of the sample, reflected in the Wt% or elemental at%.

Due to the number of samples, the results from the WDX compositional measurements are expressed graphically in Figure 4.1 where the composition calculated by WDX is plotted against the expected composition from the precursor partial pressures during growth rather than a composition calculated from another analytical

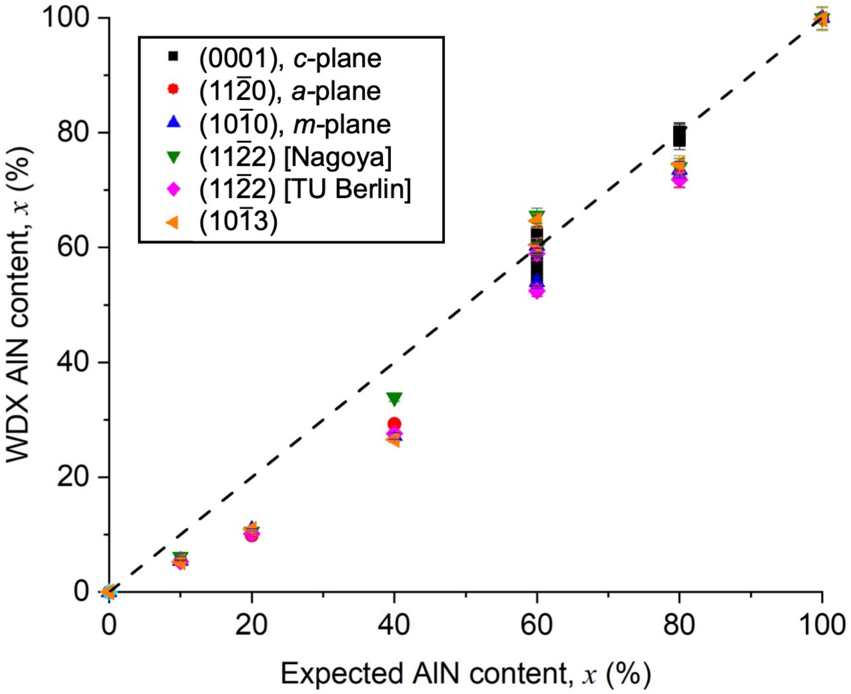

Figure 4.1: AlN content determined by WDX vs AlN content expected from the partial pressures during MOCVD growth. The different symbols/colours are used to differentiate between the $Al_xGa_{1-x}N$ crystal orientations and the source of the $Al_xGa_{1-x}N$. The black dashed line indicates perfect agreement between the expected and calculated $Al_xGa_{1-x}N$ composition

technique.

In Figure 4.1, the Al composition of the Nagoya samples is generally underestimated from the TMGa and TMAl partial pressures during growth, reflected in the WDX AlN composition being approximately 0.5 - 0.75 × less than expected for $x \leq 0.4$. For higher AlN $Al_xGa_{1-x}N$ growth cycles the dissimilarity between the expected and true composition is reduced. For all crystal orientations similar levels of Al incorporation was found consistent across both sample series. A larger variation in the composition is seen for growth cycles producing $Al_xGa_{1-x}N$ with higher AlN contents however, in general, the sample composition is within the expected range.

For the (11$\bar{2}$2) TU Berlin samples there is a good agreement between the compositions calculated via WDX, with what was expected from the $Al_xGa_{1-x}N$ growth conditions and with the results obtained on the Nagoya samples. Growth cycles aiming to produce $Al_xGa_{1-x}N$ with a composition $x=$ 0.6 show a fair amount of composition variation ($x=$ 0.54-0.62) due to the number of samples produced however generally the AlN content is around the $x=$ 0.6 level. The compositional variation is also comparable to the variation seen across the different crystal orientations in the Nagoya set of samples. There is a strong agreement between the composition of the samples grown with an expected AlN content of $x=$ 0.8 with little compositional variation seen across the multiple samples ($x=$ 0.79 - 0.8). The compositional agreement produced and the variation of the $x=$ 0.8 TU Berlin samples is better than that found across the different orientations of the Nagoya samples.

Previous publications investigating MOCVD grown $Al_xGa_{1-x}N$ films have found a greater Al incorporation for a-plane $(11\bar{2}0)$ [163] and semi-polar $(11\bar{2}2)$ [164] orientations compared to c-plane due to differences in the mobility of the adatoms within these orientations and the orientation/density of dangling bonds on these surfaces. For pulsed MOCVD growth the Al incorporation for was found to increase for $(10\bar{1}3)$ and $(10\bar{1}0)$ orientations compared to $(11\bar{2}2)$ and (0001) agreeing with the conclusion that the increased number of cation dangling bonds increases Al incorporation [165]. However, for continuous growth as performed for our samples there are consistent levels of Al incorporation for all crystal orientations. Dinh attributes this to the strong Al-N bond preventing the desorption of already incorporated Ga atoms [59].

Knowing that there was a dissimilarity between the expected AlN composition and that calculated via WDX the results from the WDX measurements were then compared to XRD results measured by the respective collaborators. This was done to establish whether the disagreement seen in Figure 4.1 was due to the WDX underestimate the composition of the $Al_xGa_{1-x}N$ films, particularly when $x \leq 0.4$, or if there was simply lesser Al incorporation for these growth cycles. The comparison between the WDX and XRD results are shown in Figure 4.2.

In Figure 4.2 there is a strong agreement between WDX and XRD when calculating the composition of the $Al_xGa_{1-x}N$ films, regardless of the $Al_xGa_{1-x}N$ crystal orientation or the sample composition. The results shown Figure 4.2 imply that when $x \leq 0.4$ the reduced composition of the Nagoya samples compared to what was

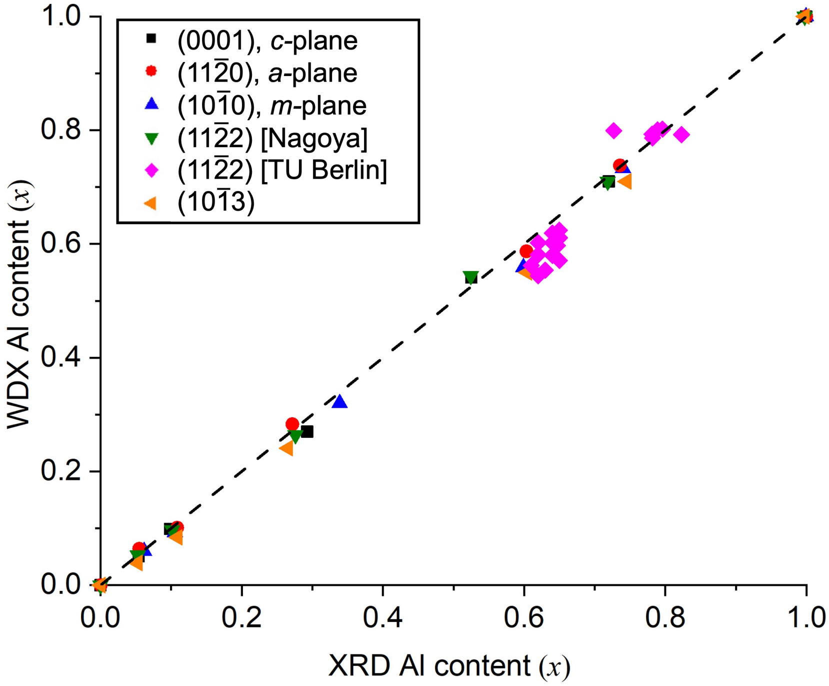

Figure 4.2: AlN content determined by WDX vs AlN content determined by XRD. XRD data is courtesy of Drs Duc V. Dinh and Humberto Foronda . The different symbols/colours are used to differentiate between the $Al_xGa_{1-x}N$ crystal orientations and the source of the $Al_xGa_{1-x}N$. The black dashed line indicates perfect agreement between the $Al_xGa_{1-x}N$ composition determined by WDX and XRD

expected is the true sample composition, rather than a shortcoming of the WDX technique/recipe used during these measurements.

Two tables summarising the WDX, XRD and CL results found later in this chapter are shown below with the Nagoya results found in Table 4.1 and the TU Berlin results in 4.2

Sample	**Crystal Orientation**	**x from WDX (%)**	**x from XRD (%)**	**CL NBE energy (eV)**
A1	(0001)	5.4	5.1	3.53
A2	(0001)	9.9	9.9	3.64
A3	(0001)	29.3	27.0	4.08
A4	(0001)	41.0	-	4.29
A5	(0001)	72.0	71.0	5.05
A6	(0001)	0.0	0.0	3.42
A7	(0001)	100.0	100.0	-
A8	(0001)	52.5	54.1	4.60
B1	$(11\bar{2}0)$	5.5	6.4	3.51
B2	$(11\bar{2}0)$	10.9	10.1	3.62
B3	$(11\bar{2}0)$	27.2	28.3	3.91
B4	$(11\bar{2}0)$	53.9	-	4.49
B5	$(11\bar{2}0)$	73.6	73.8	4.98
B6	$(11\bar{2}0)$	0.0	0.0	3.39
B7	$(11\bar{2}0)$	100.0	100.0	-
B8	$(11\bar{2}0)$	60.3	58.7	4.54
C1	$(10\bar{1}0)$	6.2	6.0	3.55
C2	$(10\bar{1}0)$	10.6	9.3	3.65
C3	$(10\bar{1}0)$	33.9	32.0	4.09
C4	$(10\bar{1}0)$	65.6	-	4.59
C5	$(10\bar{1}0)$	74.0	73.3	4.93
C7	$(10\bar{1}0)$	100	100	-
C8	$(10\bar{1}0)$	59.9	55.9	4.43

Sample	**Crystal Orientation**	**x from WDX (%)**	**x from XRD (%)**	**CL NBE energy (eV)**
D1	$(11\bar{2}2)$	5.3	5.3	3.51
D2	$(11\bar{2}2)$	10.2	9.7	3.62
D3	$(11\bar{2}2)$	27.6	26.4	3.98
D4	$(11\bar{2}2)$	58.9	-	4.67
D5	$(11\bar{2}2)$	71.2	71.0	4.99
D6	$(11\bar{2}2)$	0.0	0.0	3.41
D8	$(11\bar{2}2)$	52.5	54.4	4.68
E1	$(10\bar{1}3)$	5.3	4.9	3.51
E2	$(10\bar{1}3)$	10.9	8.4	3.62
E3	$(10\bar{1}3)$	26.6	24.1	3.98
E4	$(10\bar{1}3)$	64.7	-	4.67
E5	$(10\bar{1}3)$	74.5	71.1	4.99
E6	$(10\bar{1}3)$	0.0	0.0	3.41
E7	$(10\bar{1}3)$	99.7	100.0	3.41
E8	$(10\bar{1}3)$	60.5	54.9	4.68

Table 4.1: Summary of WDX, XRD and CL results performed on a series of MOCVD grown $Al_xGa_{1-x}N$ samples from Nagoya University. XRD measurements and analysis were performed by Dr Duc V. Dinh at Nagoya University

4.3.1 Silicon doping

When measuring silicon doping in III-Nitride materials using WDX there is an overestimation of the Si content when compared to other analytical techniques such as SIMS. The reason behind this has been attributed to Si surface contamination typically seen in MOCVD III-Nitride growth [137]. This Si contamination was found to be permanent, with plasma and HF treatment having a minimal effect [137] resulting in the incorrect determination of the dopant density through WDX.

To mitigate this a correction method was derived using SIMS and WDX data to

Sample	**Crystal Orientation**	**x from WDX (%)**	**x from XRD (%)**	**CL NBE energy (eV)**
TS5600	$(11\bar{2}2)$	58.1	62.0	4.61
TS5597	$(11\bar{2}2)$	58.0	64.0	4.65
TS5585	$(11\bar{2}2)$	60.2	64.0	4.71
TS5565	$(11\bar{2}2)$	57.1	65.0	4.64
TS5599	$(11\bar{2}2)$	55.4	63.0	4.59
TS5593	$(11\bar{2}2)$	61.1	65.0	4.73
TS5587	$(11\bar{2}2)$	62.4	62.0	4.76
TS5602	$(11\bar{2}2)$	60.2	64.0	4.73
TS5740-2	$(11\bar{2}2)$	61.9	64.0	4.73
TS5669	$(11\bar{2}2)$	54.4	62.0	4.55
TS5634-3	$(11\bar{2}2)$	56.2	61.0	4.56
TS5740-3	$(11\bar{2}2)$	59.7	64.7	4.67
TS5770	$(11\bar{2}2)$	80.2	79.6	5.03
TS5769	$(11\bar{2}2)$	80.1	78.9	5.02
TS5712	$(11\bar{2}2)$	79.3	78.1	5.02
TS5775	$(11\bar{2}2)$	79.9	72.7	5.07
TS5762	$(11\bar{2}2)$	79.2	82.3	5.05
TS5776	$(11\bar{2}2)$	78.6	78.2	5.06

Table 4.2: Summary of WDX, XRD and CL results performed on MOCVD grown $(11\bar{2}2)$ oriented $Al_xGa_{1-x}N$ samples from TU Berlin. XRD measurements and analysis were performed by Dr's Humberto Foronda and Johannes Enslin at TU Berlin

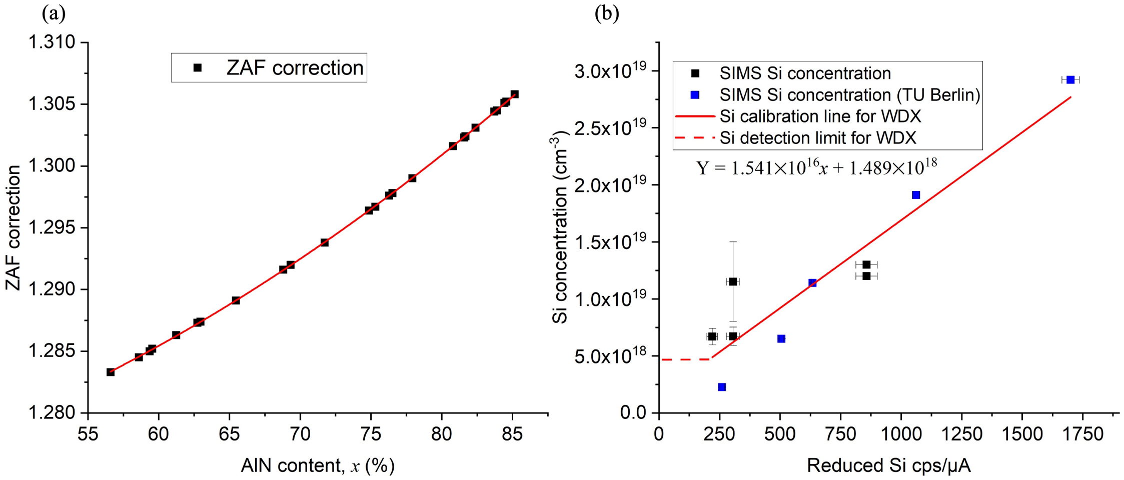

Figure 4.3: Silicon concentration calibration method reducing value produced by WDX to that of SIMS. (a) Total ZAF correction for $Al_xGa_{1-x}N$ as a function of AlN composition (x). The red line is a parabolic fitted function used to determine the $Al_xGa_{1-x}N$ ZAF between $x = 0.55$ - 0.85 (b) Si concentration (cm^{-3}) determined by SIMS against the reduced Si X-ray count rate (cps/μA) within GaN. Blue markers identify results from SIMS measurements taken on the samples from TU Berlin. Black markers are from samples outwith this study. The solid red line is the linear fitted relationship between all data points (equation shown in inset). The dashed red line indicates the lower detection limit where calibration cannot be accurately performed ($\leq$200 cps/μA)

accurately reduce the Si content to a value closer to the true approximation. The exact calibration method can be found in [137] but the summarised process is found here:

1. The Si X-ray counts must be made comparable for all samples and beam conditions. This is done by first converting the Si raw X-ray counts into cps/μA.
2. As the number Si X-ray counts will be affected by the AlN composition of the sample (*see ZAF corrections*), the cps/μA is adjusted to the respective X-ray counts in pure GaN. This is done by multiplying the cps/μA by the GaN/Sample ZAF correction ratio for Si K_α X-rays (1.2602/Sample ZAF).

The sample ZAF can be taken from the calculated calibration curve shown in Figure 4.3a.

3. The reduced Si X-ray counts in cps/μA are then used to calculate the adjusted Si dopant concentration in GaN (cm^{-3}) using the calibration line in Figure 4.3b (red line). The calibration line in Figure 4.3b is generated using SIMS and WDX data taken on multiple Al$_x$Ga$_{1-x}$N samples with the samples from TU Berlin marked as blue squares.

4. The adjusted Si concentration is then reconverted back to the concentration within Al$_x$Ga$_{1-x}$N.

   This Si concentration corresponds to what the expected concentration would be if measured through SIMS. A lower limit is set on the calibration due to the detection limit of WDX, this is identified in Figure 4.3b set as a reduced Si X-ray count of 200 cps/μA (dashed red line).

The results of this calibration method are shown in Figure 4.4a, with the x = 0.6 and 0.8 series treated separately. The Si concentration is taken from the GaN calibration line (black data markers) in 4.3b and then converted to the respective Si concentration for the AlN content of the samples (red data markers).

The 200 cps/μA lower limit originates from previous studies by Spasevski found in [137]. As part of this investigation a series of Al$_x$Ga$_{1-x}$N samples with low levels of Si doping were measured by SIMS. SIMS identified the samples to have Si concentrations on the order of 10^{17}cm^{-3}. WDX measurements performed on the same samples produced Si count rates of approximately 200 cps/μA. These count rates were found to be comparable to a sample with a much higher level of Si doping with WDX producing a count rate of 220 cps/μA and SIMS measuring the dopant concentration to be 3.6×10^{18}cm^{-3}. An unintentionally doped sample also produced a similar count rate of 192 cps/μA. From these results it was deduced that WDX was unable to accurately differentiate the Si dopant concentration from the contaminant background level below a particular count rate. This was set to be 200 cps/μA

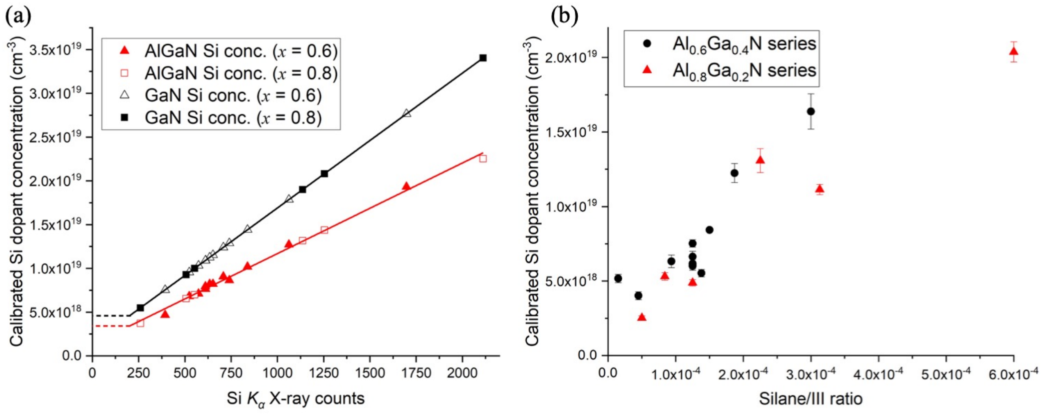

Figure 4.4: (a) Calibrated Si concentration (cm^{-3}) as a function of Si X-ray count rate (cps/μA). Red solid line is the linear relation between Si count rate and concentration in Al$_x$Ga$_{1-x}$N (red squares for $x = 0.8$, red triangles for $x = 0.6$). Black solid line and data markers is the corresponding relationship between Si count rate and concentration for GaN materials. (b) Calibrated Si concentration (cm^{-3}) as a function of silane/group III precursor ratio during growth for the TU Berlin Al$_x$Ga$_{1-x}$N samples calculated using GaN calibration method. Black circles are for the $x =$ 0.6 series of samples and red triangles for $x = 0.8$

corresponding to what was produced from samples with Si concentrations below the detection limit of WDX.

The detection limit being set at a reduced Si X-ray count of 200 cps/μA corresponds to a Si concentration of approximately 2.4×10^{18}cm^{-3} in GaN, increasing to 4.6×10^{18}cm^{-3} in pure AlN [137]. While WDX has a lower detection limit of approximately 10 ppm (0.001 WT%) [166] the limit for Si measurement in Al$_x$Ga$_{1-x}$N quoted here is higher at 35 ppm due to the surface contamination issues mentioned earlier. These values also apply to measurements using a beam energy of 10 keV, increases (decreases) to the beam energy would decrease (increase) the impact of surface contamination possibly reducing (increasing) the detection limit for Si doping measurements in Al$_x$Ga$_{1-x}$N by WDX.

Figure 4.4b shows the relationship between the Si concentration within the film and the Si availability during growth through the silane/III precursor ratio. The samples exhibit a linear increase in the Si concentration with increasing silane/III ratio regardless of the AlN molar fraction present in the sample. This shows the Si incorporation is independent of the Al composition for $(11\bar{2}2)$ material agreeing with results from *c*-plane [162] and other studies on $(11\bar{2}2)$ $Al_xGa_{1-x}N$ [167].

4.3.2 Electronic properties

The electrical properties of these materials were studied in greater detail by Dr Humberto Foronda, using room temperature Hall effect measurements to determine the carrier concentration, mobility and resistivity within the films [66].

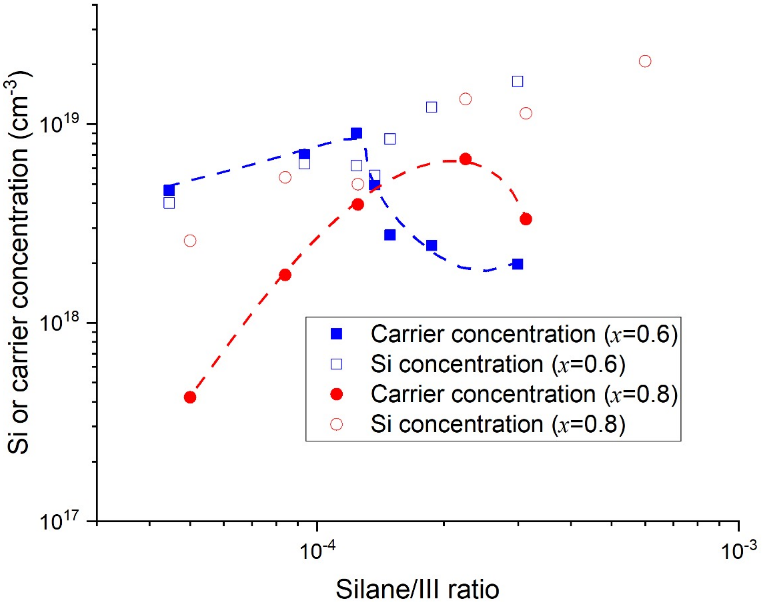

Figure 4.5: Si concentration and carrier concentration in $(11\bar{2}2)$ $Al_xGa_{1-x}N$ against silane/III ratio for series of sample with $x = 0.6$ and 0.8 AlN compositions. The red and blue dashed lines are guides for the eye. Adapted from [66], data is courtesy of Dr Humberto Foronda

The Si dopant concentration determined through WDX and respective carrier concentration is plotted against silane/III ratio in Figure 4.5 for both sets of $(11\bar{2}2)$ $Al_xGa_{1-x}N$ samples ($x = 0.6$ and 0.8) from TU Berlin. Note that Dr Foronda did not perform Hall effect measurements on every sample as some samples were grown with the same silane/III ratio.

For low silane/III rations there is good agreement between the Si dopant and carrier concentration present within the films for both Al compositions. The carrier concentration linearly increases with Si concentration until reaching a maximum carrier concentration of $9{\times}10^{18}$cm^{-3} (Si $\approx 6.2{\times}10^{18}$cm^{-3}) at silane/III ratio of $1.25{\times}10^{-4}$ for $x = 0.6$ and $6.7{\times}10^{18}$cm^{-3} (Si $\approx$1.3$\times10^{19}$cm^{-3}) at silane/III ratio of $2.25{\times}10^{-4}$ for $x = 0.8$. Beyond this maximum point the carrier concentration begins to decrease with increasing Si composition. This "knee-like" behaviour corresponds to the material entering the self-compensation regime. The high Si concentration leads to the formation of Si related V_{III} complexes (e.g. V_{III}.3Si) reducing the carrier concentration [168, 169]. Here, as the Al composition is increased from $x = 0.6$ to 0.8 the "knee" maximum shifts to a higher Si concentrations unlike in c-plane material where the opposite is seen for high Al fraction $Al_xGa_{1-x}N$ [170].

In the $x = 0.6$ series for low silane/III ratios the Hall measurements indicate that prior to the "knee" there is a greater carrier concentration in these samples than there is Si present. Foronda explains that possible explanations for this may be the incorporation of other impurities, particularly oxygen, which SIMS determined to be present in high concentrations ($6{\times}10^{18}$cm^{-3}) due to increased incorporation rate for semi-polar orientations [66].

Another consequence of of Si doping in high AlN $Al_xGa_{1-x}N$ which must be considered here is the transition of the Si dopant into a compensating acceptor defect known as a *DX* center. Rather than substituting into a regular lattice, Si in a *DX* center induces a large lattice distortion resulting in electron trapping at the *DX* center [171]. This effectively turns the Si donor into a compensating acceptor, reducing the carrier concentration present in the $Al_xGa_{1-x}N$ [172]. The critical AlN composition in which this transition occurs is disputed with hybrid functions calculations determining it to be $x = 0.94$ [173] however other theoretical values have found the transition to occur at much lower AlN compositions of $x = 0.23$ and $x = 0.6$ [172]. In Figure 4.5 samples with high levels of Si doping present with a higher carrier concentration for the $x = 0.8$ series of samples than the $x = 0.6$. If the Si dopants were forming a *DX* centers the opposite would be expected as the activation energy of the dopants in the $x = 0.8$ series would be substantially higher than the $x = 0.6$ series. Therefore, the reason for the differences in carrier concentration between the two Al_xGa_{1-x} series is attributed to variations in the critical Si concentration before the dopants enter the self-compensation regime.

While here we have shown successful Si doping in semi-polar $Al_xGa_{1-x}N$ for high AlN compositions which shows promise for the development of efficient deep UV III-Nitride LEDs (counteracting the doping and QCSE effects mentioned in Chapter 2) there are other factors which may assist the work presented here. One possibility mentioned previously is Ge doping over Si, with both dopants showing compensation behaviour however higher carrier concentrations were achieved in $Al_{0.3}Ga_{0.7}N$ films through Ge doping [169]. However it remains unknown whether the same behaviour will be observed is higher AlN content films or for semi-polar material. This may also be limited by the Ge *DX* transition in $Al_xGa_{1-x}N$, predicted at a critical composition of $x= 0.5$ [169].

Another alternative to explore is co-doping, with significant increases in the $Al_xGa_{1-x}N$ conductivity observed through Si-Ge [174] and Si-In [175] co-doping with the latter producing an $Al_xGa_{1-x}N$ photodetector with enhanced quantum efficiency (EQE $\approx$60%)

The results from carrier mobility measurements taken on these samples are shown in Figures 4.6(a) and (b) respectively. The results are in good agreement both with each other and with the carrier concentration results shown in 4.5. Here the "knee-like" trend is mirrored with the maximum(minimum) carrier mobility(resistivity) occurring at the same point identified in 4.5. For the $x = 0.6$ series this corresponds to a maximum carrier mobility of 24 $\mathrm{cm}^2\mathrm{V}^{-1}\mathrm{S}^{-1}$, film resistivity of 0.03 Ωcm for a carrier concentration of $9.0 \times 10^{18}\mathrm{cm}^{-3}$ and a carrier mobility of 21 $\mathrm{cm}^2\mathrm{V}^{-1}\mathrm{S}^{-1}$, film resistivity of 0.05 Ωcm for a carrier concentration of $6.7 \times 10^{18}\mathrm{cm}^{-3}$ in the $x = 0.8$ series.

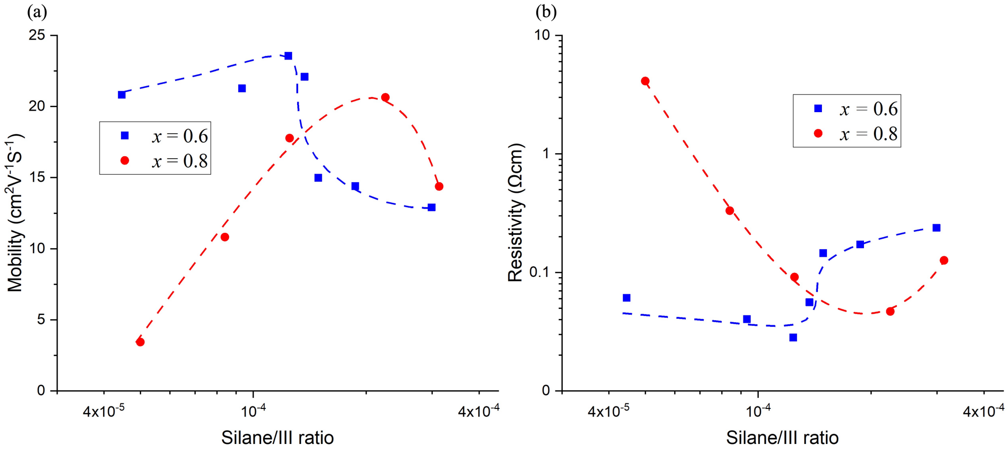

Figure 4.6: (a) Carrier mobility and (b) film resistivity in $(11\bar{2}2)$ $Al_xGa_{1-x}N$ against silane/III ratio for series of sample with $x = 0.6$ and 0.8 AlN compositions. The red and blue dashed lines are guides for the eye. Adapted from [66], data is courtesy of Dr Humberto Foronda

4.4 Optical Properties

Room temperature cathodoluminscence measurements were performed on all samples. RT CL spectra were acquired using a focussed electron beam with the same beam conditions as the WDX measurements [176]. The CL signal for the samples from Nagoya was collected using a reflecting objective built-in to the EPMA which was focused directly into an Oriel MS125 spectrometer with a focal length of 125 mm. The dispersed light was then detected using an Andor 1600-channel electron-multiplying charge-coupled device. The spectrometer used within these measurements was equipped with a 600 lines/mm grating blazed at 200nm.

An older CL system was used for the TU Berlin samples where the signal was focussed into an optical fibre before being transmitted into an Andor Shamrock 163 spectrometer with a focal length of 163 mm. This spectrometer was equipped with a 300 lines/mm grating blazed at 500nm. The older CL system used for these measurements was sufficient enough to allow CL detection across the UV-visible range but the use of the optical fibre resulted in luminescence intensity losses in the deeper UV. To counteract this the system was adapted over time to enhance UV detection with the most improved design used for the Nagoya CL measurements.

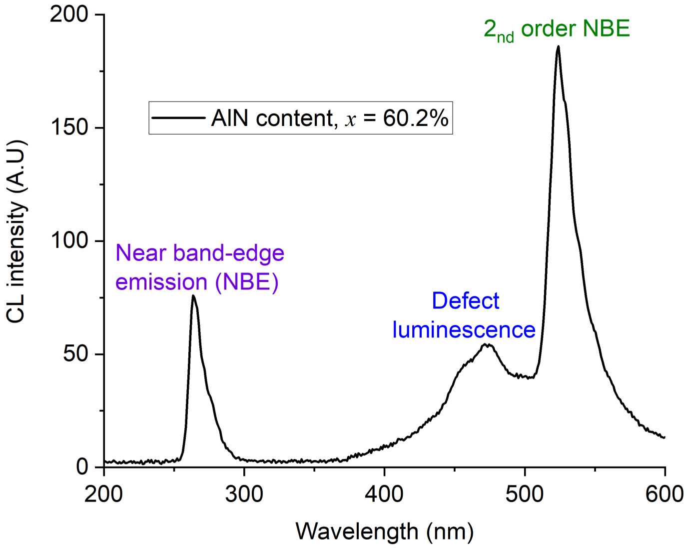

Figure 4.7: Example RT CL spectrum taken from sample TS5585 x= 0.60 identifying the main luminescence bands seen for $Al_xGa_{1-x}N$ samples

An example spectrum taken from one of the TU Berlin samples with AlN content = 60.2% is shown in Figure 4.7. The near band-edge emission (NBE) is the band of the greatest importance from the CL measurements, consisting of emission from the direct recombination of a CB electron with VB hole and therefore indicative of the approximate optical bandgap of the material [177, 178].

The broad defect luminescence peak is a result of the multiple deep lying defects in the bandgap as donor or acceptor states involving V_{Ga} [179] or V_{Ga} complex states with impurities e.g V_{Ga} - O_N [180–182]. These defects can be detrimental to the performance of LEDs, acting as non-radiative recombination pathways therefore impacting the efficiency of these devices. Therefore, by analysing the spectral properties of the defect band the feasibility of the material/growth mechanism for device application can be determined. The 2nd order peak is due to 2nd order diffraction of the NBE emission and is observed at a wavelength 2 × λ_{NBE}. Typically the intensity of the 2nd order luminescence would be much greater than the NBE emission. As the 2nd order emission wavelength lies on near/on the grating blaze this is not the case for the TU Berlin samples as seen in Figure 4.7.

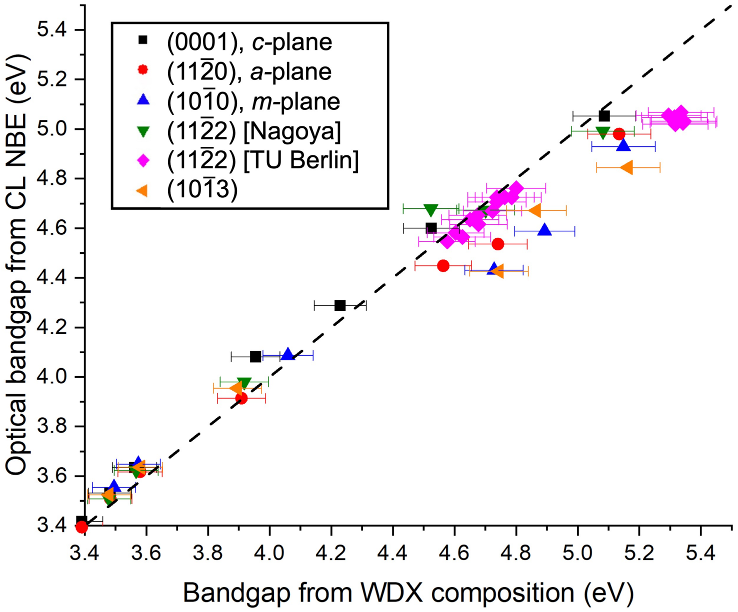

Figure 4.8: Optical bandgap of $Al_xGa_{1-x}N$ materials derived from the CL NBE emission vs the expected bandgap of the material from the composition determined by WDX using Equation 2.1. The different symbols/colours are used to differentiate between the $Al_xGa_{1-x}N$ crystal orientations and the source of the $Al_xGa_{1-x}N$. The black dashed line indicates a a gradient of 1 and perfect agreement between the expected and calculated bandgap

From the CL NBE emission the optical bandgap has been derived and plotted against the expected bandgap from the material composition in Figure 4.8. The bandgap was calculated from the $Al_xGa_{1-x}N$ composition using Equation 2.1 with a bowing parameter of b=0.9 eV and the results of the WDX measurements. No CL measurements could be completed on the AlN (or near pure AlN) for each crystal orientation due to sample charging, poor luminescence and the difficulty in measuring CL down to almost 200 nm.

From Figure 4.8, in general, the optical bandgap is close to that expected from the material composition for all crystal orientations for moderate AlN contents, $x \leq 0.4$. As the level of Al alloying is increased to $x \approx 0.6$ the agreement between the two

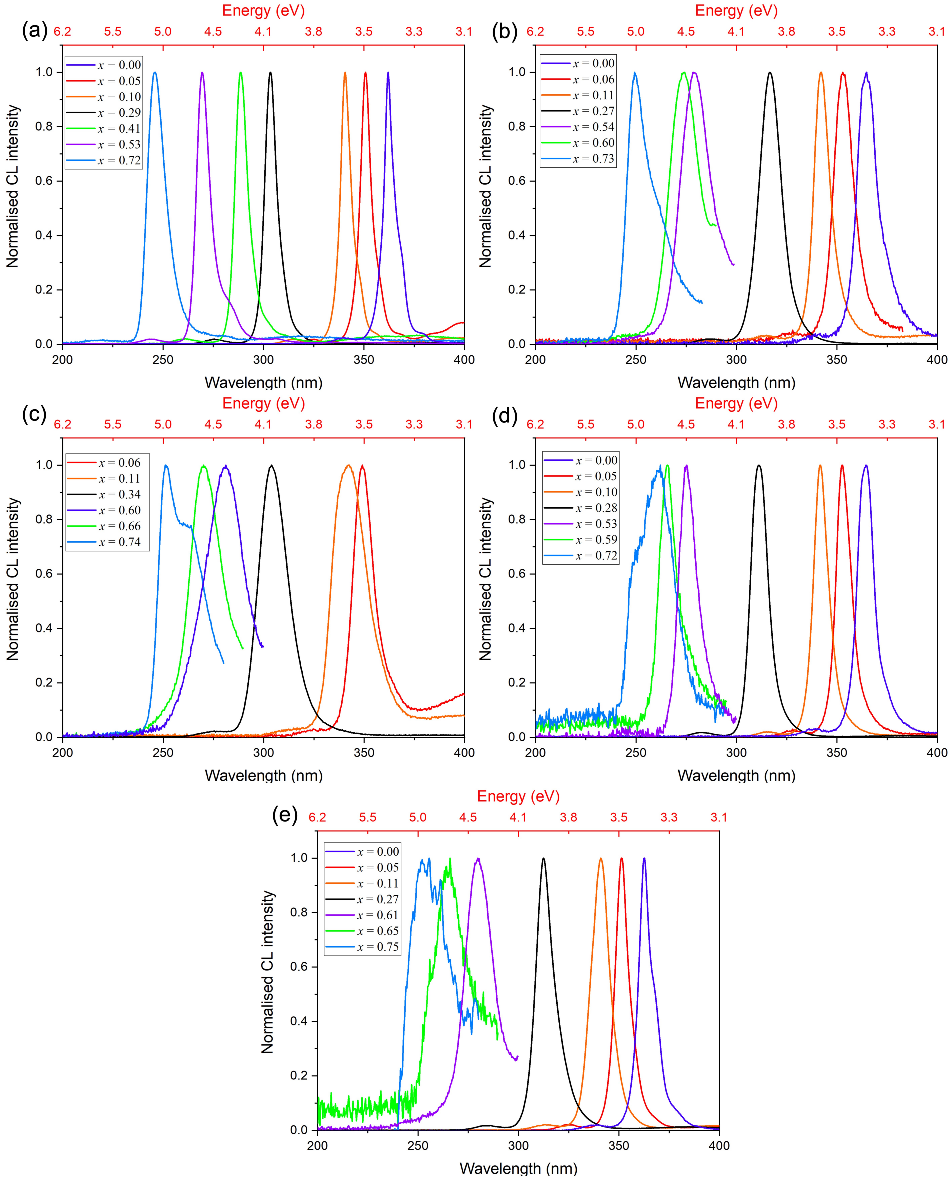

Figure 4.9: Normalised NBE CL intensity against wavelength (nm) [energy (eV) secondary x-axis] for Nagoya $Al_xGa_{1-x}N$ of various compositions grown along crystal orientations, specifically: (a) Polar c-plane (0001), (b) non-polar m-plane $(10\bar{1}0)$, (c) non-polar a-plane $(11\bar{2}0)$, (d) semi-polar $(11\bar{2}2)$ & (e) semi-polar $(10\bar{1}3)$ $Al_xGa_{1-x}N$. Different colours are used to differentiate the spectra by their composition (x) in each sub-panel.

experimental methods begins to weaken for both non-polar [$(11\bar{2}0)$ & $(10\bar{1}0)$] and the semi-polar $(10\bar{1}3)$ materials resulting in a lower energy NBE emission than expected. For higher AlN content films, $x \geq 0.6$, the agreement further breaks down for these orientations and also begins to break down for the semi-polar $(11\bar{2}2)$ orientation.

For the samples from Nagoya, non c-plane films generally display with a reduced CL NBE intensity compared to polar samples of similar composition. Accompanying the reduced NBE intensity of these samples is the increase in NBE FWHM with the peak either exhibiting as a broadened single or as two distinct double peaks. The normalised CL spectra Figure 4.9 show that for all crystal orientations, as the Al composition of the sample increases the peak width also increases. For samples with the highest AlN contents $x \approx 0.6$-0.75 the double NBE peak is evident (note that in Figure 4.9 (d) & (e) the weak NBE intensity is producing the highly jagged spectra when $x \approx 0.6$-0.75, *green and blue data lines*). 2nd order emission and defect luminescence has been removed from some spectra to avoid peak overlaps hence why for some spectra the peak does not go to 0 intensity on the lower energy edge.

This broadening/double NBE emission may be explained by a number of factors. Growth on non-c-plane orientations results in an increased surface roughness compared to the c-plane films, particularly for non-polar materials which show square, "slate-like" morphology for AlN and GaN films [183–185]. Compositional variations across the edge and surface of these features produce recombination centres of different energies resulting in the broadened NBE emission. This effect magnifies for higher AlN content films as Al adatoms have a reduced surface mobility compared to Ga making them unable to diffuse to the edge of these features therefore increasing the surface roughness [161].

An increased density of basal plane stacking faults (BSFs) may also be responsible for the broadening. BSF bound excitons can result in a broadened and redshifted NBE emission in $Al_xGa_{1-x}N$, as evident in Refs. [81,82,186,187]. The density of BSFs present within a film increases greatly when growing on non-c-plane orientations [161] and with increasing Al composition [82] therefore further broadening the NBE emission as seen in Figure 4.9.

Atomic force microscopy (AFM) imaging was performed by Dr Duc V. Dinh to

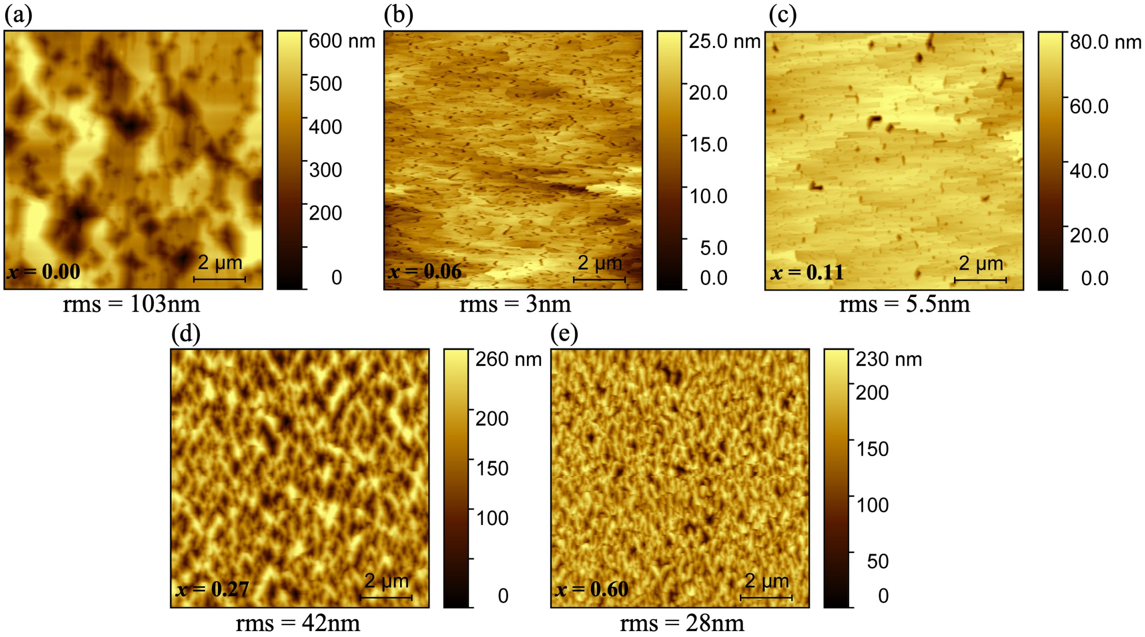

Figure 4.10: AFM images showing sample roughness for non-polar a-plane $(11\bar{2}0)$ oriented $Al_xGa_{1-x}N$ films with sample composition (a) x=0.00, (b) x=0.06, (c) x=0.11, (d) x=0.27 & (e) x=0.60. Figures are courtesy of Dr Duc V. Dinh

determine the surface roughness of the films. Results shown for non-polar a-plane $(11\bar{2}0)$ and semi-polar $(10\bar{1}3)$ oriented films in Figures 4.10 and 4.11 respectively. Figures 4.10 (a)-(c) show the formation of coalesced $Al_xGa_{1-x}N$ films with minimal surface morphology due to the low AlN content within the layers. Increasing the AlN content prevents the formation of a complete $Al_xGa_{1-x}N$ layer instead resulting in the onset of smaller surface grains as seen in Figure 4.10(d) increasing the surface roughness. Further increases to the AlN content increases the density and decreases the size of the grains as seen in Figure 4.10(e). No AFM imaging was performed on the highest Al content sample ($x = 0.73$)

AFM results on the semi-polar $(10\bar{1}3)$ samples, Figure 4.11, show similar behaviour to the $(11\bar{2}0)$ films. The lowest Al content samples (a)-(c) show the most coalesced film surface with formation of smaller structures as the level of Al alloying

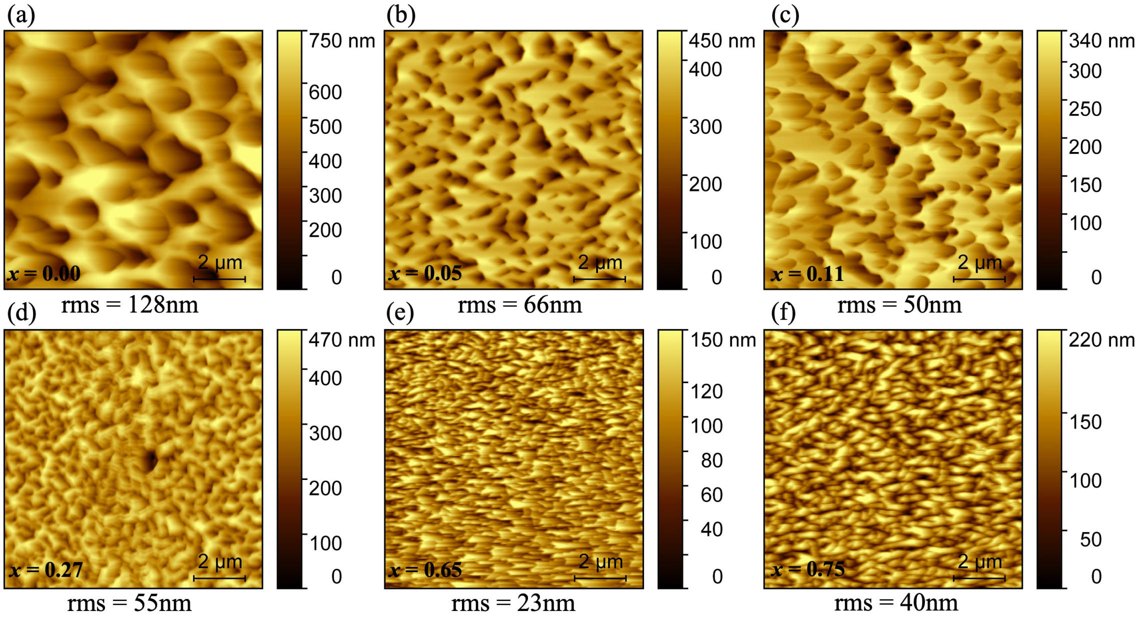

Figure 4.11: AFM images showing sample roughness for semi-polar $(10\bar{1}3)$ oriented $Al_xGa_{1-x}N$ films with composition (a) x=0.00, (b) x=0.05, (c) x=0.11, (d) x=0.27, (e) x=0.65 & (f) x=0.75. Figures are courtesy of Dr Duc V. Dinh

increases in (d)-(f). Note that the surface morphology is noticeably poorer in Figure 4.11 (a)-(c) than Figure 4.10 (a)-(c) due to the difficulty in growing $(10\bar{1}3)$ material. However within the $(10\bar{1}3)$ series there are far fewer surface structures within (a)-(c) than for the higher Al content films (d)-(e).

The results from the AFM measurements support the conclusion that the NBE peak broadening for high Al content $Al_xGa_{1-x}N$ films seen in Figures 4.9(b) and (d) is because of the increase in sample roughness. Though not quantified through mapping there will be compositional inhomogeneity within these surface features resulting in recombination centres with different NBE emission energies producing the broadened peaks. The same logic may be applied when moving from c-plane polar growth to non/semi-polar orientations where there is a degradation in crystal quality due to the difficulty in growing materials with these orientations. This produces the broadened emission for the non/semi-polar films, Figures 4.9(b)-(e), compared to

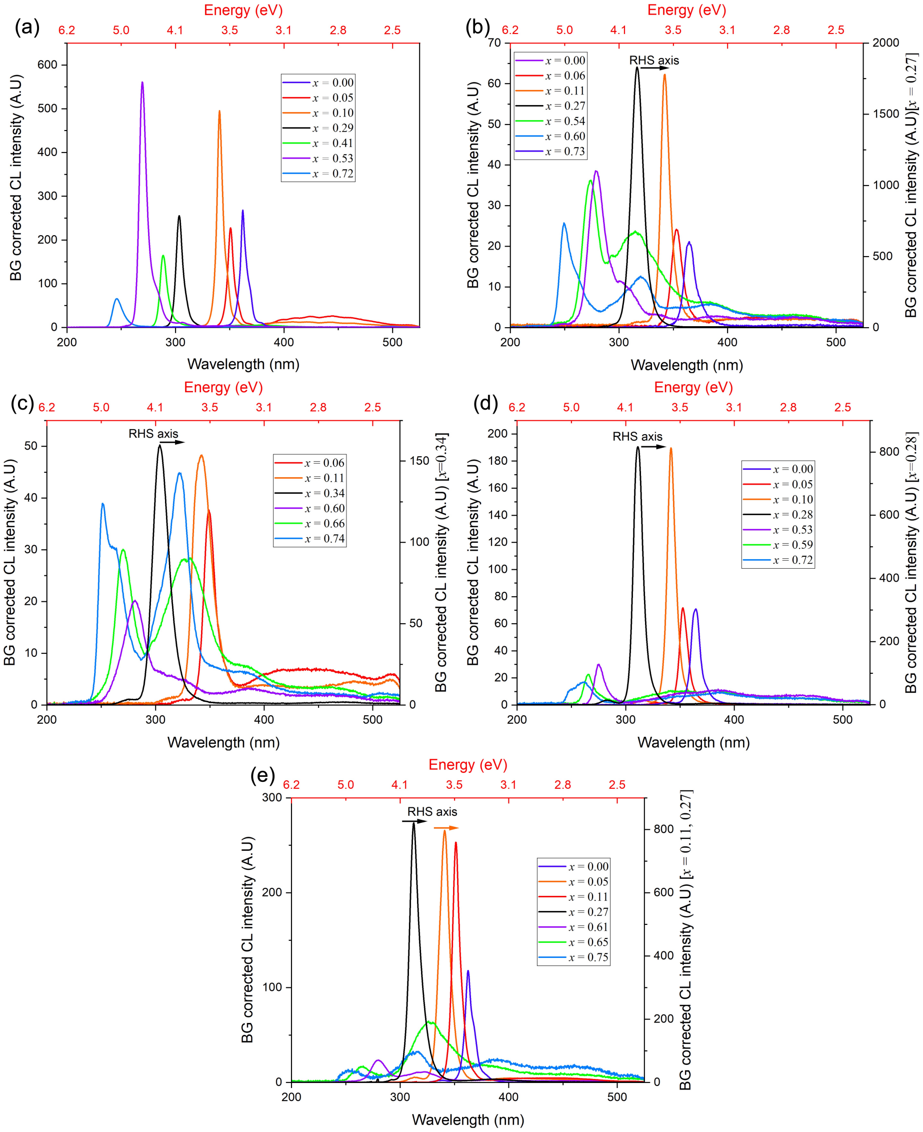

Figure 4.12: Background corrected CL intensity against wavelength (nm) [energy (eV) secondary x-axis] for Nagoya $\mathrm{Al}_x\mathrm{Ga}_{1-x}\mathrm{N}$ of various compositions grown along crystal orientations, specifically: (a) Polar c-plane (0001), (b) non-polar m-plane $(10\bar{1}0)$, (c) non-polar a-plane $(11\bar{2}0)$, (d) semi-polar $(11\bar{2}2)$ & (e) semi-polar $(10\bar{1}3)$ $\mathrm{Al}_x\mathrm{Ga}_{1-x}\mathrm{N}$. Different colours are used to differentiate the spectra by their composition (x) in each sub-panel.

(a).

Figure 4.12 shows the background corrected CL spectra acquired from each sample within each series. Generally, materials with a lower Al composition exhibit higher luminescence intensity than those with higher Al contents. Interestingly, the NBE emission intensity is greatest for samples grown with expected Al content of x=0.4 (black spectra) for all non/semi-polar materials. The black spectra also show little evidence of lower energy defect related luminescence unlike for higher AlN fraction samples, where the defect related bands are present in all non/semi-polar materials for $x \geq 0.6$ (green, light blue and purple spectra).

Some of the spectra shown in Figure 4.12 are influenced by Fabry-Pérot interference fringes produced due to the difference in refractive index between the nitride layer and the sapphire substrates. These fringes produce the “wavelike” pattern prominent in the defect luminescence bands of the spectra making the wavelength/energy deconvolution of related peaks difficult. The energies are therefore approximated in future discussion rather than calculated through peak fitting.

Defect bands previously observed in $Al_xGa_{1-x}N$ thin films have been attributed to DAP recombination involving shallow donors from Si impurities and cation vacancies, V_{III}, and their related complexes with oxygen [167,179,180,188]. Depending on the charge state of the cation vacancy multiple defect peaks may arise. In polar c-plane and semi-polar $(11\bar{2}2)$ $Al_xGa_{1-x}N$ three V_{III} related defect peaks were found corresponding to the V_{III} vacancy $(V_{III})^{-3}$, a single oxygen complex $(V_{III}\text{ complex})^{-2}$ and double oxygen complex $(V_{III}\text{ complex})^{-1}$ [167,189].

The peak energy of these transitions is dependent on the $Al_xGa_{1-x}N$ composition however the relation between Al content and emission energy is highlighted in [167] for polar and $(11\bar{2}2)$ material. For Al contents of x=0.4-0.8 the expected emission wavelength of DAP transitions involving these V_{III} acceptors corresponds to $\lambda \approx$550-410nm for $(V_{III})^{-3}$, 440-345nm for $(V_{III}\text{ complex})^{-2}$ and 340-270nm for $(V_{III}\text{ complex})^{-1}$ with strong correlation between the two crystal orientations.

In Figures 4.12(b)-(e) the intense defect peak seen in the green and blue spectra ($x \approx$ 0.65 and 0.75 respectively) and with weaker intensity in the purple ($x \approx$ 0.6) lie within the energy range attributed to DAP transitions involving the $(V_{III}\text{ complex})^{-1}$.

The broad defect band present for the lower Al content samples, $x \approx$ 0.05-0.10, in Figures 4.12(a)-(c) (red and orange spectra) could also be within the range expected for these ($\mathrm{V_{III}}$ complex)$^{-1}$ transitions.

The films with a high Al composition also show evidence of a peak lying within the ($\mathrm{V_{III}}$ complex)$^{-2}$ range albeit with a reduced intensity compared to ($\mathrm{V_{III}}$ complex)$^{-1}$ with the peak position lying within the 370-400 nm range. The peak presenting at the end of the spectral range (500-525nm) for the lower Al content samples in 4.12(c) are also within the range expected for the ($\mathrm{V_{III}}$ complex)$^{-1}$.

Within GaN the crystal orientation of the material was found to promote the incorporation of particular impurities with oxygen increasing in concentration from polar - semipolar ($11\bar{2}2$) - nonpolar ($11\bar{2}0$) [190]. The increased density of oxygen results in a greater luminescence intensity of defect related bands (with respect to NBE emission) in agreement with the results here. Other possible explanations for the defect peaks observed here may be related to carbon based defects/complexes [171] attributed to yellow band defect luminescence in GaN [182, 190]. Carbon incorporation is found to increase with increasing Al content (as well as oxygen) [191] and has previously been attributed to produce broad luminescence peaks of energy $\approx$ 3.6 - 3.9 eV in photoluminescence measurements on semi/non-polar $\mathrm{Al}_x\mathrm{Ga}_{1-x}\mathrm{N}$ ($x \approx$0.5-0.75) [165] in agreement with the results here.

4.4.1 Conclusion

The optical and compositional properties of two sets of MOCVD grown $\mathrm{Al}_x\mathrm{Ga}_{1-x}\mathrm{N}$ samples grown upon polar, non-polar and semi-polar crystal orientations have been determined through the electron microscopy techniques of WDX and cathodoluminscence.

The first set of samples were Si doped ($11\bar{2}2$) $\mathrm{Al}_x\mathrm{Ga}_{1-x}\mathrm{N}$ grown with moderate-high levels of Al ($x \approx$ 0.6 & 0.8). The Si dopant concentration was determined first using WDX and then calibrated using the method highlighted in [137] to reduce the effect of Si surface contamination on the measurement. Si incorporation was found to be independent of the $\mathrm{Al}_x\mathrm{Ga}_{1-x}\mathrm{N}$ composition with comparable Si contents found in the $x \approx$ 0.6 & 0.8 series for similar growth conditions in agreement with c-plane grown $Al_xGa_{1-x}N$.

Electronic properties of these materials were determined through Hall effect measurements. Results indicate that as with c-plane a critical Si doping concentration exists before self-compensation effects begin, reducing the conductivity of the films as V_{III}.Si complexes begin to form causing the "knee-like" behaviour in the carrier concentration, mobility and resistivity. Conversely to c-plane $Al_xGa_{1-x}N$ the Si concentration at which the "knee" maximum occurs increases with Al composition. There is also evidence of a high degree of impurity oxygen present due to its increased incorporation within semi-polar $(11\bar{2}2)$ orientations which may be affecting the film carrier concentration.

The second set of samples were grown over the entire Al compositional range upon 5 different crystal orientations: polar c-plane (0001), non-polar m-plane $(10\bar{1}0)$ & a-plane $(11\bar{2}0)$ and semi-polar planes $(11\bar{2}2)$ & $(10\bar{1}3)$. Growth cycles aiming to produce $Al_xGa_{1-x}N$ with low Al contents $x<0.5$ resulted in an Al composition lower than expected (0.5 ×) from the partial pressures of the elemental precursors however improved for higher Al growth. Similar levels of Al incorporation were found regardless of crystal orientation, in disagreement with previous investigations on non c-plane and non-continuous MOCVD growth.

Optical studies revealed good agreement between the near band-edge emission energy and the material bandgap expected from the WDX composition for moderate-low Al compositions $x \leq 0.5$ with a bowing parameter of 0.9 eV. The agreement between the two begins to break down for higher Al contents as the homogeneity of the film deteriorates with the $(10\bar{1}0)$ and $(10\bar{1}3)$ orientations showing the greatest difference in energy. The compositional inhomogeneity is also reflected in the CL spectra with increasing FWHM and double peaks appearing within the NBE, although other factors may be contributing. This formation of surface structures causing the compositional phase separation has been confirmed through AFM imaging. CL spectra also show variation in the intensity of defect luminescence across each crystal orientation with non-polar and $(10\bar{1}3)$ orientations showing the greatest intensity, likely due to V_{III} complexes with impurity oxygen.

A strong correlation between XRD and WDX compositional measurements and with PL and CL optical measurements has been proven through this investigation. Results show that when transitioning from polar to non/semi-polar oriented growth the incorporation of Al to produce high AlN $Al_xGa_{1-x}N$ films should not be affected. The crystal quality and incorporation of impurities is impacted through growth on these orientations however resulting in compositional variations and a large density of oxygen related cation vacancy complexes. This produces high intensity defect bands in the luminescence spectra and NBE broadening, particularly for high Al films. Therefore before these semi/non-polar materials can be implemented in optical devices such as LEDs careful growth control methods must be established to produce high crystal quality $Al_xGa_{1-x}N$ comparable to polar growth.

Chapter 5

Indium-gallium oxide

5.1 Introduction

The ultrawide bandgap of Ga_2O_3 allows for its use within photodetectors operating within deep UV ranges. As stated in Chapter 2, high quality Ga_2O_3 have been grown on a number of different substrates through various growth techniques allowing the manufacturing of Ga_2O_3 photodetectors through various means [87, 192–194]. The typical cut-off wavelength of Ga_2O_3 photodetectors is approximately 250-280nm [18] lying within the UV-C spectral region and leading to applications within underwater, space and non-line of sight communication systems [9–11]; ozone-layer monitoring [15]; flame detection for both military and safety purposes [16, 17].

As with other semiconductor families such as the III-Nitrides, the functionality can be extended by producing ternary alloys may be produced through alloying with alike binary materials. This allows the material bandgap to be tuned and allows operation within the lower UV energy ranges (e.g UV-B). Again, as stated in Chapter 2 this is typically achieved through alloying with In_2O_3 forming an indium-gallium oxide alloy, $(In_xGa_{1-x})_2O_3$ (IGO).

IGO alloys have also been grown through various techniques albeit with different crystal quality. Two reports describe the use of sputtering methods to produce IGO films over a large In content range, ∼0-60 at% for [195] and ∼15-19 at% for [45] with both studies producing amorphous films. Despite the poor crystal quality clear bandgap redshifts are observed in each case with a 280-320 nm shift in detector cut off with [45] and a reduced bandgap of ∼350nm (∼3.5 eV) for an In content of 50 at% in [195]. Sol-gel synthesised films also exhibit successfully redshifted bandgaps with greater shifts observed for higher In contents across the $x\sim$ 0-0.3 range for [14] and between 0.6-0.7 in [196]. PLD with different targets has been used to successfully grow IGO films across the entire In compositional range, successfully reducing the bandgap from 5.1 to 3.8 eV [197].

Kokubun *et al.* [14] found that alongside the redshifting in spectral response wavelength with the addition of In the photodetector performance was improved. A heightened detector peak responsivity was reported, increasing by 3 orders of magnitude ($\approx 10^{-4}$ - 10^{-1} A/W) for an increase in In content, x, from $\approx$ 0 to 0.2. The same behaviour was seen for MOCVD grown IGO films where an In content $x\approx 0.2$ produces photodetectors with greatly heightened responsivity compared to a Ga_2O_3 counterpart (0.79 A/W vs 319.1 A/W) [198].

Another consistent observation within IGO films grown across a large In content range is deterioration of the film crystallinity. For low In contents there is a substitution of In with Ga within the monoclinic β-Ga_2O_3 crystal. When the In content increases above $x\approx 0.4$ a phase separation begins and the crystal forms a mixed state: monoclinic from β-Ga_2O_3, cubic from In_2O_3 and a hexagonal phase from $InGaO_3$ [14, 44]. The crystal possesses the In_2O_3 cubic (bixbyite) phase once $x>$ 0.7-0.8. The crystallographic impact on the device properties was further studied by [44] determining how the compositional and phase change would impact the Schottky barrier diode behaviour. An approximation of the optical band gap relation to indium content and relevant bowing parameter was also derived.

Within this chapter the compositional and optical properties of a combinatorial piece of IGO from the same wafer as [44] was determined. The enhanced precision of WDX provides a quality check on the predetermined EDX composition while providing a more rigorous trace element analysis of the stated Si content. CL spectroscopy was used to generate new characterising information from the luminescent behaviour of the material which was previously undetermined. Both the WDX and CL spectroscopy measurements were supplemented with simultaneous mapping. An additional set of MBE grown IGO samples were also measured with the above mentioned techniques and further analysed through transmission spectroscopy to determine the optical bandgaps. The results from the measurements on the two different sources of IGO materials were then correlated to determine how the material properties may be related to the growth technique used.

5.2 Properties of PLD grown IGO

This combinatorial piece of indium-gallium oxide was grown and provided by Dr Holger von Wenckstern at the Universität Leipzig. A version of the growth details for this sample is found here, rewritten from details provided by the grower in [44] and [99].

The IGO film was grown directly upon a 51 mm diameter *c*-plane sapphire wafer through CCS PLD. A segmented ablation target was used to produce the composition gradient with the target being composed of In_2O_3, Ga_2O_3 and a small concentration of SiO_2 (0.1% WT) to sufficiently achieve *n*-type conductivity in the film. Oxygen background pressure and temperature were kept constant during the growth, at $3{\times}10^{-4}$ mbar and 650°C respectively. From the large wafer a smaller 5 mm × 51 mm strip sample was cut.

The WDX and CL measurements were performed on a JEOL JXA-8530F EPMA. As in Chapter 4 two WDX measurements were completed to determine the entire composition of the film:

1. The major element components (In, Ga & O) were determined using a beam energy of 10 keV, 40 nA beam current and a beam spot size of 10μm. X-rays were counted for 60s at the peak position and 30s at each side of the peak for the background.

2. Due to the reduced concentration the Si dopant density was measured separately. This measurement used a greater beam current of 400 nA and extended

X-ray counting times of 360s on the peak and 180s for each background. The remaining parameters remained the same as measurement 1.

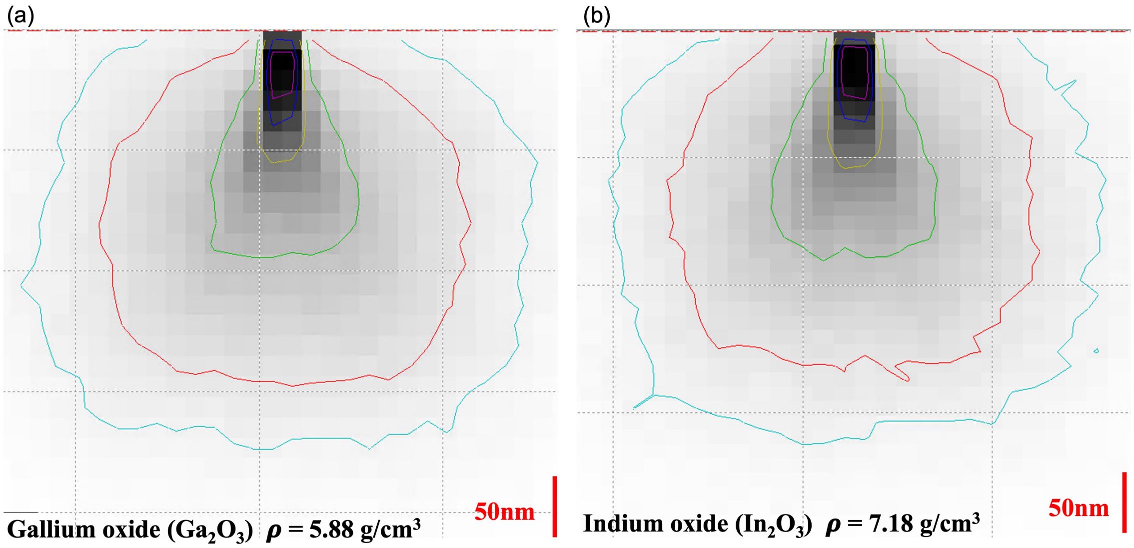

Figure 5.1: CASINO simulation results showing the beam excitation volume within an (a) Ga_2O_3 film (ρ = 5.88 g/cm^3) (b) In_2O_3 film (ρ = 7.18 g/cm^3) using 20000 electrons per simulation with an energy of 10 keV

The results from the two measurements were then combined using the JEOL EPMA software and the entire composition of the film was recalculated. Qualitative scans were completed prior to the quantitative measurements which indicated there were no other measurable trace elements or impurities. CASINO simulations were performed prior to any WDX measurements, as the composition (and density) of the IGO film was unknown a Ga_2O_3 and In_2O_3 film were simulated instead. CASINO indicates that for a 10 keV electron beam energy the penetration depth is approximately 300-350 nm within these films. This means that X-ray generation should be contained within the upper film where the smallest film thickness was expected to be in this 300 - 350 nm range. The results of these simulations are shown in Figure 5.1.

The *k*-ratios used to determine the material compositions were calculated using the following standards: InP for In, bulk Si for Si and unintentionally-doped bulk

Ga_2O_3 for Ga and O. A thallium acid phthalate (TAP) crystal was used for the Ga L_α and Si K_α X-rays, a pentaerythritol (PET) for In L_α X-rays and a synthetic layered pseudo-crystal was required for the O K_α X-rays [162]. A number of measurement points with ~200 μm spacing were taken along the length of the sample providing an adequate sampling rate to observe the compositional gradient within the sample.

The quality of the WDX measurement was assessed through two methods: Firstly, the calculated Wt% for each composition must lie between 98-102% (with 100% indicating a perfect measurement). Any measurements with a Wt% outside of this boundary was discounted. A secondary check on the calculated O at% was also performed. To match the stoichiometry of the two binary semiconductors the O atomic fraction should be 60%, if the calculated O at% value lies outwith the 58 - 62 % range then it was also discounted.

RT CL spectra were acquired using a focussed electron beam with the same beam conditions as the WDX measurements [176]. The CL signal was collected using a built-in reflecting objective, focused into an optical fibre with 105 µm optical diameter which was then coupled into an Andor Shamrock 163 spectrometer with a focal length of 163 mm The dispersed light was then detected using an Andor 1600-channel electron-multiplying charge-coupled device. The spectrometer used within these measurements was equipped with a 300 lines/mm grating blazed at 500 nm.

5.2.1 Compositional characterisation

Due to the large number of measurement points the result from each individual WDX measurement cannot be displayed therefore the results are displayed graphically in Figure 5.2. Initial observations are that the WDX results mirror that of the EDX results in [44]. A constant O atomic fraction of ~60% was observed across the whole sample length apart from within the initial 5 mm, this is attributed to an increase in sample roughness in the high In content regions. As the O content remains fairly constant the changes to the In and Ga contents mirror each other, the increasing Ga content across the sample length produces a near equal decrease in the In. The

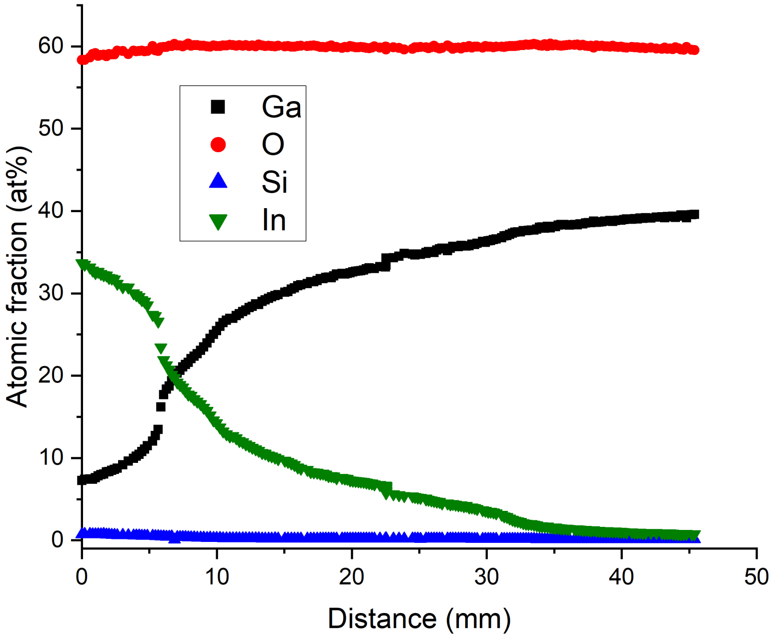

Figure 5.2: Quantitative WDX results acquired from a combinatorial IGO/sapphire sample showing the Ga, O, Si and In atomic fraction (at%) against the measurement spatial distance across the sample length (mm)

measurements indicate the In (Ga) atomic fraction decreases (increases) from a value of 33.7 at% (7.3 at%) to 0.8 at% (39.1 at%) over a 45.4 mm distance with noticeable composition gradient changes at ∼ 5 mm, 10 mm, 25 mm & 35 mm. Rather than the stated constant 0.6 at% as indicated by EDX the Si content appears to be dependent on the In composition, quantified as being 0.7 at% in the high In regions and 0.1 at% in the low.

Figure 5.3 shows a comparison of the Si and In atomic fractions across the sample length. Though varying in magnitude, there is a visible correlation between the composition of the two elements with changes to the compositional gradients of the two elements also aligning. The link between the two elements can be explained by three factors:

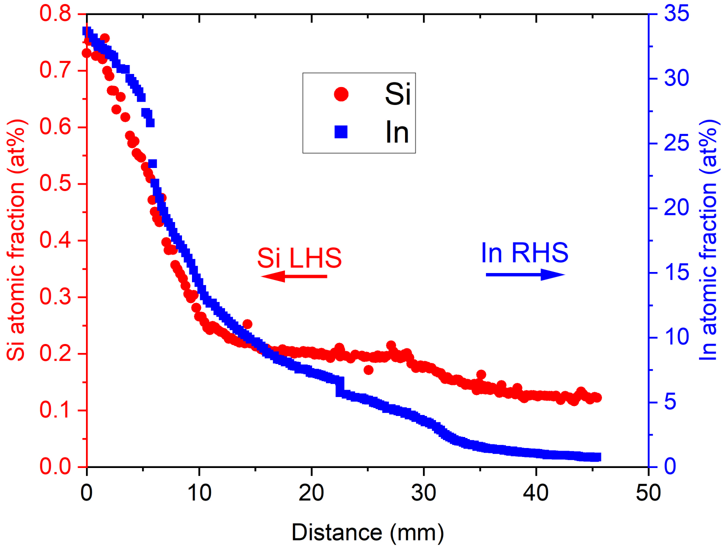

Figure 5.3: Comparison between the calculated Si and In atomic fractions within the combinatorial IGO/sapphire sample against the the measurement spatial distance across the sample length (mm). Red circle data markers indicate the she Si at% and are read of the left-hand side axis and the blue squares indicate the In at % and are read off the right-hand side axis

1. The growth conditions used allow increased Si incorporation rates with PLD growth for high In content films vs high Ga.

2. During the manufacturing of the segregated PLD target an uneven amount of SiO_2 was added, with a larger amount being present in the In_2O_3 side.

3. Interference due to overlapping X-ray lines. Exotic In X-ray lines and higher order reflections overlapping with the Si K_α line used for quantification would result in some In X-rays being counted within the Si quantification. As the In content is increased additional X-rays are further added to the quantification and the apparent Si content increases.

Figure 5.4 shows three qualitative X-ray spectra around the Si K_α peak used for

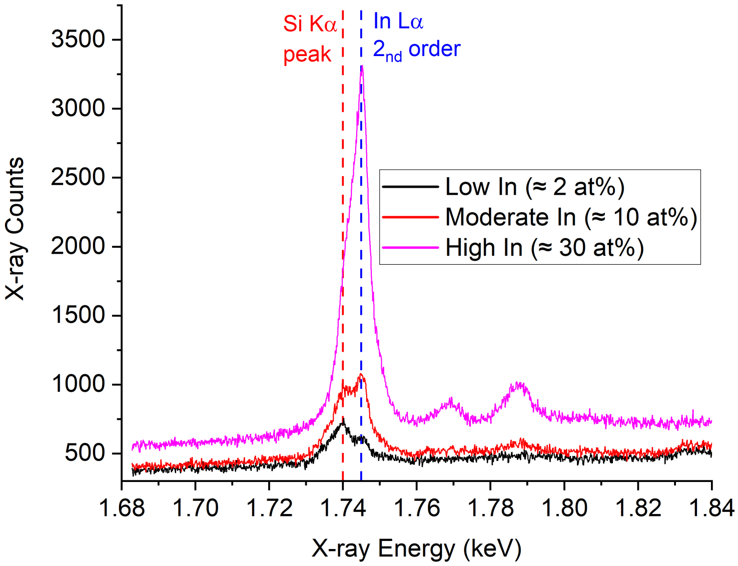

Figure 5.4: X-ray counts as a function of energy around the Si K_α peak energy for low (black spectrum, $\sim$ 2 at%), moderate (red spectrum, $\sim$ 10 at%) and high In (pink spectrum, $\sim$ 30 at%) content regions of the IGO sample. X-ray energies for the Si K_α (E=1.740 keV) & In L_α 2nd order (E=3.487/2 = 1.744 keV) are marked with red and blue dashed lines respectively.

the quantification. Within the low In scan (black spectrum) two peaks are clearly visible, the Si K_α peak showing with a larger height than the neighbouring In L_α 2nd order peak. The proximity of these peak energies unfortunately means there is a peak overlap, both peaks can be visibly resolved however the overlap means the height of both peaks has been exaggerated. Moving to a higher, moderate, In content (red spectrum) shows similar behaviour to the low however now the enlarged In composition results in the L_α 2nd order peak being the dominant peak and the exaggerated Si K_α peak now displaying with fewer counts. At high In contents (pink spectrum) the sheer number of In counts has resulted in the Si peak becoming unresolvable by eye and is merely a shoulder of the large In peak.

The results in Figure 5.4 confirm that factor 3 (peak overlaps) are the explanation for the Si-In composition relation (Figure 5.3). Knowing this, assuming that factors 1 (In content assisting Si incorporation) and 2 (inconsistent SiO_2 concentrations in each target segment) can be discounted and that the Si concentration is linear throughout the entire sample, the best approximation for the Si doping within the film would be at the lowest In content (0.8 at%), giving a value for the Si atomic fraction to be 0.12 at%.

A WDX map providing a visual representation of the composition of the IGO sample is shown in Figure 5.5. The cyan line intersecting the map indicates the approximate region were the WDX point measurements in Figure 5.2 were taken. In general, the compositional gradient only exists along the horizontal axis apart from at the region with the greatest In content.

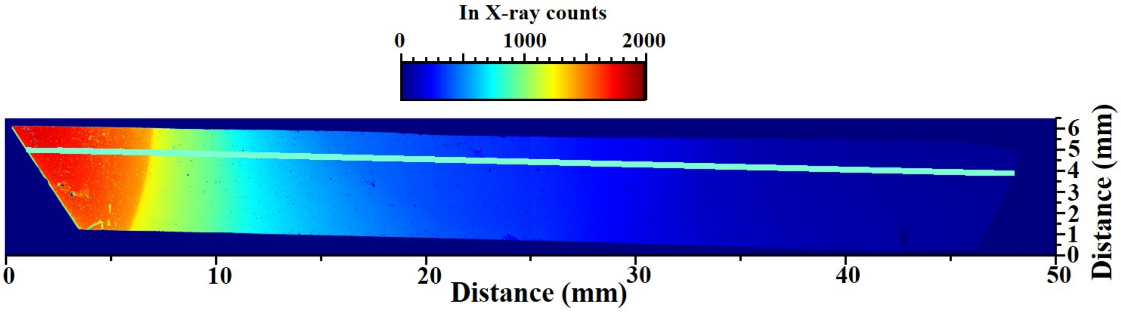

Figure 5.5: 5000 × 650 pixel WDX map (0.1 × 0.1 μm pixel size) showing the In L_α X-ray counts produced from a piece of IGO. Map was acquired using a 10 keV, 40nA focussed electron beam current with 250ms pixel dwell time.

Lastly, electron beam backscattered-diffraction (EBSD) measurements were performed by Dr Gunasekar Naresh-Kumar at three points across the sample corresponding to areas with the three crystallographic states: monoclinic, mixed and cubic. Indexed EBSD patterns identifying the crystal phase at these points is shown in Figure 5.6. Unlike the studies referred to in Chapter 5.1 where the IGO samples are mainly amorphous, this sample exhibits good crystal quality at both the high and low In regions. Unsurprisingly, the mixed phase moderate IGO regions were found to have low crystal quality.

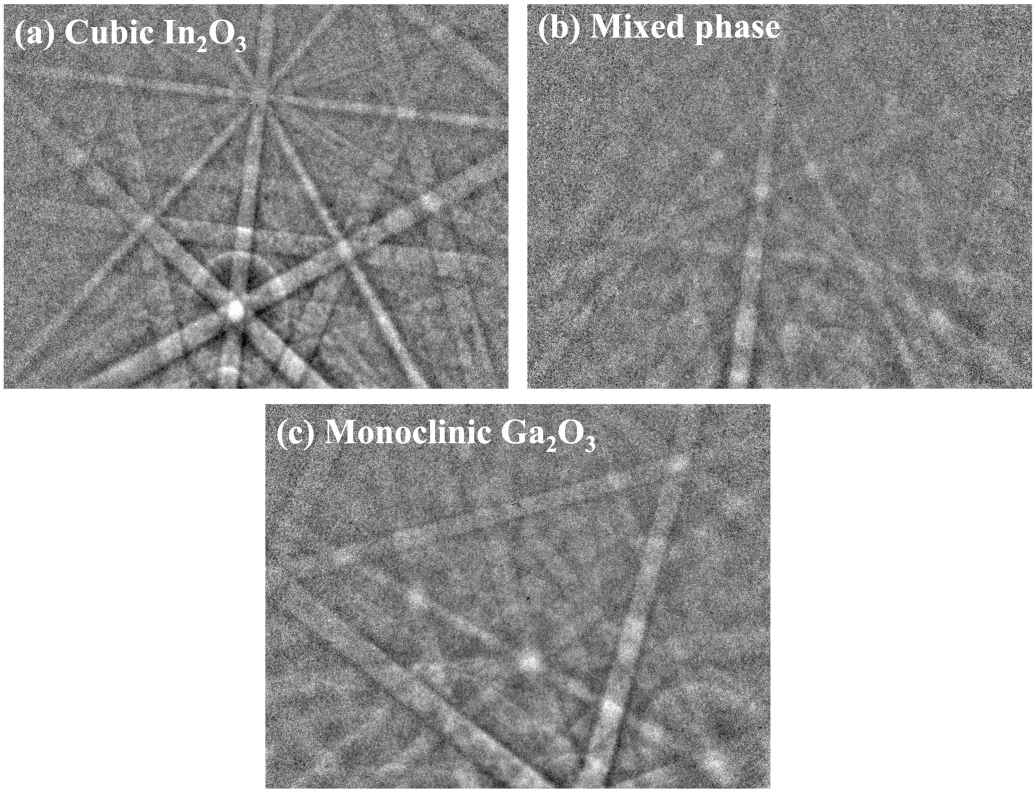

Figure 5.6: EBSD patterns from the IGO samples taken at three separate points at approximate distances of (a) 3 mm, (b) 8mm & (c) 40 mm across the length of the sample.

The diffraction pattern in Figure 5.6(a) confirms the presence of cubic In_2O_3 however two different crystal structures have been identified: Space group $Ia\bar{3}$ corresponding to the bixbyite structure and a previously unidentified cubic group $I2_13$. The presence of this space group has not been confirmed here through simulations however published studies discuss the existence of $I2_13$ cubic In_2O_3 and its properties have been investigated through DFT calculations [199]. The poor crystal quality of the mixed phase state results in a poor diffraction pattern in Figure 5.6(b) which did not allow any crystal structures to be definitively indexed. The pattern in Figure 5.6(c) from the region of low In (high Ga) was clearly indexed as possessing the monoclinic structure due to film content being near pure Ga_2O_3.

5.2.2 Optical properties

Ga_2O_3 luminescence typically shows with three main luminescence bands: A UV ($\sim$ 3.2 eV), blue ($\sim$ 2.7 eV) and green band ($\sim$ 2.3 eV) [200, 201]. UV emission is attributed to the recombination of free electrons with self-trapped holes (STHs) or self-trapped excitons. As mentioned in Chapter 2 STHs are intrinsic defects found within Ga_2O_3 with two STH sites existing in β-Ga_2O_3 due to the non-fully bonding of O atoms in the monoclinic crystal [55]. Donor-acceptor pair recombination (DAP) between oxygen vacancies (V_O) [donors] and gallium vacancies (V_{Ga}) [acceptors] is generally said to be the source of the broad blue emission [201]. Green emission is generally attributed to defect luminescence involving extrinsic impurities (e.g Sn, Si and Be) [202, 203] with the intensity of the luminescence found to be dependent on oxygen availability during growth [200], suggesting that DAP recombination is responsible but the exact mechanism remains unknown. A rare red emission ($\sim$ 690 nm) has also been reported in Ga_2O_3 associated to Cr or Fe impurities [204].

The luminescence on In_2O_3 is poorly understood. Room temperature photoluminescence (PL) has produced broad blue band emission ($\sim$ 470 nm) in In_2O_3 powders and nanowires [205, 206]. Low temperature PL and CL revealed similar results with a peak centred around $\sim$ 420 nm [207]. In all cases the luminescence is attributed to recombination involving V_O. Lower energy broad band emission at $\sim$ 570 nm and 630 nm was observed through PL in In_2O_3 thin films and nanobelts, again attributed to V_O with no other impurity elements detected which may be responsible [208, 209]. STHs do exist in In_2O_3 yet the luminescence expected from electron recombination is predicted to be in the infrared spectral region [56].

Room temperature CL spectroscopy measurements were taken along the length of the sample to probe the optical properties and understand how the luminescence develops as the composition changes from Ga_2O_3 to In_2O_3. The luminescence within the combinatorial IGO sample would be expected to transition between that of Ga_2O_3 to In_2O_3. Due to the lack of near band edge or excitonic recombination the luminescence is not indicative of the semiconductor bandgap.

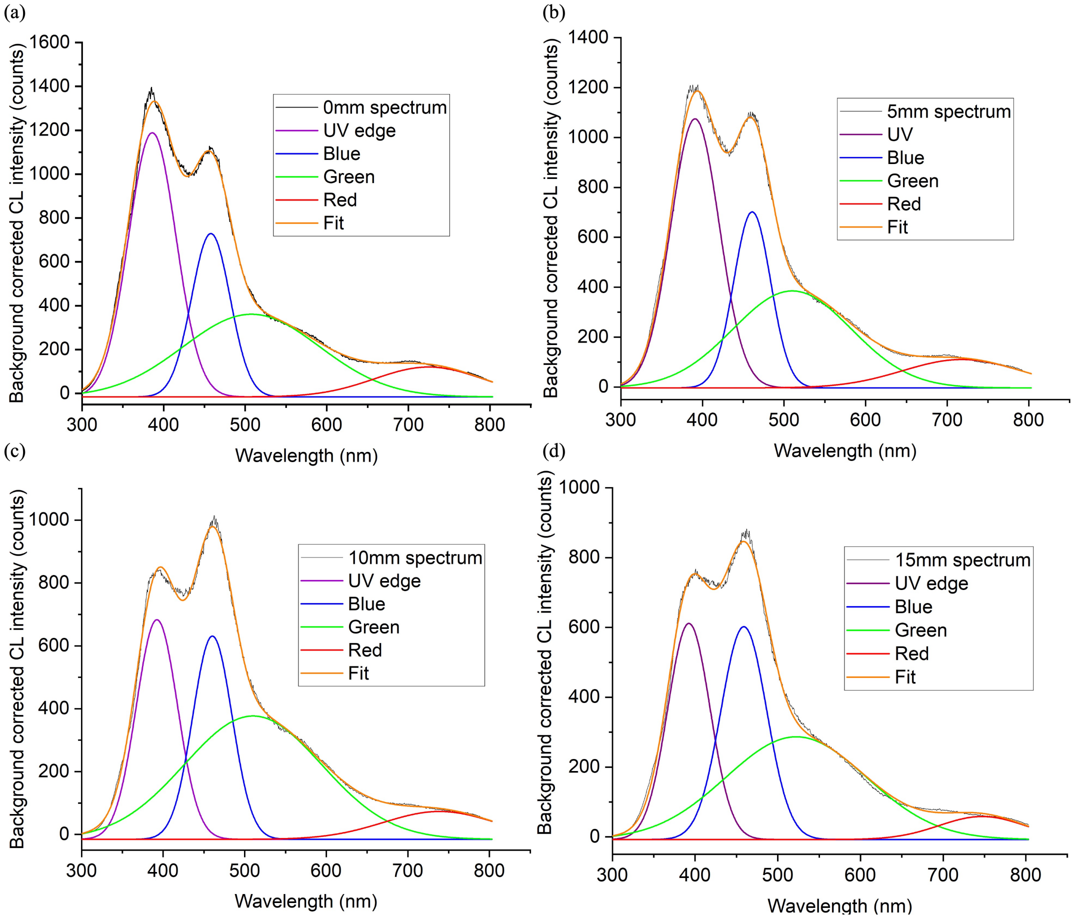

Figure 5.7: Room temperature CL spectra showing the background corrected CL intensity (counts) as a function of wavelength (nm) Spectra were acquired from IGO sample using a focussed 10 keV electron beam with a 40 nA beam current from distances of (a) 0 mm, (b) 5 mm, (c) 10 mm and (d) 15 mm from the low In (high Ga) end of the sample (Inverse of WDX direction). In each panel the black trace is the experimentally measured CL spectrum, the deconvolved UV, blue, green and red peak locations produced by Gaussian peak fitting are shown in their respective colours (purple for UV). The orange trace is the sum of the individual Gaussian peaks

While acquiring the CL spectra with a beam energy of 10 keV, luminescence from the sapphire substrate was detected at the low In side of the sample as this region had a smaller film thickness. To prevent this luminescence interfering with the film spectra a reduced beam energy of 6 keV was used. Spectra were acquired at 1 mm intervals across the sample length until no CL could be detected. Due to the mixed phase state and the poor luminescence observed in In_2O_3 material the intensity of the emission is also expected to gradually decrease, because of this the CL signal was initially acquired from the opposite side to the WDX (low Ga).

Gaussian peak fitting was performed on the generated spectra, identifying the peak amplitude, FWHM and centre wavelength for the three spectral bands mentioned above. Any other peaks resolvable by eye were also included within the fitting.

Example spectra taken at distances of 0 mm, 5 mm, 10 mm and 15 mm are shown in Figure 5.7. The spectra within Figures 5.7(a) & (b) resembles that typically seen from CL measurements on pure β-Ga_2O_3 with UV emission around 380-390 nm (~3.2 eV) dominating, a weaker blue emission at 460-470 nm (2.6-2.7 eV) and a faint broad green emission in the 500-530 nm (2.4-2.3 eV) range [193, 210, 211]. Figures 5.7(c) & (d) show the same three peaks however with modulated amplitude resulting in blue emission becoming dominant with UV emission suppressed.

The modulation of these two peaks has been seen in the luminescence of IGO [212] and other ternary alloys [213], in the presence of impurities [214] and through neutron irradiation [215]. This implies that the blue peak intensity is dependent on the density of V_{Ga} within the film. The alloying with In appears to have increased the V_{Ga} density, simultaneously increasing blue emission while decreasing the occurrence of STHs and quenching the UV emission.

Note that the UV peak appears to have a shoulder corresponding to higher energy UV emission at approximately 350 nm. The exact energy of this peak could not be resolved definitively but has been reported [53, 102, 215]. The origin of this emission is disputed, some attribute STH emission solely to this peak with the UV emission observed here at $\sim$ 370 nm being another form of DAP recombination [53]. Hybrid functional calculations determine the STH recombination emission energy with Ga_2O_3 to be approximately 3.1 eV [56]. This is in agreement with the observations here however the two distinct STH sites within monoclinic Ga_2O_3 may result in two

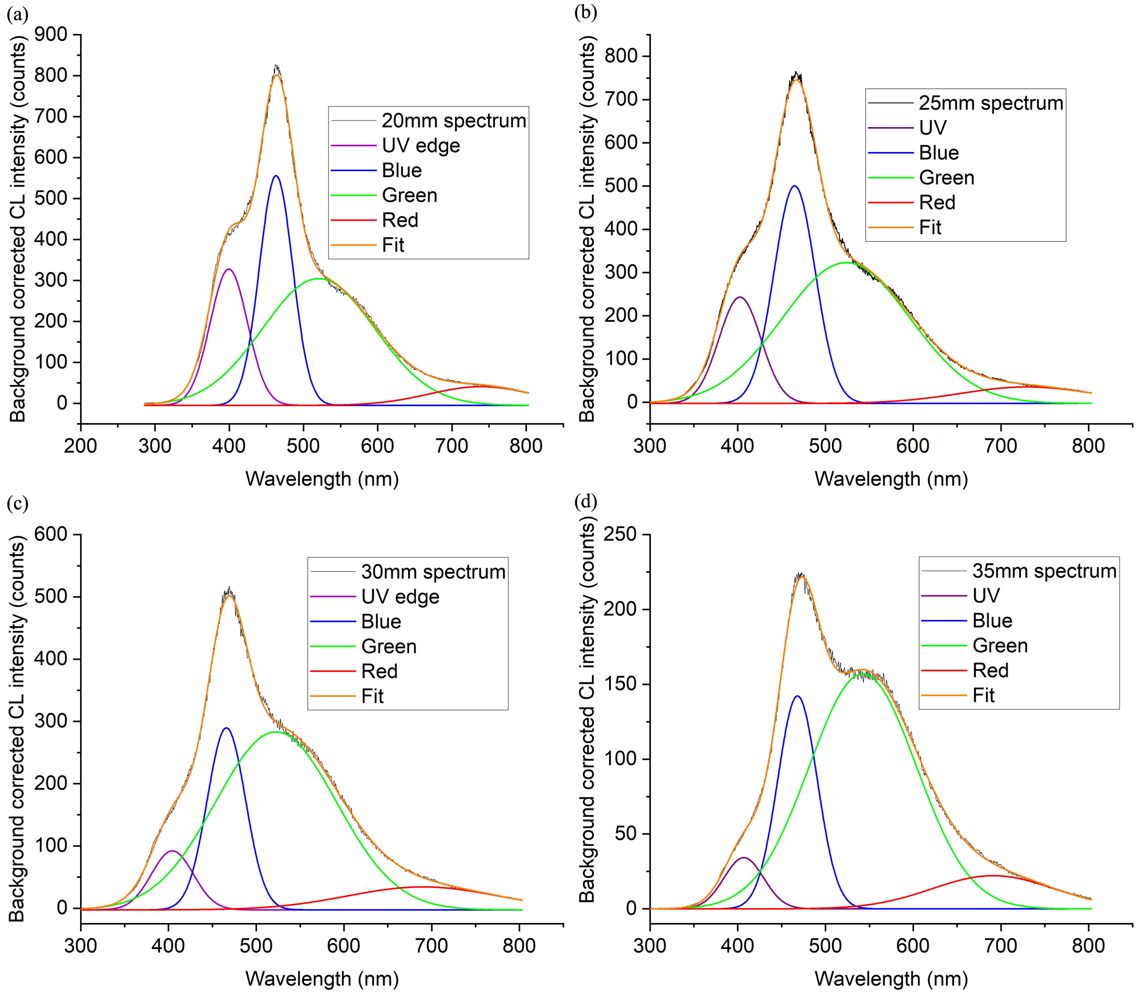

Figure 5.8: Room temperature CL spectra showing the background corrected CL intensity (counts) as a function of wavelength (nm) Spectra were acquired from IGO sample using a focussed 10 keV electron beam with a 40 nA beam current from distances of (a) 20 mm, (b) 25 mm, (c) 30 mm and (d) 35 mm from the low In (high Ga) end of the sample (Inverse of WDX direction). In each panel the black trace is the experimentally measured CL spectrum, the deconvolved UV, blue, green and red peak locations produced by Gaussian peak fitting are shown in their respective colours (purple for UV). The orange trace is the sum of the individual Gaussian peaks

different emission energies corresponding to the 370-380 nm peak clearly observed here and the higher energy, weaker intensity peak at 350 nm.

For all spectra in Figure 5.7 the In alloying has increased the relative intensity of green emission due to the increase in the V_{Ga}. This allows greater density of V_{Ga}+In complexes to form, with the different complex states acting as the donor levels forming the broad emission [56,213]. Though red emission has been seen within $\beta-Ga_2O_3$ [204] the peak observed between 700-800 nm in Figure 5.7 is due to second order reflections from the UV peak rather than an emission band from the IGO film.

A similar set of spectra to Figure 5.7 taken from the midpoint of the IGO film at distances of 20 mm, 25 mm, 30 mm and 35 mm is shown in Figure 5.8. The spectra seen in Figures 5.8(a) & (b) emphasises the luminescence behaviour seen in 5.7(c) & (d). As you move across the sample length, along the increasing In composition gradient there is further suppression of the UV emission and enhancement of blue, the intensity of green emission continues to increase relative to the UV and blue.

Further increasing the In content then results in the domination of green emission once deconvolved, as seen in Figures 5.8(c) & (d). At these distances across the film length the In and Ga contents are starting to become equal, there will therefore be a large density of V_{Ga} complexes and anti-sites allowing DAP recombination involving the deep lying donor states to become the primary recombination mechanism.

As the IGO film transitions from the monoclinic structure into the mixed phase crystallographic state the CL signal is drastically reduced with no definitive peaks observed therefore analysis was halted at a distance of 35 mm. Figure 5.9 shows the development of the luminescence as the In composition is increased along the film length. To prevent some spectra being masked by those in front some count multiplication (0.9-1.2 ×) has been applied so the three main emission peaks can be seen, every second CL spectrum has also been shown for clarity. The modulation between the UV and blue peaks can clearly be seen moving along the sample length with the increasing In content. The broad green band CL counts stay moderately constant within all spectra however as the total luminescence decreases the relative intensity of the green emission has increased. The diminishing red emission simultaneously with the UV reduction also confirms the source of the 700-800 nm emission to be a

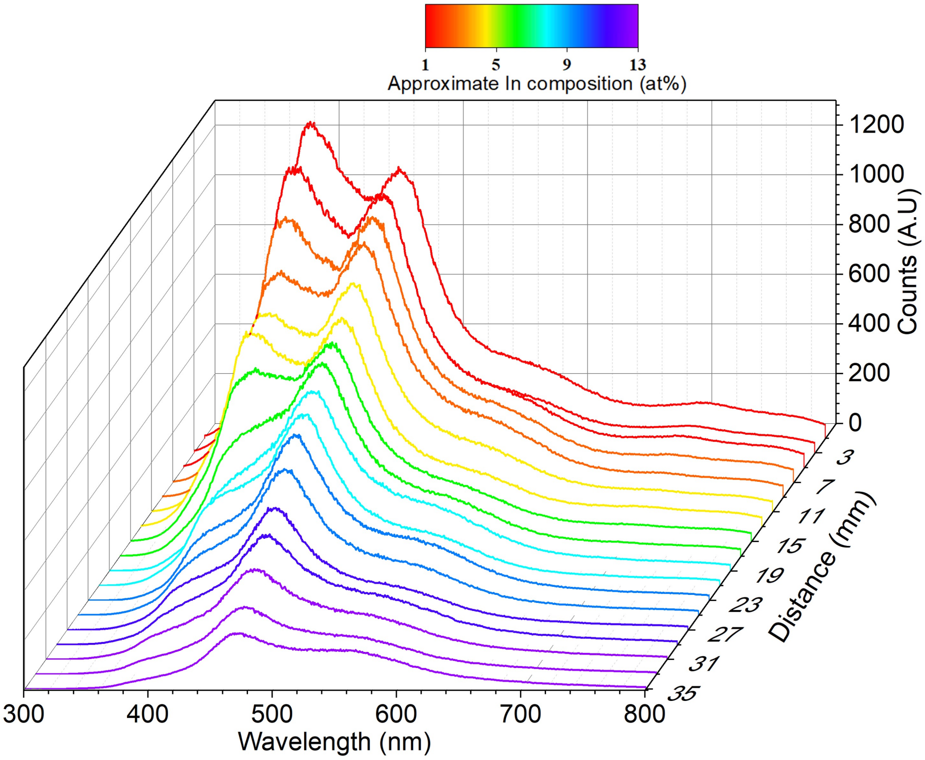

Figure 5.9: Background corrected CL intensity as a function of wavelength (nm) acquired from IGO samples using a focussed 10 keV electron beam with a 40 nA beam current. A spectrum is shown for every 2 mm intervals from distances 1-35 mm. The colour-bar scale shows the approximate In composition (at %, determined through WDX) at the point where the spectrum was obtained

second order reflection from the UV.

The shift in peak luminescence from UV to blue and the increase in the relative intensity of green emission is also accompanied by a shift in the peak wavelength of all three of these spectral bands. In Figure 5.10 a clear red shift of all three spectral bands can be seen however to different extents.

In Figure 5.10(a) the UV emission follows a nonlinear red shift with light amounts of In (1-3 at%) inducing a large shift in the UV wavelength from ∼385 nm to 395 nm. Increasing the In content further continues to redshift the emission further with

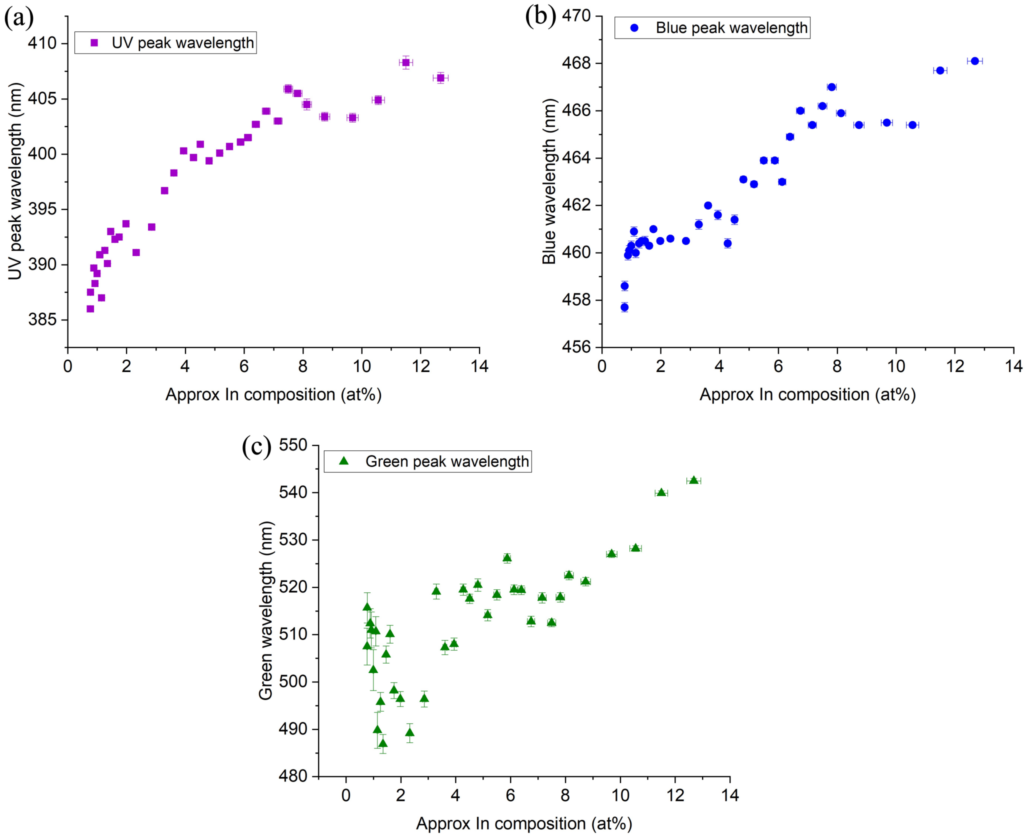

Figure 5.10: Deconvolved emission peak wavelength (nm) from CL measurements as a function of In composition (at%) determined by WDX for the three main luminescence bands of: Ga_2O_3(a) UV (purple square data markers), (b) blue (blue circles) and (c) green (green triangles)

an In composition of ∼9 at% required to redshift the wavelength by a further 10 nm. The shift in the UV emission then begins to level off, with a minimal change observed as the In content is increased beyond this level. As UV emission is suppressed for greater In contents there is greater difficulty in the deconvolution of this peak hence the greater error for these data points. A total redshift from 386 nm to 406.9 nm was observed as the In composition was increased up to 12.7 at% [corresponding to $x = 0.32$ in $(In_xGa_{1-x})_2O_3$] resulting in a total redshift of 0.16 eV.

The shifts observed for the blue, Figure 5.10(b), and the green, 5.10(c), follow a more linear behaviour. For the lowest In contents (0.8 at%) the blue peak wavelength was determined to be approximately 458 nm, slight increases in the In composition to 1 at% results in the clustering of data points around the 460 nm mark. From this point the peak wavelength increases linearly to a maximum of 468.1 nm resulting in a total redshift of 0.06 eV. Due to the broadness of the green emission and the weak intensity for low In compositions the peak wavelength was difficult to accurately determine at these points resulting in the large uncertainty and the range of peak wavelengths when the In content is ≤ 3 at%. Increasing the In content results in green emission becoming prominent allowing reliable deconvolution of the peak wavelength. For greater In compositions it can be concluded that the green emission redshift follows a linear trend with the wavelength determined to be 542.5 nm when the In content is 12.7 at% ($x = 0.32$). Taking the green peak wavelength for the lowest In composition to be 500 nm, extracted from the centre of the cluster of data points, this results in a total redshift of 0.19 eV.

The redshift in all cases is attributed to the band gap reduction within the material. Using the bowing equation from [44] to determine the optical band gap reductions, it is determined that greatest reduction is by 0.43 eV for In contents of 12.7 at% ($x = 0.32$). The redshifts observed for all three spectral bands are within this range therefore this is the probable reason for the bandgap shift however there may be other contributing factors such as differences in the strain present in the film.

5.3 Properties of MBE grown IGO

A set of MBE grown sample were provided by Dr Partha Mukhopadhyay from CREOL at the University of Central Florida. The samples were grown by Dr Isa Hatipoglu using the following method:

IGO samples were grown using plasma-assisted MBE. Knudsen effusion cells acted as the indium and gallium sources while oxygen was supplied by an SVT Associates plasma source. Surface contamination was removed from the substrate prior to the growth stage through high temperature annealing (780– 800°C) and through etching with dilute HF and then rinsed with de-ionized water. A standard

Sample	**WDX (Wt%)**	$\boldsymbol{x}$ **(%)**	**In at%**	$\mathbf{T}_{Ga}$ **(°C)**	$\mathbf{T}_{In}$ **(°C)**	$\mathbf{T}_{Growth}$ **(°C)**
172	99.7	18.3	7.2	980	770	600
173	100.2	25.0	9.8	980	790	600
175	99.6	18.7	7.4	980	770	550
176*	99.4	18.6	7.4	975	770	550
178	99.5	16.3	6.5	980	770	450
179	99.2	13.0	5.2	980	770	500
180	100.4	36.8	14.3	980	800	450
181	100.2	24.1	9.5	980	800	500
182	99.4	21.4	8.5	975	790	550
183	100.1	31.6	12.5	980	800	550

Table 5.1: Summary of growth conditions, sample properties and WDX compositional results for all IGO samples. Sample 176 grown with a reduced oxygen flow rate of 2.5 sccm (marked with an *)

oxygen flow rate and plasma power of 3 sccm and 300W were used for all samples (apart from one sample with a oxygen flow rate of 2.5 sccm) with the amount of In and Ga available during the growth varied by altering the effusion cell temperature. A thin Ga_2O_3 nucleation layer was grown directly upon the sapphire substrate prior to IGO growth. The growth times were kept constant for each sample, at 1 hour for the nucleation layer and 4.5 hours for the IGO film. This resulted in an expected film thickness of approximately 650 ± 100 nm.

5.3.1 Compositional characterisation

As with the PLD combinatorial sample all WDX measurements were performed on a JEOL JXA-8530F EPMA. As the samples are unintentionally doped only one WDX measurement was required to determine the entire composition of the film. A beam energy of 10 keV, 40 nA beam current and a beam spot size of 10μm was used to determine the In, Ga and O composition. X-rays were counted for 60s at the peak position and 30s at each side of the peak for the background. The *k*-ratios were determined using the same standards as with the PLD sample: InP for In, and unintentionally-doped bulk Ga_2O_3 for Ga and O. The growth parameters and compositional details for each sample are given in Table 5.1

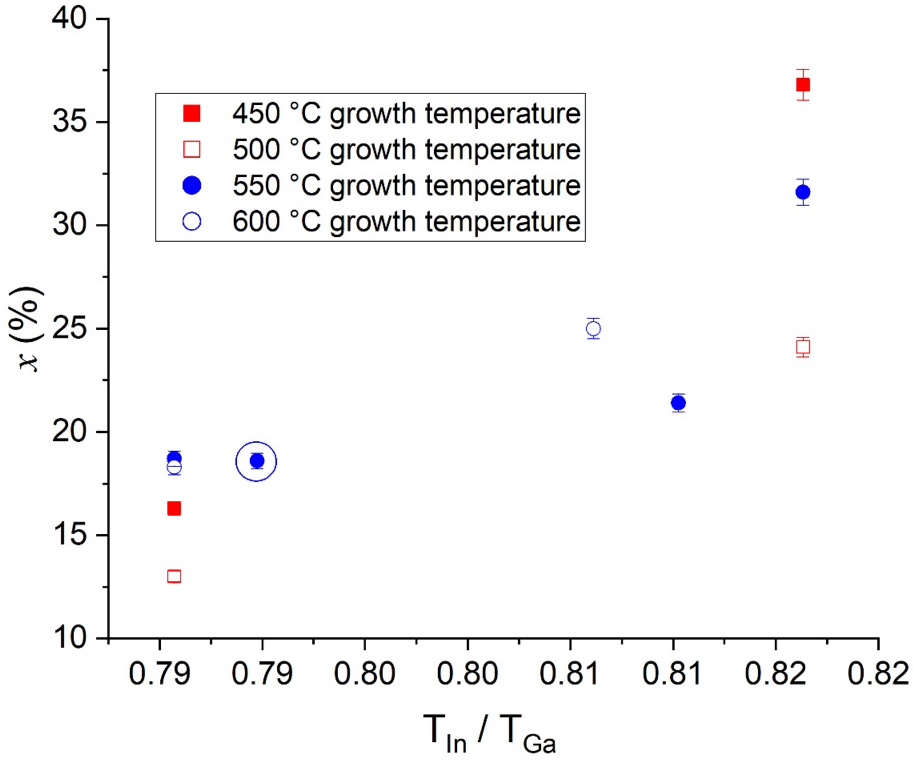

Figure 5.11: $(In_xGa_{1-x})_2O_3$ composition determined by WDX plotted against the temperature ratio of the In and Ga effusion cells during the growth process. Data points are separated by their growth temperatures (red filled squares for 450 °C, hollow squares for 500 °C. Blue filled circles for 550 °C, hollow circles for 600 °C). Sample 176 grown with a lower oxygen flux is identified by the surrounding blue ring

The IGO film composition is plotted against the ratio of the In and Ga cell temperatures during the growth process. For all growth temperatures the expected trend is seen where increasing T_{In}/T_{Ga} increases the film composition as more In becomes available for incorporation. The only sample where this does not apply is sample 176 (marked by blue ring).

As there are a low number of samples grown at each growth temperature it is difficult to draw conclusions regarding how the growth temperature impacts the In incorporation. Therefore, the lower growth temperature samples (red filled and hollow squares, 450°C and 500 °C respectively) and higher temperature ones (blue circles and rings, 550°C and 600 °C respectively) have been grouped together. From this it appears that lower temperature growth enhances the In incorporation however the lack of data points, especially in the moderate T_{In}/T_{Ga} region, reduces the strength of this claim. This behaviour has been seen in MOCVD growth of IGO films [198] with higher temperatures increasing the In desorption rate subsequently reducing the film composition.

To assess the uniformity of the samples topography high resolution SE imaging was performed. SE images for the samples grown at temperatures of 600 and 550 °C are shown in 5.12. The lowest In content sample, 172 [5.12(a)], presents with a smooth, fully coalesced IGO film grown under 600°C conditions. As the In availability is increased, rough “flake” like features begin to form as seen for sample 173 in Figure 5.12(b).

Reducing the growth temperature to 550 °C results in the onset of these flake like structures in sample 175, Figure 5.12(c), grown with the same Ga and In availability as 172. Sample 176 in Figure 5.12(d) again shows increased roughness when grown under similar conditions however the “flake” structures have broken down into clusters of multiple smaller features. This is likely due to the sample being grown under poorer oxygen conditions preventing the clusters coalescing into a complete structure. Sample 182, 5.12(e), continues to show the “flake” structures however individual flakes have merged into ridge like structures on the film. This behaviour continues onto sample 183 where the ridges appear to have coalesced into a more complete film with a small density of individual flakes protruding from the film.

Further reducing the growth temperatures to 500 °C continues the trends see

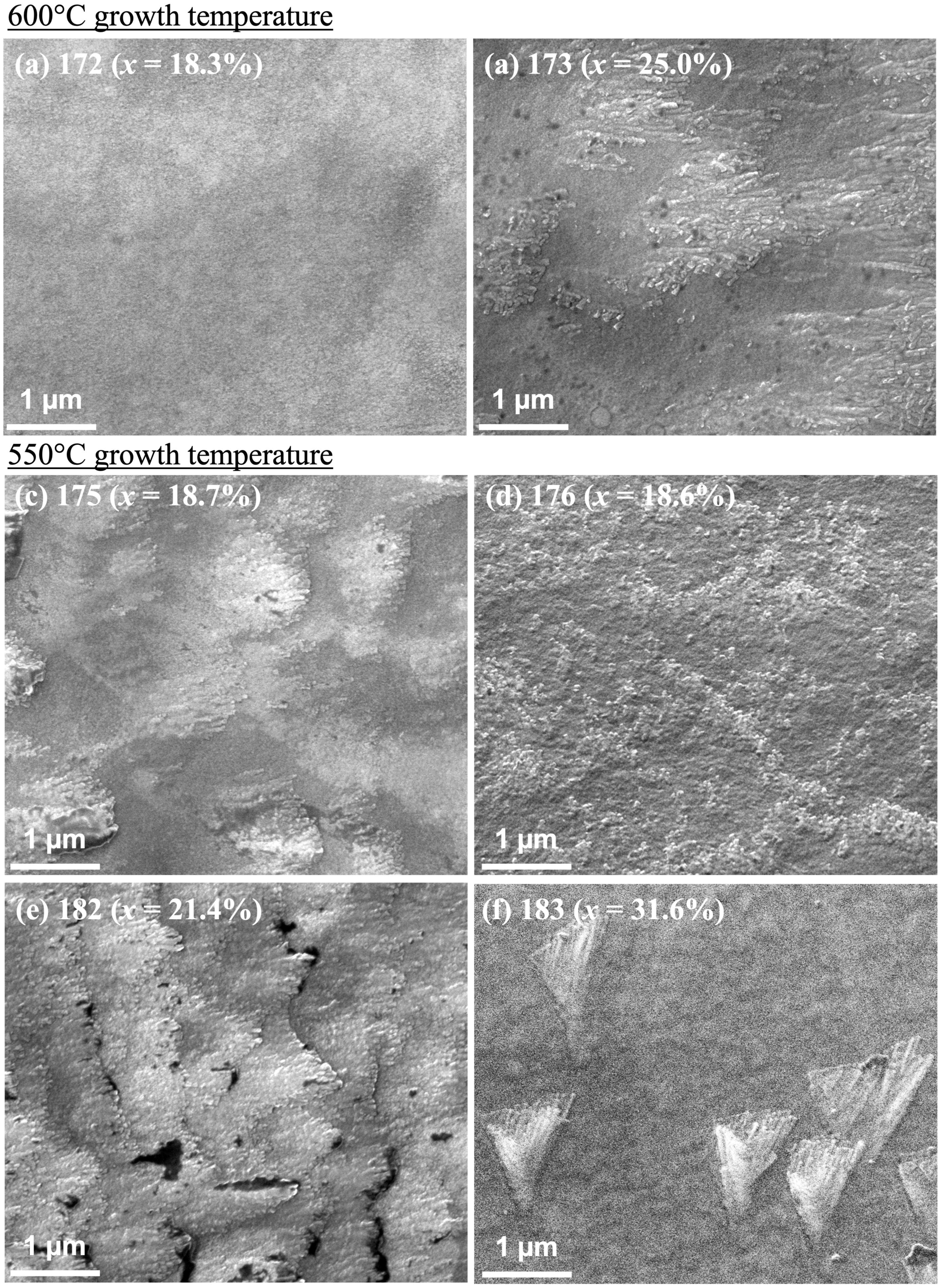

Figure 5.12: Plan-view SE images showing the sample surface of samples (a) 172 & (b) 173 grown at a temperature of 600 °C and samples (c) 175, (d) 176, (e) 182 & (f) 183 grown at a temperature of 500 °C. Images were acquired with a beam energy of 30 keV.

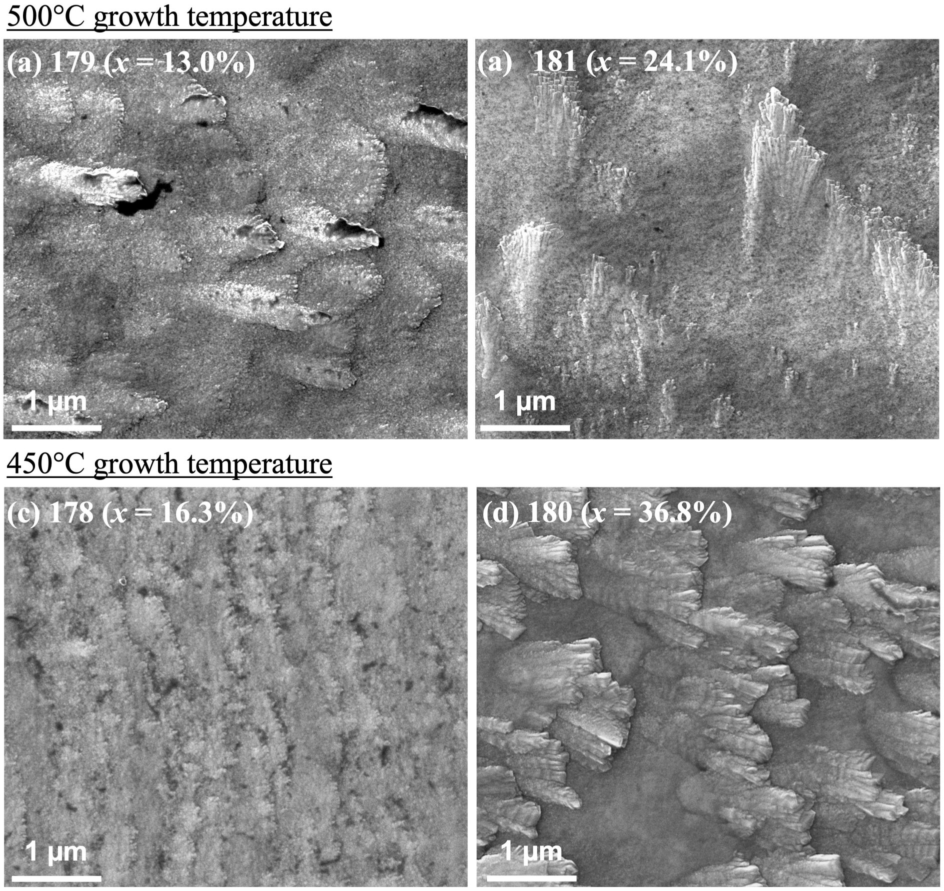

Figure 5.13: Plan-view SE images showing the sample surface of samples (a) 179 & (b) 181 grown at a temperature of 500 °C and samples (c) 178 & (d) 180 grown at a temperature of 450 °C. Images were acquired with a beam energy of 30 keV.

for the higher temperature growth. Lower In compositions result in the "flake" like structures seen for sample 179, 5.13(a), which then merge into the large ridge structures for moderate In contents as in sample 181, 5.13(b). At the lowest growth temperature of 450 °C the sample with the lowest In availability, 178, presents with a fully formed film 5.13(c) presenting with a similar surface seen for higher temperature growth with the same In and Ga availability albeit with a reduce In content, 5.12(a). Increasing In availability for sample 180 5.13(d) mirrors that of sample 183 [5.12(f)] where a fully formed IGO film has formed however there is now a much larger density of crystalline protrusions extending from the film.

From the SE images it would suggest that higher temperature growth would be preferred when growing IGO films with lower In contents and that lower temperature growth promotes uniformity of the film for higher In contents yet the formation of flake-like and crystalline protrusions are unavoidable apart from within the lowest In composition films. The onset of these structures with increasing In availability suggests they are high In_2O_3 regions of the IGO film possibly presenting as defined structures as they take on a different crystal structure to that of the film. To confirm this WDX mapping was performed, the results of which are shown in Figure 5.14. The maps from samples 172 and 178 are omitted as they showed little to no compositional contrast.

From Figure 5.14 it can be seen that the features and contrast seen in the SE images in Figures 5.12 and 5.13 are areas of a higher In composition than the surrounding IGO film. This is true for all of the features seen in the SE images regardless of size however for the samples with larger “flake” and ridged structures (173, 175, 181, 182 & 183) there is an increasing In compositional gradient running through the structure. For samples 176, 179 & 180 the structures exist more as singular entities with a continuous composition though some variation is seen for the larger structures. Due to the height variation between the structures and the underlying film the In compositional variation will be exaggerated at the upper and lower concentrations within the WDX maps. The compositional variation within the film has been assessed by analysing the histogram from each WDX map, shown in Figure 5.15.

In general it is seen that films featuring a lower In composition present with a more uniform composition throughout. As the In content within the films increases there is a greater separation between the lower In content film and the high In content features resulting in the broadening of the histogram. There also appears to be a greater broadening of the peaks for samples grown at higher temperatures despite having similar In availability during the growth (samples 175, 179 and 178). The compositional separation and histogram broadening will also be dependent on

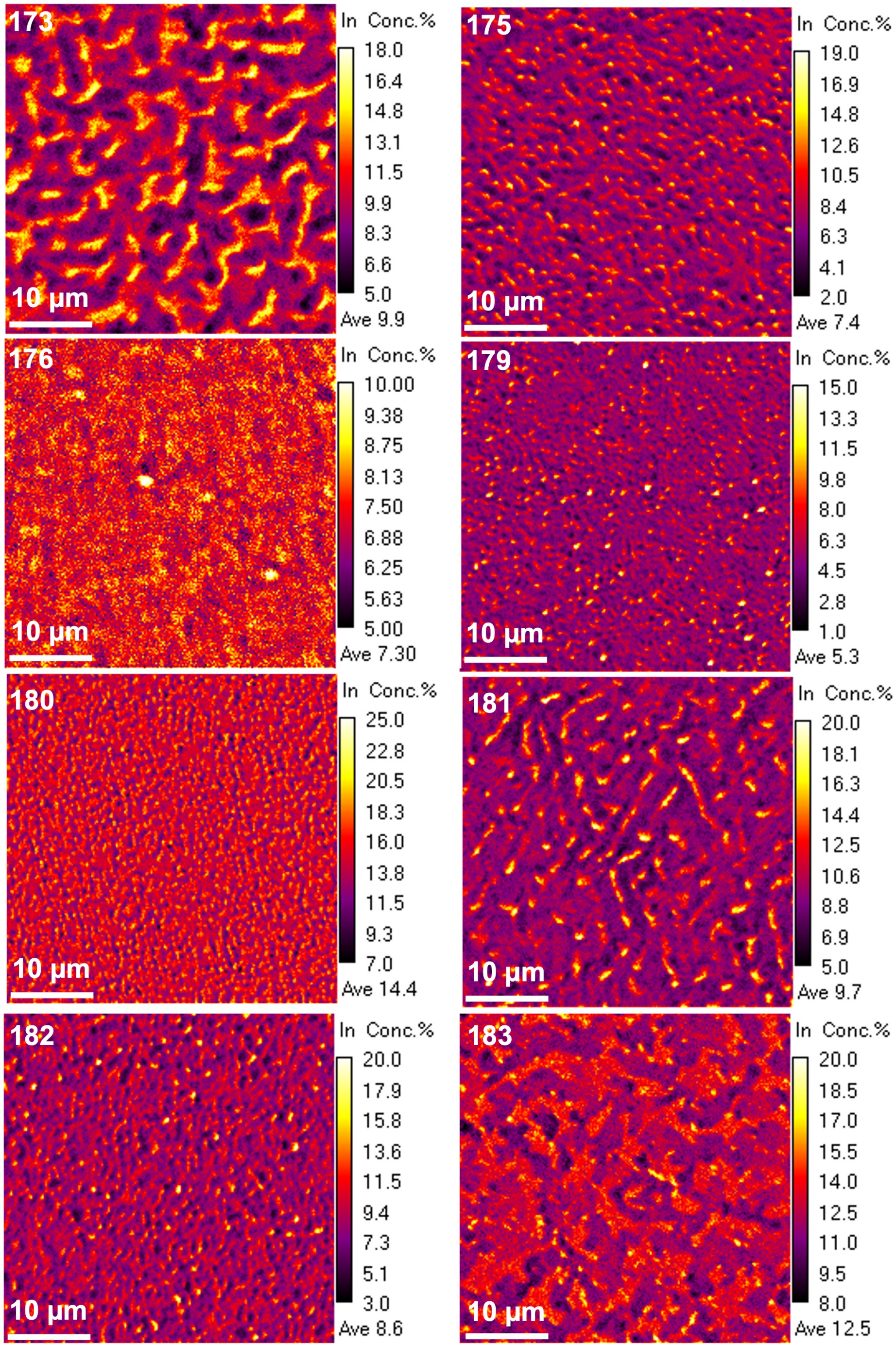

Figure 5.14: 100 × 100 pixel (40 μm ×40μm) plan-view In L_α WDX maps on IGO samples.

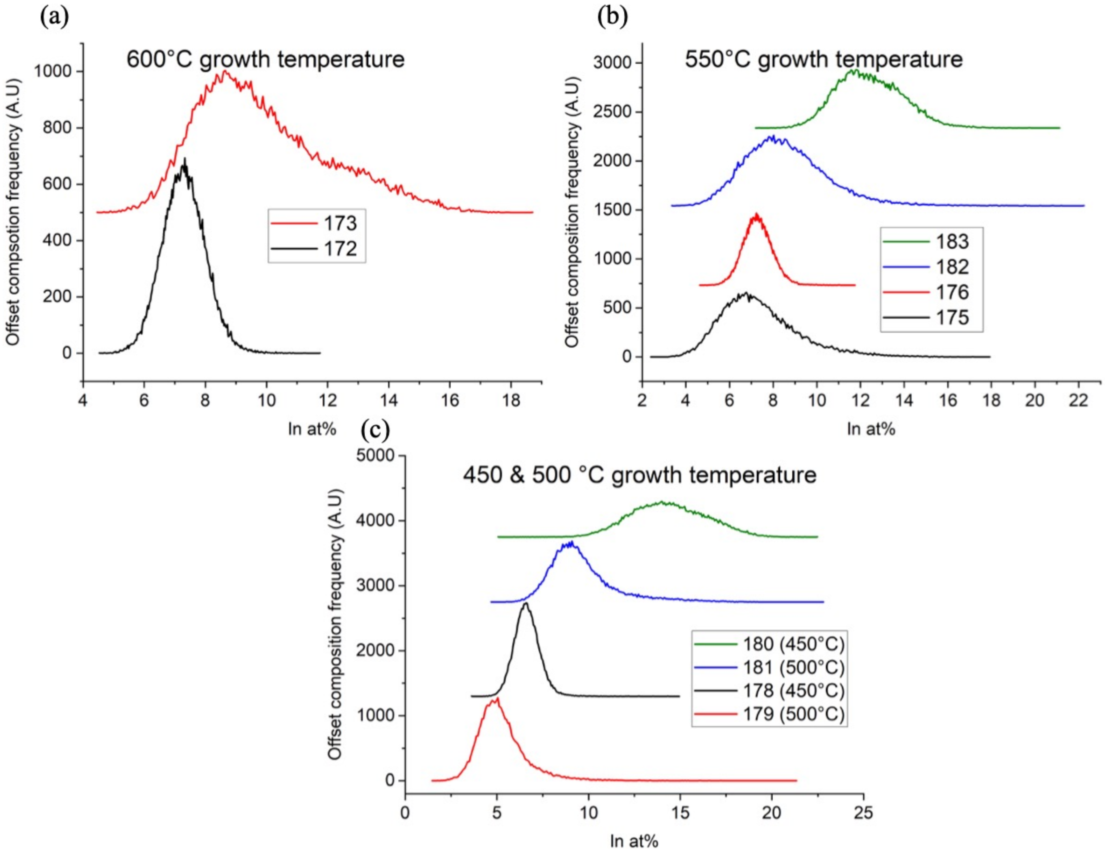

Figure 5.15: Histogram showing the pixel frequency as a function of In compositions (at%) from the In L_α WDX maps shown in Figure 5.14. The Histograms for each sample are separated by their growth temperature: (a) 600 °C growth temperature, (b) 550 °C and (c) 500-450 °C.

the average In composition within the sample, with higher In contents resulting in a greater difference between high and low In regions.

5.3.2 Optical properties

The reciprocal CL maps that were acquired showed poor to no luminescence originating from the high In composition regions of the sample and a similar spectrum acquired for the PLD sample in 5.1 from the low In regions. CL point measurements have therefore been acquired over a larger area of the sample to ignore the effects

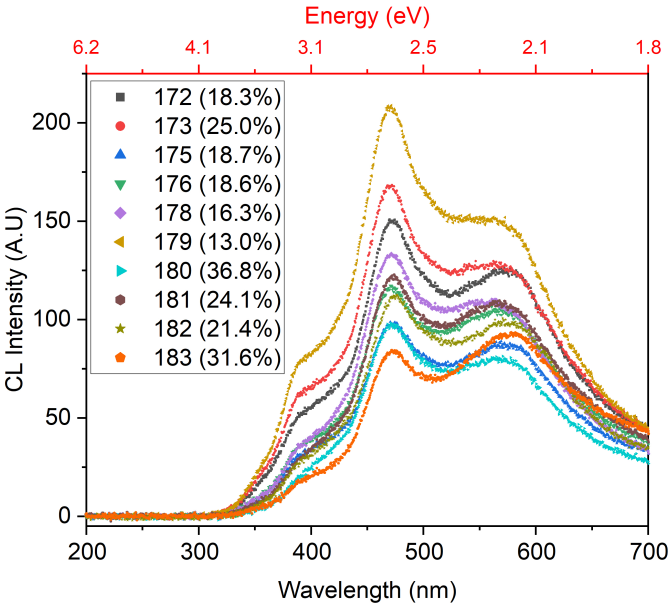

Figure 5.16: Background corrected CL intensity as a function of wavelength (nm) acquired from MBE grown IGO samples using a focussed 10 keV electron beam with a 40 nA beam current. Different data markers/colours correspond to the different IGO samples with the IGO composition (x) shown in the Figure legend.

of the high and low In regions. An example room temperature CL spectrum for each sample is shown in Figure 5.16. As with the PLD sample the three main luminescence peaks match that to Ga_2O_3 (UV, blue and green). In general the peaks behave in the same manner with regards to the level of In alloying: simultaneous suppression of UV and enhancement of blue emission and the relative intensity of green emission increasing. For sample 183 ($x = 31.6\%$) the green emission is found to be the main luminescence peak, previously unseen within the PLD samples. Again, Gaussian peak fitting has been performed to identify the peak wavelengths for each emission for all samples.

Comparing to 5.10 the UV and green emission generally follows the same peak shift trends for MBE and PLD grown samples. However the blue emission wavelength does not show a clear dependence on In concentration, unlike the PLD sample where

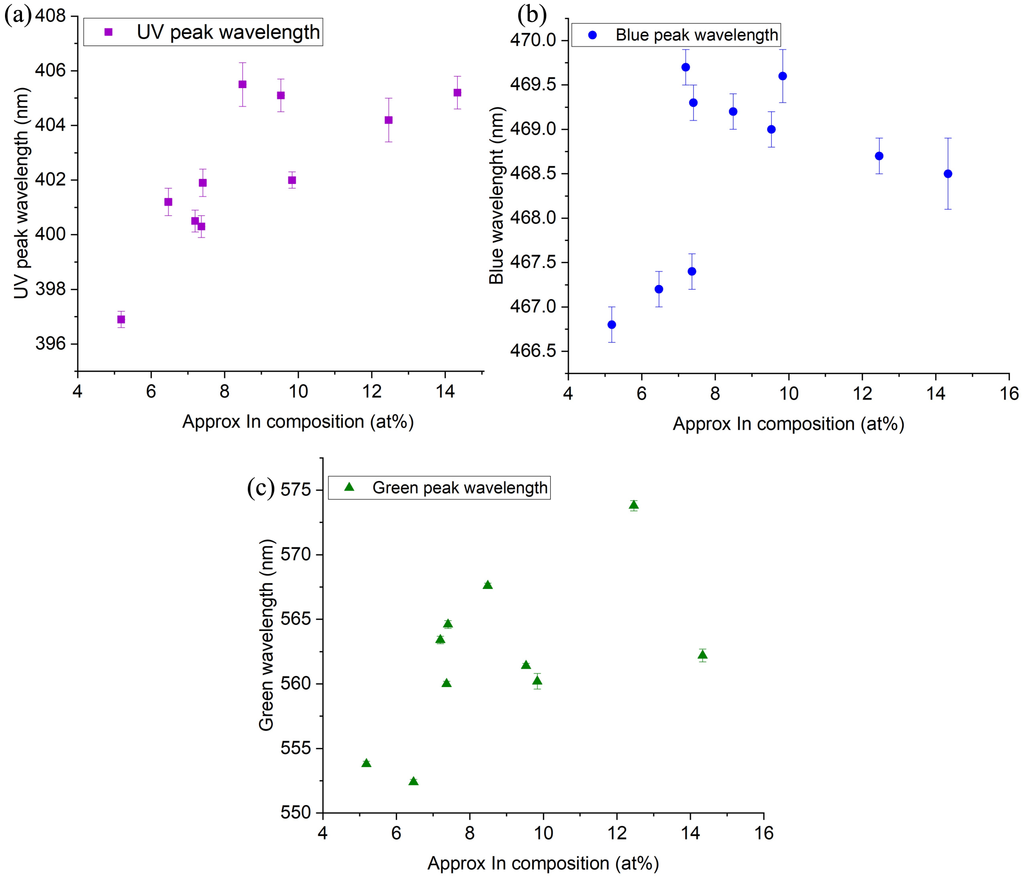

Figure 5.17: Deconvolved emission peak wavelength (nm) of MBE grown IGO samples as a function of In composition (at%) determined by WDX for the three main luminescence bands of: Ga_2O_3(a) UV (purple square data markers), (b) blue (blue circles) and (c) green (green triangles).

there was a clear linear trend. In Figure 5.17(a) the UV emission shows the greatest redshift with small increases in the In content, increasing from 396.9 nm by ∼4-5 nm when In content increased from 5.2 at% to 7-8 at%. As the In content is increased further the magnitude of the shift decreases with UV emission at 405.2 nm for In content of 14.3 at%, corresponds to a total redshift of 0.06 eV over the compositional range observed here.

Blue emission appears to follow no trend in 5.17(b), the lowest blue emission observed here was for the lowest In composition sample (5.2 at%) at 466.8 nm, the greatest at 469.7 nm when at 7.2 at% and the highest In sample showing 468.5 nm blue emission. This would result in the greatest redshift being 0.02 eV for blue emission. The green emission show a weak linear redshifting dependency on the In content, with the increasing In content from 5.2 at% to 14.3 at% producing an approximate shift from 555 nm to 572.5 nm, corresponding to a 0.07 eV redshift. For both the green and blue emission, samples 173 and 183 show lower wavelength emission than expected. This is likely due to the luminescence from the two compositional regions of the sample (high In features and low In film) interfering and the higher intensity luminescence from the low In region dominating hence screening the shift in the high In regions.

Figure 5.18 collates the results from Figures 5.10 and 5.17, the dashed lines in for each panel are guides for the eye. In general the results from both measurements show good agreement with respect to the redshift for all three peaks. There is near perfect agreement with the UV emission in Figure 5.18(a), as the UV emission is dependent on STH which are intrinsic to Ga_2O_3 this isn't surprising. The MBE samples appear to have stronger red shifts for blue and green emission 5.18(b) and (c) respectively though the trends with increasing In content are consistent with both PLD and MBE growth. Differences in the redshift between the two samples may be due to different degrees of strain, crystallinity (MBE samples being polycrystalline and the PLD showing fairly good crystal quality [Figure 5.6])and the composition separation between high and low In regions in the MBE samples interfering with the 'true' shift.

As the bandgap reduction is the most likely mechanism responsible for the red shift of the emission peaks, UV-vis transmission spectroscopy was performed, the results of which are shown in Figure 5.19. Though the transmission curves do not follow the exact order that would be expected from the In composition determined through WDX there is a clear bandgap redshift seen for all samples when compared to the Ga_2O_3 reference sample. The transmission spectroscopy measurements determine the optical bandgap of the IGO films to be between 3.7 – 3.9 eV depending on In content. This corresponds to an approximate bandgap shift between 1.2-1.4

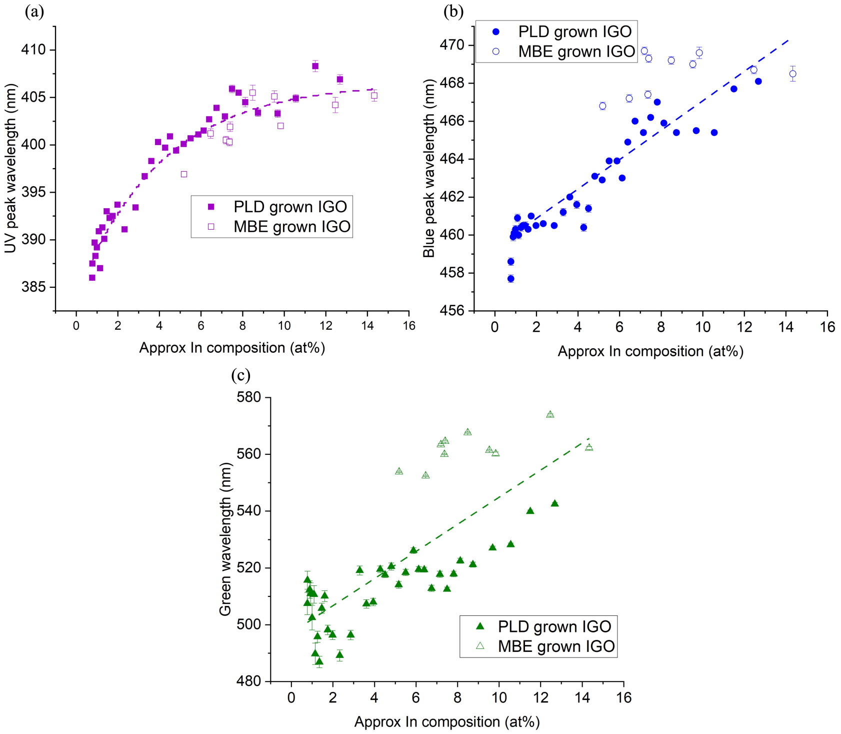

Figure 5.18: Deconvolved emission peak wavelength (nm) of MBE grown IGO samples and PLD combinatorial IGO sample as a function of In composition (at%) determined by WDX for the three main luminescence bands of: Ga_2O_3(a) UV (purple square data markers), (b) blue (blue circles) and (c) green (green triangles). Filled symbols represent the PLD grown IGO data points and hollow represent the MBE samples, the dashed lines in each panel are guides for the eyes

eV range over the x= 0.13 - 0.32 range, with the largest shift seen for sample 181 1.44 eV and the smallest for sample 179 1.17 eV. The value for the optical bandgap has been estimated using the midpoint of the transmission edge therefore may be slightly higher than if calculated through curve fitting or the Tauc method [217].

While bandgap reduction is expected to be the mechanism behind the shift there are other considerations. Wang [210] states that the peakshifts in Ga_2O_3 are associated to a shift in the peak centroid due to intensity shifts. As there are multiple underlying defects/impurities that may be responsible for the luminescence peaks in

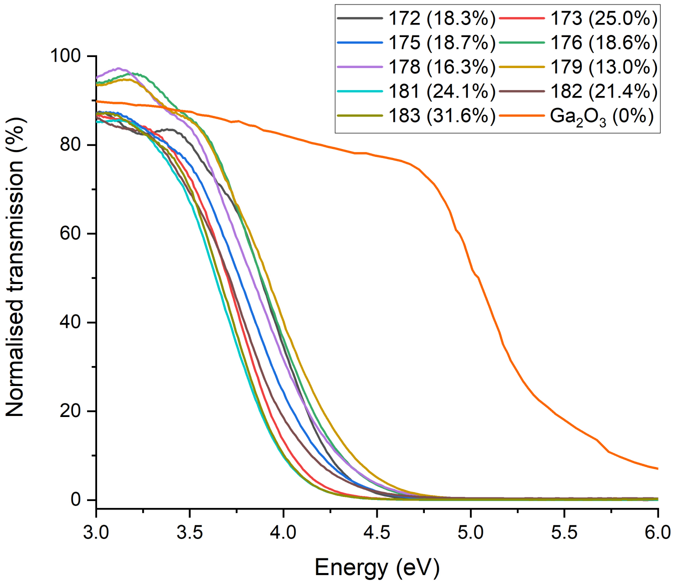

Figure 5.19: Normalised optical transmittance (%) as a function of energy (eV) acquired from the MBE grown IGO samples indicating the shift in optical bandgap. Data is was acquired at the University of Strathclyde and is courtesy of Dr Naresh Kumar-Gunasekar. MBE grown Ga_2O_3/sapphire reference sample from [216] is shown to indicate the total shift in bandgap due to the In alloying. Different line colours used to identify the different samples with the In composition quoted in the Figure legend.

Ga_2O_3 a large increase in a particular defects/impurity can result in the enhancement of defect or DAP based luminescence, with the enhanced intensity being large enough to produce shift in the broad peak centroid [210].

From these values the relationship between the In composition of the IGO film and the optical bandgap has been plotted and derived in Figure 5.20. As all the $(In_xGa_{1-x})_2O_3$ samples have a composition within the $x=$ 0.13 - 0.32 range the bowing parameter cannot be accurately determined as this requires materials over the entire In compositional range. Despite this, the MBE IGO samples show a clear bandgap reduction with the magnitude of the reduction being dependent on the level of In alloying.

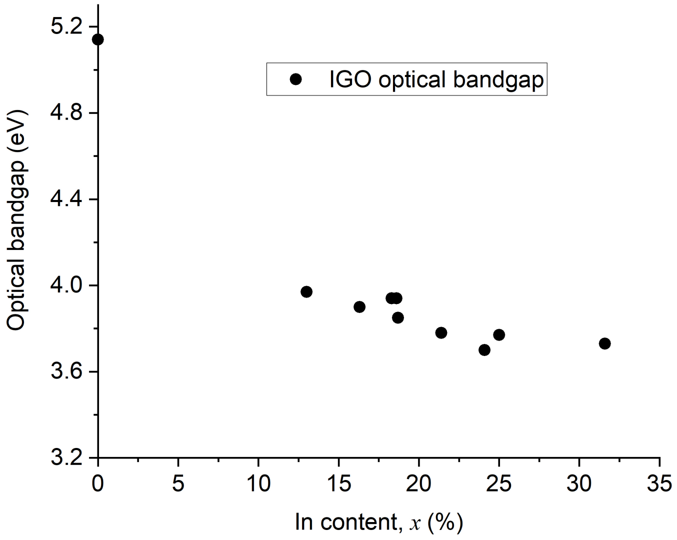

Figure 5.20: Optical bandgap of the IGO films derived from the transmission spectroscopy results in Figure 5.19 as a function of In composition (x).

Other studies on IGO films (theoretical and experimental) are summarised in [218]. For the lower In compositions found here (x= 0.1) published results determine the optical bandgap of the IGO films to be between 5 - 4.2 eV whereas for higher In compositions (x= 0.3) the bandgap varied between 4.6 - 4 eV. Summarising the results from all studies, Von Wenckstern determines there to be a strong bandgap reduction from 4.9 - 4.1 eV for $0 \leq x \leq 0.4$. The magnitude of the bandgap reduction in the results of this chapter is considerably larger than this and than the previous mentioned studies [14, 44]. The difference in bandgap energy is likely due to the compositional inhomogeneity of the MBE samples however strain may also be a contributing factor. Differences in how the optical bandgap was determined must also be considered.

It is expected that further increasing the In composition of the MBE samples would reduce the semiconductor bandgap further, as seen with the results shown in [218]. However the magnitude of the bandgap is unknown due to the discrepancy between the bandgap of the low In content MBE samples and published results. The results of [218] suggest that there would be a gradually bandgap reduction down to 3.6 eV in pure In_2O_3 (x = 1.0). This would conflict with the results here as IGO films with compositions of x= 0.3 have bandgaps comparable to this value. However, as mentioned in Chapter 2, the bandgap of In_2O_3 is not well established, quoted as being between 2.7 - 3.8 eV [44–47]. Therefore further increasing the In content of the MBE samples may reduce the bandgap closer to the 2.7 eV value. The unknown impact of band bowing must be considered, possibly reducing the IGO bandgap dependence on In composition at the higher end of the In compositional scale.

5.3.3 Conclusion

This chapter has featured the characterisation of indium-gallium oxide semiconductor alloys grown through two growth methods pulsed laser deposition and molecular beam epitaxy. WDX spectroscopy was used to determine the level of In alloying and the dopant densities present in the samples. The PLD sample featured a gradual In compositional gradient that spanned up to In $\approx$ 33.7 at% allowing the crystal phase change to be investigated through EBSD with results agree that a bixbyite-mixed phase change occurs for moderate In contents and mixed-cubic for high In content fims, these measurements also identified a previously unseen cubic group for high In content IGO films, $I2_13$. MBE grown IGO films presented with In contents up to 14.3 at% however were polycrystalline and featured undesired surface structures corresponding to a separation of high and low In contents within the film, confirmed through SE imaging and WDX mapping.

Cathodoluminscence measurements on the IGO films show luminescence resembling that of Ga_2O_3 featuring UV, blue and green emission peaks. Through the In alloying there was a modulation of the UV and blue emission intensities: UV emission from STHs in the β-Ga_2O_3 monoclinic crystal dominating for low In compositions but Blue DAP recombination involving V_{Ga} quenching the UV for moderate-high In contents as the V_{Ga} density is increased. The increase in V_{Ga} density also enhances green emission, with the relative intensity increasing gradually with increasing In content, eventually dominating the emission for the highest In content films (14.3

at%). As well as intensity shifts each spectral band exhibited clear red shifts with increasing In content albeit to different degrees: UV showing 10nm shifts for low levels of In alloying (2-3 at%) and a further 10 nm shift which then levels of for In contents $\geq$14 at%; Blue emission shows a constant linear increase of 10 nm over the same composition range and 40-60 nm linear shifts were observed for the green emission 5.18. The shifts in emission energies are attributed to bandgap shifts from the In alloying, this was confirmed through UV-vis transmission spectroscopy, 5.19, showing an approximate bandgap shift of 1.2-1.4 eV with the largest shift observed being 1.44 eV for sample 181. In general the bandgap reduction within the IGO films was found to be dependent on the In composition, with the magnitude of the reduction increasing with increasing levels of alloying.

These results show the successful alloying of Ga_2O_3 with In to produce an IGO alloying with a reduced bandgap allowing the material to be suitable for photodetectors operating in the UV-C and UV-B range. Luminescence spectroscopy revealed that alloying with In there is a large increase in the gallium vacancy defect density which must be further investigated to understand the implications on the device properties of the material.

Chapter 6

Tin-gallium oxide

6.1 Introduction

As established in Chapter 5 it is possible to alloy Ga_2O_3 with indium to reduce the material bandgap for use within the UV-B spectral range. The breakdown in crystal structure with increasing In content [44] sets an limit on the level of alloying before the material becomes undesirable for applications within UV optical devices and photodetectors [9–11, 15–17]. Therefore alternative alloys should be investigated to overcome the crystallographic shortcomings of IGO materials.

Rather than alloying with indium oxide we have taken the alternative approach of using tin oxide to form a tin-gallium oxide (TGO) to reduce the material bandgap (SnO_2 $E_g \approx 3.6$ eV [219]). The low abundance of indium in the earth compared to tin (0.25ppm for In vs 2.2ppm for Sn [220]) also makes TGO alloys more sustainable than their In counterpart.

Sn has been commonly used as a dopant in β-Ga_2O_3 to produce n-type conductivity within the material [221] but little is known about material properties when the Sn content is increased to alloying levels.

TGO films have been grown using the sol-gel process [192] and atomic layer deposition [222] over a large composition range, however both growth techniques result in limited crystal quality. Optical transmission spectroscopy measurements taken on these films indicate a bandgap reduction of approximately 0.5–0.6 eV with Sn contents of $x\approx$ 0.2-0.25 where x indicates the Sn content in the formula $(\mathrm{Sn}_x\mathrm{Ga}_{1-x})_2\mathrm{O}_3$. Higher quality TGO films have been grown using MBE on sapphire substrates [223] and show a similar redshift in the optical bandgap of approximately 0.1 and 0.45 for Sn contents of $x = 0.1$ and 0.3 respectively, compared with Ga_2O_3. From these films it has been possible to to produce TGO photodetectors ($x = 0.1$) with significantly increased photocurrent and enhanced responsivity, compared to a Ga_2O_3 based device. CVD has also proven capable of growing TGO films with similar device characteristics as MBE grown material [224].

Here a number of TGO samples have been grown using plasma-assisted MBE upon various material substrates with varying Sn contents. The level of Sn alloying in each film has been probed using WDX spectroscopy. Optical properties have been characterized using cathodoluminescence spectroscopy identifying the impact of the Sn on the material luminescence compared to Ga_2O_3. UV-vis transmission spectroscopy assisted in determining the optical bandgap of the samples. Both analytical techniques were then correlated using joint WDX and hyperspectral CL mapping, allowing luminescence peak shifts and intensity fluctuations to be assigned to particular compositional regions of the samples. Alongside the TGO characterization, samples were manufactured in the UV photodetectors. The device properties of these photodetectors were evaluated, determining the Sn influence on the detector operation allowing the benefits of TGO based devices over Ga_2O_3 ones to be established.

All the TGO samples in this study were grown at CREOL, University of Central Florida by Dr Isa Hatipoglu and Dr Partha Mukhopadhyay.

6.2 Compositional properties of TGO films

The plasma-assisted MBE growth mechanism used to produce the TGO samples has been detailed in the following publications [52,216,225,226]. Here the general growth process shall be summarised, explaining key details consistent for all samples and highlighting growth parameters that change depending on the substrate used in each growth cycle.

TGO epilayers were grown using plasma-assisted MBE on (010) and (-201) bulk single crystal Ga_2O_3, (0001) sapphire and (111) silicon. Knudsen effusion cells acted as the tin and gallium sources while oxygen was supplied by an SVT Associates plasma source. Surface contamination was removed from the substrate prior to the growth stage through high temperature annealing (780 – 800°C) and etching with dilute HF followed by rinsing with de-ionized water. For the Si, (010) and (-201) Ga_2O_3 substrates TGO films were grown at 600 °C while a reduced temperature of 500°C was used for the sapphire substrate. A standard oxygen flow rate and plasma power of 2.5 sccm and 300W were used for all samples with the amount of Sn and Ga available during the growth varied by altering the effusion cell temperature. For one silicon substrate sample and all samples grown on sapphire substrates there is a thin Ga_2O_3 nucleation layer present to reduce the lattice mismatch between the TGO layer and substrate.

The growth rate differed between the substrates resulting in approximate TGO film thicknesses ranging between 0.125 and 1.25 μm, as seen in Table 6.1 below. Due to the variation in sample thicknesses different beam conditions were required when performing the WDX and CL analyses to ensure primary excitation remained within the TGO layer. As with the IGO samples (*Chapter 5*) all WDX and CL measurements were performed on a JEOL JXA-8530F EPMA. As the samples are unintentionally doped, only bulk element WDX measurements were required to determine the entire composition of the film.

A 40 nA beam current and a beam spot size of 10μm were used for all measurements when determining the Sn, Ga and O composition. A beam energy of 6 keV was used when analysing the TGO films upon the Si, (010) and (-201) Ga_2O_3 substrates, a reduced beam energy of 5 keV was required for the thinner sapphire substrate samples. These parameters were predetermined through CASINO Monte Carlo simulations [144] on β-Ga_2O_3. Results indicated that at a beam energy of 6 keV 90% of the beam energy is deposited within a depth of 175 nm in β-Ga_2O_3 ($\rho =$ 5.88 g/cm^3), whereas for the reduced beam energy of 5 keV 90% of the beam energy is deposited within a depth of <125 nm. We would expect the Sn alloying to increase the film density towards the SnO_2 density (ρ = 6.95 g/cm^3) although only slightly (ρ = 6 - 6.2 g/cm^3) as there is only a moderate level of Sn alloying. Therefore, by performing the calculation for Ga_2O_3, we slightly underestimate the real density of the film, and overestimate the size of the interaction volume, which ensures that the X-ray generation remains within the TGO film.

Substrate	**Film Thickness (µm)**	**Total Wt%**	**$(Sn_xGa_{1-x})_2O_3$ *x (%)***	**T_{Ga} (°C)**	**T_{Sn} (°C)**
(010)-Ga_2O_3	0.25	101.2	0.2	1000	690
(010)-Ga_2O_3	0.25	100.2	5.6	1000	750
(010)-Ga_2O_3	0.25	101.8	0.2	1000	660
(010)-Ga_2O_3	0.25	101.6	6.1	1000	780
(-201)-Ga_2O_3	0.5	100.8	2.7	980	830
(-201)-Ga_2O_3	0.5	100.8	2.6	980	800
(-201)-Ga_2O_3	0.5	101.1	2.4	980	800
(-201)-Ga_2O_3	0.5	101.8	2.1	1000	835
(111) Si	1.25	97.3	2.2	1000	810
(111) Si*	1.25	102.7	2.1	1000	795
(0001) Sapphire*	0.125	95.9	10.8	900	730
(0001) Sapphire*	0.125	98.6	11.0	900	750
(0001) Sapphire*	0.125	97.4	11.1	900	800

Table 6.1: Summary of growth conditions, sample properties and WDX compositional results for all TGO samples. Samples featuring a Ga_2O_3 nucleation layer are identified with a (*)

During quantitative WDX, X-rays were counted for 60s at the peak position and 30s at each side of the peak for the background. The *k*-ratios used to determine the material compositions were calculated using the following standards: cassiterite (SnO_2) for Sn, and unintentionally-doped bulk β-Ga_2O_3 for Ga and O. A thallium acid phthalate (TAP) crystal was used for the Ga L_α and Sn L_α X-rays and a synthetic layered pseudo-crystal was required for the O K_α X-rays [162]. For each sample multiple measurement points (minimum of 9 per sample) were taken (0.25–0.5 mm spacing) and averaged to determine the material composition.

The results from the WDX quantitative measurements and the growth parameters specific to each sample are shown in Table 6.1. The random error from these measurements was found to be negligible within the precision quoted here (random error in x (%) being $< 0.1\%$). No total error has been quoted as there will also be a systematic uncertainty present, estimated to be about 2%. This systematic uncertainty may occur due to multiple factors such as surface contamination (especially impacting low energy measurements), less well-known matrix corrections for non K_α X-rays and differences between the cassiterite standard and the TGO film (e.g. stoichiometry difference between SnO_2 vs Sn_2O_3) [227].

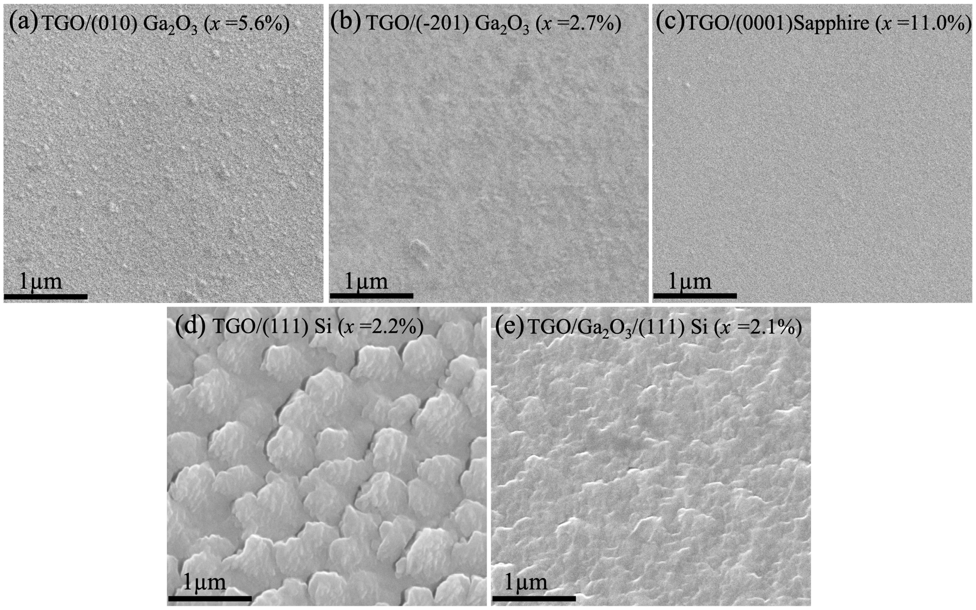

Figure 6.1: Secondary electron images of TGO samples. (a) TGO/(010)-Ga_2O_3 (x=5.6%), (b) TGO/(-201)-Ga_2O_3 (x=2.7%), (c) TGO/(0001) Sapphire (x=11.0%), (d) TGO/(111) Si (x=2.2%) and (e) TGO/Ga_2O_3/(111) Si (x=2.1%).

The crystal quality of the samples was assessed using SE imaging and through

X-ray diffraction (XRD). SE imaging was performed on the JXA-8530F EPMA and the XRD was completed at the University of Central Florida using a PANalytical X'Pert Cu-$K_{\alpha 1}$ beam (λ = 1.5405 Å).

Example SE images taken of the TGO films grown on each substrate are shown in 6.1 where the surface morphology and quality can be viewed. A fully coalesced TGO film was found for the two Ga_2O_3 substrates and the sapphire substrate, shown in Figures 6.1(a)–(c). The granular contrast indicating greater surface roughness in Figure 6.1(a) is attributed to the Sn alloying, as lower Sn content samples (x= 0.2%) on (010)-Ga_2O_3 substrates do not exhibit this surface roughness (not shown), Figures 6.1(b) and (c) show a smoother film surface. The smoother surface morphology may be directly related to the substrate with (201)-Ga_2O_3 or (0001) sapphire substrates promoting greater film crystallinity. The growth conditions must also be considered with each substrate having a different TGO growth rate: ~30-45 nm/hour for sapphire, ~120-130 nm/hour for (201)-Ga_2O_3 and ~80 nm/hour for(010)-Ga_2O_3. The lower growth temperature for the sapphire substrate (500°C growth vs 600°C for the other substrates) may also reduce the sample surface roughness for heteroepitaxial growth (sapphire substrates) vs homoepitaxial films (Ga_2O_3 substrates).

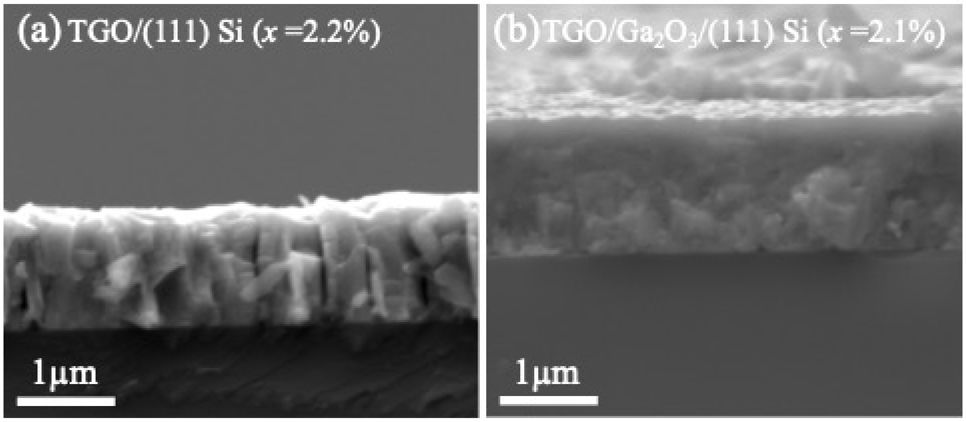

Figure 6.2: Cross sectional SE images of TGO samples: (a) TGO/(111) Si (x=2.2%) and (b) TGO/Ga_2O_3/(111) Si (x=2.1%).

Figures 6.1(d) and (e) show the effect the Ga_2O_3 buffer layer has on crystallinity and film quality of the TGO film. The TGO film grown directly upon Si exhibits poor morphology featuring voids surrounding large flake-like structures composing the film. The inclusion of the Ga_2O_3 buffer layer reduces the occurrence of these voids and the flake structures coalesce into a more complete TGO layer, Figure 6.1(e). The voids may extend deep within the TGO film, forming empty channels which can propagate to the Si substrate as seen in Figure 6.2(a). Utilising the Ga_2O_3 buffer layer not only improves the surface quality of the TGO film but enhances crystallinity throughout the film, drastically reducing the occurrence of the voids and produces a more coalesced TGO film as seen in 6.2(b)

The voids in 6.1(d) pose an issue for the quantification of the TGO composition. These voids form empty channels which allow electron propagation deep within the film and could result in X-ray generation within the Si substrate. The average weight total percentage (total Wt%) in Table 6.1 indicates this has had a minimal effect on our composition calculations. The Wt%'s for our measurements are close to 100% providing a high level of confidence in the compositions produced. Usually a confidence range of between 98-102 Wt% is set however a larger deviation from 100% is accepted for the sapphire substrate samples due to moderate sample charging caused by the insulating nature of the substrate.

To determine the crystal orientations present in the films ω-2θ XRD measurements have been performed for samples grown on each substrate. Measurements were performed by Dr's Isa Hatipoglu and Partha Mukhopadhyay at the University of Central Florida, the results of these measurements have been extracted from their relevant publications [52, 216, 225, 226]. Note that the measurements on the TGO/(010)-Ga_2O_3 and TGO/sapphire films may be from similar samples not included within this study. These XRD measurements were also reported prior to receiving the samples for WDX measurement and therefore the quoted TGO compositions may be inconsistent with the results in Table 6.1. The results of the XRD measurements are shown in Figure 6.3.

As TGO is a relatively unknown material the XRD database categorising the peaks to orientations and materials is fairly unknown.

The broad peak between 59-60 ° in 6.3(a) was identified as the (113) TGO peak within the monoclinic structure with the position of this peak shifting towards lower

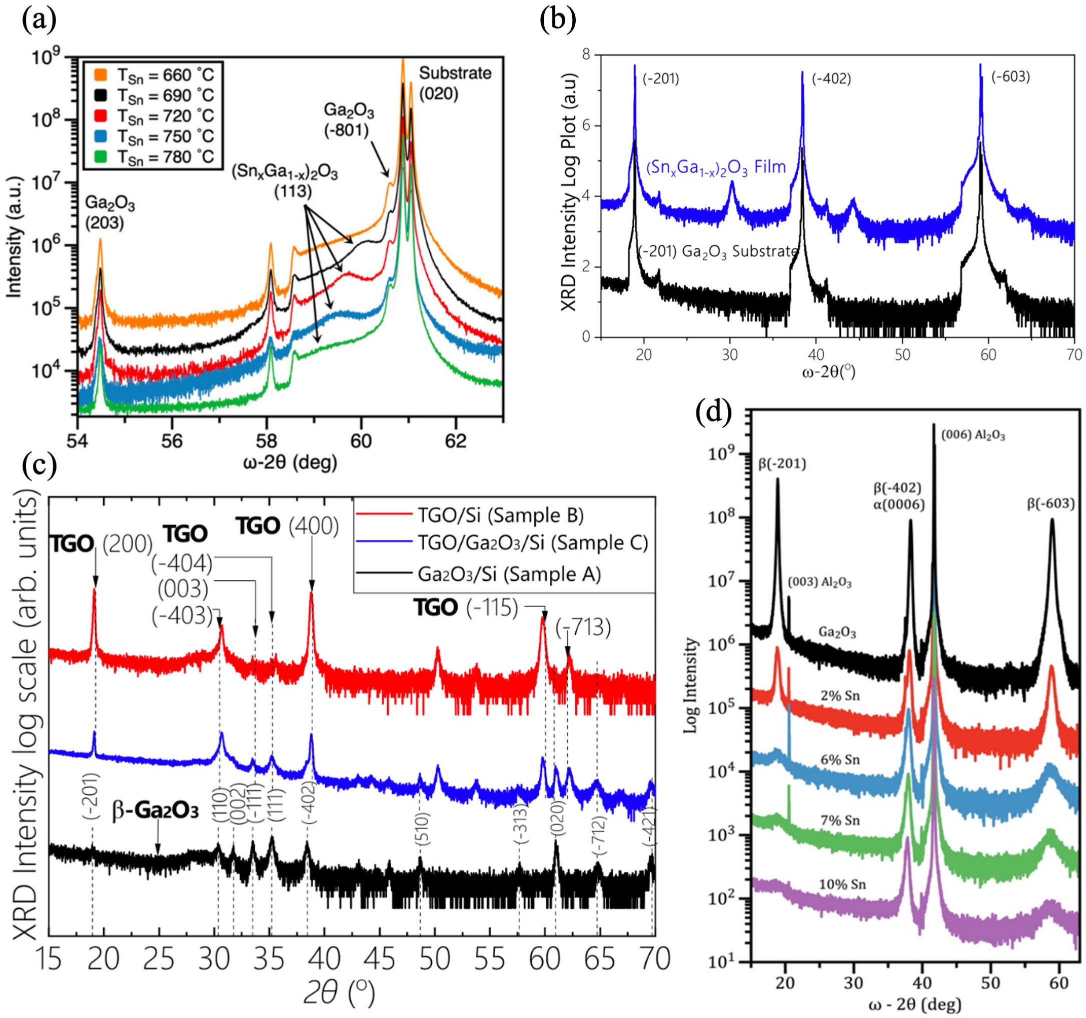

Figure 6.3: Comparative XRD intensity plots as a function of ω-2θ angle acquired for the TGO films upon each substrate: (a) TGO/(010)-Ga_2O_3, [225], (b) TGO/(-201)-Ga_2O_3 [52], (c) TGO/(111) Si [226] and (d) TGO/(0001) sapphire [216]. Figure extracted from their respective citation.

.

ω-2θ angles with increasing Sn availability/composition [225]. In 6.3(b) the peaks prominent in the TGO layers but not the (-201)-Ga_2O_3 substrate at 30.3° and 44.4° possibly identify monoclinic TGO planes [52].

The TGO samples with Si substrates are polycrystalline leading to the complex

XRD ω-2θ spectra seen in 6.3(c). The peak at approximately 37-38° is prominent for TGO layers in 6.3(b)-(d), corresponding to the (-402) β-Ga_2O_3 however for increasing Sn contents the peak shifts to lower ω-2θ angles, as described in [216]. Similar peak shifting is seen for the (113) monoclinic TGO peak between 59-60 ° in 6.3(a) [225].

Generally the TGO takes on the monoclinic crystal structure of β-Ga_2O_3 however there is evidence for the formation of other polymorphs. In 6.3(d) the height of the peaks at approximately 20° and 60° decrease with increasing Sn content while the height of the 37-38° peak is unaffected. The peak for the (-402) β-Ga_2O_3 is also adjacent/overlaps with the (0006) peak for α-Ga_2O_3 ($\theta \sim 40°$) [228]. A possible explanation for this is that that α type material may be starting to form [225] at higher Sn contents for the sapphire substrate samples , likely due to the lower growth temperature used (500 °C) [211].

Another possible explanation for the peak height modulation is the formation of κ-Ga_2O_3 which is not discussed in [225]. The presence of Sn has been shown to promote the formation of κ-phase material during epitaxial growth of Ga_2O_3 on (0001) sapphire substrates , shown to occur for low levels of Sn doping ($x \geq 0.1\%$) [229, 230]. For $(11\bar{2}0)$ sapphire substrates α-phase and mixed phase materials have occurred for higher levels of doping ($x \geq 5\%$) therefore the formation of non β-phase material here would not be unexpected [230].

To determine the Sn incorporation rate dependence on the growth conditions and material substrate the WDX composition has been plotted against the ratio of the Sn and Ga effusion cell temperatures in Figure 6.4.

Firstly, the reduced substrate temperature for the sapphire substrate samples (500 °C, inverted triangular data points) compared to the other substrates (600 °C) results in significantly higher Sn incorporation. For MBE grown Ga_2O_3:Sn using single crystal homogeneous substrates it has been shown that there is an increase in carrier concentration for crystals grown at lower substrate temperatures (540 °C) compared to higher temperature growth (600 °C) [23]. However, the MBE Sn incorporation rate with reduced growth temperature is still disputed. Very little change in the Sn dopant concentration has been reported when the growth temperature was reduced from 700 °C to 600 °C [231]. Interestingly in the same report a significantly

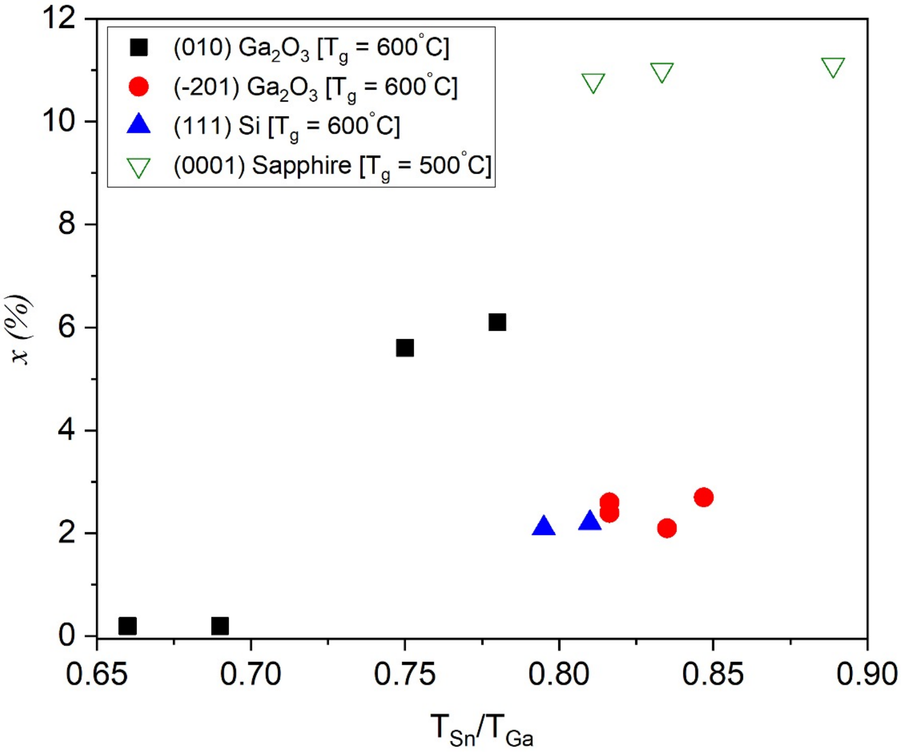

Figure 6.4: $(Sn_xGa_{1-x})_2O_3$ composition determined by WDX as a function of the temperature ratio of the Sn and Ga effusion cells during the growth process. TGO samples with different substrates are distinguished using different data points markers

.

higher Sn concentration was achieved during 800 °C growth compared to 900 °C (approximately 10×) for various levels of Sn availability. While this behaviour is seen for doping levels of Sn compared to the Sn alloying present here this could indicate there being a preferential substrate temperature of ∼500 °C or less to maximise Sn incorporation within Ga_2O_3. Further evidence for this comes from previous growth attempts at the University of Central Florida where negligible Sn incorporation was achieved at growth temperatures of 750 °C [216]. Though lower temperature growth was found to increase Sn incorporation this induced additional issues such as poorer surface morphology [232,233] and the formation of other Ga_2O_3 polymorphs [194,216] such as the evidence of α-Ga_2O_3 formation in Figure 6.3(d).

Similar Sn incorporation was found for the (201)-Ga_2O_3 Ga_2O_3 (circles) and (111) Si (filled triangles) substrate samples which share similar growth conditions (see Table 6.1) but it is noteworthy that there is a much larger level of Sn incorporation for samples with (010)-Ga_2O_3 substrates (squares) than (201) despite the lower T_{Sn}/T_{Ga} ratios during (010) growth. A similar trend has been seen for other more widely studied Ga_2O_3 alloys. For AGO films grown by MBE on (201) and (010) Ga_2O_3 substrates there was a roughly 50% uptake of Al for films grown on (201) Ga_2O_3 compared to (010) when grown under the same conditions [234]. The β-Ga_2O_3 crystal structure features two types of Ga sites, octahedral and tetrahedral which are alternatively exposed in the (201) growth direction, unlike the (010) direction which features octahedral-only stacking. It has been found that Al has a preference to substitute into the octahedral site, only integrating within the preferred site for (-201) growth [48,234,235]. The greater size of the Sn atoms compared to Ga makes the octahedral sites preferential for Sn incorporation within bulk Ga_2O_3 due to the similarity in $Ga_{\mathbf{II}} - O$ (octahedral Ga site) bond length in Ga_2O_3 (2.02 Å) to $Sn - O$ in SnO_2 (2.2 Å) [37]. The Al preference for octahedral incorporation in β-Ga_2O_3 is due to the octahedral only coordination in corundum Al_2O_3 [236]. As both Al and Sn share this preference for octahedral incorporation it is therefore unexpected to see the greater Sn incorporation levels for (010) oriented growth compared to (-201) as seen here.

There appears to be a correlation between the Sn uptake and film thickness with the thinnest films displaying the largest alloy concentration (see Table 6.1) however this is considered unrelated. An Sn composition gradient would be expected to be seen if this was the case, with the largest Sn concentration at the substrate interface which would gradually reduce as the film thickness is increased. Cross-sectional WDX mapping reveals this not to be the case as the TGO film has a near-uniform Sn profile (see further within chapter)

6.3 Optical properties

Room temperature CL spectra were acquired using a focussed electron beam with the same beam conditions as the WDX measurements for each substrate [176]. The CL signal was collected using a built in reflecting objective, focused into an optical fibre with 105 µm optical diameter which was then coupled into an Andor Shamrock 163 spectrometer with a focal length of 163 mm. The dispersed light was then detected using an Andor 1600-channel electron-multiplying charge-coupled device. The spectrometer used within these measurements was equipped with a 300 lines/mm grating blazed at 500 nm.

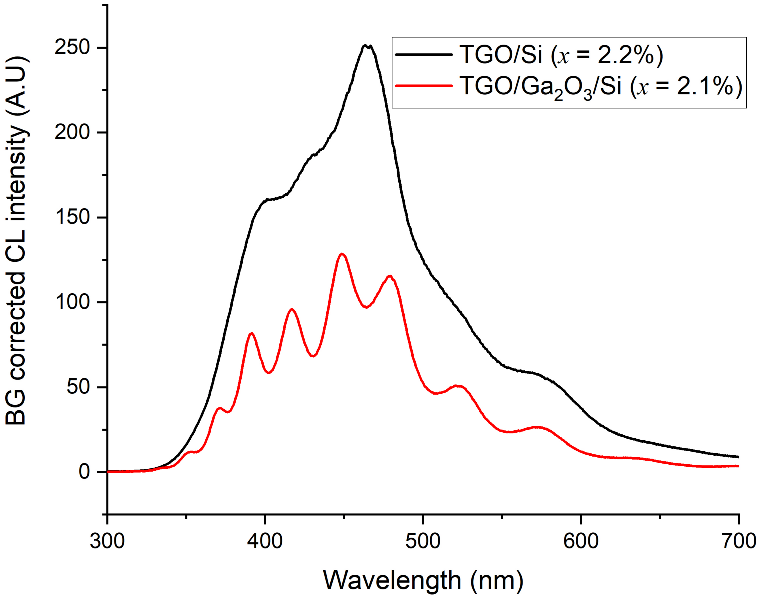

Figure 6.5: Background corrected CL intensity spectra as a function of wavelength (nm) acquired from TGO/Si and TGO/Ga_2O_3/Si samples showing Fabry-Pérot interference fringes

.

The difference between the refractive index of the Si substrate and TGO film (and Ga_2O_3 buffer) results in Fabry-Pérot interference fringes modulating the spectra, as seen in Figure 6.5. The impact of the Ga_2O_3 buffer can also been seen as the improved interface between the TGO/Ga_2O_3 buffer and the Si substrate amplifies the height of the interference fringes present. To mitigate the effect of these fringes CL spectra were extracted from cross-sectional maps, allowing a comparison to be made across the different substrates, *see below*.

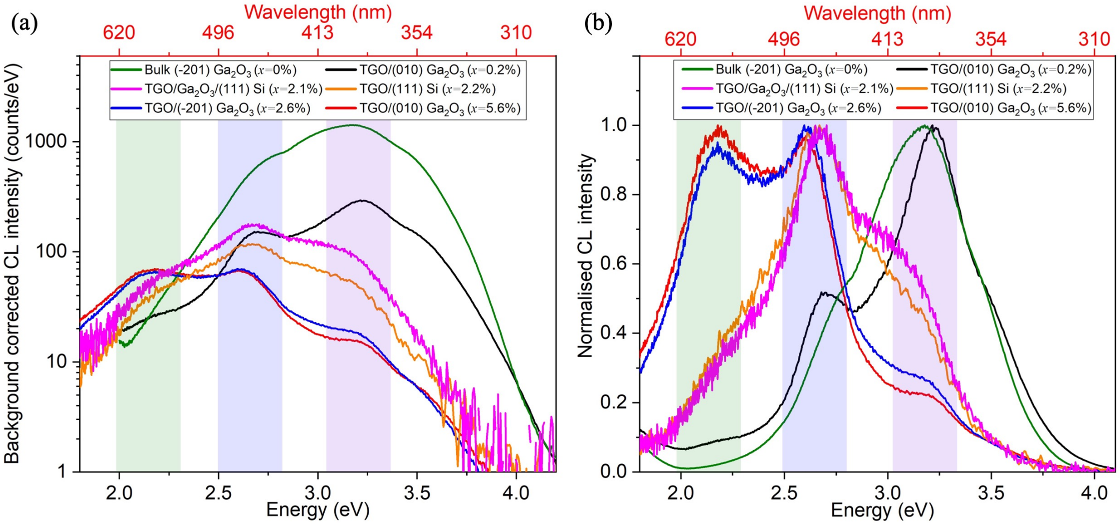

Figure 6.6: Example (a) raw and (b) normalised CL intensity as a function of energy (eV) [wavelength (nm) shown in secondary x-axis] obtained from TGO films on various substrates: TGO/(010) Ga_2O_3 with high and low Sn content, TGO/Si, TGO/Ga_2O_3/Si, TGO/(-201) Ga_2O_3 and a (-201) Ga_2O_3 bulk single crystal. Different line colours are used to identify the spectra acquired from the different samples with the sample composition shown in the Figure legend. Shading shows the approximate energy of the three mentioned spectral bands

.

Figure 6.6 shows the raw (log scale) and normalised cathodoluminescence spectra obtained from a selection of the TGO films and a Ga_2O_3 bulk single crystal. The sapphire substrate samples showed weak CL and are excluded from this figure. The magnified Sn composition of these samples being the main reason for the lack of luminescence and partially due to the reduced beam energy required for these measurements (5 keV vs. 6 keV). The samples in Figure 6.6 show three main luminescence bands, as typically seen for Ga_2O_3 luminescence: UV (3.1 eV), blue (2.7 eV) and green (2.2 eV) [200, 201]. Slight variations in the energy of these luminescence bands is expected depending on the level of Sn alloying present, *explained later in section.*

As mentioned in Chapter 5, UV emission in Ga_2O_3 is attributed to the recombination of free electrons with self-trapped holes (STHs) [56], an intrinsic defect of β-Ga_2O_3 due to the non-fully bonding of oxygen on one of the three distinct oxygen binding sites in the β-Ga_2O_3 [55]. DAP recombination involving V_O and V_{Ga} is responsible for blue emission [201] and green emission is attributed to defect luminescence involving extrinsic impurities (e.g Sn, Si and Be) [202, 203].

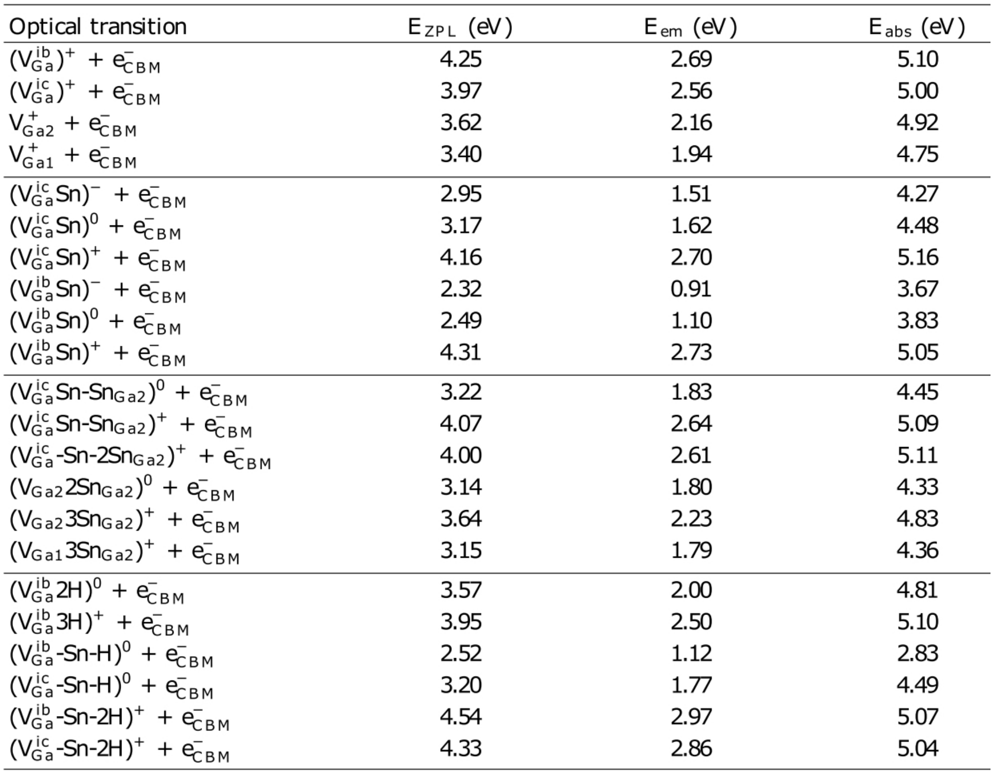

Optical transition	E_{ZPL} (eV)	E_{em} (eV)	E_{abs} (eV)
$(V_{Ga}^{ib})^{+} + e_{CBM}^{-}$	4.25	2.69	5.10
$(V_{Ga}^{ic})^{+} + e_{CBM}^{-}$	3.97	2.56	5.00
$V_{Ga2}^{+} + e_{CBM}^{-}$	3.62	2.16	4.92
$V_{Ga1}^{+} + e_{CBM}^{-}$	3.40	1.94	4.75
$(V_{Ga}^{ic}Sn)^{-} + e_{CBM}^{-}$	2.95	1.51	4.27
$(V_{Ga}^{ic}Sn)^{0} + e_{CBM}^{-}$	3.17	1.62	4.48
$(V_{Ga}^{ic}Sn)^{+} + e_{CBM}^{-}$	4.16	2.70	5.16
$(V_{Ga}^{ib}Sn)^{-} + e_{CBM}^{-}$	2.32	0.91	3.67
$(V_{Ga}^{ib}Sn)^{0} + e_{CBM}^{-}$	2.49	1.10	3.83
$(V_{Ga}^{ib}Sn)^{+} + e_{CBM}^{-}$	4.31	2.73	5.05
$(V_{Ga}^{ic}Sn\text{-}Sn_{Ga2})^{0} + e_{CBM}^{-}$	3.22	1.83	4.45
$(V_{Ga}^{ic}Sn\text{-}Sn_{Ga2})^{+} + e_{CBM}^{-}$	4.07	2.64	5.09
$(V_{Ga}^{ic}\text{-}Sn\text{-}2Sn_{Ga2})^{+} + e_{CBM}^{-}$	4.00	2.61	5.11
$(V_{Ga2}2Sn_{Ga2})^{0} + e_{CBM}^{-}$	3.14	1.80	4.33
$(V_{Ga2}3Sn_{Ga2})^{+} + e_{CBM}^{-}$	3.64	2.23	4.83
$(V_{Ga1}3Sn_{Ga2})^{+} + e_{CBM}^{-}$	3.15	1.79	4.36
$(V_{Ga}^{ib}2H)^{0} + e_{CBM}^{-}$	3.57	2.00	4.81
$(V_{Ga}^{ib}3H)^{+} + e_{CBM}^{-}$	3.95	2.50	5.10
$(V_{Ga}^{ib}\text{-}Sn\text{-}H)^{0} + e_{CBM}^{-}$	2.52	1.12	2.83
$(V_{Ga}^{ic}\text{-}Sn\text{-}H)^{0} + e_{CBM}^{-}$	3.20	1.77	4.49
$(V_{Ga}^{ib}\text{-}Sn\text{-}2H)^{+} + e_{CBM}^{-}$	4.54	2.97	5.07
$(V_{Ga}^{ic}\text{-}Sn\text{-}2H)^{+} + e_{CBM}^{-}$	4.33	2.86	5.04

Figure 6.7: Emission energies of V_{Ga} defects with Sn and H complexes copied from [52]. “CC model parameters for V_{Ga} complexed with Sn and H donors, including ZPL energy (E_{ZPL}), classical emission (E_{em}) and absorption (E_{abs}) energies. Obtained from HSE(0.33,0.20) dv calculations.”

.

In Figure 6.6(a) there is a clear decrease in the overall luminescence intensity of the thin films as the level of Sn alloying level is increased, with the greatest intensity being for the pure Ga_2O_3 substrate and weakest for TGO where $x = 5.6\%$. The gradual decrease in intensity with increasing Sn concentration implies that structural dislocations or defect levels lying within the bandgap, either directly from the incorporation of Sn or induced through the alloying have increased the number of non-radiative recombination pathways present within the semiconductor. Also accompanying the decrease in overall intensity is a modulation of the peak intensities for the three aforementioned spectral bands, this is more clearly seen in the normalised CL data in Figure 6.6(b).

Initial observations from Figure 6.6(b) show that for TGO films the peak luminescence occurs within the blue spectral region compared to the UV for Ga_2O_3. The quenching of the UV luminescence within the TGO films implies that DAP recombination is now the dominant recombination mechanism. The enhancement of the blue emission suggests the increased presence of V_{Ga} induced through the Sn alloying. As the green emission is strictly found within the films with a considerable level of Sn alloying this indicates that the emission is related to the addition of Sn, potentially through vacancy complexes involving Sn or the greater V_{Ga} density induced through alloying.

Hybrid functional calculations have identified that the formation of Sn based defects within β-Ga_2O_3 result in optical transitions between free electrons and V_{Ga} and $V_{Ga} - \mathrm{Sn}$ complexes which have emission energies within these spectral ranges, the results of these calculations have been reproduced from Ref. [52] and are shown in Figure 6.7.

Density-functional theory (DFT) is a highly useful computation technique used to establish the fundamental properties of semiconductor materials. DFT has been shown to be highly accurate, in good agreement with experimentally derived results [29,41] and is therefore the standard method used for theoretically analysing defects within semiconductor materials [179]. The hybrid functionals used by Varley to calculate the results in 6.7 are a form of DFT particularly useful in determining the electronic properties of wide bandgap semiconductors where there are shortcomings of general DFT [30]. These quantum mechanical calculations are used to understand the electronic structure of a material from first principles; determining the local quantum mechanical interactions between the electrons present within a crystal using only the atomic configuration and no prior knowledge of the material properties. From these calculations a number of crystallographic and structural properties can be then be extracted e.g band structure (Figure 2.3), lattice constants, defect formation energies [237].

From these calculations the specific defects/complexes attributed to the blue emission from the TGO films involve free electron recombination with a hole located on the V_{Ga}^{ib} or V_{Ga}^{ic} interstitial Ga sites resulting in emission energies of 2.69 eV and 2.56 eV respectively. Recombination transitions involving the Sn complexes with these interstitial Ga sites, $(V_{Ga}^{ib}\mathrm{Sn})^{+}$ and $(V_{Ga}^{ic}\mathrm{Sn})^{+}$ also lie within the broad blue emission range, with emission energies of 2.73 eV and 2.70 eV respectively [52]. These interstitial vacancies relate to the “split/half” Ga vacancy where a Ga atom neighbouring a V_{Ga} relaxes into an intermediate interstitial site between the vacancy and the original atomic site [53]. Here the V_{Ga}^{ib} & V_{Ga}^{ic} refer to two of the five possible interstitial relaxation sites [54]. Mechanisms responsible for the green emission may be the recombination of free electrons with holes trapped within the $\mathrm{V}_{Ga(\mathrm{II})}$ (octahedral Ga vacancy) or the $(\mathrm{V}_{Ga(\mathrm{II})}3\mathrm{Sn})^{+}$ complex with emission energies of 2.16 eV and 2.23 eV respectively.

The increasing intensity of the blue and green luminescence with increasing Sn content in the CL measurements (Figure 6.6) also reinforces that the defects identified by the DFT calculations in Figure 6.7 are the likely sources of these optical bands. The possible sources of blue emission identified by the DFT calculations are all related to V_{Ga}, correlating well with the onset and increasing strength of blue emission with increasing Sn levels of alloying, known to increase the V_{Ga} density and possibly promote the formation of split interstitials [54]. In Figure 6.6(b) the strongest green emission is found for the TGO samples with the highest level of Sn alloying (x = 2.6 - 5.6%) compared to the weaker emission for lower levels of alloying (x = 0 - 2.2%) also agreeing with the DFT results showing the $(\mathrm{V}_{Ga(\mathrm{II})}3\mathrm{Sn})^{+}$ complex is a likely defect responsible for this emission.

Despite the strong correlation between computational and experimental work (in both an energy and intensity aspect) there may be other possible explanations for the green emission such as: STH emission occurring from STHs within SnO_2, with an emission energy calculated to be 2.27 eV [56]; transitions involving oxygen interstitials (O_i) [238, 239] with the O_i density greatly increased through the Sn alloying or by transitions directly involving the Sn atoms [240]. For the level of alloying in the relevant samples we would expect Sn to directly substitute for Ga in the Ga_2O_3 lattice avoiding the formation of SnO_2 so the STH emission process would be an unlikely explanation for green emission in the TGO films. The green luminescence in other wide bandgap oxide semiconductors such ZnO has also been attributed to cation vacancy defect transitions, such as V_{Zn}, agreeing with the conclusions here but as stated, similarly to Ga_2O there may be multiple sources/factors for this luminescence [241, 242].

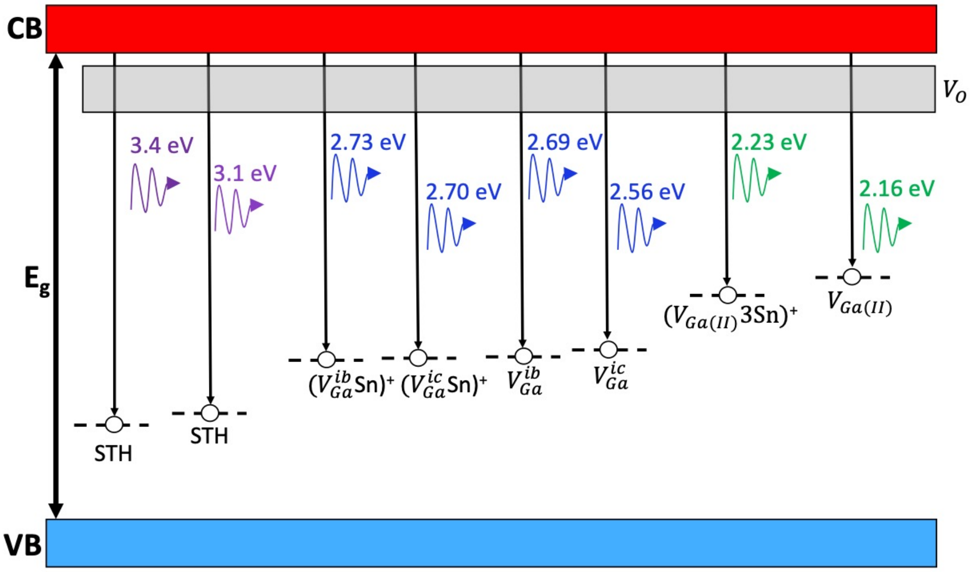

Figure 6.8: Energy level diagram for TGO using the results shown in Figure 6.7. Figure has also been adapted based on the work of [53, 243]

.

Using the results of the hybrid functional DFT calculations shown in Figure 6.7 and the work of [53,243] an energy level diagram of TGO has been constructed and is shown in Figure 6.8. In Figure 6.8 transitions producing UV emission corresponding to electron recombination with the two STH sites in the β-Ga_2O_3 crystal are shown as 3.4 eV and 3.1 eV with the energy quoted for these transitions coming from published results [53]. In the spectra shown in Figure 6.6, the 3.1 eV transition is the source of the prominent UV emission, the higher energy 3.4 eV is partially seen as a shoulder on the green and black spectra.

Possible sources of blue and green emission identified through the DFT calculations are also shown, where a combination of these may result in the broad band spectra of Figure 6.6. A broad V_O donor band is also shown which may be involved with DAP recombination mechanisms classically described as contributing to the blue and green emission in Ga_2O_3. Note that in Figure 6.6 there is no direct band-to-band recombination in Ga_2O_3, hence there is no NBE emission corresponding to the TGO bandgap as there was for the $Al_xGa_{1-x}N$ samples in Chapter 4.

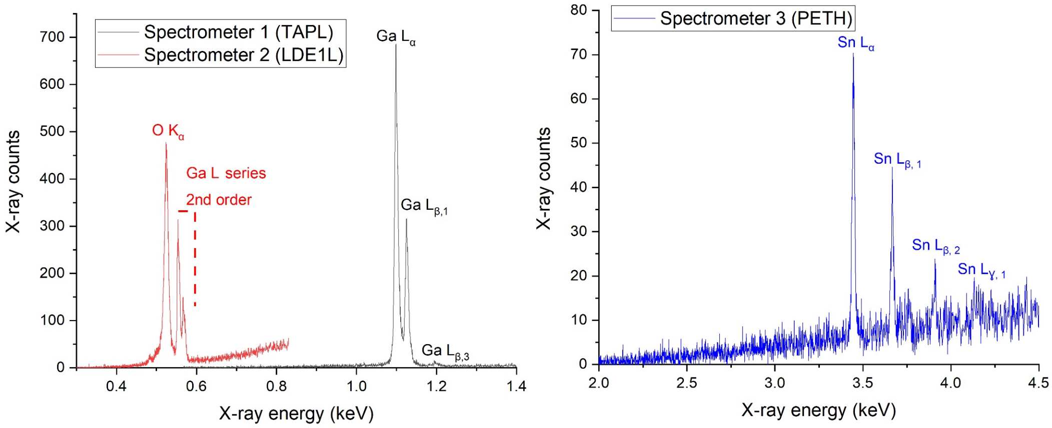

Figure 6.9: Example qualitative WDX scans showing X-ray counts as a function of X-ray energy. Spectra acquired from a TGO film and identify key elements of Sn, Ga and O are present with no detectable trace elements.

.

Trace element WDX scans did not identify any bulk impurity elements that may be responsible for the observed emission, an example of this is shown in Figure 6.9.

To further correlate the optical behaviour with the incorporation of Sn combined WDX and CL cross sectional mapping was performed, with both signals simultane-

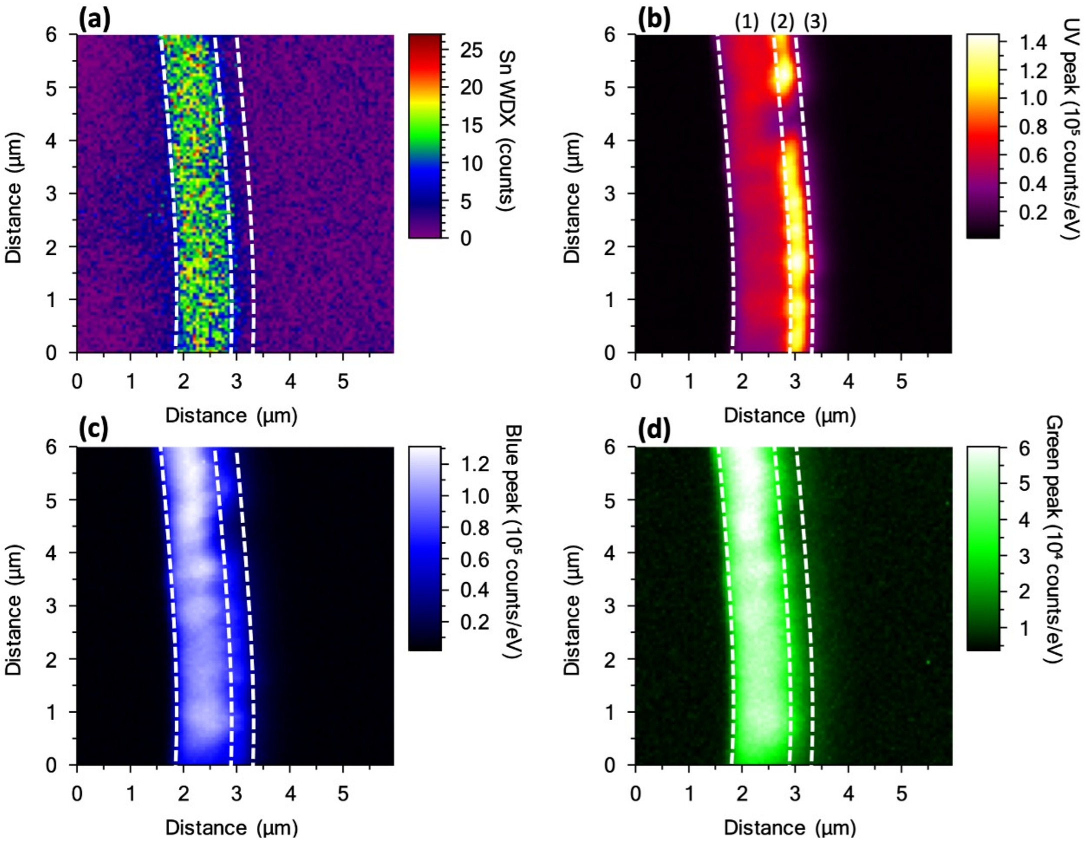

Figure 6.10: Cross sectional joint WDX and CL maps (100 × 100 pixel, 60μm × 60μm) taken from the TGO/Ga_2O_3/Si sample (x = 2.1%). (a) Sn L_α X-ray counts, (b-d) peak intensity maps of three spectral regions, specifically (b) UV [2.9-3.3 eV], (c) blue [2.6-2.8 eV] and (d) green [2.1-2.4 eV]. Spectral intensity at each pixel are shown in the colourbar of each Figure

.

ously acquired in one scan. A CL hyperspectral image was collected and monochromatic CL maps were extracted from this dataset. Figure 6.10 shows the results from the mapping measurements on the TGO/Ga_2O_3/Si sample with Sn=2.1%. The thin Ga_2O_3 buffer layer was added to improve the surface quality of the sample (as seen in Figure 6.2) and was found to have a minimal effect on the Sn incorporation rate [226]. Figure 6.10(a) shows a WDX map recording the Sn L_α X-ray counts and 6.10(b)–(d) show the CL maps for the three main spectral bands mentioned previously; (b) UV [2.9–3.3 eV], (c) blue [2.6–2.8 eV] and (d) green [2.1–2.4 eV]. Broad energy ranges are used to account for the redshifting of the peak energies with respect to Ga_2O_3 (*explained further in the chapter*). The three sections of the material are marked above Figure 4(b); (1) = 2.1% TGO, (2) Ga_2O_3 buffer and (3) Si.

Firstly, it can be seen in Figure 6.10(a) that the Sn L_α X-ray counts are exclusive to a thin film ($\approx$1.25μm) corresponding to region (1) in Figure 6.10(b). The Ga_2O_3 buffer layer [region (2)] cannot be seen in 6.10(a) but is clearly seen in 4(b) and (c) where the sample cross section is noticeably thicker than in 4(a). CL intensity variations between the two layers also help identify the distinct regions of the cross section. The Si substrate is present in region (3) but is not highlighted by the signals used in this figure. The UV emission shown in 4(b) can be separated into two distinct zones: a bright UV peak in the Ga_2O_3 buffer layer (2×10^4 counts) and a diminished emission within the TGO film (1×10^4 counts). Figure 6.10(c) shows the inverse of (b) with the brightest blue emission occurring in the TGO layer (2×10^4 counts) while the Ga_2O_3 displays a reduced intensity (0.5×10^4 counts). This reinforces the observation that the UV quenching and blue enhancement seen in Figure 6.6 are due to the Sn alloying. The green emission seen within the TGO films is shown to be all but eliminated within the Ga_2O_3 buffer layer, shown in 6.10(d). The observation that the green emission is confined to the TGO film agrees with published studies stating that green emission was only present in Ga_2O_3 films containing impurities such as Sn [202, 240]. This helps reinforce the claims here that the green emission originates from DAP recombination involving holes trapped at alloying induced gallium vacancies, V_{Ga}, or recombination involving Sn related complexes.

This measurement was replicated for the TGO/(-201)-Ga_2O_3 sample for x = 2.7% as seen in Figure 6.11. In this case, region (1) corresponds to the TGO film and region (2) is the (-201) Ga_2O_3 substrate with the regions identified above 6.11(b). The behaviour seen here replicates that of Figure 6.10 for the UV emission (Figure 6.11(b)) though to a greater extent as the UV luminescence is nearly completely suppressed within the high Sn region identified in Figure 6.11(a).

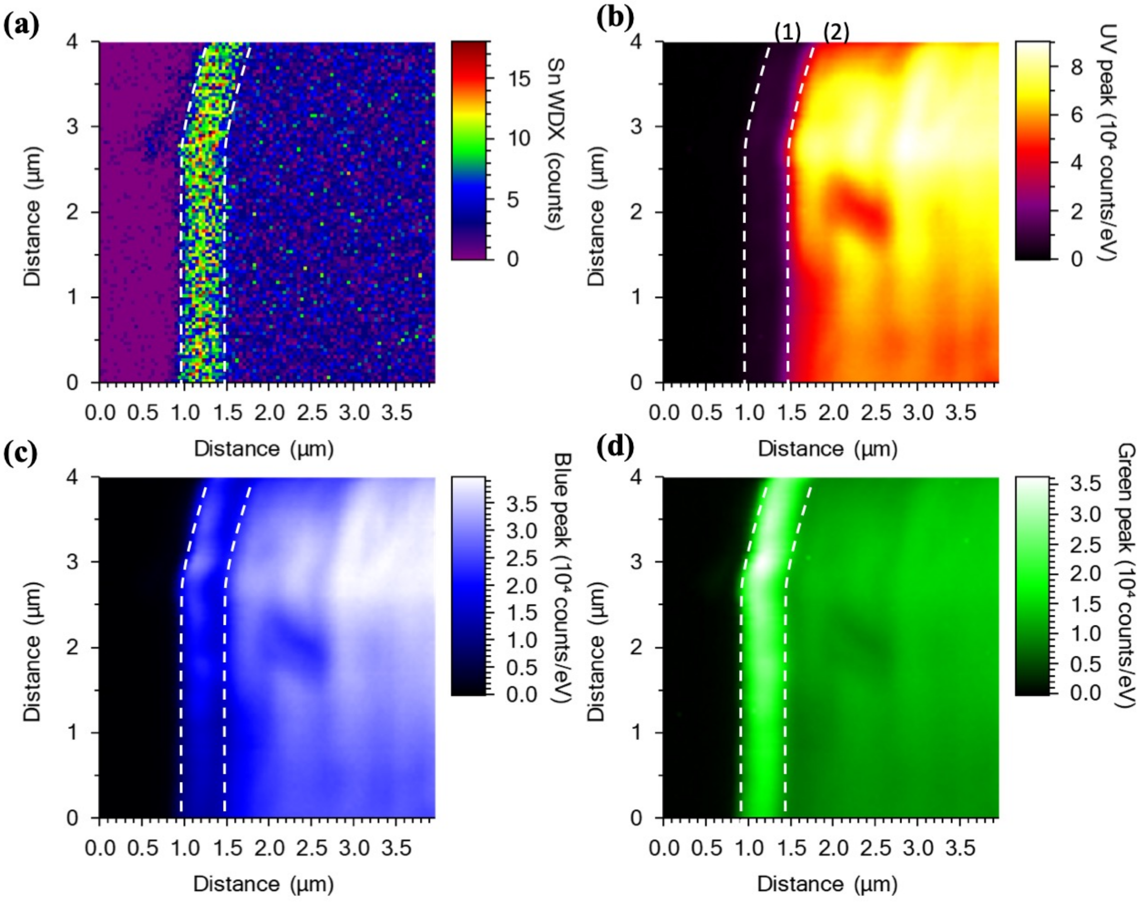

Figure 6.11: Cross sectional joint WDX and CL maps (100 × 100 pixel, 40μm × 40μm acquired from the TGO/(-201)-Ga_2O_3 sample (x =2.7%). (a) Sn L_α X-ray counts, (b-d) peak intensity maps of three spectral regions, specifically (b) UV [2.9-3.3 eV], (c) blue [2.6-2.8 eV] and (d) green [2.1-2.4 eV]. Spectral intensity at each pixel are shown in the colourbar of each Figure

.

The blue luminescence in Figure 6.11(c) differs from the previous example where blue luminescence was enhanced in the TGO layer compared to the Ga_2O_3 buffer. Here the luminescence levels are comparable at the film-substrate boundary but strong blue luminescence is seen within the (-201)-Ga_2O_3 substrate. As the CL point measurements taken from the TGO sample and (-201)-Ga_2O_3 substrate (Figure 6.6) show much stronger blue emission in the TGO film compared to the substrate the behaviour in Figure 6.11(c) is likely an experimental issue. The most likely explanation is due to an uneven surface due to the fracturing of the sample to make the cross-section, emphasising the luminescence intensity in the (-201)-Ga_2O_3 substrate. Areas of high blue intensity in region (2) of Figure 6.11(c) also correspond to high intensity areas in Figures 6.11(b) and (d) reinforcing that this is an optical focusing issue rather than an effect of the Sn alloying.

The behaviour in Figure 6.11(d) again agrees with both Figure 6.10 and the CL point spectra in Figure 6.6 with the greatest intensity of green emission being in the TGO film due to the greater density of V_{Ga} and Sn complexes.

As mentioned earlier when referring to Figure 6.10 there is a redshifting of the peak wavelength of the three main spectral bands mentioned above alongside the UV luminescence suppression (blue and green enhancement) with increasing Sn content. Figure 6.12 plots the wavelength of the deconvolved peak energy for the UV, blue and green luminescence peaks against the Sn content determined by WDX. Within each band there is a clear redshifting of the peak, with an Sn content of $\approx$6% inducing a redshift of 0.13 eV for the blue (Figure 6.12(b)) and 0.1 eV for the green, Figure 6.12(c). Due to the lack of green luminescence in Ga_2O_3 there are no data points where Sn=0% and the redshift is based off the peak energy where Sn $\approx$0.2%. The shift in UV luminescence, plotted in Figure 6.12(a), is nonlinear with lower Sn contents ($\approx$2%) inducing an approximate redshift of 0.2 eV and no further shift for further Sn incorporation ($\geq$6%). This nonlinear shift for the UV band could be due to interfering UV emission from an underlying Ga_2O_3 layer (either a buffer layer or the Ga_2O_3 substrates). The two sources of UV emission overlap within the CL spectra (see Figure 6.6) and cannot be individually deconvolved so that the peak energy is then taken from the broadened UV peak and may not identify the 'true' redshifted TGO UV emission. Again, as mentioned in Chapter 5, peak centroid shifts due to intensity modulations may be a contributing factor [210] to the luminescence shifts.

The mechanism causing the redshift of these emission bands can't be determined with definite certainty, but multiple factors may be responsible. The reduction of

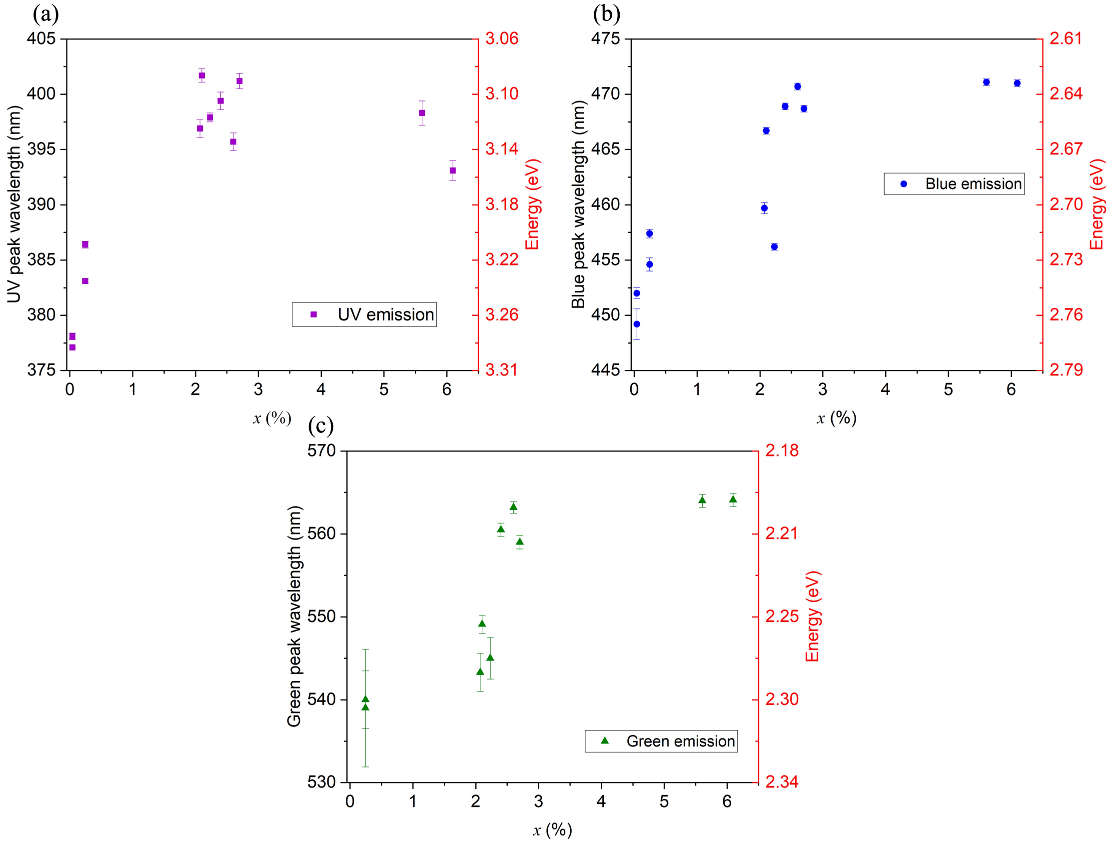

Figure 6.12: Deconvolved emission peak wavelength (nm) (energy (eV) on secondary y-axis, RHS) from CL measurements as a function of Sn composition (x) determined by WDX for the three main luminescence bands of: Ga_2O_3(a) UV (purple square data markers), (b) blue (blue circles) and (c) green (green triangles)

.

the semiconductor bandgap due to the Sn alloying is the most probable reason for this shift [219]. The formation of non-β-TGO films is also possible, such as α-type material, evident in the XRD traces seen in Figure 6.3(d). However, the occurrence of these polymorphs cannot be identified through the other analytical techniques used here. Strain induced by the lattice mismatch is also likely to affect this redshift with a different contribution expected for each substrate. A negligible effect would be expected for the TGO films grown on native Ga_2O_3 substrates, Ga_2O_3/sapphire samples have previously been shown to have slight compressive strain [244] however as other polymorphs may be present in the TGO/sapphire films this cannot be confirmed definitively. To confirm the shifting of the bandgap UV-vis transmission spectroscopy measurements were performed on the TGO/sapphire substrate samples.

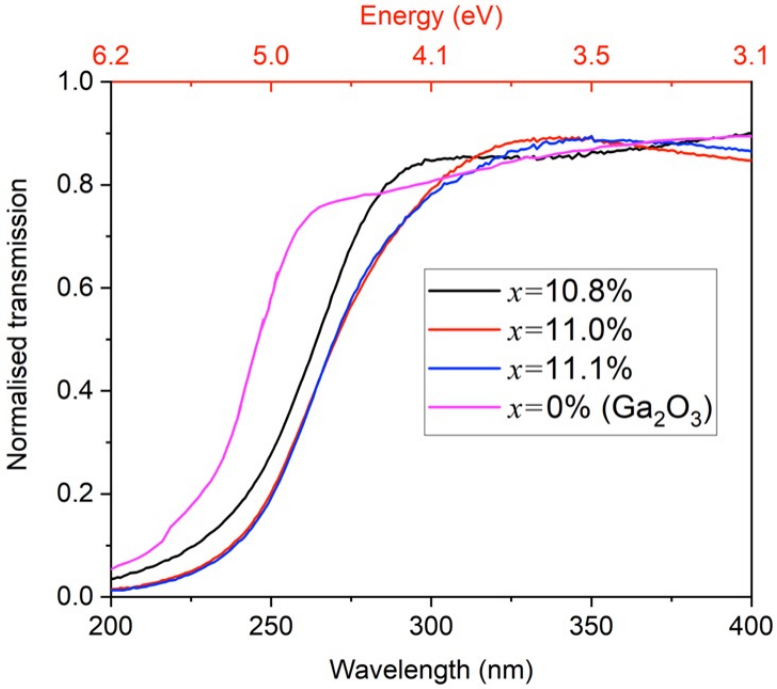

Figure 6.13: Normalised optical transmittance (%) as a function of wavelength (nm) acquired from TGO/sapphire samples indicating the shift in optical bandgap. MBE grown Ga_2O_3/sapphire reference sample from [216] is shown to indicate the total shift in bandgap due to the In alloying. Different line colours used to identify the different samples with the Sn composition quoted in the Figure legend.

.

Figure 6.13 shows the optical transmission curves from the three TGO/sapphire samples and a Ga_2O_3/sapphire reference sample. As expected, the transmission cut-off edge for the sample with the lowest Sn content (x =10.8%) is at the lowest wavelength which is then redshifted for the samples with increased levels of Sn. The optical bandgap of these samples has been estimated using the midpoint of the transmission edge, resulting in an optical bandgap of 4.78 eV for x =10.8% and 4.69 eV for x =11.0% and x =11.1%, corresponding to shifts of -0.3eV and -0.39eV compared to the 0% sample, with the optical bandgap reduced due to the Sn alloying in all cases. The bandgap shifts here are greater than that expected for this level of Sn alloying [223] but do not consider the impact of band bowing which may increase the magnitude of the shift. However, as previously mentioned, XRD measurements performed on these samples indicate the possibility that α- or κ-phase Ga_2O_3 is beginning to form, see Figure 6.3. As α-Ga_2O_3 and κ-Ga_2O_3 have a larger bandgap than β-Ga_2O_3 (≈5.1-5.3 eV [21] and ≈4.9 eV respectively [229]) the total magnitude of the shift observed may be magnified if these polymorphs have formed.

6.4 Device properties

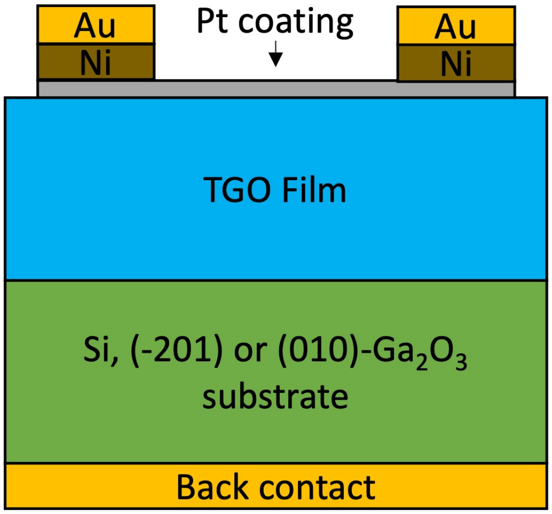

Figure 6.14: Schematic of vertical Schottky barrier photodetector manufactured from TGO thin films

In order to assess the viability and performance of the TGO films as solar-blind photodetectors the films analysed here were manufactured into vertical Schottky barrier devices (disregarding the sapphire substrate samples), see Chapter 2.3. A schematic of the device architecture is shown in Figure 6.14. The specific device fabrication details for each substrate may be found in their respective publications [52, 225, 226]. The back contact of the device was either a Ti/Al/Ni (20/100/50 nm) or Ti/Au (20/100 nm) ohmic back contact depending on which TGO/substrate was being fabricated. The thin Pt coating ($\approx$ 3nm) acted as the Schottky barrier ($\theta \sim$5.5 eV [226]) in the device while still allowing adequate transmission of the UV light. All the device fabrication and measurements in this chapter were completed by Dr Isa Hatipoglu or Dr Partha Mukhopadhyay at the University of Central Florida.

The spectral responsivity of the devices was measured to determine the impact of the Sn on the wavelength/energy of the peak responsivity and the the dependence of Sn on the absolute value of the responsivity. The results of these measurements are shown in Figure 6.15 where (a) corresponds to the TGO/Si substrate samples (and a Ga_2O_3/Si reference), (b) TGO/(010)-Ga_2O_3 and (c) TGO/(-201)-Ga_2O_3.

A clear observation in Figure 6.15 across all material substrates is the redshifting of the peak responsivity energy with increasing Sn content. This is seen with respect to the Ga_2O_3 ($x \approx 0\%$) reference samples in 6.15(a) and (b) and within 6.15(b) and (c) for samples with different levels of Sn alloying. This is consistent with the previous transmission spectroscopy results (Figure 6.13) and agrees with the shifts in CL spectral peaks (Figure 6.12). The dependence of the peak responsivity wavelength shift increases with Sn content for each substrate as shown in 6.15(d) with the Sn alloying having a greater effect on the TGO photodetectors based on Si or (-201)-Ga_2O_3 substrates compared to a much reduced impact on the TGO/(010)-Ga_2O_3 devices.

In order to examine how the magnitude of the redshift in the CL peaks compares to the shift in peak responsivities of the TGO photodetectors the two are plotted together in Figure 6.16. Again as seen in Figure 6.6 and 6.12 there is a clear redshifting in the peak responsivity of TGO photodetectors with light Sn alloying ($x =$ 0.02 - 0.06; red, black and blue spectra, circle markers) compared to a photodetector with minimal Sn content ($x < 0.01$, green spectra, circle markers). While the CL peaks tended to redshift further with increasing Sn content, outwith the substrate grouping, the redshift in peak responsivity shows no clear dependence on the TGO

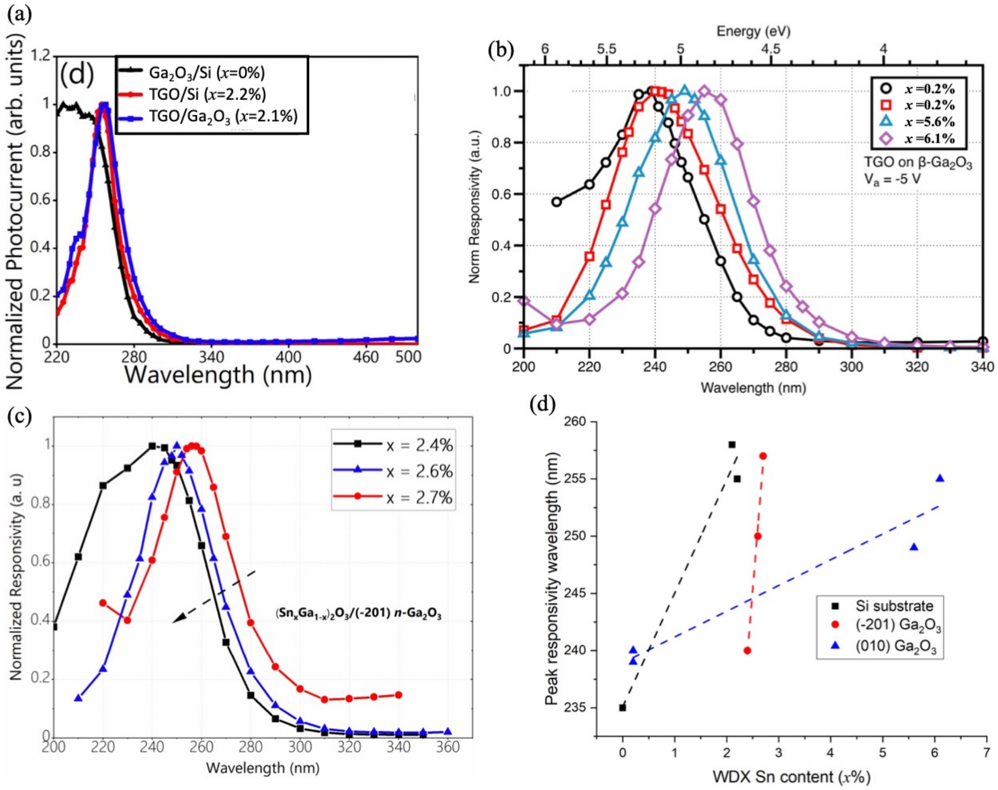

Figure 6.15: Normalised spectral responsivity of TGO photodetectors as a function of wavelength (nm) measured with bias of -5V. Results are grouped by the substrate of the TGO film: (a) Si [226], (b) (010)-Ga_2O_3 [225] and (c) (-201)-Ga_2O_3 [52]. Figures extracted/adapted from their respective citations. (d) shows the peak responsivity wavelength value (nm) as a function of Sn composition (x). The different data markers/colours identify the different samples in (a)-(c) and the different material substrates in (d). The dashed lines in (d) are guides for the eye.

Sn content other than the immediate redshift due to the light Sn alloying. If Ga_2O_3 (and TGO) exhibited direct band-to-band recombination, the NBE would be expect to show similar behaviour to the photodetector peak responsivity wavelength. However, a more obvious dependency on the Sn composition and energy comparable to the TGO bandgap would be expected for NBE emission.

The approximate shift in the peak responsivity wavelength for the TGO/Si ($x =$

Substrate	**Sn Content (x%)**	**Peak responsivity wavelength (nm)**	**Peak responsivity (A/W)**
(111) Si	0.0	235	27.4
(111) Si	2.1	258	263
(111) Si	2.2	255	2011
(-201) Ga_2O_3	2.4	240	9995
(-201) Ga_2O_3	2.6	250	35510
(-201) Ga_2O_3	2.7	257	1731
(010) Ga_2O_3	0.2	239	67
(010) Ga_2O_3	0.2	240	49
(010) Ga_2O_3	5.6	249	83
(010) Ga_2O_3	6.1	255	194

Table 6.2: Summary of responsivity measurements taken on TGO and Ga_2O_3/Si photodetectors at a bias of -5V

0.021), TGO/(-201) Ga_2O_3 ($x = 0.027$) and TGO/(010) Ga_2O_3 ($x = 0.056$) compared to the TGO/(010) Ga_2O_3 ($x = 0.002$) photodetector was calculated to be 0.38 eV, 0.36 eV, 0.21 eV respectively. The magnitude of these shifts is considerably greater than the redshifts observed for the CL peaks in Figure 6.12 and comparable to the bandgap shifts calculated from the transmission spectroscopy measurements in 6.13 however there is a lesser level of Sn alloying present in the photodetector samples compared to the sapphire samples. As mentioned previously and seen in Figure 6.15 the substrate of the TGO photodetector appears to influence the peak responsivity wavelength. This may also be reflected in the CL peak shifts, reducing the magnitude of the redshift for the high Sn TGO/(010) Ga_2O_3 samples (x=0.056 & 0.061) where a more comparable shift to the reduced bandgap may be observed.

It is notable that it is the high Sn TGO/(010) Ga_2O_3 samples (x=0.056 & 0.061) where the peak responsivity wavelength shows a weaker dependence on Sn content and the CL peak shifts observed in Figure 6.12 are of approximately the same magnitude as the TGO/(-201) Ga_2O_3 samples where $x \approx$0.02 - 0.03. It is unlikely that the reduced magnitude of the shifts observed for the CL and peak responsivity in the TGO/(010) Ga_2O_3 samples is coincidence and with no major differences in the growth of these samples other than the substrate it implies that the (010) Ga_2O_3

substrate influences the band structure of the TGO differently than the other substrates investigated. This may be a result of strain between the TGO and substrate or the substrate promoting the formation of non-β polymorphs masking the shifts may also be a contributing factor [229].

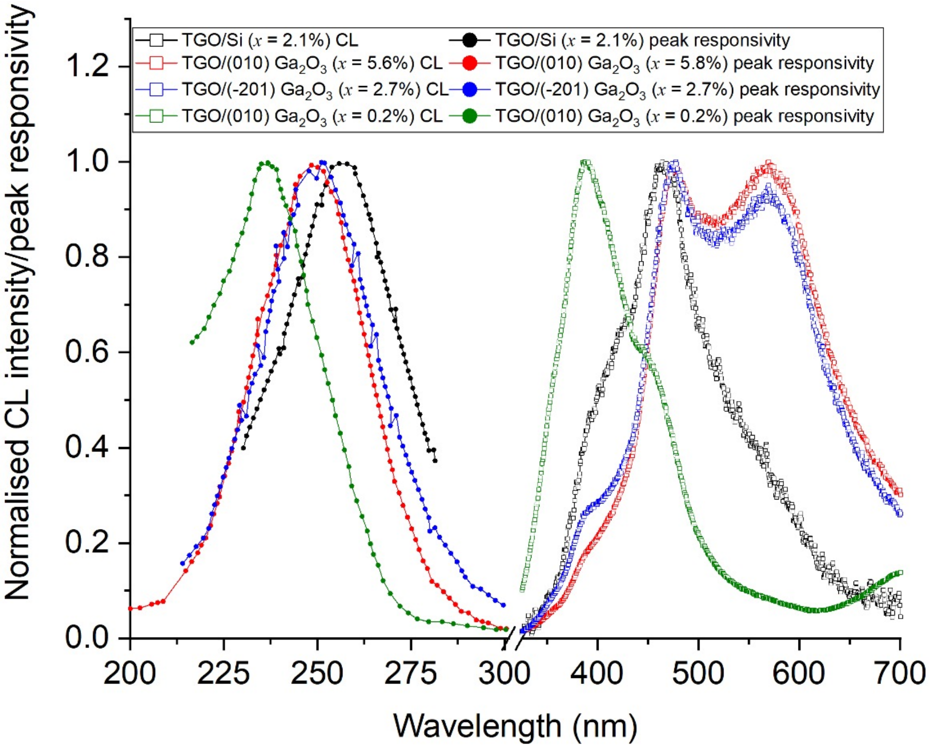

Figure 6.16: Normalised intensity/peak responsivity against the wavelength of the CL emission/peak responsivity wavelength for 4 TGO semiconductors/photodetectors. Filled circle data markers (LHS of figure) are used for the peak responsivity and hollow squares for the normalised CL spectra (RHS). Different colours of data markers are used to identify the different TGO substrates

Accompanying the shifts in peak responsivity wavelength is a enhancement of the peak responsivity magnitude, R_λ . Table 6.2 shows the peak responsivity values for each sample. For the Si substrate samples their is notable enhancement of the device responsivity with Sn alloying, increasing from 27.4 A/W for Sn content of $x = 0\%$ to a maximum of 2011 A/W when $x = 2.2\%$. Note this is for the sample without the Ga_2O_3 buffer layer. Similar behaviour is observed for (010)-Ga_2O_3 substrate samples with a muted level of enhancement, increasing from 49-67 A/W with low levels of Sn alloying $x = 0.2\%$ to a maximum of 194 A/W for the highest Sn content $x = 6.1\%$. As the measured TGO/(-201)-Ga_2O_3 substrates all feature similar Sn contents x= 2.4-2.7% it is difficult to show the level of enhancement compared to a device featuring no alloying however these samples show the highest responsivities compared to the other material substrates with a maximum of 35.5 kA/W achieved for the sample where $x = 2.6\%$. This behaviour agrees with the results of TGO metal-semiconductor-metal photodetector devices, exhibiting enhanced responsivity with increasing Sn content [216,223,224] however the peak responsivity observed for the TGO/(-201)-Ga_2O_3 devices exceeds that recorded for solar-blind photodetectors.

Another key factor in determining the quality of a photodetector is the I-V characteristics and their enhancement when under UV illumination compared to the dark current within the device. In general, the I-V curves shown in Figure 6.17 show a high degree of current enhancement under illumination. The lowest level of enhancement is found in the TGO/Si sample, with the photocurrent increasing by a factor of approximately 10 compared to the dark current, Figure 6.17(a). The enhancement for the other devices is significantly higher, despite the differing levels of dark current present the photocurrent increases by approximately 10^2-10^3 times under -5V bias as seen in Figures 6.17(b)-(d). The likely reason for the poor enhancement in the TGO/Si device is defect induced dark current from the surface roughness and nanovoids present, see Figures 6.1 & 6.2 [226].

From these measurements, critical device classifying parameters such as the gain-external quantum efficiency (gain-EQE) products (ηG) and detectivity (D^*) can be calculated. The gain-EQE allows comparison with responsivities at different peak energies while the detectivity accounts for photocurrent response and active area, with the detectivity ultimately determining the figure of merit of the photodetector.

$$\eta \mathrm{G} = \frac{hcR_\lambda}{e\lambda} \tag{6.1}$$

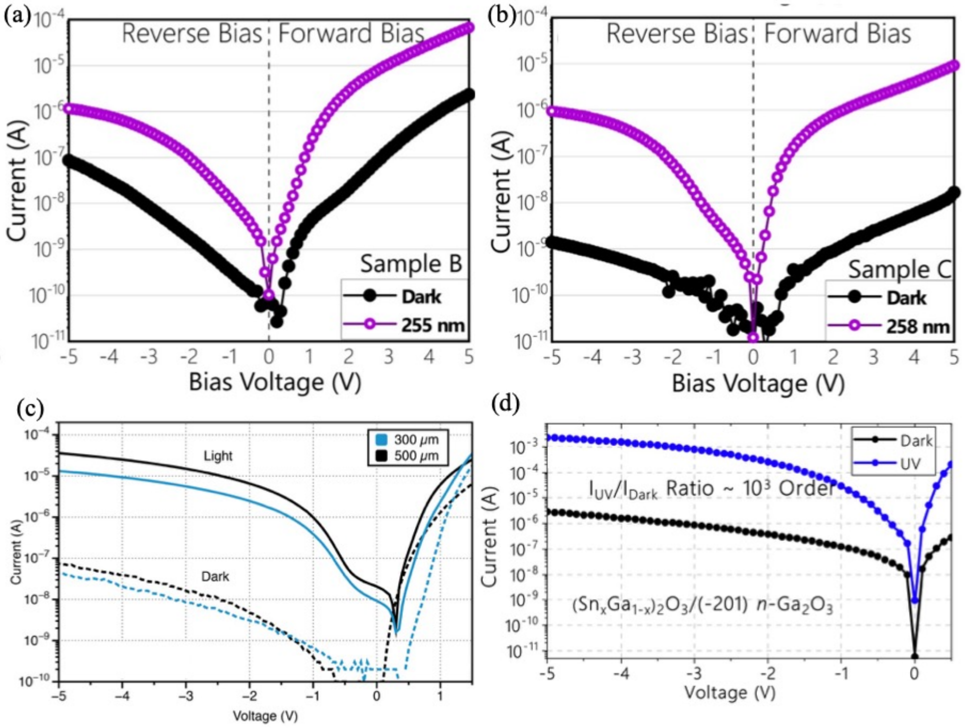

Figure 6.17: Example I-V characteristics (current (A) as a function of bias (V)) of TGO photodetectors under illumination by 30W deuterium lamp. Results are grouped by the substrate of the TGO film: (a) TGO/Si (R_λ= 2011 A/W) [226], (b) TGO/Ga_2O_3/Si (R_λ = 263 A/W) [226], (c) TGO/(010)-Ga_2O_3 [225] (R_λ = 35510 A/W) and (d) TGO/(-201)-Ga_2O_3 (R_λ = 194 A/W) [52]. Figures extracted/adapted from their respective citations.

where ηG is the gain-external quantum efficiency product, h is Planck's constant, c is the speed of light, R_λ is the peak spectral responsivity, e is the electron charge and λ the peak spectral responsivity wavelength.

$$\mathrm{D}^* = \frac{R_\lambda}{\sqrt{(2eJ_{dark})}} \tag{6.2}$$

where D* is the detectivity, R_λ is the peak spectral responsivity, e is the electron charge and J_{dark} the dark current density.

Substrate	**Sn Content ($\boldsymbol{x}$%)**	**Gain-EQE product ηG**	**Detectivity, D* (Jones, $cm\sqrt{Hz}W^{-1}$)**
(111) Si	0.0	1.51×10^{2}	6.2×10^{11}
(111) Si	2.2	9.74×10^{3}	1.11×10^{12}
(111) Si	2.1	1.27×10^{3}	1.31×10^{12}
(-201) Ga_2O_3	2.4	5.16×10^{4}	4.95×10^{12}
(-201) Ga_2O_3	2.6	1.76×10^{5}	3.30×10^{13}
(-201) Ga_2O_3	2.7	8.30×10^{3}	2.36×10^{11}

Table 6.3: Calculated gain-external quantum efficiency product and detectivity of TGO and Ga_2O_3/Si photodetectors

The values for these performance indicating parameters have been calculated for the TGO photodetectors featuring Si and (-201)-Ga_2O_3 substrates and are highlighted in Table 6.3. For the TGO detectors with a Si substrate despite the TGO/Si detector (x= 2.2%) featuring the highest peak responsivity the high dark current present results in poor detectivity and the TGO/Ga_2O_3/Si detector (x= 2.1 %) shows the greatest performance. The detectors fabricated from the TGO/(-201)-Ga_2O_3 films exhibit far greater gain-EQE product and detectivity compared to the TGO/Si samples with an ηG = 1.76×10^{5} and D* = 3.30×10^{13} calculated for the x= 2.6 % detector due to its superior peak responsivity R_λ= 3.55 kA/W.

The gain mechanism resulting in the high detector responsivity for the TGO photodetectors has been attributed to to Schottky barrier lowering due to acceptor states acting as hole traps. A schematic of this is shown in Figure 6.18. Through the Sn alloying an increased density of V_{Ga} and V_{Ga}-Sn complexes as established from the CL measurements with these defects act as hole trapping sites. As holes accumulate at these trapping sites the electric field present at the the Pt/TGO interface increases. This reduces the height of the Schottky barrier via the Schottky effect (See Chapter 2.3) increasing the rate of thermionic emission and increasing the electron tunnelling probability resulting in the increased photocurrent under UV illumination. This gain mechanism has been established with Ga_2O_3 films using proton/neutron beam irradiation to generate the deep level defects whereas here the alloying has induced the defects [245].

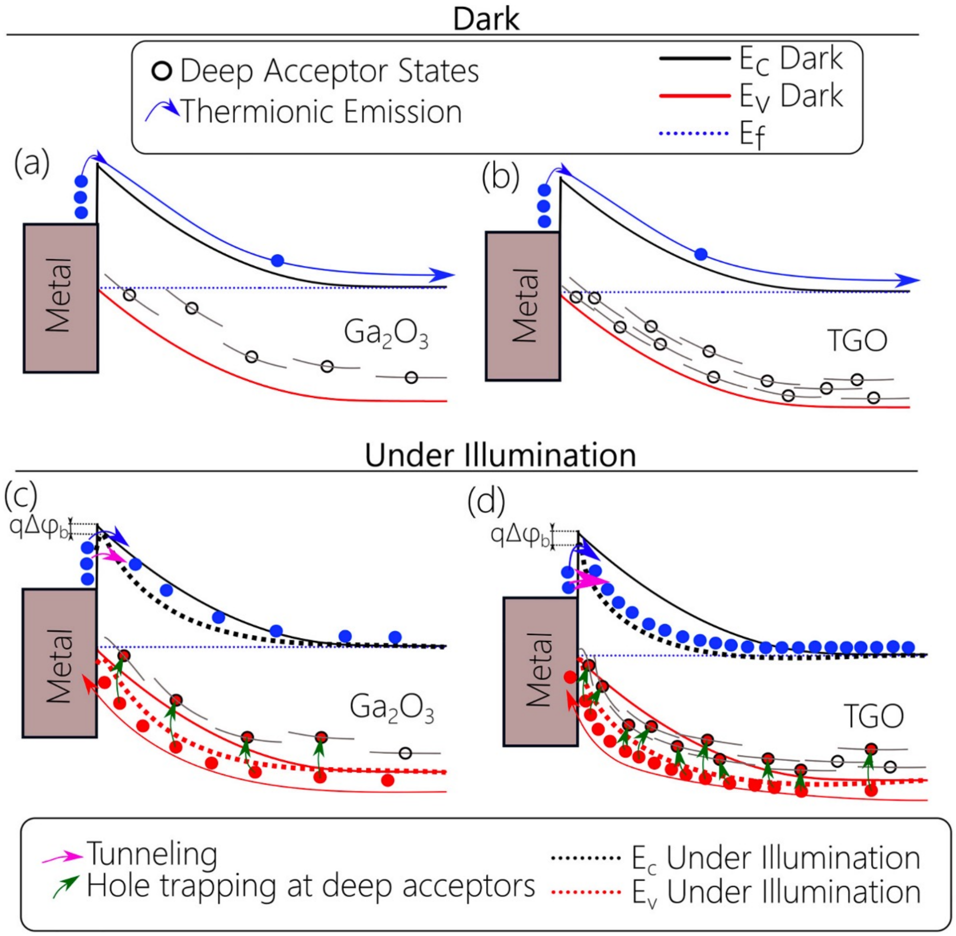

Figure 6.18: Diagram of Schottky barrier lowering and photodetector enhancement due to hole trapping. Diagram shows (a) Ga_2O_3 and (b) TGO photodetector under dark conditions with a low current from thermionic emission. UV illumination results in thermionic emission and electron tunnelling in the (c) Ga_2O_3 photodetector which is greatly enhanced in the (d) TGO photodetector due to accumulated holes [226].

Other possible explanations suggested for the high responsivity of these devices are due to impact ionization [246] and Schottky barrier lowering via self-trapped hole accumulation [247,248]. These processes are high unlikely and have been discounted as possible explanations for the high device responsivity due to the unstable nature of self-trapped holes at room temperature and the high breakdown field strength of the Ga_2O_3 based TGO films [55, 226].

6.5 Conclusion

Here a series of tin-gallium oxide thin films grown via MBE on four different material substrates have been characterised, investigating the compositional, optical and electronic properties of the semiconductors and photodetectors manufactured from the material.

WDX compositional measurements indicate that the level of Sn alloying achieved was highly dependent on Sn availability, growth temperature and the substrate choice. Lower temperature growth (500 °C vs 600 °C) produced material with a greater Sn composition evident in the TGO/sapphire films. Two Ga_2O_3 substrates with different crystal orientations, (010) and (-201), yielded TGO films with a large difference in the Sn composition despite similar growth conditions (near double Sn in (010)-Ga_2O_3 compared to (-201). This is likely due to the Sn preference to occupy octahedral Ga sites over tetrahedral within β-Ga_2O_3 and the (010) crystal orientation promoting octahedral incorporation, with similar behaviour observed for Al incorporation within aluminium-gallium oxide films grown upon the same substrates. Overall, MBE was found to be capable of growing high quality TGO thin films with Sn compositions $x \leq 0.11$.

Optical properties were determined through RT CL spectroscopy, indicating there is reduced UV and strong blue luminescence within the layers and the onset of bright green luminescence when compared to Ga_2O_3. The blue and green luminescence enhancement is attributed to an increased density of V_{Ga} induced through the Sn alloying and the formation of Sn related V_{Ga} complexes. Correlated WDX and CL hyperspectral mapping was used to confirm that the Sn incorporation was responsible for the new optical behaviour.

Accompanying the luminescence intensity modulation is an energy shift of the spectral bands within Ga_2O_3 with all three spectral bands redshifting with increasing Sn content, similarly to the IGO films in Chapter 5. This redshifting is due to bandgap lowering from the Sn alloying, confirmed through transmission spectroscopy measurements. The optical studies here confirm the ability to tune the bandgap of β-Ga_2O_3 material with SnO_2 to produce a material with a reduced bandgap similar to IGO which can then be used to produce UV-C and UV-B photodetectors.

The feasibility of photodetectors fabricated from these TGO thin films was then assessed, with the samples manufactured into vertical Schottky devices. Devices presented with superior responsivity and high gain compared to Ga_2O_3 counterparts with the greatest responsivity of R_λ= 3.55 kA/W achieved for a x= 0.026 TGO/(-201)-Ga_2O_3 device. The enhanced device performance is attributed to the high V_{Ga} and $V_{Ga}Sn$ complex densities responsible for the changes in luminescence behaviour. These defects act as hole trapping sites, reducing the height of the Schottky barrier allowing greater photocurrent under UV illumination.

The results of this investigation present in this chapter show not only that it is possible with careful control over the growth conditions and substrate choice to produce tin-gallium oxide materials of various compositions but also show the benefits that these materials may have when applied with UV optical devices. By manipulating the Sn content and therefore the acceptor defect density in the semiconductor films it is possible to create UV-C and UV-B photodetectors operating at a tuneable peak energy with superior device performance than that capable with unalloyed Ga_2O_3 devices.

Chapter 7

Impact of X-ray secondary fluorescence on semiconductor X-ray analysis

The results presented in this Chapter have been published in the first authored paper: Hunter D. A. *et al*, Microscopy & Microanalysis, Vol. 28, Iss. 5, pp.1–12 (2022) [249]. Much of the introduction, results and discussion present in this chapter will be adapted or extracted from the cited paper.

7.1 Introduction

An additional consideration when performing EDX or WDX measurements is the generation of secondary fluorescence X-ray generation outside of the predicted excitation volume, possibly across grain boundaries or outside the surface layer for multilayered structures as discussed in Chapter 3. For geological or metallurgic samples the magnitude of this effect can be quite extreme, heavily skewing compositional measurements, *see below*. Using EDX/WDX for semiconductor characterisation is a fairly unconventional use of the techniques therefore the impact of secondary fluorescence is poorly understood. As a result there is value in understanding what influence secondary fluorescence has on such data to ensure we are confident in any previous and future compositional measurements.

Experimental evidence of secondary fluorescence affecting the X-ray micro-analysis was shown for olivine minerals, with X-rays propagate through neighbouring phase boundaries of calcium rich deposits [250]. Further evidence of this effect was shown for binary material couples of Cu and Co (A block of Co and Cu clamped together) with the magnitude increasing as the electron beam moves closer to the couple interface [251]. The binary material couple material system was used as a basis for X-ray microanalysis simulations attempting to successful model secondary fluorescence [252, 253]. In order to reduce the required processing power to produce these simulations Ritchie developed DTSA-II to provide quick but accurate modelling of EDX measurements with secondary fluorescence included [145, 254].

Secondary fluorescence was also found to produce an unrecognisable error when performing computational quantitative measurements on film-substrate materials involving thin heavy-metal films with substrate secondary fluorescence contributing nearly 10 % of the total X-rays generated [255,256]. The results from an adaptation of the simulations performed by Pouchou featuring Cu-metal film-substrates materials (Cu-Ge, Ge-Cu in [256]) showing the impact of secondary fluorescence is shown in Figure 7.1. As the beam excitation volume is enclosed within the upper Cu layer an expected result of Cu = 100 at% would be expected if only primary fluorescence was considered. However as their is secondary fluorescence present there is a number of substrate X-rays generated and detected skewing the quantification. Note that the smallest film thickness shown is when the beam excitation volume is contained within the upper layer.

Errors of these magnitudes would be a serious issue for our quantifications. As these simulations follow the same material geometry as semiconductor thin films then similar errors may be present in WDX analyses. Therefore DTSA-II has been used to investigate the magnitude of secondary fluorescence for three wideband semiconductor films on their typical substrates. In section 7.2 the individual contribution from CSF and BSF on on the elemental atomic fractions quantified by WDX will be investigated for a series of $Al_xGa_{1-x}N$ of varying film thicknesses deposited on

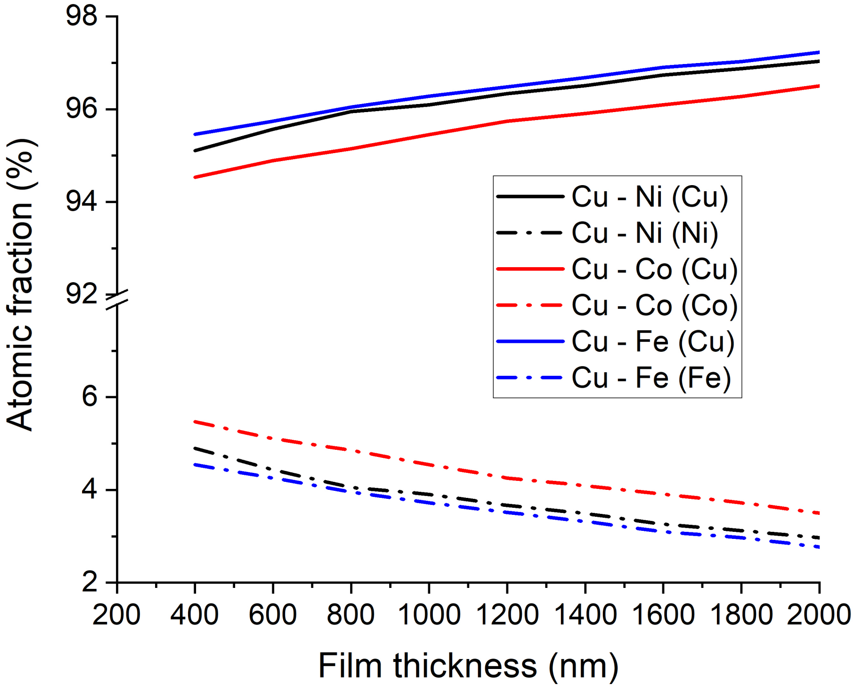

Figure 7.1: DTSA-II simulations results showing the effect of secondary fluorescence on the quantification of a Cu film with three different transition metal substrates (Ni, Co Fe). The skewed atomic fraction (at%) is plotted as a function of film thickness (nm). The Cu – Ni (Cu) corresponds to the quantified value of Cu within the Cu film – Ni substrate system with different line colours used for the different layered materials.

both GaN and AlN substrates. Section 7.3 investigates the impact of secondary fluorescence on WDX data measured from a thin layer of $In_xAl_{1-x}N$ on a thick GaN underlayer. Finally 7.4 investigates the secondary fluorescence impact on tin-gallium oxide $(Sn_xGa_{1-x})_2O_3$ quantification and the beam parameter influence on the magnitude of secondary fluorescence.

Methodology

DTSA-II was used to simulate electron beam induced X-ray generation within the previously mentioned materials. The underlying raw X-ray counts from the simulations were then converted into *k*-ratios to give a value for the material composition. For each DTSA-II simulation there were 3 compositions generated:

1. A composition using only the primary characteristic X-rays.

$$\frac{I_{unk}(Char)}{I_{std}(Char)} \tag{7.1}$$

2. A combination of the primary characteristic X-rays and any X-rays produced through CSF

$$\frac{I_{unk}(Char+CSF)}{I_{std}(Char+CSF)} \tag{7.2}$$

3. The total X-ray counts from all generation methods (primary fluorescence, CSFs and BSFs).

$$\frac{I_{unk}(Char+CSF+BSF)}{I_{std}(Char+CSF+BSF)} \tag{7.3}$$

For each simulation a beam energy of 10 keV and a probe dose of 400 nAs were used, *unless otherwise stated*. Multiple electron trajectories were applied within DTSA-II to reduce the randomness between simulations. For each film thickness and composition 16 simulations were completed, compiled and averaged to produce the average X-ray counts which were used to calculate the *k*-ratios. For all investigations in this publication the smallest film thickness simulated is the minimum required to prevent the primary excitation penetrating into the second layer.

In the cases where the atomic composition was calculated the *k*-ratios were submitted into CalcZAF to generate a quantification of the sample layer. *ZAF* corrections were calculated using the Love-Scott II package in CalcZAF with the Reed/Armstrong option for *F* correction. CalcZAF was used to calculate the material quantification from the X-ray counts produced by DTSA-II due to the greater precision (not accuracy) obtainable in the outputted quantification than for the integrated quantification tool within DTSA-II. For each simulation the material composition was first determined with consideration of only primary X-ray generation (Eq. 7.1) and the resulting base composition was then subtracted from subsequent quantifications featuring secondary X-ray generation (CSF and/or BSF) to derive the effect that secondary fluorescence has on the elemental atomic fractions (at%). The following standards and X-ray lines were used for all quantifications: AlN for Al K_α and N K_α; GaN for Ga L_α; InP for In L_α, silicon for Si L_α and cassiterite (SnO_2) for Sn L_α and O K_α X-rays.

7.2 $Al_xGa_{1-x}N$ on GaN & AlN

Two $Al_xGa_{1-x}N$ alloys have been investigated, with $x = 0.3$ and 0.7, and each composition simulated for a GaN and an AlN substrate. This represents typical $Al_xGa_{1-x}N$ alloys at moderate ends of the compositional range [162]. CASINO simulations indicate the excitation volume is contained within the $Al_xGa_{1-x}N$ film when the film thicknesses are 600 nm and 700 nm for $x = 0.3$ ($\rho = 5.28$ g/cm^3) & 0.7 ($\rho = 4.13$ g/cm^3), respectively. As these measurements were performed with a beam energy of 10 keV the highest X-ray energy that may be generated are Ga K_α X-rays (E= 9.25 keV).

Firstly, consider the impact of CSF only, shown in Figure 7.2. The change in k-ratio has been calculated by subtracting the result of Equation 7.1 from Equation 7.2. Positive (negative) numbers on the vertical axis indicate an increase (decrease) in the k-ratio of an element in the film.

At a beam voltage of 10 kV the Al K absorption edge (E = 1.56 keV) is considered to have the highest energy in the $Al_xGa_{1-x}N$ material system in these simulations. Thus, no additional Al K_α X-rays are produced by CSF. It is theoretically possible to generate Al K_α X-rays through CSF from Ga K_α X-rays at this beam voltage however the probability of generating Ga K_α X-rays and subsequent Al K_α CSFs is so low that the counts generated through this process are negligible. Therefore, for all film thicknesses the Al k-ratio will remain constant, as seen in Figure 7.2a.

For Ga however, there is a sufficient energy difference between the Al K_α X-ray

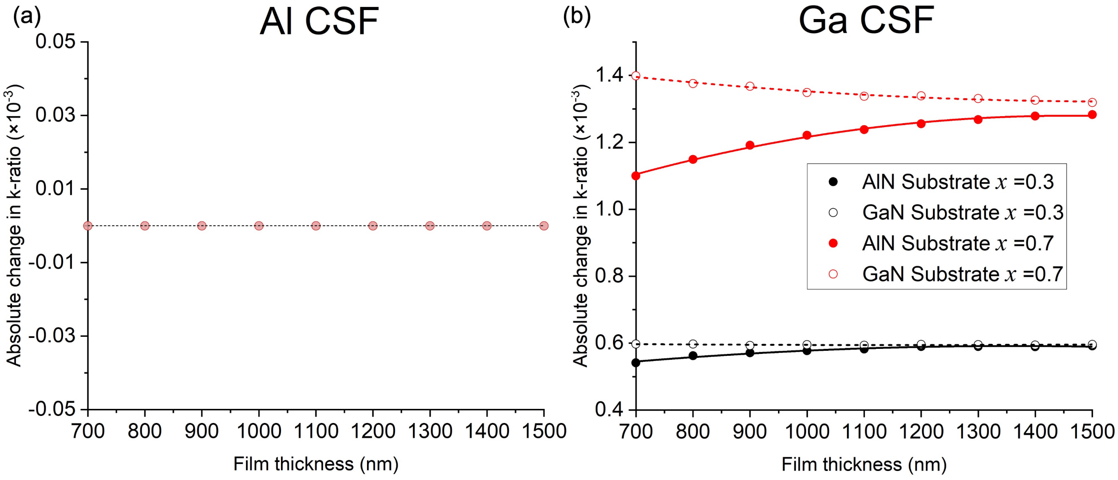

Figure 7.2: The change in reported atomic percentage for (a) Al and (b) Ga due to CSF as a function of film thickness (nm). Filled circles are used to identify results for the AlN substrate and hollow for GaN. Two $Al_xGa_{1-x}N$ alloys are shown in each figure where $x = 0.3$ ($\rho = 5.28$ g/cm^3, black markers) & 0.7 ($\rho = 4.13$ g/cm^3, red markers). The lines (solid and dashed) are calculated fits from their corresponding data points

(E= 1.49 keV) and the Ga L absorption edge (E= 1.29 keV) that additional Ga L_α X-rays can be excited by CSF, increasing the Ga L_α X-ray counts, as seen by the positive changes in k-ratios in Figure 7.2b. As the Al composition, x, is increased the number of Al K_α X-rays generated by primary excitation is increased. Therefore, there are are additional X-rays capable of generating Ga L_α CSF X-rays.

In Figure 7.2b the difference between the AlN (circles) and GaN (rings) substrates is minimal with the greatest difference in k-ratio being 0.3×10^{-3} for $x = 0.7$ and $< 0.1\times10^{-3}$ for $x = 0.3$. The substrate effect begins to nullify as the film thickness is increased, containing a larger fraction of the secondary excitation volume within the film. The change in k-ratio when the measurement has become independent from substrate fluorescence is approximately 1.3×10^{-3} for $x = 0.7$ and 0.6×10^{-3} for $x = 0.3$. The increased density for the $Al_xGa_{1-x}N$ film when $x = 0.3$ compared to $x = 0.7$ means CSF becomes independent from the substrate at a quicker rate. Overall, the maximum change in Ga k-ratio observed is 1.4×10^{-3} for a 700nm film where x

= 0.7 with a GaN substrate.

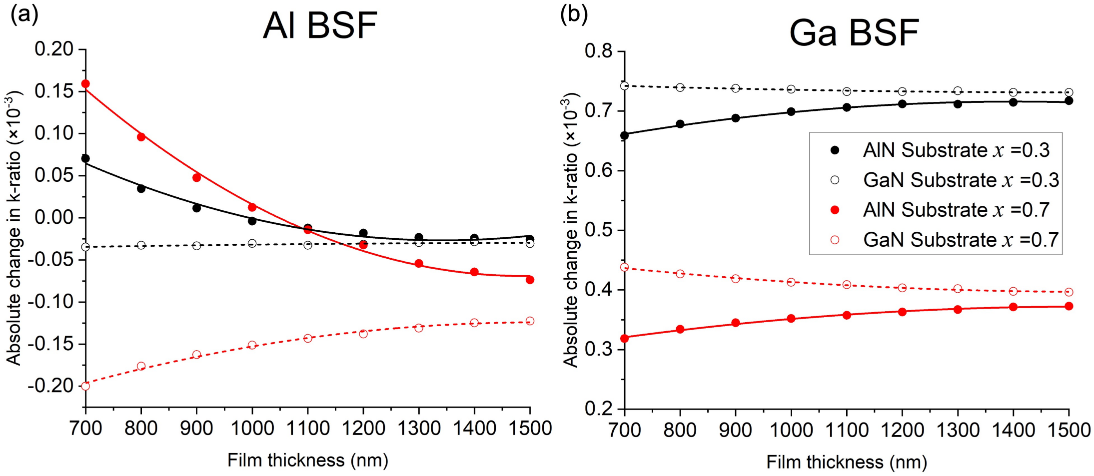

Figure 7.3: The change in reported atomic percentage for (a) Al and (b) Ga due to BSF as a function of film thickness (nm). Filled circles are used to identify results for the AlN substrate and hollow for GaN. Two $Al_xGa_{1-x}N$ alloys are shown in each figure where $x = 0.3$ ($\rho = 5.28$ g/cm^3, black markers) & 0.7 ($\rho = 4.13$ g/cm^3, red markers). The lines (solid and dashed) are calculated fits from their corresponding data points.

When BSF is considered there will now be an impact on both the Al and the Ga X-ray counts and subsequent k-ratios. The change in k-ratio for BSF has been calculated by subtracting the result of Equation 7.2 from Equation 7.3.

The first thing to note in Figure 7.3 is that when an element is present in both the film and the substrate (e.g Al in AlGaN/AlN) that element always experiences a greater increase, evidence that the bremsstrahlung radiation is capable of reaching the substrate and generating BSF X-rays. As X-ray absorption is dictated by the MAC of an element it is expected that BSF would have the largest effect on Ga as the MAC of Ga is always greater than that of Al within the 0-10 keV energy range, with the largest differences being in the energy range between the Ga L X-ray and Al K X-ray absorption edges (E=1.29 keV and 1.56 keV respectively). Despite L X-ray transitions having a poorer fluorescent yield compared K to transitions this is still seen when comparing Figure 7.3a to 7.3b [257]. As the Ga MAC is very large at the Al K_α X-ray energy there is a large degree of X-ray reabsorption preventing the emission of the Al X-rays, reducing the impact BSF has on the Al k-ratio.

Comparing the effect of CSF to BSF for Ga (Figure 7.2b to 7.3b) the convergence point between the two substrates occurs at greater film thicknesses, indicating that high energy BSF is capable of generating a greater number of substrate X-rays unlike CSF. In Figure 7.3a at low film thicknesses the sheer number of Al atoms in the film when $x = 0.7$, and the AlN substrate (red circles, whole red line) produces the greatest change in k-ratio for Al by BSF, 0.15×10^{-3}. For Ga the greatest change by BSF is 0.75×10^{-3}. occurs when $x = 0.3$ and a GaN substrate (black rings, dashed black line), 7.3b.

The change in k-ratio for each element is useful for describing the behaviour of each individual effect however does not translate well when describing the impact of secondary fluorescence on the calculated composition of a material. Changes in the k-ratio are not always reflected in the quantified composition due to the normalisation process masking changes in nitride molar fraction. Therefore, the results shown in Figures 7.2 and 7.3 have now been combined and quantified to produced the change in nitride molar fraction (x in $\mathrm{Al}_x\mathrm{Ga}_{1-x}\mathrm{N}$), shown in 7.4. This normalisation procedure assumes the N content present in the film is exactly 50%.

As there are only two materials to be considered within the quantification any changes experienced by one (e.g. GaN) will result in an equal but opposite change for the other (AlN). The overall change observed within the GaN molar percent is a slight increase, <0.1%, for all alloy compositions, approximately 0.07% for the high AlN content alloy ($x = 0.7$) and 0.03% for the low AlN alloy ($x = 0.3$). The increased value for GaN is dominated by the increase produced from CSF, which is why the largest change is observed for $x = 0.7$ with the largest number of Al atoms to act as sources for CSF.

The non-zero convergence points for the results from the two substrates at large film thicknesses is due to a combination of BSF being uncorrected for by F during the quantification and the F correction being present when quantifying the k-ratio from Equation 7.1. No fluorescence is present when quantifying the k-ratio from Equation 7.1 but the calculation still assumes there is and attempts to correct for it

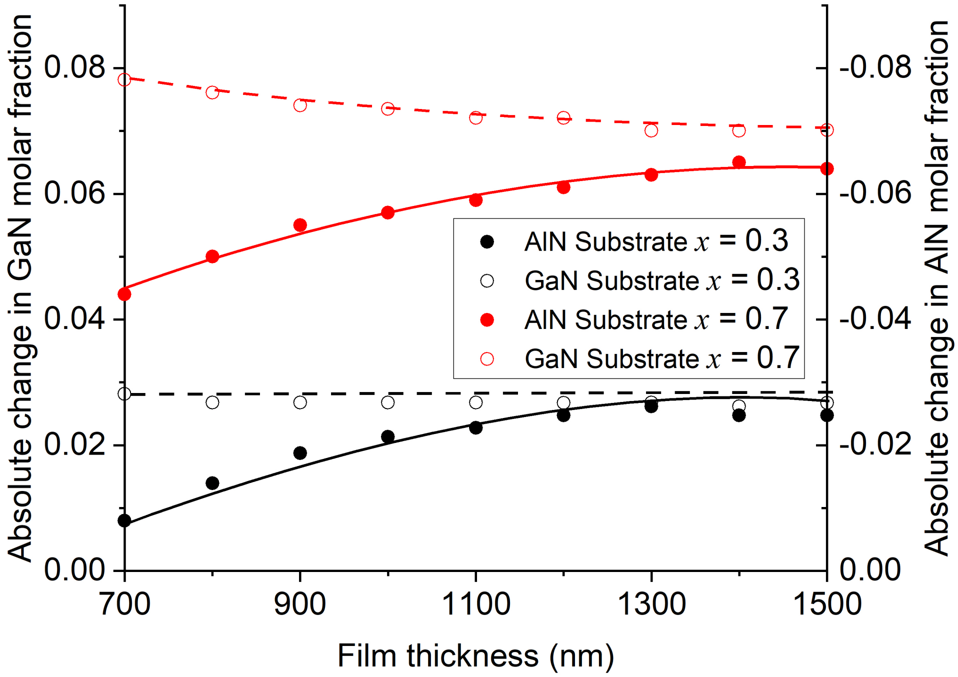

Figure 7.4: The change in molar fraction for GaN (left axis) and AlN (right axis) due to the combined effect of CSF + BSF as a function of film thickness (nm). Filled circles are used to identify results for the AlN substrate and hollow for GaN. Two $Al_xGa_{1-x}N$ alloys are shown in each figure where $x = 0.3$ ($\rho = 5.28$ g/cm^3, black markers) & 0.7 ($\rho = 4.13$ g/cm^3, red markers). The lines (solid and dashed) are calculated fits from their corresponding data points.

via the F correction (CalcZAF does not allow the F correction to be switched-off).

When x= 0.3 the final F correction value was determined to be 0.9930 compared to the larger correction of 0.9906 when x= 0.7 (F = 1 in the case of zero fluorescence). As the CSF excitation of Ga is the most dominant contribution of secondary fluorescence the larger F correction is due to the increased Al content resulting in greater excitation, and reduced re-absorption, of Ga CSF explaining the larger molar fraction change for higher x in Figure 7.4.

When compared to the work on transition metal binary couples and metallic films [251, 255, 256] the impact of secondary fluorescence found here is largely unaffected. In some cases secondary fluorescence produces a change in apparent Wt% of 1-3 orders of magnitude [258, 259] whereas here the impact is minimal. The reduced beam energy used within semiconductor characterisation compared to geological/metallurgy (typically 5-10 keV vs 30 keV) is likely responsible. Knowing that secondary fluorescence produces a low magnitude change in the calculation of the material composition we can now be confident that previous results (Chapter 4 & [66,137,162,167]) are unaffected by these effects. The variation in the results from secondary fluorescence would be contained within the experimental uncertainty and would not need to be specifically addressed for WDX measurements on $Al_xGa_{1-x}N$ materials.

7.3 $In_xAl_{1-x}N$ on GaN

The impact of secondary fluorescence on WDX data measured from a thin layer of $In_xAl_{1-x}N$ on a thick GaN underlayer was also investigated. The high energy of the In $L_{\alpha 1}$ X-ray (E = 3.287 keV) makes the presence of In in the film particularly relevant as there will now be a greater CSF excitation volume than in the previous investigation. Indium also posses a large MAC influencing how secondary fluorescence effects the other elements present.

This study also allows a check to be performed on a past investigation: E. Taylor *et al.* [260] reported the unexpected incorporation of gallium in films of $In_xAl_{1-x}N$ using WDX. The source of the gallium impurity was determined to be contamination from the growth chamber; however secondary fluorescence from substrate gallium could have augmented the quantified concentration of gallium impurities within the film and it is therefore important to verify the source of these unexpected X-rays.

Figure 7.5 shows the effect of CSF on the k-ratio for all elements present in the material system. For this material CSF shows different behaviour to that in Chapter 4.1, with the element with the highest energy X-ray, In, acting as both a source of CSF and generating additional X-rays. This is due to higher energy In L transition

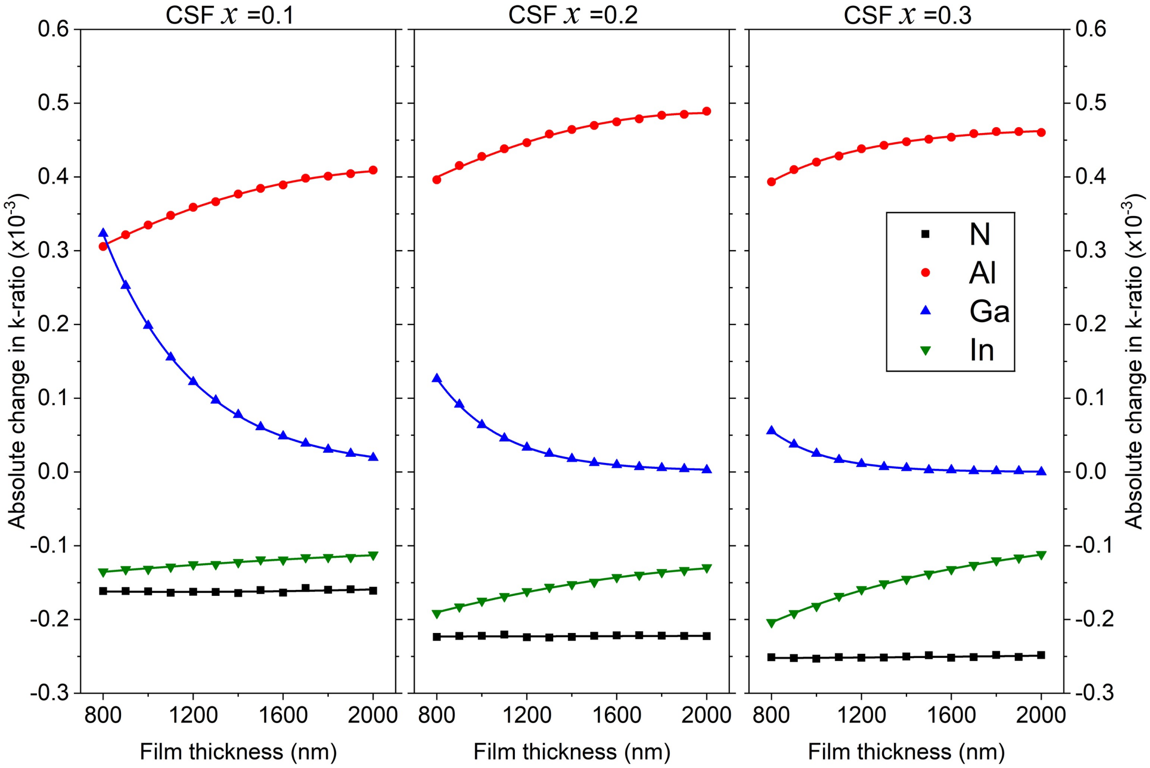

Figure 7.5: The change in k-ratio under the influence of CSF for Al (red circles), Ga (blue triangles), In (inverted green triangles) and N (black circles) as a function of film thickness (nm). Three $In_xAl_{1-x}N/GaN$ alloys are shown in the Figure varying in composition from left to right: $x = 0.1$ ($\rho = 3.62$ g/cm^3), 0.2 ($\rho = 3.97$ g/cm^3) & 0.3 ($\rho = 4.33$ g/cm^3). The solid lines are calculated fits from their corresponding data points.

X-rays (e.g $L_{\gamma 1}$) having a sufficient overvoltage to generate $L_{\alpha 1}$ X-rays. As the energy difference between the higher energy X-rays $L_{\alpha 1}$ is still low the probability of this process occurring is relatively low, resulting in a small number of In CSF X-rays. In Figure 7.5 it is seen that the overall change in the k-ratio for In is always negative for the three alloy compositions (green triangles) however increasing the film thickness suppresses the decrease in k-ratio as In $L_{\alpha 1}$ X-rays are self-generated from the higher energy L X-rays. The overall decrease in the k-ratio due to the effect of CSF on In (and N) is attributed to differences in X-ray generation/emission rates between the standard and film which would be corrected for by the ZAF factors once the k-ratio is quantified.

The blue triangles in Figure 7.5 indicate that there is now an apparent presence of Ga within the film. This stems from Al and In X-rays propagating within the GaN substrate subsequently generating Ga CSF X-rays. As with the $Al_xGa_{1-x}N$ alloys in 4.1 increasing the film thickness contains more of the CSF excitation volume within the film and suppresses the presence of "false" Ga. Again, increasing the film composition from x=0.1 through to 0.3 reduces the primary and subsequent CSF excitation volume while increasing the content of high MAC In atoms, in turn quenches both the generation and emission of the "false" Ga CSF X-rays.

The Al CSF behaviour (red circles in 7.5) in this system is less straightforward. For x= 0.1 & 0.2 the k-ratio increases due to Al $K_{\alpha1}$ X-rays being generated by the high energy In X-rays with the high In content film emphasising the effect as more In sources of CSF excitation are introduced in the film. Further increase of x to 0.3 then begins to suppress the increase in Al k-ratio as the greater In content begins to enhance X-ray reabsorption. The low MAC for N and high rate of N $K_{\alpha1}$ X-ray reabsorption by the other present elements results in an insignificant change in the N X-ray counts resulting in the constant decrease in N k-ratio (black squares in 7.5).

When compared to the CSF results in 7.1 (Figure 7.2) the behaviour here is extremely similar with CSF having the greatest effect on the element with the second highest absorption edge (Al) due to excitation from the highest X-ray energy in the system (In). However, the degree of substrate excitation (and emission) can now be clearly examined with the "false" Ga being present for all film thicknesses when x= 0.1 & 0.2 with a maximum change in k-ratio occurring at the smallest film thickness, 800 nm (approximately 0.31×10^{-3} and 0.12×10^{-3} respectively). When x= 0.3 the "false" Ga is negated at film thicknesses $>$ 1800 nm due to the increased film density. The greatest difference in Ga k-ratio occurring for a film thickness of 800 nm was approximately 0.06×10^{-3}.

The effect of including BSF within the quantification is now considered in Figure 7.6. As with CSF there is now the presence of "false" Ga produced from BSF excitation of the GaN substrate, seen by the blue triangles in Figure 7.6. Mirroring the

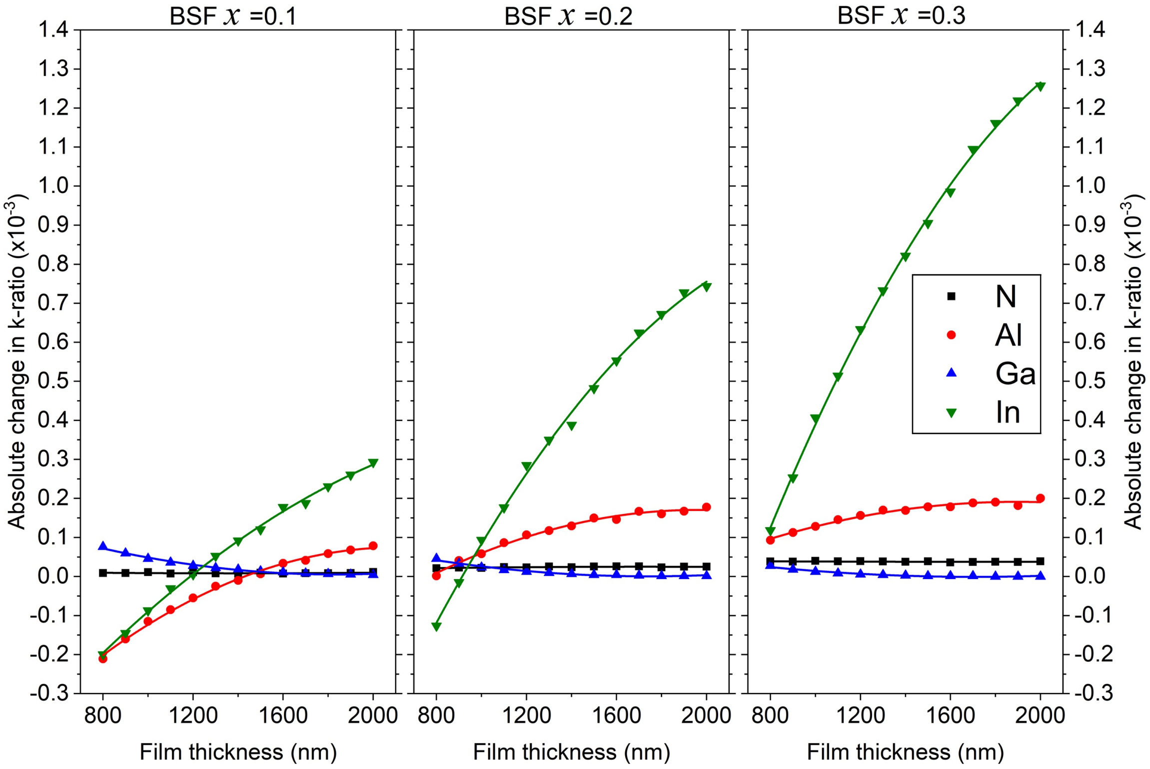

Figure 7.6: The change in k-ratio under the influence of BSF for Al (red circles), Ga (blue triangles), In (inverted green triangles) and N (black circles) as a function of film thickness (nm). Three $In_xAl_{1-x}N/GaN$ alloys are shown in the Figure varying in composition from left to right: $x = 0.1$ ($\rho = 3.62$ g/cm^3), 0.2 ($\rho = 3.97$ g/cm^3) & 0.3 ($\rho = 4.33$ g/cm^3). The solid lines are calculated fits from their corresponding data points.

behaviour for CSF, the extra Ga X-ray counts quickly decreases to 0 with an increase in both film thickness and composition. The magnitude of the change in k-ratio is notably smaller for BSF than CSF, being 0.1×10^{-3} for all compositions simulated. The Ga BSF X-ray counts are negated for film thicknesses of approximately 1700 nm, 1400 nm and 1200 nm for x values of 0.1, 0.2 and 0.3 respectively.

The black squares in Figure 7.6 indicate there is little change in N when BSF is included in k-ratio calculations and no change seen as the film thickness is increased. As x is increased there is a small increase in the N k-ratio as the increased In concentration results in the generation of more bremsstrahlung continuum X-rays, allowing N to produce a small additional number of BSF X-rays.

Similarly, to CSF the *k*-ratio for In is initially reduced when BSF X-rays are included with this behaviour now extending to Al as well (green inverted triangles and red circles in Figure 7.6 respectively). As the film thickness is increased more of the BSF excitation volume is enclosed within the film, reducing substrate excitation and the generation of “false” Ga X-rays, increasing the number of Al and In BSF X-rays generated therefore increasing the *k*-ratio of the two elements.

As x is increased the In *k*-ratio begins to massively increase, dominating continuum absorption with the superior MAC compared to Al, reaching a maximum *k*-ratio increase of approx. 1.25×10^{-3} at the largest film thicknesses. The Al *k*-ratio continues to increase as x increases but the effect of increasing the film thickness is suppressed for the high In content films. Again, the increased In content in the films will result in the generation of a greater number of continuum X-rays, helping to magnify the behaviour seen when $x = 0.1$ but the emission of Al BSF X-rays will be negated by reabsorption from the superior MAC of In. The greatest change in Al *k*-ratio still occurs when $x = 0.3$ peaking at a value of approximately 0.2×10^{-3}.

As with 7.1 the combined effect of both secondary fluorescence mechanisms has been calculated and quantified through calcZAF assuming a constant N content of 50%. Figure 7.7 shows an increase in molar fraction for InN and GaN, mirroring the overall increase in *k*-ratio however, the AlN must now decrease to compensate for the increase in the other molar percentages due to the normalisation within the calculation.

As the Ga X-ray counts are rising from 0 when only primary fluorescence is considered the GaN molar fraction (red circles in Figure 7.7) can only decrease to 0%, any additional X-rays are reflected with a positive increase in the molar fraction. The largest contribution from secondary fluorescence is BSF affecting the In X-ray counts, nearly 3× the magnitude of the next highest contribution (Al CSF) when $x = 0.3$. Despite the decrease in *k*-ratio through CSF the magnitude of the BSF increase in *k*-ratio dominates producing the increase in the InN molar fraction (blue triangles). As these two values are increasing the AlN molar fraction decreases to compensate during the normalisation (black squares).

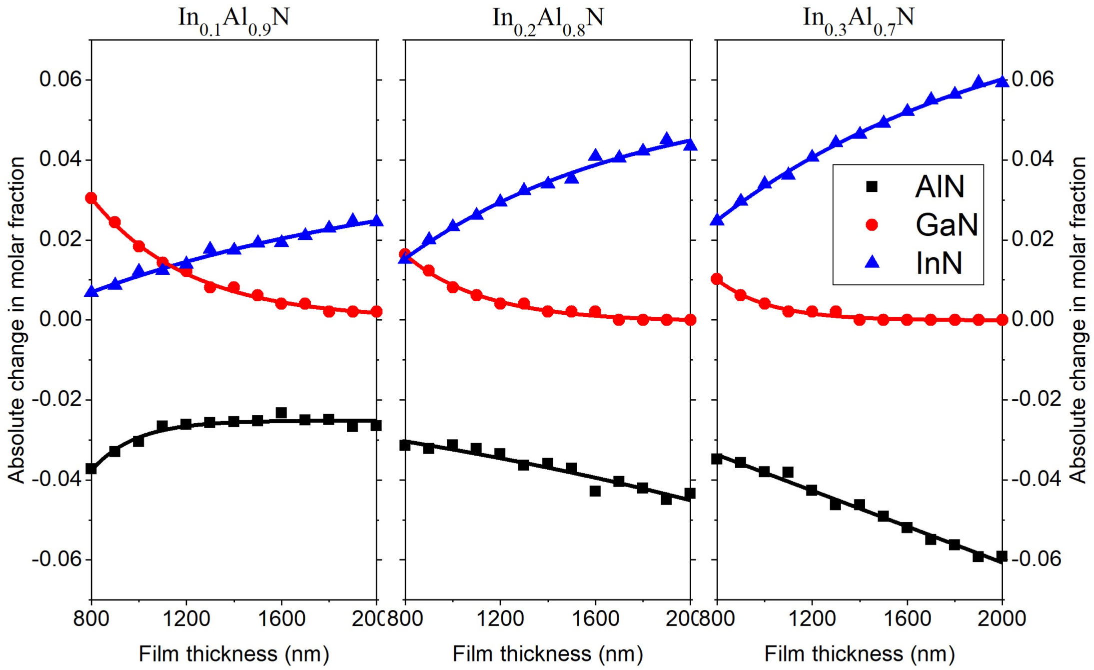

Figure 7.7: The change in k-ratio under the influence of CSF + BSF on the quantified AlN (black squares), GaN (red circles) and InN (blue triangles) composition as a function of film thickness (nm). Three $In_xAl_{1-x}N/GaN$ alloys are shown in the Figure varying in composition from left to right: $x = 0.1$ ($\rho = 3.62$ g/cm^3), 0.2 ($\rho = 3.97$ g/cm^3) & 0.3 ($\rho = 4.33$ g/cm^3). The solid lines are calculated fits from their corresponding data points.

From Figure 7.7 the amount of GaN calculated to be within the material with a 1 μm film thickness as a result of secondary fluorescence is found to be approximately 0.018% when x=0.1, further decreasing to 0.01% and 0.003% when x=0.2 and 0.3 respectively. For x=0.1 the increase in molar percent for InN is 0.012% and the decrease in AlN is -0.03% for a 1 μm film. For x=0.2 0.3 the increase in InN grows to approximately 0.022% and 0.035% respectively. When x=0.1 the AlN change is compensating for the increase in both GaN and InN, but as the InN content in the alloy increases the number of Ga X-rays abruptly decreases and the AlN begins to compensate for just the increase in InN, explaining the change in trend for AlN for thinner film thicknesses. Again, the change in AlN is small, with decreases of approximately -0.032% and -0.039% for x=0.2 and 0.3 respectively. As with the elemental changes the magnitude of all the changes to the molar percent for the three III-nitride binary materials sums to 0.

As with 7.1 the magnitude of the change is minimal and well within the uncertainty margins if measured experimentally. We can therefore be confident of our results when experimentally characterising these materials. This confirms that when large amounts of GaN are unexpectedly detected, as in [260], that the cause is likely to be due to material impurities rather than secondary fluorescence.

For III-nitride materials the effect of secondary fluorescence within the material is by no means great enough to produce a large change in the quantification of the material when operating at a beam energy of 10 keV. When performing compositional analyses on a film within a film-substrate material then substrate X-rays interfering with the material quantification have also found to be negligible under the same conditions.

7.4 $(Sn_xGa_{1-x})_2O_3$ on Si

As the previous investigations established that secondary fluorescence has a minimal effect on the measurement of the major element constituents in semiconductor alloys the effect on low concentration and trace element analyses has been determined. This has been completed by simulating the X-ray analyses performed on the $(Sn_xGa_{1-x})_2O_3$/Si sample from Chapter 6 and [226]. At the time when these simulations were completed, WDX measurements on this sample determined the atomic fractions within the $(Sn_xGa_{1-x})_2O_3$ film to be approximately 60% O, 38% Ga and 2% Sn. It is expected that the Sn would replace Ga in Ga_2O_3, although the possible formation of the tin oxide polymorph SnO_2 means that the elemental atomic fractions may deviate from the 2:3 metal:oxygen ratio. The Sn concentration will therefore be discussed in terms of atomic percent, at%. The relative gallium and tin concentrations were then varied from Sn = 1 at% to 4 at%. As the individual contribution of CSF and BSF on the material k-ratio have been determined we will now only present the results as the total effect secondary fluorescence has on the elemental at%.

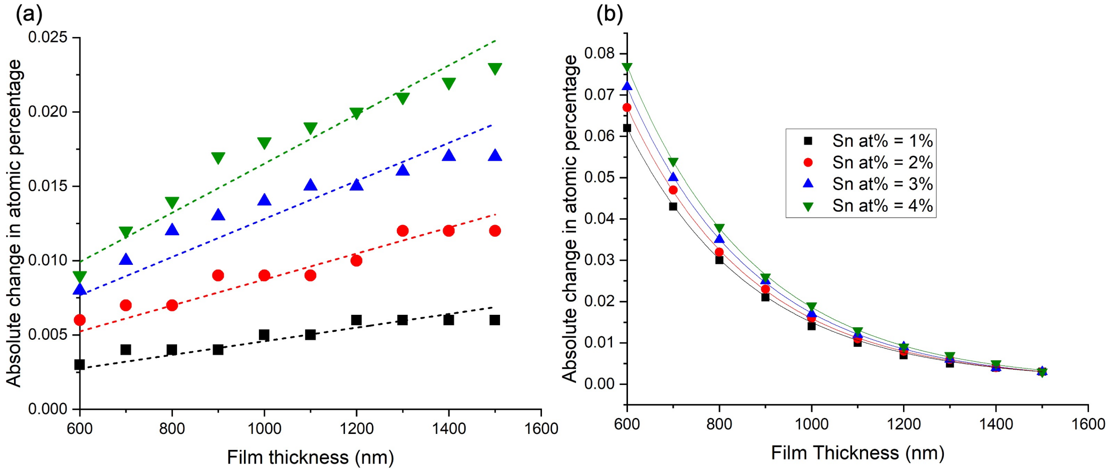

Figure 7.8: The change in atomic fraction (at%) under the influence of secondary fluorescence as a function of film thickness (nm) for (a) Sn & (b) Si in a TGO/Si alloy. The results from four alloys are shown where Sn at% is varied from 1 to 4% which are identified using different data markers/colours. The dashed (Sn) and solid lines (Si) are fits calculated from their corresponding data points.

As the previous studies established that secondary fluorescence has a minimal effect on the compositional measurement of the major elemental constituents in semiconductor alloys the focus is now on the low concentration elements of tin and the substrate silicon. The apparent change in at% for tin and silicon are plotted in Figure 7.8. Again, the overall magnitude of the secondary fluorescence contribution is very low, with a 0.1 at% difference being observed for both the film Sn, Figure 7.8(a) and the substrate Si, Figure 7.8(b).

Figure 7.8(a) shows that the secondary fluorescence mechanisms result in the marginal increase in the Sn at% coming exclusively from BSF due to Sn L_α being the highest energy X-ray in the system. As with In L_α in the previous example, there is CSF of Sn L_α X-rays generated by higher energy L-shell Sn X-rays but the number of these events is so low as to have a negligible impact. The high Sn MAC results in an increase in bremsstrahlung absorption as the Sn concentration is increased resulting in a larger increase in the Sn at%, similarly to indium in the previous example.

Figure 7.8(b) shows the amount of "false" silicon that has been included in the material quantification due to X-rays originating from secondary fluorescence in the substrate. The Si K absorption edge has an energy of E= 1.84 keV, so excitation of the K_α X-ray line is by either BSF or by CSF generated by Sn L_α X-rays, with increasing concentrations of Sn generating more Si X-rays by CSF. As before increasing the film thickness contains the secondary excitation volume within the upper layer reducing the number of Si X-rays generated.

While this secondary volume has little effect on the quantification of the bulk material it would become significant when analysing dopants within the film. As mentioned in Chapter 2 Si commonly used n-type dopant within Ga_2O_3 [35, 38] and WDX has previously been used to determine the dopant density within semiconductor films [162, 167]. If the Si-doped semiconductor film were grown on a silicon substrate then secondary fluorescence would contribute to an incorrect calculated concentration of dopants. For example in Figure 7.8, a 1 μm film with Sn = 2 at% produced a quantified atomic value for Si = 0.016 at% which translates to a Si dopant density on the order of 10^{18} atoms cm^{-3}.

In order to understand how this this "false" concentration of Si could be reduced a set of variable beam energy simulations were completed. As the beam energy is varied the penetration depth of the electrons will change, modifying the size of the primary (and subsequent secondary) excitation volumes. By increasing the distance between the excitation volume and Si substrate it is expected the "false" concentration will be greatly reduced, therefore the following simulations were conducted to investigate the Si concentration dependence on beam energy.

Figure 7.9 shows how the quantified silicon concentration varies as a function of acceleration voltage. To generate sufficient Sn L_α X-rays the lowest beam energy employed was 7 keV, approximately twice the energy of the Sn L_α X-ray. As the beam energy is increased beyond 12 keV the primary excitation volume becomes comparable to the film thickness, so no higher energy simulations were performed.

Figure 7.9 indicates that during experimental WDX/EDX measurements the

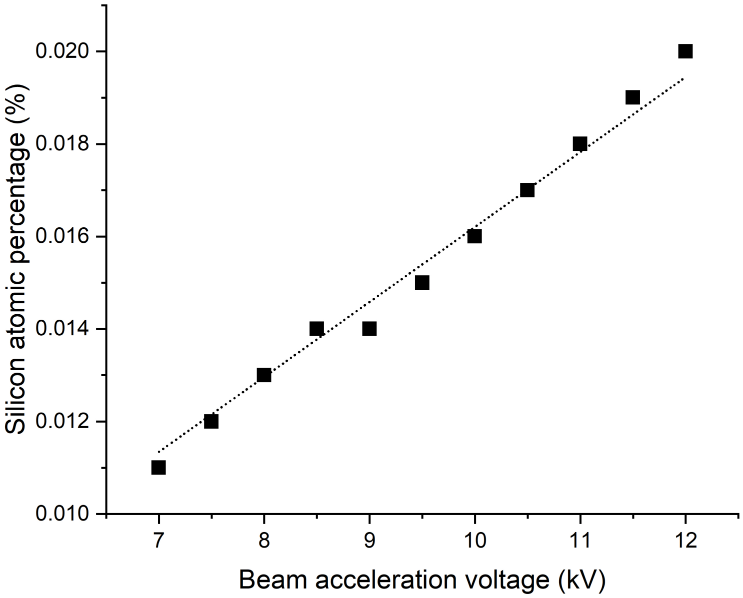

Figure 7.9: The quantified amount of "false" silicon (at%) in a TGO film due to secondary fluorescence from the sample substrate as a function of beam acceleration voltage (kV). A 1 μm film of TGO/Si with Sn = 2 at% was simulated for multiple beam voltages between 7 and 12 kV.

magnitude of secondary fluorescence can be reduced by using the lowest possible beam voltage, reducing the primary excitation volume, keeping X-ray generation further away from the film-substrate boundary. By keeping the beam energy as low as possible, at 7 keV, the amount of "false" silicon present in the film is reduced by over 30% compared to 10 keV (0.016% to 0.011%), however secondary fluorescence Si K_α X-rays are still present at a level sufficient to skew the silicon quantification. The magnitude of these effects is dependent on film bulk composition, and specifically the energy of the X-rays used for quantification, but the trends and reduction methods will be relevant for any film-substrate system where a dopant element is present in the substrate.

7.5 Conclusion

This study has investigated the impact of X-ray secondary fluorescence on compositional X-ray analyses of semiconductor thin films through computational simulations. In total three different types of semiconductors were analysed: $Al_xGa_{1-x}N$, $In_xAl_{1-x}N$ and $(Sn_xGa_{1-x})_2O_3$ with the results of which highlighted in their own sections. Various compositions and substrate combinations were investigated for each semiconductor.

While secondary fluorescence was proven to be highly detrimental to the analysis of metallic alloys, binary couples and layered materials the impact on bulk semiconductor quantitative measurements was found to be negligible, modifying the calculated composition <0.1 at% for all three cases. The reasoning behind this low impact is attributed to the typical beam conditions used for semiconductor characterisation compared to geological and metallurgy analyses. The reduced beam energy for these measurements (∼10 keV) does not allow for the generation of high energy X-rays which are responsible for the large impact of secondary fluorescence in the metallic systems. The low beam energy also restricts the primary and secondary excitation volumes within the material, nullifying the generation of substrate X-rays through fluorescence.

The inability to generate high energy X-rays under thin film beam conditions is the reason behind the minuscule impact on the quantification. Therefore, it is expected that the results presented here on semiconductor thin films would generally mirror that performed on metallurgic and geological specimens when using beam conditions suitable for thin film analyses. Operating within a lower energy regime would still be expected to minimise the impact of X-ray secondary fluorescence within these specimens: For example, when measuring transition metal alloy concentrations in layered systems or the composition within a mineral with known grain boundaries.

Secondary fluorescence would start to have a more detrimental effect on thin film quantification, possibly comparable to bulk metallurgic samples, when the electron beam energy has sufficient overvoltage to generate a large number of K_α X-rays. As mentioned in Chapter 7.2 and 7.3 Ga and In use L_α X-rays during quantification. If using the beam conditions typical for metallurgic and geological samples (30 keV+) it would be possible to generate K_α X-rays, known to generate a large number of CSFs [256] due to their increased energy (In K_α 24.21 keV, Ga K_α 9.25 keV vs, L_α = 3.29 keV and Ga L_α = 1.10 keV). There would also be a vastly magnified number of bremsstrahlung X-rays with much greater energy capable of BSF.

The beam energy at which secondary fluorescence goes from being negligible to adverse would be dependent on the elements present in the specimen and the energy of the characteristic X-rays used for quantification. Increasing the beam energy would gradually enhance the impact of BSF but as mentioned for CSF larger effects would begin to be seen when the beam energy has a sufficient overvoltage to generate high energy K_α X-rays. For metallic systems Yuan [259] quotes an approximate 10× increase in the CSF and BSF X-ray intensity for overvoltages of 5 kV and 10 kV respectively for Cr K_α X-rays within three various metal alloys. For metallic bilayers an lesser intensity increase of 5× for CSF and 2× for BSF was found for a 5 kV overvoltage. The Cr K_α X-ray transitions used in the quantification had a higher energy than acceptable for thin film analyses (Cr K_α = 5.5 keV) therefore for semiconductor WDX measurements a lesser effect would be expected. This is due to a combination of the reduced beam energy required to accurately analyse the film and the poorer fluorescence yield of L_α X-ray transitions [257].

Despite secondary fluorescence having a negligible effect on major element analyses, secondary fluorescence was found to have a adverse effect on trace element quantification of dopants within semiconductors. When the semiconductor dopant is an element present in the substrate (e.g $\mathrm{Sn}_x\mathrm{Ga}_{1-x})_2\mathrm{O}_3$:Si with a Si substrate) the dopant density cannot be accurately determined through WDX. Variable beam energy simulations established that the magnitude of this effect can be reduced by operating with the lowest beam energy possible, restricting the excitation volumes to the shallow depths within the film hence reducing the substrate influence.

The results from this study reinforce the confidence of previously completed WDX compositional measurements on semiconductor thin films and also highlighting particular situations which may require additional care in order to produce a highly accurate, quantified semiconductor composition. As the results from these investigations show secondary fluorescence as a “null result” this does not guarantee that more exotic and complex semiconductor thin films may be affected or if larger beam energies are used. Therefore, integrating a suitable correction program or transitioning to a quantification package with an existing correction for secondary fluorescence [259, 261, 262] may also be required to confirm that secondary fluorescence can be considered negligible in WDX measurements.

Chapter 8

Summary

This chapter summarises the work presented in this thesis, particularly the investigations detailed in the previous four chapters, bringing together the key results and conclusions from the completed experimental work . A small section highlighting possible future advancements on the research presented here is also provided.

8.1 Summary of thesis

The work presented here features the characterisation of wide bandgap semiconductor materials, primarily determining the optical and compositional properties of $Al_xGa_{1-x}N$ and ternary alloys of Ga_2O_3 (indium-gallium oxide, IGO, and tin-gallium oxide, TGO) using the electron microscopy techniques of wavelength-dispersive X-ray spectroscopy (WDX) and cathodoluminscence (CL). This was assisted by measurements from other experimental characterisation techniques such as EBSD, XRD, SIMS, AFM and transmission spectroscopy.

The history and motivation for the work completed here is written in Chapter 1, alongside a brief statement about what topics feature in the subsequent chapters. Chapter 2 describes the background information about the semiconductor materials which is fundamental to the understanding of the experimental work presented in the later chapters. The properties of Ga_2O_3 and III-nitride, particularly $Al_xGa_{1-x}N$ are detailed, explaining their individual crystallographic properties, alloying capabilities, doping behaviour and the semiconductor defects unique and common across both materials. The chapter also details the semiconductor growth techniques that feature in this thesis and the general considerations of semiconductor epitaxial growth (e.g substrate choice, advantages of each growth mechanism). The final section discusses the applications of these semiconductor materials within optical devices and the current limitations of these devices, the driving force of researching the materials within this thesis.

Chapter 3 explains the principles behind the electron microscopy techniques heavily used within this thesis (WDX and CL). General electron microscopy is discussed, explaining the theory and instrumentation used within the EPMA and the setup, detection method and measurement capabilities of WDX and CL. The software used to complete and supplement the experimental work here is also discussed.

The characterisation of two sets of $Al_xGa_{1-x}N$ materials is detailed in Chapter 4. TU Berlin provided a set of MOVPE grown semi-polar $(11\bar{2}2)$ $Al_xGa_{1-x}N$ samples with a high AlN content ($x \approx 0.6$ - 0.8) which was also Si doped. An array of polar, semi-polar and non-polar $Al_xGa_{1-x}N$ samples with AlN content spanning the entire compositional range was provided by Nagoya University, in total five different crystal orientations of $Al_xGa_{1-x}N$ were grown. The $Al_xGa_{1-x}N$ composition determined by WDX agreed with that determined prior through transmission spectroscopy and XRD measurements with Al incorporation found to be generally independent of crystal orientation for the Nagoya samples however greater compositional variation was found for high levels of AlN alloying ($x \approx 0.4$ - 0.8). Si dopants in the semi-polar TU Berlin samples showed self-compensating behaviour with increasing dopant concentration as seen for polar material, however the maximum dopant levels before compensation occurs were found to be dependent on Al composition. CL measurements show blue-shifting of the NBE peak with increasing Al content for all samples with good agreement between the WDX and CL when calculating the material optical bandgap. However the agreement breaks down for higher Al content samples due to compositional inhomogenity of the samples, reflected in the broadening of the NBE peaks and confirmed through AFM imaging. CL spectra also show high levels of defect related luminescence for semi- and non-polar materials compared to polar

$Al_xGa_{1-x}N$, attributed to oxygen related V_{III} complexes.

Chapter 5 discusses the properties of indium-gallium oxide alloys grown through PLD and MBE. A long combinatorial piece of IGO was provided by Leipzig University with In compositions varying from 0.8 - 33.7 In at% and the University of Central Florida provided a series of MBE grown IGO samples with compositions from $x = 13$ - 36.8 in $(In_xGa_{1-x})_2O_3$ determined through WDX. The PLD sample showed crystallographic variation with increasing In content confirmed through EBSD, going from monoclinic for low In contents, mixed phase of monoclinic-hexagonal-cubic for moderate and cubic for high In contents. WDX mapping and SE imaging of the MBE samples showed a high degree of compositional variation and surface roughness dependent on both growth temperature and In availability during growth. CL spectra indicate strong luminescence in the UV, blue and green spectral ranges for both sets of IGO. UV luminescence being attributed to STH emission, blue being DAP recombination involving V_{Ga} and green involving V_{Ga} and complexes involving the alloyed In. Increasing In content modulates the spectral intensity of the three luminescence bands, decreasing UV and increasing blue and green as the V_{Ga} and V_{Ga} In complex density increases. The wavelength/energy of the peak luminescence of the three bands also redshifts with increasing In content compared to Ga_2O_3, indicative of the reduction in material bandgap. The magnitude of the shift was found to be nonlinear for UV emission, increasing from 385 - 395 nm shifts for low levels of In alloying (2-3 at%) and a further 10 nm shift which then levels off at $\approx$405 nm for In contents $\geq$14 at%. Blue emission wavelength increasing linearly by 10nm between 460 - 470 nm for In contents $\geq$14 at%, green luminescence shows a similar dependence however different magnitudes of redshift were observed for the PLD and MBE samples, PLD increasing by 40 nm from $\approx$500 nm for the PLD and by 60 nm for the MBE samples.

Chapter 6 contains similar analysis to Chapter 5 however on a set of tin-gallium oxide samples grown upon various substrates. Sn incorporation was found to be dependent on three factors: Sn availability, substrate choice and growth temperature. Low temperature growth (500 °C vs 600 °C) increased Sn incorporation while (010) Ga_2O_3 substrates produced near double the Sn incorporation compared to (-201) under similar growth conditions, likely due to the Sn preference to occupy octahedral Ga sites over tetrahedral. Optical studies show the same three luminescence bands as the IGO samples with the same modulation of the UV vs the blue and green luminescence intensity with increasing Sn content. Combined WDX and CL cross sectional mapping also confirm the UV suppression and onset of green and intense blue emission within regions of high Sn content. DFT calculations confirm that the source of blue and green emission is likely to involve the increased density of V_{Ga} and either V_{Ga} and V_{Ga}+Sn complexes respectively. Redshifting of the peak wavelength of these spectral bands was again observed and attributed to the bandgap reduction due to the Sn alloying, confirmed through transmission spectroscopy. Photodetectors fabricated from these TGO films present with enhanced spectral responsivity and high gain in the lower energy UV regions compared to their standard Ga_2O_3 counterparts with the increased V_{Ga} density produced through alloying acting as hole trapping sites, reducing the height of the Schottky barrier and producing the high gain observed.

Moving away from experimental work, Chapter 7 is a computational study investigating the impact of X-ray secondary fluorescence on compositional WDX measurements of semiconductor thin films. Secondary fluorescence across compositional boundaries can heavily skew the quantification of geological and metallurgic specimens but was found to be negligible for the investigation of semiconductor thin films, likely due to the lower energy beam conditions used for these measurements. This was found to be true for multiple semiconductor materials ($Al_xGa_{1-x}N$, $In_xAl_{1-x}N$ & Ga_2O_3) grown upon different material substrates with varying levels of alloying. Results show that secondary fluorescence must be considered when performing trace element analyses, particularly when the trace element is also present in the substrate e.g Si doping within Ga_2O_3/Si materials. Variable beam voltage simulations confirm that the impact of secondary fluorescence on these trace element measurements can be suppressed by using the lowest acceptable beam energy for the material system under measurement, reducing the primary excitation volume and subsequent secondary fluorescence excitation volume, restricting it to the film layer. The secondary fluorescence impact results may be mostly negligible but add confidence to the experimental work completed in previous chapters, ensuring results are not skewed and indicate a near exact composition for the materials analysed.

8.2 Future work

The work completed in this thesis investigates semiconductor materials and alloys for uses in UV emitters and photodetectors however additional research must be completed to fully evaluate the feasibility of these materials including additional measurements advancing on what has been determined here.

Through investigation of semi- and non-polar $Al_xGa_{1-x}N$ materials an attempt has been made to mitigate the impact of the QCSE and improve the efficiency of $Al_xGa_{1-x}N$ based LEDs. This is not the only issue hindering the efficiency of theses devices though, the major issues of *n*-type doping in high AlN films and general *p*-type doping must be assessed as well. The electronic properties of *n*-type doped semi-polar $Al_xGa_{1-x}N$:Si was lightly touched on here but must now be continued through the growth and investigation of doped $Al_xGa_{1-x}N$ films on the other crystal orientations investigated here. Deeper understanding of the defects present in these films will also help improve the quality of these materials and their applied devices, identifying the specific defects involved in the broad band luminescence seen from CL measurements and how their formation is suppressed or enhanced for semi- and non-polar growth.

The TGO and IGO alloys in this study have confirmed the ability to reduce the bandgap of Ga_2O_3 allowing the fabrication of UV-B photodetectors, however the influence of the growth parameters on the alloy incorporation still has unanswered questions, particularly for the In. Further growth of these materials however with varied growth conditions would allow the factors that impact incorporation to be determined, especially growth temperature which was found to heavily impact the Sn incorporation rate in the TGO films. Once a greater understanding of the alloy incorporation is understood a proper degree of control over the material bandgap must be developed, allowing the fabrication of tuned photodetectors operating in desired spectral ranges.

Having numerous samples with compositions spanning a greater Sn and In compositional range, particularly in the compositional gaps of the alloys investigated here would also allow the bandgap dependence on alloy concentration to be accurately determined through additional transmission spectroscopy measurements and spectral peak energy/wavelength dependence on bandgap to be determined with through the deconvolution of additional CL spectra. The large sample pool would also allow rigorous examination of the photodetector properties from devices fabricated from these materials, seeing whether the ultra high responsivities shown here can be replicated or possibly enhanced further.

Lastly, the study of Ga_2O_3 alloys in this thesis only features alloys known to reduce the semiconductor bandgap, alternatively investigating alloys such as AGO increasing the bandgap of the material would be of interest. The investigation of these alloys is relatively still in its infancy and each new alloy brings about its own challenges and difficulties similar to that mentioned in this thesis (e.g poor crystal quality, phase changes) but would help develop an understanding of what is capable from Ga_2O_3 alloys and the advantageous and detrimental properties of the materials when used in optical devices similarly to the III-nitrides. It would be of great benefit to know if the bandgap increase from AGO is reflected in the increased energy of the luminescence bands, opposite to seen here in IGO and TGO.

List of Figures

List of Tables

Bibliography

[1] N. Holonyak and S. F. Bevacqua, "Coherent (visible) light emission from Ga(As1-xPx) junctions," *Applied Physics Letters*, vol. 1, pp. 82–83, dec 1962.

[2] H. P. Maruska and J. J. Tietjen, "The preparation and properties of vapor-deposited single-crystal-line GaN," *Applied Physics Letters*, vol. 15, no. 10, pp. 327–329, 1969.

[3] H. Amano, M. Kito, K. Hiramatsu, and I. Akasaki, "P-type conduction in Mg-doped GaN treated with low-energy electron beam irradiation (LEEBI)," *Japanese Journal of Applied Physics*, vol. 28, pp. L2112–L2114, dec 1989.

[4] S. Nakamura, Y. Harada, and M. Seno, "Novel metalorganic chemical vapor deposition system for GaN growth," *Applied Physics Letters*, vol. 58, no. 18, pp. 2021–2023, 1991.

[5] Y. Taniyasu, M. Kasu, and T. Makimoto, "An aluminium nitride light-emitting diode with a wavelength of 210 nanometres," *Nature*, vol. 441, no. 7091, pp. 325–328, 2006.

[6] S. Iwaguch, K. Matsumura, Y. Tokuoka, S. Wakui, and N. Kawashima, "Sterilization system using microwave and UV light," *Colloids and Surfaces B: Biointerfaces*, vol. 25, pp. 299–304, aug 2002.

[7] W. Wang, W. Wang, Q. Fan, Y. Wang, Z. Qiao, and X. Wang, "Effects of UV radiation on humic acid coagulation characteristics in drinking water treatment processes," *Chemical Engineering Journal*, vol. 256, pp. 137–143, nov 2014.

[8] G. Matafonova and V. Batoev, “Recent advances in application of UV light-emitting diodes for degrading organic pollutants in water through advanced oxidation processes: A review,” apr 2018.

[9] D. Kedar, “Subsea ultraviolet solar-blind broadband free-space optics communication,” *Optical Engineering*, vol. 48, p. 046001, apr 2009.

[10] R. Yuan and J. Ma, “Review of ultraviolet non-line-of-sight communication,” jun 2016.

[11] R. J. Drost and B. M. Sadler, “Survey of ultraviolet non-line-of-sight communications,” 2014.

[12] M. Kneissl, T. Y. Seong, J. Han, and H. Amano, “The emergence and prospects of deep-ultraviolet light-emitting diode technologies,” mar 2019.

[13] H. Amano, R. Collazo, C. D. Santi, S. Einfeldt, M. Funato, J. Glaab, S. Hagedorn, A. Hirano, H. Hirayama, R. Ishii, Y. Kashima, Y. Kawakami, R. Kirste, M. Kneissl, R. Martin, F. Mehnke, M. Meneghini, A. Ougazzaden, P. J. Parbrook, S. Rajan, P. Reddy, F. Römer, J. Ruschel, B. Sarkar, F. Scholz, L. J. Schowalter, P. Shields, Z. Sitar, L. Sulmoni, T. Wang, T. Wernicke, M. Weyers, B. Witzigmann, Y.-R. Wu, T. Wunderer, and Y. Zhang, “The 2020 UV emitter roadmap,” *Journal of Physics D: Applied Physics*, vol. 53, p. 503001, dec 2020.

[14] Y. Kokubun, T. Abe, and S. Nakagomi, “Sol-gel prepared (Ga 1-xIn x) 2O 3 thin films for solar-blind ultraviolet photodetectors,” *Physica Status Solidi (A) Applications and Materials Science*, vol. 207, pp. 1741–1745, jul 2010.

[15] H. Chen, K. Liu, L. Hu, A. A. Al-Ghamdi, and X. Fang, “New concept ultraviolet photodetectors,” nov 2015.

[16] E. V. Gorokhov, A. N. Magunov, V. S. Feshchenko, and A. A. Altukhov, “Solar-blind UV flame detector based on natural diamond,” *Instruments and Experimental Techniques*, vol. 51, pp. 280–283, jan 2008.

[17] M.-P. Zorzano, J. Martin-Soler, and J. Gomez-Elvir, “UV Photodiodes Response to Non-Normal, Non-Colimated and Diffusive Sources of Irradiance,” in *Photodiodes - Communications, Bio-Sensings, Measurements and High-Energy Physics*, IntechOpen, sep 2011.

[18] J. Zhang, J. Shi, D. C. Qi, L. Chen, and K. H. Zhang, “Recent progress on the electronic structure, defect, and doping properties of Ga_2O_3,” 2020.

[19] M. Higashiwaki, A. Kuramata, H. Murakami, and Y. Kumagai, “State-of-the-art technologies of gallium oxide power devices,” jul 2017.

[20] H. W. Xue, Q. M. He, G. Z. Jian, S. B. Long, T. Pang, and M. Liu, “An Overview of the Ultrawide Bandgap Ga_2O_3 Semiconductor-Based Schottky Barrier Diode for Power Electronics Application,” 2018.

[21] D. Shinohara and S. Fujita, “Heteroepitaxy of corundum-structured α-Ga_2O_3 thin films on α-Al2O3 substrates by ultrasonic mist chemical vapor deposition,” *Japanese Journal of Applied Physics*, vol. 47, no. 9 PART 1, pp. 7311–7313, 2008.

[22] L. K. Ping, D. D. Berhanuddin, A. K. Mondal, P. S. Menon, and M. A. Mohamed, “Properties and perspectives of ultrawide bandgap Ga_2O_3 in optoelectronic applications,” *Chinese Journal of Physics*, vol. 73, pp. 195–212, oct 2021.

[23] M. Higashiwaki, K. Sasaki, A. Kuramata, T. Masui, and S. Yamakoshi, “Development of gallium oxide power devices,” *Physica Status Solidi (A) Applications and Materials Science*, vol. 211, pp. 21–26, jan 2014.

[24] A. J. Green, J. Speck, G. Xing, P. Moens, F. Allerstam, K. Gumaelius, T. Neyer, A. Arias-Purdue, V. Mehrotra, A. Kuramata, K. Sasaki, S. Watanabe, K. Koshi, J. Blevins, O. Bierwagen, S. Krishnamoorthy, K. Leedy, A. R. Arehart, A. T. Neal, S. Mou, S. A. Ringel, A. Kumar, A. Sharma, K. Ghosh, U. Singisetti, W. Li, K. Chabak, K. Liddy, A. Islam, S. Rajan, S. Graham,

S. Choi, Z. Cheng, and M. Higashiwaki, "β-Gallium oxide power electronics," *APL Materials*, vol. 10, no. 2, 2022.

[25] S. B. Reese, T. Remo, J. Green, and A. Zakutayev, "How Much Will Gallium Oxide Power Electronics Cost?," apr 2019.

[26] M. Bosi, P. Mazzolini, L. Seravalli, and R. Fornari, "Ga_2O_3polymorphs: Tailoring the epitaxial growth conditions," 2020.

[27] R. Roy, V. G. Hill, and E. F. Osborn, "Polymorphism of $Ga_2O_3$and the System Ga_2O_3H2O," *Journal of the American Chemical Society*, vol. 74, pp. 719–722, feb 1952.

[28] B. E. Kananen, L. E. Halliburton, K. T. Stevens, G. K. Foundos, and N. C. Giles, "Gallium vacancies in β-Ga_2O_3 crystals," *Applied Physics Letters*, vol. 110, no. 20, p. 202104, 2017.

[29] H. He, R. Orlando, M. A. Blanco, R. Pandey, E. Amzallag, I. Baraille, and M. Rérat, "First-principles study of the structural, electronic, and optical properties of Ga2 O3 in its monoclinic and hexagonal phases," *Physical Review B - Condensed Matter and Materials Physics*, vol. 74, no. 19, 2006.

[30] J. B. Varley, J. R. Weber, A. Janotti, and C. G. Van De Walle, "Oxygen vacancies and donor impurities in β-Ga2 O 3," *Applied Physics Letters*, vol. 97, no. 14, p. 142106, 2010.

[31] A. Mock, R. Korlacki, C. Briley, V. Darakchieva, B. Monemar, Y. Kumagai, K. Goto, M. Higashiwaki, and M. Schubert, "Band-to-band transitions, selection rules, effective mass, and excitonic contributions in monoclinic β-Ga2 O3," *Physical Review B*, vol. 96, no. 24, p. 245205, 2017.

[32] C. Janowitz, V. Scherer, M. Mohamed, A. Krapf, H. Dwelk, R. Manzke, Z. Galazka, R. Uecker, K. Irmscher, R. Fornari, M. Michling, D. Schmeißer, J. R. Weber, J. B. Varley, and C. G. Van De Walle, "Experimental electronic

structure of In2O3 and Ga_2O_3," *New Journal of Physics*, vol. 13, no. 14pp, p. 85014, 2011.

[33] A. Kuramata, K. Koshi, S. Watanabe, Y. Yamaoka, T. Masui, and S. Yamakoshi, "High-quality β-Ga_2O_3 single crystals grown by edge-defined film-fed growth," in *Japanese Journal of Applied Physics*, vol. 55, pp. 1202–1204, 2016.

[34] D. Y. Guo, Y. P. Qian, Y. L. Su, H. Z. Shi, P. G. Li, J. T. Wu, S. L. Wang, C. Cui, and W. H. Tang, "Evidence for the bias-driven migration of oxygen vacancies in amorphous non-stoichiometric gallium oxide," *AIP Advances*, vol. 7, p. 065312, jun 2017.

[35] F. Zhang, M. Arita, X. Wang, Z. Chen, K. Saito, T. Tanaka, M. Nishio, T. Motooka, and Q. Guo, "Toward controlling the carrier density of Si doped Ga_2O_3 films by pulsed laser deposition," *Applied Physics Letters*, vol. 109, p. 102105, sep 2016.

[36] A. T. Neal, S. Mou, S. Rafique, H. Zhao, E. Ahmadi, J. S. Speck, K. T. Stevens, J. D. Blevins, D. B. Thomson, N. Moser, K. D. Chabak, and G. H. Jessen, "Donors and deep acceptors in β-Ga_2O_3," *Applied Physics Letters*, vol. 113, p. 062101, aug 2018.

[37] M. Wang, S. Mu, and C. G. Van De Walle, "Incorporation of Si and Sn donors in β -Ga_2O_3through surface reconstructions," *Journal of Applied Physics*, vol. 130, no. 18, p. 185703, 2021.

[38] A. K. Rajapitamahuni, L. R. Thoutam, P. Ranga, S. Krishnamoorthy, and B. Jalan, "Impurity band conduction in Si-doped β -Ga_2O_3films," *Applied Physics Letters*, vol. 118, no. 7, p. 72105, 2021.

[39] M. Orita, H. Ohta, M. Hirano, and H. Hosono, "Deep-ultraviolet transparent conductive ß-Ga_2O_3 thin films," *Applied Physics Letters*, vol. 77, no. 25, pp. 4166–4168, 2000.

[40] L. L. Liu, M. K. Li, D. Q. Yu, J. Zhang, H. Zhang, C. Qian, and Z. Yang, "Fabrication and characteristics of N-doped β-Ga2O 3 nanowires," *Applied Physics A: Materials Science and Processing*, vol. 98, no. 4, pp. 831–835, 2010.

[41] C. Tang, J. Sun, N. Lin, Z. Jia, W. Mu, X. Tao, and X. Zhao, "Electronic structure and optical property of metal-doped Ga_2O_3: A first principles study," *RSC Advances*, vol. 6, pp. 78322–78334, aug 2016.

[42] A. Kyrtsos, M. Matsubara, and E. Bellotti, "On the feasibility of p-type Ga2O3," *Applied Physics Letters*, vol. 112, p. 32108, jan 2018.

[43] S. Fujita, "Wide-bandgap semiconductor materials: For their full bloom," 2015.

[44] J. E. Swallow, R. G. Palgrave, P. A. Murgatroyd, A. Regoutz, M. Lorenz, A. Hassa, M. Grundmann, H. Von Wenckstern, J. B. Varley, and T. D. Veal, "Indium Gallium Oxide Alloys: Electronic Structure, Optical Gap, Surface Space Charge, and Chemical Trends within Common-Cation Semiconductors," *ACS Applied Materials and Interfaces*, vol. 13, no. 2, pp. 2807–2819, 2021.

[45] T. H. Chang, S. J. Chang, C. J. Chiu, C. Y. Wei, Y. M. Juan, and W. Y. Weng, "Bandgap-Engineered in Indium-Gallium-Oxide Ultraviolet Phototransistors," *IEEE Photonics Technology Letters*, vol. 27, pp. 915–918, apr 2015.

[46] O. Bierwagen, "Indium oxide - A transparent, wide-band gap semiconductor for (opto)electronic applications," *Semiconductor Science and Technology*, vol. 30, p. 024001, jan 2015.

[47] S. Fujita and K. Kaneko, "Epitaxial growth of corundum-structured wide band gap III-oxide semiconductor thin films," *Journal of Crystal Growth*, vol. 401, pp. 588–592, sep 2014.

[48] C.-C. Wang, S.-H. Yuan, S.-L. Ou, S.-Y. Huang, K.-Y. Lin, Y.-A. Chen, P.-W. Hsiao, and D.-S. Wuu, "Growth and characterization of co-sputtered

aluminum-gallium oxide thin films on sapphire substrates," *Journal of Alloys and Compounds*, vol. 765, pp. 894–900, oct 2018.

[49] S.-H. Yuan, S.-L. Ou, C.-M. Chen, S.-Y. Huang, B.-W. Hsiao, and D.-S. Wuu, "Characterization of aluminum gallium oxide films grown by pulsed laser deposition," *Ceramics International*, vol. 45, pp. 702–707, jan 2019.

[50] A. K. Saikumar, S. D. Nehate, and K. B. Sundaram, "A review of recent developments in aluminum gallium oxide thin films and devices," *Critical Reviews in Solid State and Materials Sciences*, pp. 1–32, jul 2021.

[51] J. S. Speck and S. F. Chichibu, "Nonpolar and Semipolar Group III Nitride-Based Materials," *MRS Bulletin*, vol. 34, no. 5, pp. 304–312, 2009.

[52] P. Mukhopadhyay, I. Hatipoglu, Y. K. Frodason, J. B. Varley, M. S. Williams, D. A. Hunter, N. K. Gunasekar, P. R. Edwards, R. W. Martin, F. Wu, A. Mauze, J. S. Speck, and W. V. Schoenfeld, "Role of defects in ultra-high gain in fast planar tin gallium oxide UV-C photodetector by MBE," *Applied Physics Letters*, vol. 121, p. 111105, sep 2022.

[53] M. D. McCluskey, "Point defects in Ga_2O_3," *Journal of Applied Physics*, vol. 127, no. 10, p. 101101, 2020.

[54] J. M. Johnson, Z. Chen, J. B. Varley, C. M. Jackson, E. Farzana, Z. Zhang, A. R. Arehart, H. L. Huang, A. Genc, S. A. Ringel, C. G. Van De Walle, D. A. Muller, and J. Hwang, "Unusual Formation of Point-Defect Complexes in the Ultrawide-Band-Gap Semiconductor β-Ga2 O3," *Physical Review X*, vol. 9, no. 4, 2019.

[55] B. E. Kananen, N. C. Giles, L. E. Halliburton, G. K. Foundos, K. B. Chang, and K. T. Stevens, "Self-trapped holes in β-Ga_2O_3 crystals," *Journal of Applied Physics*, vol. 122, no. 21, p. 215703, 2017.

[56] J. B. Varley, A. Janotti, C. Franchini, and C. G. Van De Walle, "Role of self-trapping in luminescence and p-type conductivity of wide-band-gap oxides,"

Physical Review B - Condensed Matter and Materials Physics, vol. 85, no. 8, p. 81109, 2012.

[57] S. Mokkapati and C. Jagadish, “III-V compound SC for optoelectronic devices,” apr 2009.

[58] Z. Liu, B. R. Hyun, Y. Sheng, C. J. Lin, M. Changhu, Y. Lin, C. H. Ho, J. H. He, and H. C. Kuo, “Micro-Light-Emitting Diodes Based on InGaN Materials with Quantum Dots,” jun 2022.

[59] D. V. Dinh, N. Hu, Y. Honda, H. Amano, and M. Pristovsek, “Aluminium incorporation in polar, semi- and non-polar AlGaN layers: a comparative study of x-ray diffraction and optical properties,” *Scientific Reports*, vol. 9, no. 15802, 2019.

[60] W. Götz, N. M. Johnson, C. Chen, H. Liu, C. Kuo, and W. Imler, “Activation energies of Si donors in GaN,” *Applied Physics Letters*, vol. 68, no. 22, pp. 3144–3146, 1996.

[61] S. Fritze, A. Dadgar, H. Witte, M. Bügler, A. Rohrbeck, J. Bläsing, A. Hoffmann, and A. Krost, “High Si and Ge n-type doping of GaN doping - Limits and impact on stress,” *Applied Physics Letters*, vol. 100, no. 12, p. 122104, 2012.

[62] Y. Arakawa, K. Ueno, H. Imabeppu, A. Kobayashi, J. Ohta, and H. Fujioka, “Electrical properties of Si-doped GaN prepared using pulsed sputtering,” *Applied Physics Letters*, vol. 110, no. 4, 2017.

[63] M. D. Bremser, W. G. Perry, T. Zheleva, N. V. Edwards, O. H. Nam, N. Parikh, D. E. Aspnes, and R. F. Davis, “Growth, doping and characterization of AlxGa1-x N thin film alloys on 6H-SiC(0001) substrates,” *MRS Internet Journal of Nitride Semiconductor Research*, vol. 1, no. 8, 1996.

[64] C. G. Van De Walle, C. Stampfl, J. Neugebauer, M. D. McCluskey, and N. M. Johnson, "Doping of AlGaN alloys," in *MRS Internet Journal of Nitride Semiconductor Research*, vol. 4, 1999.

[65] K. B. Nam, J. Li, M. L. Nakarmi, J. Y. Lin, and H. X. Jiang, "Achieving highly conductive AlGaN alloys with high Al contents," *Applied Physics Letters*, vol. 81, no. 6, pp. 1038–1040, 2002.

[66] H. M. Foronda, D. A. Hunter, M. Pietsch, L. Sulmoni, A. Muhin, S. Graupeter, N. Susilo, M. Schilling, J. Enslin, K. Irmscher, R. W. Martin, T. Wernicke, and M. Kneissl, "Electrical properties of (11-22) Si:AlGaN layers at high Al contents grown by metal-organic vapor phase epitaxy," *Applied Physics Letters*, vol. 117, no. 22, p. 221101, 2020.

[67] M. L. Nakarmi, K. H. Kim, K. Zhu, J. Y. Lin, and H. X. Jiang, "Transport properties of highly conductive n-type Al-rich Al xGa 1-xN (x0.7)," *Applied Physics Letters*, vol. 85, no. 17, pp. 3769–3771, 2004.

[68] P. Pampili and P. J. Parbrook, "Doping of III-nitride materials," may 2017.

[69] R. Blasco, A. Ajay, E. Robin, C. Bougerol, K. Lorentz, L. C. Alves, I. Mouton, L. Amichi, A. Grenier, and E. Monroy, "Electrical and optical properties of heavily Ge-doped AlGaN," *Journal of Physics D: Applied Physics*, vol. 52, no. 12, 2019.

[70] A. Ajay, J. Schörmann, M. Jiménez-Rodriguez, C. B. Lim, F. Walther, M. Rohnke, I. Mouton, L. Amichi, C. Bougerol, M. I. Den Hertog, M. Eickhoff, and E. Monroy, "Ge doping of GaN beyond the Mott transition," *Journal of Physics D: Applied Physics*, vol. 49, p. 445301, oct 2016.

[71] T. Tanaka, A. Watanabe, H. Amano, Y. Kobayashi, I. Akasaki, S. Yamazaki, and M. Koike, "P-type conduction in Mg-doped GaN and Al0.08Ga0.92N grown by metalorganic vapor phase epitaxy," *Applied Physics Letters*, vol. 65, no. 5, pp. 593–594, 1994.

[72] X. Qiu, Y. Chen, E. Han, Z. Lv, Z. Song, and H. Jiang, "High doping efficiency in p-type Al-rich AlGaN by modifying the Mg doping planes," *Materials Advances*, vol. 1, pp. 77–85, apr 2020.

[73] S. Nakamura, T. Mukai, M. Senoh, and N. Iwasa, "Thermal annealing effects on P-type Mg-doped GaN films," *Japanese Journal of Applied Physics*, vol. 31, pp. 139–142, feb 1992.

[74] R. Q. Wu, L. Shen, M. Yang, Z. D. Sha, Y. Q. Cai, Y. P. Feng, Z. G. Huang, and Q. Y. Wu, "Possible efficient p-type doping of AlN using Be: An ab initio study," *Applied Physics Letters*, vol. 91, p. 39, oct 2007.

[75] H. Ahmad, J. Lindemuth, Z. Engel, C. M. Matthews, T. M. McCrone, and W. A. Doolittle, "Substantial P-Type Conductivity of AlN Achieved via Beryllium Doping," *Advanced Materials*, vol. 33, oct 2021.

[76] E. F. Schubert, *Light-Emitting Diodes (3rd Edition, 2018).* E. Fred Schubert, 2018.

[77] I. Akasaki, "Key inventions in the history of nitride-based blue LED and LD," *Journal of Crystal Growth*, vol. 300, pp. 2–10, mar 2007.

[78] H. Amano, I. Akasaki, T. Kozawa, K. Hiramatsu, N. Sawaki, K. Ikeda, and Y. Ishii, "Electron beam effects on blue luminescence of zinc-doped GaN," *Journal of Luminescence*, vol. 40-41, pp. 121–122, feb 1988.

[79] I. Akasaki, H. Amano, H. Murakami, M. Sassa, H. Kato, and K. Manabe, "Growth of GaN and AlGaN for UV/blue p-n junction diodes," *Journal of Crystal Growth*, vol. 128, pp. 379–383, mar 1993.

[80] F. Mehnke, L. Sulmoni, M. Guttmann, T. Wernicke, and M. Kneissl, "Influence of light absorption on the performance characteristics of UV LEDs with emission between 239 and 217 nm," *Applied Physics Express*, vol. 12, p. 012008, jan 2019.

[81] J. Bruckbauer, Z. Li, G. Naresh-Kumar, M. Warzecha, P. R. Edwards, L. Jiu, Y. Gong, J. Bai, T. Wang, C. Trager-Cowan, and R. W. Martin, "Spatially-resolved optical and structural properties of semi-polar (11 22) Al x Ga1-x N with x up to 0.56," *Scientific Reports*, vol. 7, pp. 1–10, sep 2017.

[82] H.-M. Huang, Y.-C. Wu, and T.-C. Lu, "Exciton Localization Behaviors of Basal Stacking Faults in a-Plane AlGaN Alloys," *Journal of The Electrochemical Society*, vol. 158, p. H491, mar 2011.

[83] Z. Bryan, I. Bryan, S. Mita, J. Tweedie, Z. Sitar, and R. Collazo, "Strain dependence on polarization properties of AlGaN and AlGaN-based ultraviolet lasers grown on AlN substrates," *Applied Physics Letters*, vol. 106, no. 23, p. 232101, 2015.

[84] R. G. Banal, M. Funato, and Y. Kawakami, "Optical anisotropy in [0001]-oriented Alx Ga1-x N/AlN quantum wells (x¿0.69)," *Physical Review B - Condensed Matter and Materials Physics*, vol. 79, no. 12, 2009.

[85] K. B. Nam, J. Li, M. L. Nakarmi, J. Y. Lin, and H. X. Jiang, "Unique optical properties of AlGaN alloys and related ultraviolet emitters," *Applied Physics Letters*, vol. 84, pp. 5264–5266, jun 2004.

[86]

[87] J. Xu, W. Zheng, and F. Huang, "Gallium oxide solar-blind ultraviolet photodetectors: A review," 2019.

[88] T. F. Kuech, "Metal-organic vapor phase epitaxy of compound semiconductors," 1987.

[89] N. G. Young, R. M. Farrell, M. Iza, S. Nakamura, S. P. DenBaars, C. Weisbuch, and J. S. Speck, "Germanium doping of GaN by metalorganic chemical vapor deposition for polarization screening applications," *Journal of Crystal Growth*, vol. 455, pp. 105–110, dec 2016.

[90] P. Kozodoy, S. Keller, S. P. DenBaars, and U. K. Mishra, “MOVPE growth and characterization of Mg-doped GaN,” *Journal of Crystal Growth*, vol. 195, pp. 265–269, dec 1998.

[91] E. Iliopoulos and T. D. Moustakas, “Growth kinetics of AlGaN films by plasma-assisted molecular-beam epitaxy,” *Applied Physics Letters*, vol. 81, pp. 295–297, jun 2002.

[92] B. R. Tak, S. Kumar, A. K. Kapoor, D. Wang, X. Li, H. Sun, and R. Singh, “Recent advances in the growth of gallium oxide thin films employing various growth techniques - A review,” aug 2021.

[93] C. Fischer, “Crucibles,” 2017.

[94] F. Rinaldi, “Basics of Molecular Beam Epitaxy,” *Annual Report*, p. 31, 2002.

[95] A. Mazzi, *Modeling and production of metal nanoparticles through laser ablation and applications to photocatalytic water oxidation.* PhD thesis, 2017.

[96] J. Chen, M. Döbeli, A. Wokaun, and T. Lippert, “Plasma interactions with the N2O background gas: Enhancing the oxidization of alkaline-earth species for pulsed laser deposition,” *Journal of Applied Physics*, vol. 124, no. 8, p. 85308, 2018.

[97] H. M. Christen and G. Eres, “Recent advances in pulsed-laser deposition of complex oxides,” *Journal of Physics Condensed Matter*, vol. 20, p. 264005, jun 2008.

[98] J. J. Prentice, J. A. Grant-Jacob, D. P. Shepherd, R. W. Eason, and J. I. Mackenzie, “Yb-doped mixed-sesquioxide films grown by pulsed laser deposition,” *Journal of Crystal Growth*, vol. 491, pp. 51–56, jun 2018.

[99] H. Von Wenckstern, D. Splith, A. Werner, S. Müller, M. Lorenz, and M. Grundmann, “Properties of Schottky Barrier Diodes on (InxGa1-x)2O3 for 0.01 x 0.85 Determined by a Combinatorial Approach,” *ACS Combinatorial Science*, vol. 17, no. 12, pp. 710–715, 2015.

[100] H. von Wenckstern, M. Kneiß, A. Hassa, P. Storm, D. Splith, and M. Grundmann, "A Review of the Segmented-Target Approach to Combinatorial Material Synthesis by Pulsed-Laser Deposition," *Physica Status Solidi (B) Basic Research*, vol. 257, p. 1900626, jul 2020.

[101] S. L. Ou, D. S. Wuu, Y. C. Fu, S. P. Liu, R. H. Horng, L. Liu, and Z. C. Feng, "Growth and etching characteristics of gallium oxide thin films by pulsed laser deposition," *Materials Chemistry and Physics*, vol. 133, pp. 700–705, apr 2012.

[102] Q. Feng, F. Li, B. Dai, Z. Jia, W. Xie, T. Xu, X. Lu, X. Tao, J. Zhang, and Y. Hao, "The properties of gallium oxide thin film grown by pulsed laser deposition," *Applied Surface Science*, vol. 359, pp. 847–852, dec 2015.

[103] A. V. Moholkar, S. S. Shinde, A. R. Babar, K. U. Sim, Y. bin Kwon, K. Y. Rajpure, P. S. Patil, C. H. Bhosale, and J. H. Kim, "Development of CZTS thin films solar cells by pulsed laser deposition: Influence of pulse repetition rate," *Solar Energy*, vol. 85, pp. 1354–1363, jul 2011.

[104] T. P. Nguyen, Y. T. Hsieh, J. C. Chen, C. Hu, and H. B. Nguyen, "Effect of crucible and crystal rotations on the convexity and the thermal stress in large size sapphire crystals during Czochralski growth," *Journal of Crystal Growth*, vol. 468, pp. 514–525, jun 2017.

[105] C. H. Chen, J. C. Chen, C. W. Lu, and C. M. Liu, "Numerical simulation of heat and fluid flows for sapphire single crystal growth by the Kyropoulos method," in *Journal of Crystal Growth*, vol. 318, pp. 162–167, North-Holland, mar 2011.

[106] D. A. Neumayer and J. G. Ekerdt, "Growth of group III nitrides. A review of precursors and techniques," *Chemistry of Materials*, vol. 8, no. 1, pp. 9–25, 1996.

[107] H. Yavaş, E. Ercan Alp, H. Sinn, A. Alatas, A. H. Said, Y. Shvyd'ko, T. Toellner, R. Khachatryan, S. J. Billinge, M. Zahid Hasan, and W. Sturhahn, "Sapphire analyzers for high-resolution X-ray spectroscopy," *Nuclear Instruments*

and Methods in Physics Research, Section A: Accelerators, Spectrometers, Detectors and Associated Equipment, vol. 582, pp. 149–151, nov 2007.

[108] A. Saxler, P. Kung, C. J. Sun, E. Bigan, and M. Razeghi, "High quality aluminum nitride epitaxial layers grown on sapphire substrates," *Applied Physics Letters*, vol. 64, no. 3, pp. 339–341, 1994.

[109] P. Kung, "The rise of III-nitrides: An introduction," in *Optoelectronic Devices: III Nitrides* (M. R. Mohamed Henini, ed.), pp. 9–22, Elsevier, 2004.

[110] X. Ma, R. Xu, Y. Mei, L. Ying, B. Zhang, and H. Long, "Crystalline anisotropy of β-Ga_2O_3thin films on a c-plane GaN template and a sapphire substrate," *Semiconductor Science and Technology*, vol. 37, no. 3, p. 5, 2022.

[111] S. Nakagomi and Y. Kokubun, "Crystal orientation of β-Ga 2O 3 thin films formed on c-plane and a-plane sapphire substrate," *Journal of Crystal Growth*, vol. 349, pp. 12–18, jun 2012.

[112] K. H. L. Zhang, V. K. Lazarov, P. L. Galindo, F. E. Oropeza, D. J. Payne, H. H.-C. Lai, and R. G. Egdell, "Domain Matching Epitaxial Growth of In2O3 Thin Films on α-Al2O3(0001)," *Crystal Growth & Design*, vol. 12, no. 2, pp. 1000–1007, 2012.

[113] R. L. Weiher and R. P. Ley, "Thermal Expansion of Indium Oxide," jun 1963.

[114] J. Orloff, "A Comparison of Lanthanum Hexaboride , Cold FIeld Emission and Thermal Field Emission Electron Guns for Low Voltage Scanning Electron Microscopy," *Scanning Electron Microscopy*, vol. 3, Jan 1984.

[115] N. Erdman, N. Kikuchi, A. Laudate, and V. Robertson, "The field-emission gun scanning electron microscope enables fast and accurate analysis of materials with high spatial resolution," Tech. Rep. 9, Sep 2009.

[116] R. F. Egerton, *Physical principles of electron microscopy: An introduction to TEM, SEM, and AEM, second edition.* Springer US, 2016.

[117] R. Bormann, *Development and characterization of an electron gun for ultrafast electron microscopy.* PhD thesis, Georg-August-University Göttingen, 2015.

[118] JEOL, “Electron probe micro-analyzer (EPMA), JXA-8230,” tech. rep., 2012.

[119] M. Ezzahmouly, A. Elmoutaouakkil, M. Ed-Dhahraouy, H. Khallok, A. Elouahli, A. Mazurier, A. ElAlbani, and Z. Hatim, “Micro-computed tomographic and SEM study of porous bioceramics using an adaptive method based on the mathematical morphological operations,” dec 2019.

[120] E. Sánchez, M. Torres Deluigi, and G. Castellano, “Mean atomic number quantitative assessment in backscattered electron imaging,” in *Microscopy and Microanalysis*, vol. 18, pp. 1355–1361, Dec 2012.

[121] J. I. Goldstein, D. E. Newbury, J. R. Michael, N. W. Ritchie, J. H. J. Scott, and D. C. Joy, *Scanning electron microscopy and x-ray microanalysis.* New York, NY: Springer New York, 2017.

[122] N. W. Ritchie, D. DeGaetano, D. Edwards, L. Niewoehner, F. Platek, and J. M. Wyatt, “Proposed practices for validating the performance of instruments used for automated inorganic gunshot residue analysis,” *Forensic Chemistry*, vol. 20, Aug 2020.

[123] D. E. Newbury and N. W. Ritchie, “Performing elemental microanalysis with high accuracy and high precision by scanning electron microscopy/silicon drift detector energy-dispersive X-ray spectrometry (SEM/SDD-EDS),” nov 2014.

[124] N. W. Ritchie, D. E. Newbury, and J. M. Davis, “EDS measurements of X-ray intensity at WDS precision and accuracy using a silicon drift detector,” in *Microscopy and Microanalysis*, vol. 18, pp. 892–904, 2012.

[125] F. Sgaramella, M. Miliucci, M. Bazzi, D. Bosnar, M. Bragadireanu, M. Carminati, M. Cargnelli, A. Clozza, G. Deda, L. De Paolis, R. Del Grande, C. Fiorini, C. Guaraldo, M. Iliescu, M. Iwasaki, P. King, P. Levi Sandri, J. Marton, P. Moskal, F. Napolitano, S. Niedźwiecki, K. Piscicchia,

A. Scordo, H. Shi, M. Silarski, D. Sirghi, F. Sirghi, M. Skurzok, A. Spallone, M. Tüchler, J. Zmeskal, and C. Curceanu, "The SIDDHARTA-2 calibration method for high precision kaonic atoms x-ray spectroscopy measurements," *Physica Scripta*, vol. 97, jan 2022.

[126] O. Instruments NanoAnalysis, "Silicon Drift Detectors Explained,"

[127] L. Strüder, P. Lechner, and P. Leutenegger, "Silicon drift detector - The key to new experiments," nov 1998.

[128] S.-Y. Yang, "Electron Probe Microanalysis In Geosciences: Analytical Procedures And Recent Advances," *Atomic Spectroscopy*, vol. 43, jan 2022.

[129] P. Zimmermann, S. Peredkov, P. M. Abdala, S. DeBeer, M. Tromp, C. Müller, and J. A. van Bokhoven, "Modern X-ray spectroscopy: XAS and XES in the laboratory," nov 2020.

[130] R. Wuhrer and K. Moran, "A new life for the wavelength-dispersive X-ray spectrometer (WDS): Incorporation of a silicon drift detector into the WDS for improved quantification and X-ray mapping," in *IOP Conference Series: Materials Science and Engineering*, vol. 304, p. 012021, IOP Publishing, jan 2018.

[131] N. Brodusch, K. Zaghib, and R. Gauvin, "Improvement of the energy resolution of energy dispersive spectrometers (EDS) using Richardson–Lucy deconvolution," *Ultramicroscopy*, vol. 209, p. 112886, feb 2020.

[132] EDAX, "Benefits of WDS Spectral Resolution for Elemental Confirmation," tech. rep.

[133] A. Ul-Hamid, H. M. Tawancy, A. R. I. Mohammed, S. S. Al-Jaroudi, and N. M. Abbas, "Quantitative WDS analysis using electron probe microanalyzer," *Materials Characterization*, vol. 56, no. 3, pp. 192–199, 2006.

[134] O. I. Analytical, "Evolution of the WDS technique,"

[135] H. Matysiak, M. Zagorska, J. Andersson, A. Balkowiec, R. Cygan, M. Rasinski, M. Pisarek, M. Andrzejczuk, K. Kubiak, and K. J. Kurzydlowski, “Microstructure of haynes® 282® superalloy after vacuum induction melting and investment casting of thin-walled components,” *Materials*, vol. 6, no. 11, pp. 5016–5037, 2013.

[136] P. Camus, “Factors Affecting WDS Performance Superiority over EDS,” *Microscopy and Microanalysis*, vol. 21, no. S3, pp. 1629–1630, 2015.

[137] L. Spasevski, B. Buse, P. R. Edwards, D. A. Hunter, J. Enslin, H. M. Foronda, T. Wernicke, F. Mehnke, P. J. Parbrook, M. Kneissl, and R. W. Martin, “Quantification of Trace-Level Silicon Doping in Al x Ga 1-x N Films Using Wavelength-Dispersive X-Ray Microanalysis,” *Microscopy and Microanalysis*, vol. 27, no. 4, pp. 696–704, 2021.

[138] G. Love, M. G. Cox, and V. D. Scott, “Assessment of Philibert’s absorption correction models in electron-probe microanalysis,” *Journal of Physics D: Applied Physics*, vol. 8, no. 14, pp. 1686–1702, 1975.

[139] J. Colby, *Absorption correction tables for microprobe analysis: effect of critical excitation potential*, vol. 944. Office of Technical Services, Department of Commerce, 1965.

[140] S. J. Reed, “Characteristic fluorescence corrections in electron-probe microanalysis,” *British Journal of Applied Physics*, vol. 16, pp. 913–926, jul 1965.

[141] J. Philibert and R. Tixier, “Electron penetration and the atomic number correction in electron probe microanalysis,” *Journal of Physics D: Applied Physics*, vol. 1, pp. 685–694, jun 1968.

[142] J. Philibert, “X-ray optics and x-ray microanalysis,” in *Proceedings of the Third International Symposium, Stanford University*, p. 379, Academic Press New York, NY, 1963.

[143] D. E. Newbury, “Standardless quantitative electron-excited x-ray microanalysis by energy-dispersive spectrometry: What is its proper role?,” *Microscopy and Microanalysis*, vol. 4, no. 6, p. 585–597, 1998.

[144] D. Drouin, A. R. Couture, D. Joly, X. Tastet, V. Aimez, and R. Gauvin, “CASINO V2.42 - A fast and easy-to-use modeling tool for scanning electron microscopy and microanalysis users,” *Scanning*, vol. 29, pp. 92–101, may 2007.

[145] N. Ritchie, “Spectrum simulation in dtsa-ii,” 2009-10-01 2009.

[146] M. A. Khan, M. Shatalov, H. P. Maruska, H. M. Wang, and E. Kuokstis, “III-nitride UV devices,” *Japanese Journal of Applied Physics, Part 1: Regular Papers and Short Notes and Review Papers*, vol. 44, no. 10, pp. 7191–7206, 2005.

[147] M. Kneissl, T. Kolbe, C. Chua, V. Kueller, N. Lobo, J. Stellmach, A. Knauer, H. Rodriguez, S. Einfeldt, Z. Yang, N. M. Johnson, and M. Weyers, “Advances in group III-nitride-based deep UV light-emitting diode technology,” *Semiconductor Science and Technology*, vol. 26, no. 1, p. 14036, 2011.

[148] V. Fiorentini, F. Bernardini, F. D. Sala, A. Di Carlo, and P. Lugli, “Effects of macroscopic polarization in III-V nitride multiple quantum wells,” *Physical Review B - Condensed Matter and Materials Physics*, vol. 60, no. 12, pp. 8849–8858, 1999.

[149] T. Mukai, M. Yamada, and S. Nakamura, “Characteristics of InGaN-Based UV/Blue/Green/Amber/Red Light-Emitting Diodes,” *Japanese Journal of Applied Physics*, vol. 38, no. 7A, pp. 3976–3981, 1999.

[150] H. Masui, S. Nakamura, S. P. DenBaars, and U. K. Mishra, “Nonpolar and semipolar III-nitride light-emitting diodes: Achievements and challenges,” *IEEE Transactions on Electron Devices*, vol. 57, pp. 88–100, jan 2010.

[151] M. Monavarian, A. Rashidi, and D. Feezell, "A Decade of Nonpolar and Semipolar III-Nitrides: A Review of Successes and Challenges," *Physica Status Solidi (A) Applications and Materials Science*, vol. 216, p. 1800628, jan 2019.

[152] C. H. Lin, S. Tamaki, Y. Yamashita, H. Miyake, and K. Hiramatsu, "Effects of AlN buffer layer thickness on the crystallinity and surface morphology of 10-μm-thick a-plane AlN films grown on r-plane sapphire substrates," *Applied Physics Express*, vol. 9, p. 081001, aug 2016.

[153] K. Balakrishnan, V. Adivarahan, Q. Fareed, M. Lachab, B. Zhang, and A. Khan, "First demonstration of semipolar deep ultraviolet light emitting diode on m-plane sapphire with AlGaN multiple quantum wells," *Japanese Journal of Applied Physics*, vol. 49, pp. 0402061–0402063, apr 2010.

[154] R. Akaike, S. Ichikawa, M. Funato, and Y. Kawakami, "AlxGa1-xN-based semipolar deep ultraviolet light-emitting diodes," *Applied Physics Express*, vol. 11, p. 061001, jun 2018.

[155] C. P. Wang and Y. R. Wu, "Study of optical anisotropy in nonpolar and semipolar AlGaN quantum well deep ultraviolet light emission diode," *Journal of Applied Physics*, vol. 112, p. 033104, aug 2012.

[156] Y. H. Ra, S. Kang, and C. R. Lee, "Ultraviolet Light-Emitting Diode Using Nonpolar AlGaN Core–Shell Nanowire Heterostructures," *Advanced Optical Materials*, vol. 6, p. 1701391, jul 2018.

[157] D. Cameron, P. M. Coulon, S. Fairclough, G. Kusch, P. R. Edwards, N. Susilo, T. Wernicke, M. Kneissl, R. A. Oliver, P. A. Shields, and R. W. Martin, "Core-Shell Nanorods as Ultraviolet Light-Emitting Diodes," *Nano Letters*, vol. 23, 2022.

[158] P. Waltereit, O. Brandt, A. Trampert, H. T. Grahn, J. Monniger, M. Ramsteiner, M. Relche, and K. H. Ploog, "Nirtride semiconductors free of electrostatic fields for efficient white light-emitting diodes," *Nature*, vol. 406, pp. 865–868, aug 2000.

[159] S. Adhikari, O. L. C. Lem, F. Kremer, K. Vora, F. Brink, M. Lysevych, H. H. Tan, and C. Jagadish, “Nonpolar AlxGa1xN/AlyGa1yN multiple quantum wells on GaN nanowire for UV emission,” *Nano Research*, vol. 15, pp. 7670–7680, aug 2022.

[160] D. V. Dinh, H. Amano, and M. Pristovsek, “Nonpolar m-plane Al x Ga 1-x N layers grown on m-plane sapphire by MOVPE,” *Journal of Crystal Growth*, vol. 512, pp. 100–104, 2019.

[161] D. V. Dinh, N. Hu, Y. Honda, H. Amano, and M. M. Pristovsek, “Untwinned semipolar (10-13) AlxGa1xN layers grown on m-plane sapphire,” *Semiconductor Science and Technology*, vol. 34, pp. 1–8, oct 2019.

[162] G. Kusch, F. Mehnke, J. Enslin, P. R. Edwards, T. Wernicke, M. Kneissl, and R. W. Martin, “Analysis of doping concentration and composition in wide bandgap AlGaN:Si by wavelength dispersive x-ray spectroscopy,” *Semiconductor Science and Technology*, vol. 32, no. 3, p. 35020, 2017.

[163] D. Y. Han, H. J. Li, G. J. Zhao, H. Y. Wei, S. Y. Yang, and L. S. Wang, “Aluminum incorporation efficiencies in A- and C-plane AlGaN grown by MOVPE,” *Chinese Physics B*, vol. 25, no. 4, 2016.

[164] J. Stellmach, F. Mehnke, M. Frentrup, C. Reich, J. Schlegel, M. Pristovsek, T. Wernicke, and M. Kneissl, “Structural and optical properties of semipolar (1122) AlGaN grown on (1010) sapphire by metal-organic vapor phase epitaxy,” *Journal of Crystal Growth*, vol. 367, pp. 42–47, mar 2013.

[165] D. V. §, N. Hu, Y. Honda, H. Amano, and M. Pristovsek, “Pulsed-flow growth of polar, semipolar and nonpolar AlGaN,” *Journal of Materials Chemistry C*, vol. 8, pp. 8668–8675, jul 2020.

[166] V. G. Batanova, A. V. Sobolev, and V. Magnin, “Trace element analysis by EPMA in geosciences: detection limit, precision and accuracy,” *IOP Conference Series: Materials Science and Engineering*, vol. 304, p. 012001, jan 2018.

[167] L. Spasevski, G. Kusch, P. Pampili, V. Z. Zubialevich, D. V. Dinh, J. Bruckbauer, P. R. Edwards, P. J. Parbrook, and R. W. Martin, "A systematic comparison of polar and semipolar Si-doped AlGaN alloys with high AlN content," *Journal of Physics D: Applied Physics*, vol. 54, no. 3, p. 12, 2021.

[168] M. C. Wagener, G. R. James, and F. Omnès, "Intrinsic compensation of silicon-doped AlGaN," *Applied Physics Letters*, vol. 83, no. 20, pp. 4193–4195, 2003.

[169] S. Washiyama, K. J. Mirrielees, P. Bagheri, J. N. Baker, J. H. Kim, Q. Guo, R. Kirste, Y. Guan, M. H. Breckenridge, A. J. Klump, P. Reddy, S. Mita, D. L. Irving, R. Collazo, and Z. Sitar, "Self-compensation in heavily Ge doped AlGaN: A comparison to Si doping," *Applied Physics Letters*, vol. 118, p. 042102, jan 2021.

[170] F. Mehnke, X. T. Trinh, H. Pingel, T. Wernicke, E. Janzén, N. T. Son, and M. Kneissl, "Electronic properties of Si-doped Alx Ga 1 - X N with aluminum mole fractions above 80no. 14, p. 145702, 2016.

[171] J. L. Lyons, A. Janotti, and C. G. Van De Walle, "Effects of carbon on the electrical and optical properties of InN, GaN, and AlN," *Physical Review B - Condensed Matter and Materials Physics*, vol. 89, no. 3, p. 35204, 2014.

[172] J. S. Harris, B. E. Gaddy, R. Collazo, Z. Sitar, and D. L. Irving, "Oxygen and silicon point defects in Al0.65Ga0.35 N," *Physical Review Materials*, vol. 3, no. 5, 2019.

[173] L. Gordon, J. L. Lyons, A. Janotti, and C. G. Van De Walle, "Hybrid functional calculations of D X centers in AlN and GaN," *Physical Review B - Condensed Matter and Materials Physics*, vol. 89, p. 085204, feb 2014.

[174] P. Bagheri, P. Reddy, S. Mita, D. Szymanski, J. H. Kim, Y. Guan, D. Khachariya, A. Klump, S. Pavlidis, R. Kirste, R. Collazo, and Z. Sitar, "On the Ge shallow-to-deep level transition in Al-rich AlGaN," *Journal of Applied Physics*, vol. 130, no. 5, p. 55702, 2021.

[175] R. McClintock, A. Yasan, K. Mayes, D. Shiell, S. R. Darvish, P. Kung, and M. Razeghi, "High quantum efficiency AlGaN solar-blind p-i-n photodiodes," *Applied Physics Letters*, vol. 84, no. 8, pp. 1248–1250, 2004.

[176] R. W. Martin, P. R. Edwards, K. P. O'Donnell, M. D. Dawson, C. W. Jeon, C. Liu, G. R. Rice, and I. M. Watson, "Cathodoluminescence spectral mapping of III-nitride structures," *Physica Status Solidi (A) Applied Research*, vol. 201, pp. 665–672, mar 2004.

[177] G. Steude, T. Christmann, B. K. Meyer, A. Goeldner, A. Hoffmann, F. Bertram, J. Christen, H. Amano, and I. Akasaki, "Optical investigations of AlGaN on GaN epitaxial films," in *MRS Internet Journal of Nitride Semiconductor Research*, vol. 4, pp. 244–249, Cambridge University Press, 1999.

[178] P. R. Edwards and R. W. Martin, "Cathodoluminescence nano-characterization of semiconductors," *Semiconductor Science and Technology*, vol. 26, no. 6, pp. 64005–64013, 2011.

[179] C. G. Van De Walle and J. Neugebauer, "First-principles calculations for defects and impurities: Applications to III-nitrides," 2004.

[180] P. Kamyczek, E. Placzek-Popko, V. Kolkovsky, S. Grzanka, and R. Czernecki, "A deep acceptor defect responsible for the yellow luminescence in GaN and AlGaN," in *Journal of Applied Physics*, vol. 111, p. 113105, 2012.

[181] T. Mattila and R. Nieminen, "Point-defect complexes and broadband luminescence in GaN and AlN," *Physical Review B - Condensed Matter and Materials Physics*, vol. 55, no. 15, pp. 9571–9576, 1997.

[182] T. Ogino and M. Aoki, "Mechanism of yellow luminescence in GaN," *Japanese Journal of Applied Physics*, vol. 19, pp. 2395–2405, dec 1980.

[183] J. Nishinaka, Y. Taniyasu, T. Akasaka, and K. Kumakura, "Surface morphology control of nonpolar m-plane AlN homoepitaxial layers by flow-rate modu-

lation epitaxy," *Physica Status Solidi (B) Basic Research*, vol. 254, p. 1600545, feb 2017.

[184] A. Hirai, B. A. Haskell, M. B. McLaurin, F. Wu, M. C. Schmidt, K. C. Kim, T. J. Baker, S. P. Denbaars, S. Nakamura, and J. S. Speck, "Defect-mediated surface morphology of nonpolar m -plane GaN," *Applied Physics Letters*, vol. 90, p. 121119, mar 2007.

[185] M. Bobea Graziano, I. Bryan, Z. Bryan, R. Kirste, J. Tweedie, R. Collazo, and Z. Sitar, "Structural characteristics of m-plane AlN substrates and homoepitaxial films," *Journal of Crystal Growth*, vol. 507, pp. 389–394, feb 2019.

[186] I. Tischer, M. Frey, M. Hocker, L. Jerg, M. Madel, B. Neuschl, K. Thonke, R. a.R. Leute, F. Scholz, H. Groiss, E. Müller, and D. Gerthsen, "Basal plane stacking faults in semipolar AlGaN: Hints to Al redistribution," *Physica Status Solidi (B) Basic Research*, vol. 251, pp. 2321–2325, nov 2014.

[187] Z. Li, L. Wang, L. Jiu, J. Bruckbauer, Y. Gong, Y. Zhang, J. Bai, R. W. Martin, and T. Wang, "Optical investigation of semi-polar (11-22) AlxGa1-xN with high Al composition," *Applied Physics Letters*, vol. 110, no. 9, p. 91102, 2017.

[188] G. Kusch, M. Nouf-Allehiani, F. Mehnke, C. Kuhn, P. R. Edwards, T. Wernicke, A. Knauer, V. Kueller, G. Naresh-Kumar, M. Weyers, M. Kneissl, C. Trager-Cowan, and R. W. Martin, "Spatial clustering of defect luminescence centers in Si-doped low resistivity Al0.82Ga0.18N," *Applied Physics Letters*, vol. 107, p. 072103, aug 2015.

[189] N. Nepal, J. Li, M. L. Nakarmi, J. Y. Lin, and H. X. Jiang, "Temperature and compositional dependence of the energy band gap of AlGaN alloys," *Applied Physics Letters*, vol. 87, no. 24, pp. 1–3, 2005.

[190] S. R. Xu, Y. Hao, J. C. Zhang, Y. R. Cao, X. W. Zhou, L. A. Yang, X. X. Ou, K. Chen, and W. Mao, "Polar dependence of impurity incorporation and yellow

luminescence in GaN films grown by metal-organic chemical vapor deposition," *Journal of Crystal Growth*, vol. 312, pp. 3521–3524, nov 2010.

[191] G. Parish, S. Keller, S. P. Denbaars, and U. K. Mishra, "SIMS investigations into the effect of growth conditions on residual impurity and silicon incorporation in GaN and AlxGa1-xN," *Journal of Electronic Materials*, vol. 29, no. 1, pp. 15–20, 2000.

[192] Y. Li, Y. Li, Y. Ji, H. Wang, and D. Zhong, "Sol–gel preparation of Sn doped gallium oxide films for application in solar-blind ultraviolet photodetectors," *Journal of Materials Science*, vol. 57, no. 2, pp. 1186–1197, 2022.

[193] P. Mukhopadhyay, I. Hatipoglu, T. S. Sakthivel, D. A. Hunter, P. R. Edwards, R. W. Martin, G. Naresh-Kumar, S. Seal, and W. V. Schoenfeld, "High Figure-of-Merit Gallium Oxide UV Photodetector on Silicon by Molecular Beam Epitaxy: A Path toward Monolithic Integration," *Advanced Photonics Research*, vol. 2, p. 2000067, apr 2021.

[194] T. Oshima, T. Okuno, and S. Fujita, "Ga_2O_3 thin film growth on c-plane sapphire substrates by molecular beam epitaxy for deep-ultraviolet photodetectors," *Japanese Journal of Applied Physics, Part 1: Regular Papers and Short Notes and Review Papers*, vol. 46, pp. 7217–7220, nov 2007.

[195] T. Minami, Y. Takeda, T. Kakumu, S. Takata, and I. Fukuda, "Preparation of highly transparent and conducting Ga 2 O 3 –In 2 O 3 films by direct current magnetron sputtering," *Journal of Vacuum Science Technology A: Vacuum, Surfaces, and Films*, vol. 15, no. 3, pp. 958–962, 1997.

[196] F. Yakuphanoglu, B. Gunduz, A. A. Al-Ghamdi, W. A. Farooq, and F. El-Tantawy, "Transparent ultraviolet photodiodes based conductive gallium-indium-oxide films/p-type silicon for solar panel tracking systems," *Sensors and Actuators, A: Physical*, vol. 234, pp. 212–222, oct 2015.

[197] F. Zhang, K. Saito, T. Tanaka, M. Nishio, and Q. Guo, "Wide bandgap engineering of (GaIn)2O3 films," *Solid State Communications*, vol. 186, pp. 28–31, may 2014.

[198] I. Hatipoglu, P. Mukhopadhyay, F. Alema, T. S. Sakthivel, S. Seal, A. Osinsky, and W. V. Schoenfeld, "Tuning the responsivity of monoclinic (InxGa1-x)2O3solar-blind photodetectors grown by metal organic chemical vapor deposition," *Journal of Physics D: Applied Physics*, vol. 53, no. 45, p. 454001, 2020.

[199] C. Y. Wang, Y. Dai, J. Pezoldt, B. Lu, T. Kups, V. Cimalla, and O. Ambacher, "Phase stabilization and phonon properties of single crystalline rhombohedral indium oxide," *Crystal Growth and Design*, vol. 8, pp. 1257–1260, apr 2008.

[200] Y. Nie, S. Jiao, S. Li, H. Lu, S. Liu, S. Yang, D. Wang, S. Gao, J. Wang, and Y. Li, "Modulating the blue and green luminescence in the β-Ga_2O_3 films," *Journal of Alloys and Compounds*, vol. 900, p. 163431, apr 2022.

[201] L. Binet and D. Gourier, "Origin of the blue luminescence of -ga_2o_3," *Journal of Physics and Chemistry of Solids*, vol. 59, pp. 1241–1249, aug 1998.

[202] T. Harwig and F. Kellendonk, "Some observations on the photoluminescence of doped β-galliumsesquioxide," *Journal of Solid State Chemistry*, vol. 24, pp. 255–263, apr 1978.

[203] K. Shimamura, E. G. Víllora, T. Ujiie, and K. Aoki, "Excitation and photoluminescence of pure and Si-doped - Ga 2 O3 single crystals," *Applied Physics Letters*, vol. 92, p. 201914, may 2008.

[204] G. Naresh-Kumar, H. MacIntyre, S. Subashchandran, P. R. Edwards, R. W. Martin, K. Daivasigamani, K. Sasaki, and A. Kuramata, "Origin of Red Emission in β-Ga_2O_3 Analyzed by Cathodoluminescence and Photoluminescence Spectroscopy," *Physica Status Solidi (B) Basic Research*, vol. 258, feb 2021.

[205] L. Dai, X. L. Chen, J. K. Jian, M. He, T. Zhou, and B. Q. Hu, "Fabrication and characterization of In2O3 nanowires," *Applied Physics A: Materials Science and Processing*, vol. 75, no. 6, pp. 687–689, 2002.

[206] C. H. Liang, G. W. Meng, Y. Lei, F. Phillipp, and L. D. Zhang, "Catalytic growth of semiconducting In2O3 nanofibers," *Advanced Materials*, vol. 13, no. 17, pp. 1330–1333, 2001.

[207] M. Mazzera, M. Zha, D. Calestani, A. Zappettini, L. Lazzarini, G. Salviati, and L. Zanotti, "Low-temperature In2O3 nanowire luminescence properties as a function of oxidizing thermal treatments," *Nanotechnology*, vol. 18, sep 2007.

[208] M. S. Lee, W. C. Choi, E. K. Kim, C. K. Kim, and S. K. Min, "Characterization of the oxidized indium thin films with thermal oxidation," *Thin Solid Films*, vol. 279, no. 1-2, pp. 1–3, 1996.

[209] J. S. Jeong, J. Y. Lee, C. J. Lee, S. J. An, and G. C. Yi, "Synthesis and characterization of high-quality In2O3 nanobelts via catalyst-free growth using a simple physical vapor deposition at low temperature," *Chemical Physics Letters*, vol. 384, pp. 246–250, jan 2004.

[210] Y. Wang, P. T. Dickens, J. B. Varley, X. Ni, E. Lotubai, S. Sprawls, F. Liu, V. Lordi, S. Krishnamoorthy, S. Blair, K. G. Lynn, M. Scarpulla, and B. Sensale-Rodriguez, "Incident wavelength and polarization dependence of spectral shifts in β-Ga_2O_3 UV photoluminescence," *Scientific Reports*, vol. 8, pp. 1–7, dec 2018.

[211] L. Ghadbeigi, J. Cooke, G. T. Dang, T. Kawaharamura, T. Yasuoka, R. Sun, P. Ranga, S. Krishnamoorthy, M. A. Scarpulla, and B. Sensale-Rodriguez, "Optical Characterization of Gallium Oxide α and β Polymorph Thin-Films Grown on c-Plane Sapphire," *Journal of Electronic Materials*, vol. 50, pp. 2990–2998, jun 2021.

[212] I. López, A. D. Utrilla, E. Nogales, B. Méndez, J. Piqueras, A. Peche, J. Ramírez-Castellanos, and J. M. González-Calbet, "In-doped gallium oxide

micro- and nanostructures: Morphology, structure, and luminescence properties," *Journal of Physical Chemistry C*, vol. 116, pp. 3935–3943, feb 2012.

[213] G. Naresh-Kumar, H. MacIntyre, S. Subashchandran, P. R. Edwards, R. W. Martin, K. Daivasigamani, K. Sasaki, and A. Kuramata, "Origin of Red Emission in β-Ga_2O_3 Analyzed by Cathodoluminescence and Photoluminescence Spectroscopy," *Physica Status Solidi (B) Basic Research*, vol. 258, feb 2021.

[214] J. Díaz, I. López, E. Nogales, B. Méndez, and J. Piqueras, "Synthesis and characterization of silicon-doped gallium oxide nanowires for optoelectronic UV applications," *Journal of Nanoparticle Research*, vol. 13, no. 5, pp. 1833–1839, 2011.

[215] H. Gao, S. Muralidharan, N. Pronin, M. R. Karim, S. M. White, T. Asel, G. Foster, S. Krishnamoorthy, S. Rajan, L. R. Cao, M. Higashiwaki, H. Von Wenckstern, M. Grundmann, H. Zhao, D. C. Look, and L. J. Brillson, "Optical signatures of deep level defects in Ga_2O_3," *Applied Physics Letters*, vol. 112, no. 24, p. 242102, 2018.

[216] P. Mukhopadhyay and W. V. Schoenfeld, "Tin gallium oxide solar-blind photodetectors on sapphire grown by molecular beam epitaxy," *Applied Optics*, vol. 58, p. D22, may 2019.

[217] J. Tauc, R. Grigorovici, and A. Vancu, "Optical Properties and Electronic Structure of Amorphous Germanium," *physica status solidi (b)*, vol. 15, no. 2, pp. 627–637, 1966.

[218] H. von Wenckstern, "Group-III Sesquioxides: Growth, Physical Properties and Devices," sep 2017.

[219] M. Karmaoui, A. B. Jorge, P. F. McMillan, A. E. Aliev, R. C. Pullar, J. A. Labrincha, and D. M. Tobaldi, "One-Step Synthesis, Structure, and Band Gap Properties of SnO 2 Nanoparticles Made by a Low Temperature Nonaqueous Sol–Gel Technique," *ACS Omega*, vol. 3, pp. 13227–13238, oct 2018.

[220] U. S. G. Survey, "Rare Earth Elements — Critical Resources for High Technology," *United States Geol. Surv. Fact Sheet*, vol. 87, no. 2, pp. 1–11, 2002.

[221] S. D. Lee, K. Kaneko, and S. Fujita, "Homoepitaxial growth of beta gallium oxide films by mist chemical vapor deposition," in *Japanese Journal of Applied Physics*, vol. 55, pp. 1202–1210, 2016.

[222] F. Larsson, J. Keller, D. Primetzhofer, L. Riekehr, M. Edoff, and T. Törndahl, "Atomic layer deposition of amorphous tin-gallium oxide films," *Journal of Vacuum Science Technology A*, vol. 37, no. 3, p. 030906, 2019.

[223] X. Zhao, W. Cui, Z. Wu, D. Guo, P. Li, Y. An, L. Li, and W. Tang, "Growth and Characterization of Sn Doped β-Ga_2O_3Thin Films and Enhanced Performance in a Solar-Blind Photodetector," *Journal of Electronic Materials*, vol. 46, no. 4, pp. 2366–2372, 2017.

[224] M. M. Fan, Y. J. Lu, K. L. Xu, Y. X. Cui, L. Cao, and X. Y. Li, "Growth and characterization of Sn-doped β-Ga_2O_3 thin films by chemical vapor deposition using solid powder precursors toward solar-blind ultraviolet photodetection," *Applied Surface Science*, vol. 509, p. 144867, apr 2020.

[225] P. Mukhopadhyay and W. V. Schoenfeld, "High responsivity tin gallium oxide Schottky ultraviolet photodetectors," *Journal of Vacuum Science Technology A*, vol. 38, no. 1, p. 013403, 2020.

[226] I. Hatipoglu, D. A. Hunter, P. Mukhopadhyay, M. S. Williams, P. R. Edwards, R. W. Martin, W. V. Schoenfeld, and G. Naresh-Kumar, "Correlation between deep-level defects and functional properties of β-(Sn xGa1- x)2O3on Si photodetectors," *Journal of Applied Physics*, vol. 130, p. 204501, nov 2021.

[227] P. Gopon, J. Fournelle, P. E. Sobol, and X. Llovet, "Low-Voltage electron-probe microanalysis of Fe-Si compounds using soft X-rays," *Microscopy and Microanalysis*, vol. 19, no. 6, pp. 1698–1708, 2013.

[228] T. Kawaharamura, G. T. Dang, and M. Furuta, "Successful Growth of Conductive Highly Crystalline Sn-Doped α-Ga_2O_3 Thin Films by Fine-Channel Mist Chemical Vapor Deposition," *Japanese Journal of Applied Physics*, vol. 51, p. 40207, mar 2012.

[229] M. Kneiß, A. Hassa, D. Splith, C. Sturm, H. Von Wenckstern, T. Schultz, N. Koch, M. Lorenz, and M. Grundmann, "Tin-assisted heteroepitaxial PLD-growth of κ -Ga 2 O 3 thin films with high crystalline quality," *APL Materials*, vol. 7, no. 2, p. 22516, 2019.

[230] W. Zhang, J. Zhang, L. Chen, W. Wang, T. Zhang, N. Liu, T. Xu, H. Yang, and J. Ye, "Non-equilibrium epitaxy of metastable polymorphs of ultrawide-bandgap gallium oxide," *Applied Physics Letters*, vol. 120, p. 072101, feb 2022.

[231] A. Mauze, Y. Zhang, T. Itoh, E. Ahmadi, and J. S. Speck, "Sn doping of (010) β-Ga_2O_3films grown by plasma-assisted molecular beam epitaxy," *Applied Physics Letters*, vol. 117, p. 222102, dec 2020.

[232] H. Okumura, M. Kita, K. Sasaki, A. Kuramata, M. Higashiwaki, and J. S. Speck, "Systematic investigation of the growth rate of β-Ga_2O_3(010) by plasma-assisted molecular beam epitaxy," *Applied Physics Express*, vol. 7, no. 9, p. 95501, 2014.

[233] N. Nepal, D. Scott Katzer, and D. J. Meyer, "MBE growth and characterization of gallium oxide," in *Gallium Oxide*, pp. 31–46, Elsevier, oct 2019.

[234] V. Balakrishnan, *MBE grown aluminum oxide and aluminum-gallium oxide thin films for beta-gallium oxide power devices.* Thesis, Cornell University, 2019.

[235] B. W. Krueger, C. S. Dandeneau, E. M. Nelson, S. T. Dunham, F. S. Ohuchi, and M. A. Olmstead, "Variation of Band Gap and Lattice Parameters of β(Al x Ga 1 x) 2 O 3 Powder Produced by Solution Combustion Synthesis," *Journal of the American Ceramic Society*, vol. 99, pp. 2467–2473, jul 2016.

[236] H. Peelaers, J. B. Varley, J. S. Speck, and C. G. Van de Walle, "Structural and electronic properties of Ga_2O_3-Al2O3 alloys," *Applied Physics Letters*, vol. 112, p. 242101, jun 2018.

[237] S. Poncé and F. Giustino, "Structural, electronic, elastic, power, and transport properties of β-Ga2 O3 from first principles," *Physical Review Research*, vol. 2, no. 3, p. 33102, 2020.

[238] M. M. Chang, D. Y. Guo, X. L. Zhong, F. B. Zhang, and J. B. Wang, "Impact of 100 MeV high-energy proton irradiation on β -Ga_2O_3solar-blind photodetector: Oxygen vacancies formation and resistance switching effect," *Journal of Applied Physics*, vol. 132, no. 12, p. 123105, 2022.

[239] Q. D. Ho, T. Frauenheim, and P. Deák, "Origin of photoluminescence in β- G a2 O3," *Physical Review B*, vol. 97, p. 115163, mar 2018.

[240] Y. Usui, D. Nakauchi, N. Kawano, G. Okada, N. Kawaguchi, and T. Yanagida, "Scintillation and optical properties of Sn-doped Ga_2O_3 single crystals," *Journal of Physics and Chemistry of Solids*, vol. 117, pp. 36–41, jun 2018.

[241] A. Kohan, G. Ceder, D. Morgan, and C. G. Van de Walle, "First-principles study of native point defects in ZnO," *Physical Review B - Condensed Matter and Materials Physics*, vol. 61, no. 22, pp. 15019–15027, 2000.

[242] A. Janotti and C. G. Van De Walle, "Fundamentals of zinc oxide as a semiconductor," *Reports on Progress in Physics*, vol. 72, p. 126501, oct 2009.

[243] L. C. Tien and C. H. Ho, "Synthesis, optical characterization, and environmental applications of β-Ga2O3 nanowires," in *Gallium Oxide: Technology, Devices and Applications*, pp. 67–90, Elsevier, jan 2018.

[244] S. Rafique, L. Han, A. T. Neal, S. Mou, J. Boeckl, and H. Zhao, "Towards High-Mobility Heteroepitaxial β-Ga_2O_3 on Sapphire Dependence on The Substrate Off-Axis Angle," *physica status solidi (a)*, vol. 215, no. 2, p. 1700467, 2018.

[245] E. B. Yakimov, A. Y. Polyakov, I. V. Shchemerov, N. B. Smirnov, A. A. Vasilev, A. I. Kochkova, P. S. Vergeles, E. E. Yakimov, A. V. Chernykh, M. Xian, F. Ren, and S. J. Pearton, “On the nature of photosensitivity gain in Ga_2O_3 Schottky diode detectors: Effects of hole trapping by deep acceptors,” *Journal of Alloys and Compounds*, vol. 879, p. 160394, oct 2021.

[246] S. Oh, H. W. Kim, and J. Kim, “High Gain β-Ga 2 O 3 Solar-Blind Schottky Barrier Photodiodes via Carrier Multiplication Process,” *ECS Journal of Solid State Science and Technology*, vol. 7, no. 11, pp. Q196–Q200, 2018.

[247] H. Zhou, L. Cong, J. Ma, B. Li, H. Xu, and Y. Liu, “Suppression of persistent photoconductivity in high gain Ga_2O_3Schottky photodetectors,” *Chinese Physics B*, vol. 30, no. 12, p. 126104, 2021.

[248] A. M. Armstrong, M. H. Crawford, A. Jayawardena, A. Ahyi, and S. Dhar, “Role of self-trapped holes in the photoconductive gain of β -gallium oxide Schottky diodes,” *Journal of Applied Physics*, vol. 119, no. 10, p. 103102, 2016.

[249] D. A. Hunter, S. P. Lavery, P. R. Edwards, and R. W. Martin, “Assessing the Impact of Secondary Fluorescence on X-Ray Microanalysis Results from Semiconductor Thin Films,” *Microscopy and Microanalysis*, vol. 28, pp. 1–12, may 2022.

[250] J. A. Dalton and S. J. Lane, “Electron microprobe analysis of Ca in olivine close to grain boundaries: the problem of secondary X-ray fluorescence,” *American Mineralogist*, vol. 81, pp. 194–201, jan 1996.

[251] G. F. Bastin, F. J. van Loo, P. J. Vosters, and J. W. Vrolljk, “A correction procedure for characteristic fluorescence encountered in microprobe analysis near phase boundaries,” *Scanning*, vol. 5, pp. 172–183, jan 1983.

[252] X. Llovet, P. T. Pinard, J. J. Donovan, and F. Salvat, “Secondary fluorescence in electron probe microanalysis of material couples,” *Journal of Physics D: Applied Physics*, vol. 45, p. 225301, jun 2012.

[253] X. Llovet and G. Galan, “Correction of secondary X-ray fluorescence near grain boundaries in electron microprobe analysis: Application to thermobarometry of spinel lherzolites,” *American Mineralogist*, vol. 88, pp. 121–130, jan 2003.

[254] N. W. Ritchie, “Efficient Simulation of Secondary Fluorescence Via NIST DTSA-II Monte Carlo,” *Microscopy and Microanalysis*, vol. 23, no. 3, pp. 618–633, 2017.

[255] J.-L. Pouchou and F. Pichoir, “Electron Probe Quantitation,” in *Electron Probe Quantitation* (K. Heinrich and D. E. Newbury, eds.), ch. Quantitati, pp. 31–75, Springer US, 1991.

[256] J. L. Pouchou, “X-ray microanalysis of thin surface films and coatings,” in *Mikrochimica Acta*, vol. 138-139, pp. 133–152, 2002.

[257] M. C. Miller, “X-ray Fluorescence,” in *Passive nondestructive assay of nuclear materials* (D. Reilly, N. Ensslin, H. Smith, S. Kreiner, Los Alamos National Laboratory (U.S.), and Etats-Unis. Nuclear Regulatory Commission., eds.), pp. 313–329, US Department of Commerce, National Technical Information Service, 1991.

[258] J. H. Fournelle, S. Kim, and J. H. Perepezko, “Monte Carlo simulation of Nb Kα secondary fluorescence in EPMA: Comparison of PENELOPE simulations with experimental results,” in *Surface and Interface Analysis*, vol. 37, pp. 1012–1016, nov 2005.

[259] Y. Yuan, H. Demers, S. Rudinsky, and R. Gauvin, “Secondary fluorescence correction for characteristic and bremsstrahlung X-Rays using monte carlo X-ray depth distributions applied to bulk and multilayer materials,” *Microscopy and Microanalysis*, vol. 25, pp. 92–104, feb 2019.

[260] E. Taylor, M. D. Smith, T. C. Sadler, K. Lorenz, H. N. Li, E. Alves, P. J. Parbrook, and R. W. Martin, “Structural and optical properties of Ga auto-incorporated InAlN epilayers,” *Journal of Crystal Growth*, vol. 408, pp. 97–101, dec 2014.

[261] A. Moy and J. Fournelle, "$\phi(\rho \mathrm{z})$ Distributions in Bulk and Thin-Film Samples for EPMA. Part 2: BadgerFilm: A New Thin-Film Analysis Program," *Microscopy and Microanalysis*, vol. 27, no. 2, pp. 284–296, 2021.

[262] Y. Yuan, H. Demers, X. Wang, and R. Gauvin, "Secondary Fluorescence of 3D Heterogeneous Materials Using a Hybrid Model," *Microscopy and Microanalysis*, vol. 26, pp. 484–496, jun 2020.